UGC
University Grants Commission
Journal No.: 63571

International Journal of

Advance and Innovative Research

(Conference Special)

Part – 2

NATIONAL CONFERENCE
ON
FUNCTIONAL MATERIALS SYNTHESIS AND CHARACTERIZATION TECHNIQUES

SPONSORED BY

Dr. Babasaheb Ambedkar Marathwada University Aurangabad (M.S)

ORGANIZED BY
Department of Physics,
Vaidyanath College, Parli-Vaijnath, Dist. Beed
Saturday, 2nd March 2019

With Support and Inspirations From
RUSA Centre for Advanced Sensor Technology
Dr. Babasaheb Ambedkar Marathwada University, Aurangabad

In association with

Indian Academicians and Researcher's Association

Jawahar Education Society's

Vaidyanath College

Parli-Vaijnath, Dist. Beed - 431515, Maharashtra

Affiliated to Dr. Babasaheb Ambedkar Marathwada University, Aurangabad

NAAC Accredied a 'B' level with CGPA (2.53)

Guest Editors of Special Issue

Dr. Madhav N Rode

Dr. Dilipkumar Meshram

ABOUT COLLEGE

Jawahar Education Society's Vaidyanath College (ARTS, SCIENCE & COMMERCE) was established on June 15,1968 to cater higher education in rural area of Marathwada region. It is affiliated to Dr. Babasaheb Ambedkar Marathwada University, Aurangabad. It is accredited by NAAC at B level. The college offers UG and PG courses and has been contributing to churn out good human resource through academic process. Vaidyanath College is one of the leading institutions in the Marathwada region. It imparts education to the needy students from backward and rural areas. In the 20th century, the social workers put forward a new and life turning avenue before the society by establishing this reputed institution with a motto "Satyam Dnyanamnatam Brahma". It means "The truth, full of knowledge is the principle known as Brahma". Since 1968 it has been constantly serving to the society in various ways. The institution is focusing on the holistic development of the students by enriching adequate learning resources. In the past few years, Vaidyanath College has established a distinctive position among leading College in the Marathwada region.

ABOUT IARA

Indian Academicians and Researchers Association (IARA)   is an educational and scientific research organization of Academicians, Research Scholars and practitioners responsible for sharing information about research activities, projects, conferences to its members. IARA offers an excellent opportunity for networking with other members and exchange knowledge. It also takes immense pride in its services offerings to undergraduate and graduate students. Students are provided opportunities to develop and clarify their research interests and skills as part of their preparation to become faculty members and researcher. Visit our website www.iaraedu.com for more details.

ABOUT THE CONFERENCE

National Conference on Functional Materials Synthesis and Characterization Techniques (NCFMSCT-2019) is organized by Department of Physics, Vaidyanath College, Parli - Vaijnath considering vital role of functional materials in the development of indigenous technology the present deliberation has the objective of creating a national forum for academics, researchers, scientists and students. The conference will include participation of renowned keynote speakers, oral presentation.

A BRIEF ABOUT ORANIZING COMMITTEES

CHIEF PATRONS
Hon'ble. Jugalkishorji Lohiya
Chairman, Jahwahar Education Society's

Hon'ble. Dattapp Itke
Secretary, Jahwahar Education Society's

Hon'ble. Fulchand Karad
Vice Chairman, Jahwahar Education Society's

Hon'ble. Dr. D. G. Munde
Vice Chairman, Jahwahar Education Society's

Hon'ble. Dr.Sureshji Chaudhari
Joint Secretary, J. E. Society's

Hon'ble. Sureshji Agrawal
Treasurer, Jahwahar Education Society's

PATRON
Dr. R. K. Ippar
Principal, Vaidyanath College, Parli

ORGANIZING SECRETARY
Dr. D. V. Meshram

CONVENER
Dr. Madhav N. Rode

CO-CONVENER
Dr. V. B. Kawade

JOINT SECRETARY
Dr. B. V. Kendre

Dr. B. R. Chavan

MEMBERS
Dr. J. V. Jagatkar, Vice Principal
Asst. Prof. D. K. Andhale, JES, Director
Dr. T. A. Gitte
Asst. Prof. B. S. Satpute,
Asst. Prof. B. P. Gajbhare
Asst. Prof. M. M. Kamble
Asst. Prof. U. R. Kande

Asst. Prof. S. A. Dhande
Asst. Prof. Milind V. Sonkamble
Dr. C. T. Birajdar, SMP College, Murum
Dr. Ravindra Katre, KMJ College, Washi
Dr. R. J. Topre, Yogeshori College, Ambajogai
Dr. Mahendra Shinde, M.J.M. College, Karanjali, Nashik
Dr. Swapil Arsad, M. F. M Warad College

NATIONAL ADVISORY COMMITTEE

Prof. Dr. Aswal Dinesh, Director- CSIR-NPL, New Delhi

Prof. Dr. V. N.Mani, Scientist-F at C-MET, Govt. of India, Hyderabad

Prof. Dr.B.N.Gajbhiye, Scientist-G, DRDO, Hyderabad

Prof. Dr.GanesanV. , Centre Director-UGC,DAE,CSR,Indore

Prof. Dr. N. L. Singh, M. S. University, Vadodara, Gujrat, India

Prof. Dr. M. D. Shirsat, Director, RUSA CAST, Dr. B. A. M.University, Aurangabad

Prof. Dr.R.B.Sharma, Head & BOS Chariman , Dr.B.A.M.University, Aurangabad

Prof. Dr. G. G. Muley , Dept. of Physcis, S.G.B. University, Amaravati

Prof. Dr. M. K. Patil, MC Member & Director, School of Physical Science, S.R.T. University, Nanded

Dr. S. D. Deshpande, Dept. of Physics, Dr. B. A. M. University, Aurangabad

Prof. Dr. K. M.Jadhav, Dept. of Physics, Dr. B. A. M. University, Aurangabad

Prof. Dr. Pravina P.Pawar, Dept. of Physics Dr. B. A. M. University, Aurangabad

Prof. Mahajan A.M., Dept. of Physics, N.M.Univeristy, Jalgaon, India

Dr. Dilip Garud, Principal Adarsh College, Omerga (MS), India

Dr. Bhaskar Munde, Principal KKM College, Manwat.

Dr.Jai shri Kumar, Government college, Kharkhra (Rewari), Haryana

Dr. Aurn Kumar Gautam, C.S.A. Government P.G.College, Sehore, (M.P)

Anil Das, Dept of Physics, ST John College, Agra

Dr. K. B. Bogle, School of Physical Science, S.R.T. Univeristy, Nanded

Dr. S. S. Hussaini, Milliya College, Beed

Dr. Babasaheb Ambedkar Marathwada University,

Aurangabad - 431 004 Maharashtra (India)

Re- accredited by NAAC with 'A' Grade in 2013

Professor B.A. Chopade
M.Sc., Ph.D (Nottingham University, England)
Fogarty Fellow (Illinois University, Chicago, USA)

Vice-Chancellor

EPABX	0240 - 2403399, 2403400
Direct	0240 - 2403111
Fax No.	0240 - 2403113/2403335
E-mail	vc@bamu.ac.in
Website	www.bamu.ac.in

Ref. No. VC.Sec./2019/ 340

Date: 20 February 2019

Message

I am delighted to pen greetings to this truly significant National Conference devoted to Functional Materials Synthesis and Characterization Techniques (Physics-NCFMSCT-2019) on 2nd March 2019 sponsored by Our Dr.Babasaheb Ambedkar Marathwada University, Aurangabad.

I congratulate Convener Dr.Madhav Rode and his entire team colleagues at Vaidyanath College, Parli Vaijnath. organising such fruitful program.

I consider the program to be one of my most significant contributions to Physics researchers, academicians and students.

My best wishes to the conference.

Professor B. A. Chopade
Vice Chancellor

DR. PRITAM GOPINATH MUNDE-KHADE
Member of Parliament (Lok Sabha)
Beed, Maharashtra

Member:
● Standing Committee on Health and Family Welfare
● Committee on Welfare of OBC's

डॉ. प्रितम गोपीनाथ मुंडे–खाडे
संसद सदस्य (लोक सभा)
बीड, महाराष्ट्र

MESSAGE

I am pleased to know that, Jawahar Education Society's Vaidyanath College, Parli Vaijnath is organizing National Conference on Functional Materials Synthesis and Characterization Techniques (Physics-NCFMSCT-2019) on 2nd March 2019 sponsored by Dr.Babasaheb Ambedkar Marathwada University, Aurangabad.

I hope all the participants will enjoy this academic fest.

I extend my greetings and best wishes to organizing committee, participants.
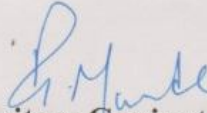
(Dr.Pritam Gopinath Munde)

Delhi Off.: 601, Narmada, Dr. B.D. Marg, New Delhi-110 001 ● Telefax: 011-23312110
Resi.: 'Yashshree', Tal. Parali, Distt. Beed-431 515 ● Telefax: 02446-222054
Mumbai Off.: 'Shubhada', Opp. Police Officers' Mess, Sir Pochkhanwala Marg, Worli, Mumbai-400 030 ● Ph.: 022-24900993 ● Fax: 022-24951493
Beed Off.: BJP Beed District Office, Opp. Superintendent Office, Vidhyanagar (W), Beed-431 122 ● Telefax: 02442-225177/233377

Chairman's Message

I am pleased to know that department of physics is organizing national conference on functional materials synthesis and characterization techniques on 2nd March 2019.

The progress of nation depends on the progress of science and technology and the higher education is effective medium to incubate the essential foundation and envisage future technological development. To create suitable surround through such national conference that provide a platform for the scientific discussion and recent development in research areas is essential.

Functional materials are now essential part of our everyday life. Development in functional materials has been improving our life. These materials are being used in various areas such as energy conversion, energy storage, and solar energy conversion and in surgery etc. The materials with improved functionality are highly demanded in the market. In such situation creating awareness among teachers and students in the rural area is very important. The present national conference organized by Department of Physics for functional materials in which eminent scientists and researchers are going to exchange their known and ideas, is really useful. I hope the deliberation will be really helpful to enhance knowledge and engrave vision of the national progress according to skill India approach of government of India. I welcome to all delegates and wish the conference a great success.

Hon'ble Jugalkishorji Lohiya
Chairman Jawahar Education Society's

Message from the Principal

Department of physics is really worthy of appreciation for organizing a National conference on functional materials synthesis and characterization techniques. This conference is sponsored by Dr. Babasaheb Ambedkar Marathwada University Aurangabad. It is my pleasure to invite the scientists, academia & researchers as well as students from all over nation to attend the NCFMSCT-2019.

All of you are acutely aware of growing interests in functional material for indigenous technological progress. This conference ensures to share an insight in recent research and cutting edge technologies as for as functional materials are concerned. I am sure that each of you will benefit from fruitful and enriching discussion in the conference.

I welcome you to this conference and look forward to your participation. Wishing the conference a grand success.

Dr. R. K. Ippar
Principal
Vaidyanath College, Parli-Vaijnath

Message from HOD

It is my great delight and proud privilege to welcome you all delegates and extend my warm welcome to the distinguished scientists, authorities and dignitaries in the national conference on functional materials, synthesis and characterization techniques going to be held on 2nd March 2019. The college has established a distinctive position among leading colleges in Marathwada region by imparting education to needy students from rural and backward areas. This year it commemorates its gold jubilee. The present conference which sponsored by Dr. Babasheb Ambedkar Marathwada University, Aurangabad is one of the special events on the eve of the gold jubilee celebration as department of physics is inherent part of the college since its establishment.

125th birth year of Prof. Meghnad Saha and birth centenary of Prof. Richard Feynman are being commemorated also. The famous visionary statement of Prof. Feynman, "There is plenty of room at the bottom" is now being realized in form of nanomaterial development which contributes excellently the functional materials development. The present conference really includes reminiscences of those great contributions which helped to develop today's functional material area. This deliberation is a small leap to create awareness and provide platform for functional materials synthesis and characterization techniques, so that it will contribute to incubate the future process of skill India for indigenous technological development for national prosperity. I really appreciate to the researchers across the country for sending the research papers for publication on call for research paper for the conference and extend my gratitude to the publisher International Journal of Advance and Innovative Research.

I am thankful to the university as well as RUSA centre for Advanced Sensor technology for support and movition for the conference

I sincerely hope the deliberation from various distinguished speakers will benefit the delegates to update their knowledge. Hope you will find the conference valuable and enjoyable. Wishing you the best for your involvement to make the event successful.

Dr. Dilipkumar V. Meshram
Head of Department
Department of Physics
Vaidyanath College, Parli-Vaijnath

International Journal of Advance and Innovative Research

Volume 6, Issue 1 (XIX): January - March 2019 : Part - 2

IJAIR

IMPACT FACTOR

7.36

International Journal of Advance and Innovative Research

ISSN : 2394-7780

ज्ञान – विज्ञानं विमुक्तये
University Grants Commission

Journal - 63571

UGC Journal Details

Name of the Journal :	International Journal of Advance & Innovative Research
ISSN Number :	
e-ISSN Number :	23947780
Source:	UNIV
Subject:	Multidisciplinary
Publisher:	Indian Academicians and Researchers Association
Country of Publication:	India
Broad Subject Category:	Multidisciplinary

CONTENTS

Research Papers

PREPARATION OF COBALT DOPED Ni-Zn FERRITE NANOPARTICLES FOR MAGNETIC AND MICROWAVE ABSORPTION PROPERTIES

Ravindra N. Kambale[1], Akhilesh Kumar Patel[2], Sandeep Kumar[3] and Vaishali Bambole[4]
[1,4]Department of Physics, University of Mumbai, Vidyanagari Campus, Mumbai
[2]Department of Physics, Indian Institute of Technology Bombay, Powai, Mumbai
[3]Magnetics and Advanced Ceramics Lab, Department of Physics, Indian Institute of Technology, Delhi

ABSTRACT

Cobalt doped Ni-Zn ($Ni_{0.3}Co_{0.2}Zn_{0.5}Fe_2O_4$) ferrite nanoparticles have been synthesized by sol-gel auto combustion technique using citric acid ($C_6H_8O_7$) as a fuel. The spectroscopic characterizations of the prepared powder were studied using X-Ray diffraction, Field emission gun scanning electron microscopy and Field emission gun transmission electron microscopy (FEG-TEM). The XRD patterns confirmsthe formation of spinel structured $Ni_{0.3}Co_{0.2}Zn_{0.5}Fe_2O_4$ ferrite nanoparticles and FEG-SEM and FEG-TEM images depicted the uniform morphology of particles with the average sizes of 35-72 nm. Vibrating Sample Magnetometer (VSM) was deployed to study the magnetic properties of the prepared powder at room temperature and saturation magnetization of the powder was 68.30 emu/g. To study the microwave absorption properties, complex permittivity and complex permeability were measured in the frequency range 2 GHz to 18GHz by vector network analyzer. The microwave absorbing properties of $Ni_{0.3}Co_{0.2}Zn_{0.5}Fe_2O_4$ ferrite nanoparticles were with the help of reflection loss. The excellent microwave absorption performance was found with the maximum reflection loss -22.63 dB in 13.52 GHz at thickness 1.0 mm.

INTRODUCTION

Currently the use of electronic gadgets, microwave oven, medical equipment, telecommunication system etc. is increasing every day and they are emitting electromagnetic radiations, which are harmful for living beings. The radiations create lot of problems to human health such as immunity loss, restlessness and damage of DNA structure [1- 4]. To get rid of these radiations, there is need of electromagnetic absorbing materials. In past, extensive investigations were carried out on these materials. There is an interest in the use of magneto-electronic based microwave absorbing materials that provide absorption over a wide band width [5, 6]. A lot of attention has been focused on development of microwave absorbing materials that are thinner, lighter weight, stronger EM waves absorption ability and wider absorption bands. Ferrites materials show the magneto-electronic properties [7-9]. Ferrite materials are studied and used as electromagnetic absorbents. Amongst ferrites materials, spinel ferrites are good electromagnetic absorbent due to their large magnetic and electric losses at gigahertz frequency [10-14]. Dielectric and magnetic losses are the important parameter for the determination of the reflection loss in the microwave absorption properties of the materials. Losses[15-19]. These losses are exhibited in these materials due to interaction between the magnetization and electric polarization. The studied spinel ferrite materials are Mg doped Ni-Cu-Zn ferrite, Cd substituted Mg ferrite, Mn-Zn-Ni ferrite[20-22].

In this paper we have synthesized Co doped Ni-Zn ($Ni_{0.3}Co_{0.2}Zn_{0.5}Fe_2O_4$) spinel ferrite nanoparticles since it has been reported that the addition of cobalt reduces the magnetic losses and anisotropy, so that Co doped nickel – zinc ferriteis fit for the application at high frequency. We also investigate their structure, magnetic and microwave absorption properties.

EXPERIMENTAL DETAILS

Cobalt doped Ni-Zn ($Ni_{0.3}Co_{0.2}Zn_{0.5}Fe_2O_4$) ferrite nanoparticles were synthesized by a sol-gel auto-combustion method using lemon juice. The stoichiometric amount of citric acid, $Ni(NO_3)_2.6H_2O$, $Co(NO_3)_2.6H_2O$, $Zn(NO_3)_2.6H_2O$, and $Fe(NO_3)_2.9H_2O$ were first dissolved separately in deionized water, obtained solutions were mixed with each other and stirred continuously for 30 min. and certain amount of lemon juice was added. The mixed solution of nitrate and lemon juice was stirred continuously for 6 hours then Ammonium hydroxide was added dropwise to adjust the PH value to 7. The clear solution was slowly evaporated at 90 ^{0}C under constant stirring to transform into a viscous gel, the gel was turn into loose powder. Finally $Ni_{0.3}Co_{0.2}Zn_{0.5}Fe_2O_4$ crystalline powder was obtained after calcining the loose precursors at 600^{0}C for 5 hours.

RESULT AND DISCUSSION

Room temperature x-ray diffraction of $Ni_{0.3}Co_{0.2}Zn_{0.5}Fe_2O_4$ ferrite nanoparticles is shown in Fig.1 (a) and corresponding Rietveld refined data is shown in Fig. 1(b). The compound crystallizes in Fd-3m space group with cubic structure and the obtained lattice parameter from Rietveld refinement is 8.41 Å. Crystal structure of the sample is shown in Fig. 1(c) with their respective positions in unit cell. In the unit cell Fe atoms occupy

octahedral position and Ni/Co/Zn occupy tetrahedral position, which is shown in Fig. 1(d). The crystallite size (D) of $Ni_{0.3}Co_{0.2}Zn_{0.5}Fe_2O_4$ ferrite nanoparticles have been calculated from the XRD line broadening of the (311) peak using Scherer's formula

$$D = \frac{k\lambda}{\beta \cos(\theta)}$$ (1)

Where, λ is the X-Ray wavelength, k is the shape factor (= 0.89), θ is the Bragg angle and β is the full width half maxima (in radian). The calculated crystallite size of the sample to be found 35- 72 nm, which is in accordance with the FEG –TEM results.

The morphology was studied with a Field Emission Gun Scanning Electron Microscope (FEG-SEM, model – JSM-7600F) and Field Emission Gun Transmission Electron Microscope (FEG-TEM-300kV, model-Tcnai G@, F30). Fig.1 (e) shows FEG-SEM image. From Fig. 1 (e), it is found that the particles are in cubic form and aggregate to some extent because of magnetic dipole interaction between them and crystallite size of the sample to be found 35-72 nm. Fig. 1(f) showsFEG-TEM image of $Ni_{0.3}Co_{0.2}Zn_{0.5}Fe_2O_4$ferrite nanoparticles and the particles are in cubic structure, which is consistent with the FEG-SEM result. FEG- SEM and FEG –TEM images clearly indicate the highly crystalline nature of the $Ni_{0.3}Co_{0.2}Zn_{0.5}Fe_2O_4$ ferrite nanoparticles. Very interestingly the micrograph reveals these nanoparticles, as single grain crystals structure, which conform that magnetic material smaller then critical size for multi-domain formation the particle is in single domain state.
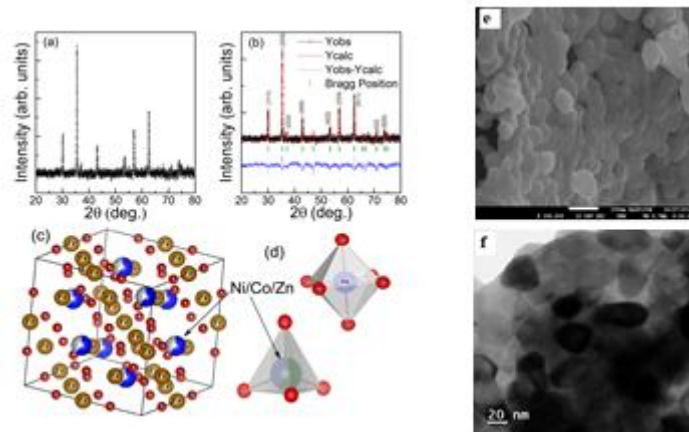
Fig.1 Room temperature XRD patterns of $Ni_{0.3}Co_{0.2}Zn_{0.5}Fe_2O_4$ ferrite nanoparticles. (b) Rietveld refine XRD for $Ni_{0.3}Co_{0.2}Zn_{0.5}Fe_2O_4$ ferrite nanoparticles. (c) Unit cell structure of $Ni_{0.3}Co_{0.2}Zn_{0.5}Fe_2O_4$ ferrite nanoparticles. (d) Tetrahedral surrounding of Ni/Co/Zn atom. and Octahedral surrounding of Fe (e) FEG-SEM image ofNi$_{0.3}$Co$_{0.2}$Zn$_{0.5}$Fe$_2$O$_4$ (f)FEG-TEM image ofNi$_{0.3}$Co$_{0.2}$Zn$_{0.5}$Fe$_2$O$_4$.

In order to study the magnetic properties of $Ni_{0.3}Co_{0.2}Zn_{0.5}Fe_2O_4$ ferrite nanoparticles, Saturation magnetizationwas measured with a vibrating sample magnetometer at room temperature (293K). Fig.2 shows the magnetization (M) versus the applied magnetic field (H) of $Ni_{0.3}Co_{0.2}Zn_{0.5}Fe_2O_4$ ferrite nanoparticles with an applied field -20 kOe $\leq$ H $\leq$ 20 kOe. The saturation magnetization M_S (emu/g) and coercivity field were found 68.30 emu/g and 0.0717 kOe respectively.
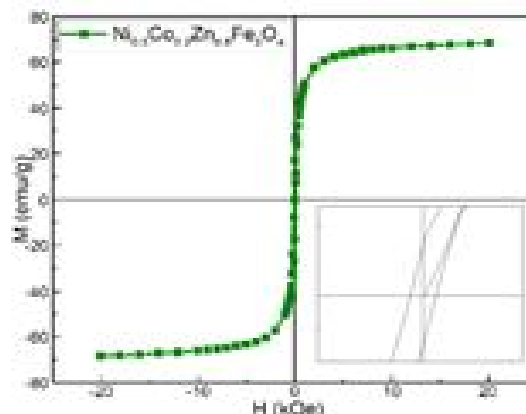
Fig-2 Shows the magnetization (M)
Versus the applied Magnetic field (H)of $Ni_{0.3}Co_{0.2}Zn_{0.5}Fe_2O_4$ ferrite nanoparticles.
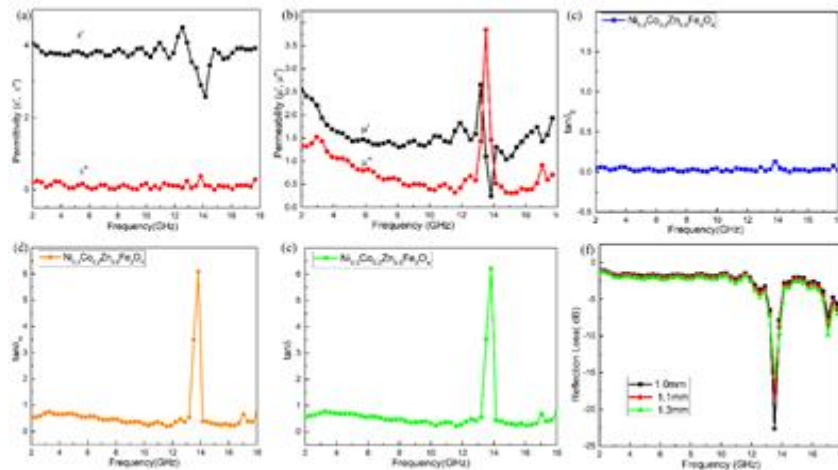
Fig. 3 Frequency dependence of (a) complex permittivity
(b) Complex Permeability (c) Dielectric loss (tan δ_E)
(d) Magnetic loss (tan δ_M) (e) tan δ (f) Reflection loss.

To investigate the microwave absorption characteristics, the complex permittivity, complex permeability, dielectric loss (tan $\delta_E = \frac{\varepsilon''}{\varepsilon'}$), magnetic loss (tan $\delta_M = \frac{\mu''}{\mu'}$) and tan δ of the sample were measured and are shown in Fig. 4. The frequency dependence of real and imaginary parts of complex permittivity of $Ni_{0.3}Co_{0.2}Zn_{0.5}Fe_2O_4$ ferrite nanoparticles in the range of 2 to 18 GHz is as shown in Fig 3(a). It can be observed that the variation of real part permittivity with frequency was almost constant with one peak of value 4.52 at frequency 13.84 GHz whereas imaginary part of permittivity was almost remains constant. Fig 3 (b) shows the frequency dependence of real and imaginary parts of complex permeability of $Ni_{0.3}Co_{0.2}Zn_{0.5}Fe_2O_4$ ferrite nanoparticles in the range of 2 to 18 GHz. It can be seen that the real and imaginary parts complex permeability both decreases with frequency up to 13GHz with peaks of values 2.68 and 3.8 at frequency 13.19GHz and 13.53GHz respectively. Frequency dependence dielectric loss and magnetic loss are shown in Fig 3(c and d). It can be seen that the dielectric losses are small (maximum value 0.13) and magnetic losses are relatively higher (maximum value 6.21) at all frequencies so this material is higher magnetic loss than electric loss. Fig 3 (e) shows the tan δ (tan δ_E +tan δ_M), which is indicative of microwave absorbing properties, tan δ has larger value 6.21 at frequency 13.52GHz,implies this material is suitable as microwave absorber for high frequency.

The measured permittivity and permeability of sample by Vector Network Analyser are used to calculate the reflection loss (RL) for different thickness using following equation

$$Refletion\ loss = 20\log_{10}\frac{|z-1|}{|z+1|} \tag{2}$$

Where, the impedance (Z) of medium is

$$Z = \sqrt{\frac{\mu_r}{\varepsilon_r}}\tanh\left[j\frac{2\pi t}{2\ \lambda}\sqrt{(\mu_r\epsilon_r)}\right]$$

Here μ_r andε_r are the measured relative complex permeability and complex permittivity of the materialrespectively, which are measured by Vector Network Analyser in the frequency range2 to 18 GHz, λ is the wavelength of incident plane wave in free space and t is the thickness of the absorbing material. Fig. 3 (f) shows the frequency dependence reflection loss of the sample at thickness 1.0mm, 1.1mm and 1.2 mm. The excellent microwave absorption has reached -22.63 dB in the frequency 13.52 GHz with thickness at 1.0 mm.

CONCLUSIONS

$Ni_{0.2}Co_{0.3}Zn_{0.5}Fe_2O_4$ ferrite nanoparticles exhibiting electromagnetic properties were successfully synthesized by sol-gel auto combustion method followed by calcination at 700^0C for 5 hrs. The X- ray diffraction analysis confirms the formation of single phase cubic structure, FEG-SEM and FEG-TEM studies have established the formation of $Ni_{0.2}Co_{0.3}Zn_{0.5}Fe_2O_4$ ferrite in cubic structure nanoparticles. The hysteresis loop demonstrate that the $Ni_{0.2}Co_{0.3}Zn_{0.5}Fe_2O_4$ ferrite is of a soft magnetic material and magnetization value of the annealed ferrite nanoparticles at $700\ ^0C$ is 68.30 emu/g. Our result indicate that the Co doped Ni-Zn ferrite exhibits excellent microwave absorption performance found with the maximum reflection loss -22.63 dB at13.52 GHz for

thickness 1.0mm over a broad band range of radar band with good electromagnetic properties. Thus, Co doped Ni-Zn ($Ni_{0.3}Co_{0.2}Zn_{0.5}Fe_2O_4$) ferrites holds a good promise as a potential microwave absorption material.

REFERENCES

1. Seema Joon, Rakesh kumar, Avanish Pratap Singh, Rajni Shukl, S.K. Dhawan, Fabrication and microwave shielding properties of free standing polyaniline-carbon fiber thin sheets, Mat. Chem. Phys. xxx (2015) 1-9.

2. K.K. Gupta, S.M. Abbas, T.H. Goswami , A.C.Abhyankar, Microwave absorption in X and Ku band frequency of cotton fabric coated with Ni–Zn ferrite and carbon formulation in polyurethane matrix J. Magn. Magn. Mat. 362, 216-225 (2014) 216-225.

3. Seyed Hossein Hosseini, A. Asadnia, Polyaniline/Fe_3O_4 coated on $MnFe_2O_4$ nanocomposite: Preparation, characterization, and applications in microwave absorption Int. J. Phy. Sci. 8 22, 1209 -1217, (2013).

4. Xiaohu Ren, Guangliang Xu, Electromagnetic and microwave absorbing properties of NiCoZn-ferrites doped with La^{3+}J. Magn. Magn. Mat. 354, 44-48 (2014).

5. J.C. Aphesteguy , A. Damiani , D. DiGiovanni , S. E. Jacobo, Microwave absorption behaviour of a polyaniline magnetic composite in the X-band Physica B,407, 3168-3171(2012).

6. Ch. Sujatha, K.Venugopal Reddy, K. Sowri Babu , A.Raman Chandran Reddy, M. Buchi Suresh, K.H. Rao, Effect of Co substitution of Mg and Zn on electromagnetic properties of NiCuZn ferrites J. Phy. Chem. of solids 74, 917 - 923 (2013).

7. Adriana M. Gaman, Mirabel C. Rezende, Christine C. Dantas, Dependence of microwave absorption properties on ferrite volume fraction in MnZn ferrite/rubber radar absorbing materials J. Magn. Magn. Mat. 323, 2782-2785 (2011).

8. Maayad Husein Flaifel, Sahrim Hj Ahmad, Mustaffa Hj Abdullah, Rozaidi Rasi, Abdul Halim Shaari, Ayman A. El-Saleh, Sivanesan Appadu Preparation, thermal, magnetic and microwave absorption properties of thermoplastic natural rubber matrix impregnated with NiZn ferrite nanoparticles, Composites Sci. Tech. 96, 103- 108 (2014).

9. Shi -Yuan Tong, Jenn-Ming Wu, Yu-Ting Huang, Mean-Jue Tung, Wen-Song Ko, Li-Chun Wang, Min-Da Yang, Design and characteristics of flexible radio-wave absorber consisted of functional NiCuZn ferrite– polymer composites J. Alloys, Comp., 509, 2263-2268 (2011).

10. R. Zahir, F. -U -.Z Chowdhury, M. M. Uddin, M.A.Hakim, Structural, magnetic and electrical characterization of Cd-substituted Mg ferrites synthesized by double sintering technique J. Magn. Magn. Mat. 410, 55-62 (2016).

11. Jong-Hyuk Kim, Sung-Soo Kim, Microwave absorbing properties of Ag-coated Ni–Zn ferrite microspheres prepared by electroless plating J. Alloys, Comp. 509, 4399-4403 (2011).

12. Pan Pengfei, Zhang Ning, Magneto dielectric effect of Mn–Zn ferrite at resonant frequency J. Magn. Magn. Mat. 416, 256 – 260 (2016).

13. Asghari Maqsood, Kishwar Khan, Structural and microwave absorption properties of Ni(1−x)Co(x)Fe2O4 (0.0≤x≤0.5) nanoferrites synthesized via co-precipitation route. J. Alloys Campd. 509: 3393–3397 (2011).

14. Li Qiao Chen,Wei Ping Liu, Jia Lin Chen, Xian Feng Yang, Jia Liu, Xiong Hui Fu, Ming Mei Wu, Facile shape and size-controlled growth of uniform magnetite and hematite nanocrystals with tunable properties Sci. China Chem. 54(6): 923–929 (2011)

15. H. Su, X. Tang, H. Zhang, Z. Zhong, J. Shen,Sintering dense NiZn ferrite by two-step sintering process J. Appl. Phy.109, 07A 501-3 (2011).

16. Tae Young Byun, Soon Cheon Bycon and Kug Sun Hong,Factors Affecting Initial Permeability of Co-substituted Ni-Zn-Cu Ferrites, IEEE Transactions on Magnetics 35, 5, 3445–3447 (1999).

17. ZhuYana Juhua Luo, Effects of Ce-Zn co-substitution on structure, magnetic and microwave absorption properties of nickel ferrite nanoparticles. J. Alloys Campd. 695, 2017,1185-1195

18. Sun Chang, Sun Kangning, Chui Pengfei, Microwave absorption properties of Ce-substituted M-type barium ferrite J. Magn. Magn. Mat. 324, 802-805 (2012).

19. Tao Shang, Qingshan Lu, Luomeng Chao, Yanli Qin, Yuehau Yun, Guohong Yun, Effects of ordered mesoporous structure and La-doping on the microwave absorbing properties of CoFe2O4 App. Surface Sci., 234, 234-242 (2018).

20. Wenjie Wang, Chongguang Zang, Qingjie Jiao, Synthesis, structure and electromagnetic properties of Mn–Zn ferrite By sol–gel combustion technique J. Magn. Magn. Mat. 349,116-120 (2014).

21. Zhu Yan, Juhua Luo, Effects of Ce - Zn co-substitution on structure, magnetic and microwave absorption properties of nickel ferrite nanoparticles J. Alloys, Comp. xxx (2016) 1-11

22. Zeng Jun, Fun Huiqing , Wing Yangi, Zhang Shiquan , Xue Jun, Cheng Xinying, Ferromagnetic and microwave absorption properties of copper oxide/cobalt/carbon fiber multilayer film composites, Thin solids Films, 520,5053 – 5059 (2012).

ABSOLUTE IONIZATION CROSS SECTION OF ORGANIC COMPOUND BY ELECTRON PROCESS

Praveen Bhatt[1], Parmjeet Kaur[2], Umesh Bhardwaj[3] and Santosh Sharma[3]

Professor[1], Department of Applied Science and Humanities, Asia Pacific Institute of Information Technology (APIIT SD INDIA) Panipat

Assistant Professor[2], Department of Applied Science and Humanities, SGI, Hathwala, Samalkha, Panipat

Associate Professor[3] and Associate Professor[4], Department of Chemistry, Hindu College, Sonipat

ABSTRACT

Collisions of electrons with molecules and atoms generate the energetic species that drive chemical and physical changes of matter in environments that vary from plasmas to living tissue. We have made a study of absolute ionization cross-sections (AICS) of inorganic cluster by electron impact. Here we have use modified Jain-Khare formula.

Keywords: ionization

I. INTRODUCTION

Quantum mechanical methods refer to calculations for which only physical constants are used as input data. Energy minimization is performed by calculating the wave functions using only constants such as me, h, e, c etc with various approximations and assumptions; no experimental data for the particular system under study is required.

The laws of quantum mechanics are firmly followed and no classical approximations are made. Semi-classical models are those for which the laws of quantum mechanics are approximated to classical laws. Most calculations in this category are in fact a combination of semi-classical approximations and semi-empirical theories.

After probing through the literature it has turn into visible that small improvement has been made in this area in recent years for atoms with Z > 2. The most comprehensive review of quantum mechanical calculations of electron impact ionization cross-sections is by Younger et al (1985)[4]. Although some progress has been made since then particularly with regard to the ionization cross-section of hydrogen (Jones & Stelbovics, 2002)[5].

Most of the theoretical work concerning to the computation of electron impact ionization cross-sections falls under the umbrella of semi-classical and semi-empirical banners.

The quantum mechanical modeling of electron impact ionization cross-sections is an innately hard task because there are two free electrons in the field of the ionized atom in the exit channel. This leads to the so-called three body problem and, in the case of electron impact ionization; this has been a particularly difficult problem to formulate.

Quantum mechanical calculations have so far been limited to selected atomic and atomic ion targets with varying success. The theory frequently disagrees with experimental results by a factor of between 2 and 10. As the atomic number, Z, increases, the theory becomes less successful. On the other hand (McGuirie, 1971; 1977; 1979)[1-3] has performed quantum mechanical calculations in the Born approximation for heavy atoms. Calculations were perfect to within 20% of experimental values for atoms in the range 2 < Z < 11 and within 30% of experimental values for atoms 19 < Z < 54 for electron energies greater than 200 eV using an extended Bethe binary encounter equation and a generalized oscillator strength model. Calculations were also performed for the ionization of individual subshells for a range of heavy atoms including Hg.

In general, as the electron energy exceeds the maximum electron impact ionization Cross-section, $\Box$max the theory and the experimental results tend to meet. This is because the interaction between the ion, the primary electron and the secondary electrons are short lived at high energy and therefore cause less perturbation to the system[6-9].

Our objective is the calculations for differential cross sections as a function of secondary electron energy and angle at fixed impinging electron energy, corresponding to the formation of various cations in electron impact dissociative ionization of the atoms and atomic molecules, organic and inorganic compound have been carried out by employing a semi empirical formalism based on theoretical approach.

The calculation of total integral cross sections for electron-impact ionization of atoms and atomic ions has, in the last 20 years, greatly benefited from the development of several non perturbative methods, which in general show very good agreement with each other and with experiment.

THEORETICAL METHODOLOGY

Even on the theoretical side several more methods are available to compute the cross sections over a wide range of atoms and molecules. For example, there is no explanation for dissociate, total, single and double ionization cross section. This formula is also applicable to calculate partial, photo, integral ionization cross sections of atoms and molecules.

The formula is useful for finding the rate coefficient of any atoms and molecules. semi-empirical formalism developed by Jain and Khare [10-13].This formula is also applicable to calculate partial, photo, integral ionization cross sections of atoms and molecules. The formula is useful for finding the rate coefficient of any atoms and molecules. This is a theoretical approach. In brief, the single differential cross sections in the complete solid angle ($\Omega = 4\Pi = \int 2\pi \sin\theta d\theta$) as a function of secondary electron energy ε corresponding to the production of ith type of ion in the ionization of a molecule by incident electron of energy E is given by equation 1:

$$Q_i(E,W,\theta) = \frac{a_0^2 R^2}{E}\left[\int_{k\to0}^{E-I_i}\left\{\begin{array}{l}\frac{E-W}{E-I_i}\frac{1}{W}df_i(W,K,\theta)\times\ln\left[1+C_i(E-I_i)\right]+\\ \frac{E-I_i}{E(\varepsilon_0^3+\varepsilon^3)}\times S_i\left(\varepsilon-\frac{\varepsilon^2}{E-\varepsilon}+\frac{\varepsilon^2}{(E-\varepsilon)^2}\right)\end{array}\right\}\right]2\pi\sin\theta d\theta .....(1)$$

Where, $W (=\varepsilon + I_i)$ is defined as energy loss suffered by the incident electron.

I_i = the ionization threshold for the production of ith type of ion,

a_0 = the Bohr radius,

ε_0 = energy parameter,

C_i = collision parameter,

S_i = number of ionizable electrons,

R = Rydberg constant and

θ = the scattering angle respectively.

In the present formulation, the dipole oscillator strengths df_i/dw are the key parameters. The oscillator strength is directly proportional to the photo ionization cross section [10-15]. Summation of PDDCS (Partial double differential cross section) over the system gives the total (DDCS) (Double differential cross section)

$$Q_i^t(E,W,\theta) = \sum_i Q_i(E,W,\theta)$$

Here it is interesting to note that $Q_i(E,W,\theta)$ is isotropic and hence the material property of molecule, i.e., the oscillator strength must be isotropic in nature. Here $df_i(W,K,\theta)$, the differential generalized oscillator strength (DGOS) in the optical limit $(K\to0)$ has been used. From Lassettre's Theorem [8-9] the DGOS in the Bethe regime is reduced to the cosine distribution form of the linear optical oscillator strengths $df_i(W,0))/dW$, i.e.

$$df_i(W,K,\theta)\to(1/4\pi)\left[1+\beta P_2(\cos\theta)\right]\times df_i(W,0)/dW,$$

Where β is the asymmetric parameter and $P_2(\cos\theta)=\frac{1}{2}(3\cos^2\theta-1)$ is the second order Legendre polynomial. In the present treatment, β is chosen as the probability of ionizing electrons in the ionization processes however, it depends on the ejected electron energy. The oscillator strengths are directly proportional to the photo ionization cross sections.

Further integration of Equation (1) with respect to the scattering angle θ (from 0 to 2π) gives the PSDCS (Partial single differential cross section)

$$Q_i(E,W) = \int Q_i(E,W,\theta)d\Omega,$$

Where differential solid angle $d\Omega$ is $2\pi\sin\theta d\theta$

Similarly, SDCS (Single differential cross section) are given as

$$Q_i^T(E,W) = \sum_i Q_i(E,W)$$

Further integration of PSDCS with respect to W from I to W_{max} (= E) results in PICS (Partial integral cross section), i.e.

$$Q_i(E) = \int Q_i(E,W)dW .$$

The present formulation requires the major input data of the photo ionization cross-sections in terms of the optical oscillator strengths.

RESULTS AND DISCUSSION

In this paper the results of the absolute ionization cross section measurements for the organic compound are calculated from threshold to 1000 eV by the use of modified Jain-Khare approach. Table 1

The Absolute total ionization cross sections along with the total ionization cross section are also summarized in Table 1.

Table-1

Absolute total ionization cross-section values for organic compound (CH2F2 and compare with Torres and Rmartinez and find good agreement.

Electron Energy (eV)   Total ionization-cross section (10^{-21} cm^2)

Fragmented ions

Energy (eV)	TIC
20	3.43708
30	9.78953
40	1.39808
50	1.61301
60	1.71469
70	1.75647
80	1.76464
90	1.75352
100	2..66601
125	2.65701
150	2.63281
175	2.59828
200	2.55832
300	2.51428
400	2.46904
500	2.42245
600	2.37659
700	2.33059
800	2.28617
900	2.24214
1000	2.15852

Figure no-01
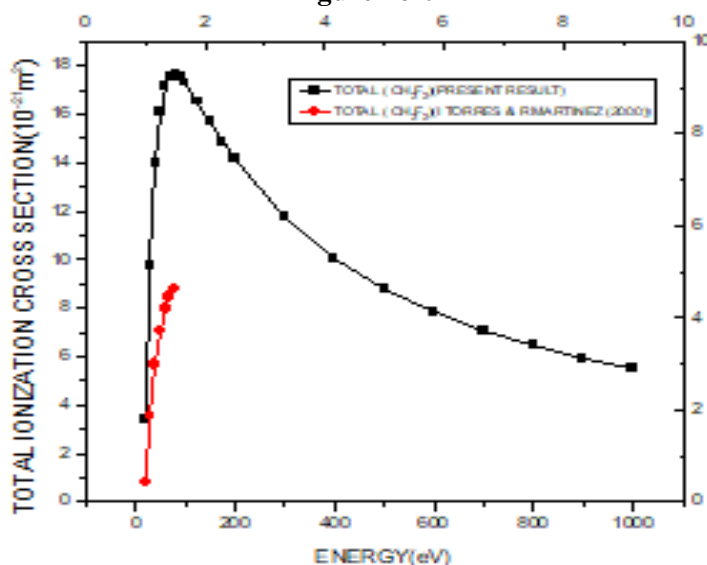
REFERENCES

1. McGuire E J (1977)."Electron ionization cross sections in the Born approximation." Phys. Rev. A 16(1), 62.

2. McGuire E J (1979)."Scaled electron ionization cross sections in the Born approximation for atoms with 55≤ Z ≤102." Phys. Rev. A 20(2), 445.

3. McGuire E J(1971)."Inelastic Scattering of Electrons and Protons by the Elements He to Na." Phys. Rev. A 3(1), 267.

4. Younger S M and Mark T D (1985)."Electron impact ionization."ed. TD Mark and GH Dunn (Berlin: Springer) Ch.2,

5. Youngera S M, Mark T D and Dunn G H (1985)."Electron impact ionization." Springer-Verlag, Wien, pp 24.

6. R. Basner, R.foest, M.Schmidt, F.Sigeneger, P.Kurunczi, K.Becker, H.Deutsch, Int. J.Mass Spectrometry and Ion Processes 153(1996)65-78.

7. S.McGinnis, Chem.Phys.Lett.232(1996)99.

8. T.W. Shyn, W.E. Sharp, Phys. Rev. A 20(1979) 2332.

9. E N Lassettre, A Skerbele and A D Michael, J. Chem. Phys. (1967) 46, 4536.

10. S.P. Khare, Planet. Space Sci. 17 (1969) 1257.

11. S.P. Khare, W.J. Meath, J. Phys. B 20 (1987) 2101.

12. P. Bhatt, S.Pal, J. Electron Spectro. Related Phenomenon 129(2003)35-41.

13. P. Bhatt, S.Pal, J. of Mass Spectrometry 229(3)(2003)151-156.

14. Satyendra Pal, J. Phys.: Conf. Ser. (2009)163, 012030.

15. Satyendra Pal, J.Phys. Scr. (2011) 19.

POA MATRIX CLADDING MODIFIED OPTICAL FIBER UREA BIOSENSOR

B. Sunil[1], D. K. Gaikwad[2], V. G. pahurkar[3], G. G. Muley[4], P. P. Pawar[5]
[1,2,5]Department of physics Dr. Babasaheb Ambedkar Marathwada university, Aurangabad
[3,4]Department of Physics, Sant Gadge Baba Amravati University, Amravati

ABSTRACT
Present investigation reported the POA (Polyaniline doped oxalic acid) cladding modified optical fiber intrinsic biosensor for quantitative determination of urea. The cladding modification technique was exploited on small unclad portion of optical fiber. Further, the enzyme-Urease immobilized on modified region by cross-linking method via glutarldehyde solution. The modified POA matrix was characterized by X-Ray diffraction, Ultra Violet-Visible and Fourier Transform spectroscopy. The sensitivity of developed biosensor was analyzed by acquiring absorption spectrum from UV-Vis. Spectrophotometer. The 0.1 M to 100 mM concentration range was preferred for analyze sensitivity of prepared biosensor. The developed biosensor shows the very good response towards selected concentration of urea comparable with buffer solution (Ph 7.4).

Keywords: FTIR, optical fiber biosensor, urea, UV-Vis., XRD

INTRODUCTION
Application of biosensor in various fields such medical, agriculture, environment, food processing, military etc. always attracted to researcher. Generally biosensor defined by an analytical device comprising biologically active compound with a compatible transducer, which gives the bio-chemical signal into a recognizable signal. The main components of biosensors are bioreceptor, immobilization matrix, transducer and signal analyzer. These mentioned components decide the performance of biosensor [*Singh et.al, 2008*]. Thus, the challenging task for researcher is the proper selection of these components in fabrication of biosensor. The various types of biomolecules such as urea, glucose, cholesterol etc. are very much dangerous for human beings above the permissible limit in the body. The biomolecules urea above the permissible limit creates the many dangerous diseases in human body such as congestive heart, urinary tract obstruction, gastrointestinal disorders, chronic or acute renal failure, burns, dehydration, starvation, shock, malnutrition, little dietary protein in the diet, liver diseases, hepatic failure, nephritic syndrome and cachexia [*Botewad et.al, 2018*].

In biosensor fabrication different types of transducers, immobilization matrix and various types of sensing mechanics are used. Over the other types of biosensor optical fiber biosensors (FOB) have the extraordinary properties such as small size, flexibility, ruggedness, inherent possibility for remote measurements, multiplexing capability, and immunity to electromagnetic interference. In the subtypes of FOB the evanescent wave absorption spectroscopy has particular interest, due to its simple design and low cost, useful in harsh environment and sensing at isolated locations [*Choudhury et. al, 2003, Pahurkar et. al, 2015*].

Main and very important factor in biosensor fabrication is the immobilization supportive matrix because it solely decides the performance of biosensors. Various types of immobilization matrices are found to use in biosensor fabrications. Intrinsic conducting polymers (ICP) found best candidates as immobilization matrix owing to their ability to have their chemical and physical properties tailored over a wide range of characteristics. Polymeric matrices have the beneficiary characteristics for the fabrication of biosensors, such as biocompatible, flexible, and cost-effective. As a immobilization matrix various ICP are used Viz. polyacetylene (PA), Polyaniline (PANI), Polypyrrole (PPY), Poly(p-phenylene) (PPP), Poly(p-phenylenevinylene) (PPV), Polythiophenes (PTH). From the above mentioned ICPs, PANI has vastly studied owing to its ability of reversible doping/ dedoping character, modified electrical conductivity, pH switching properties and good environmental stability [Sen et al 2016, Pahurkar et. al 2015].

Herein, we reported the urea biosensor using optical fiber transducer via cladding modification technique by Polyaniline doped oxalic acid (POA) matrix. The biocompatibility of POA matrix was analyzed by immobilizing enzyme urease for urea sensing application. Developed biosensor shows very good sensitivity towards urea in the range 0.1 M to 1μM with higher reproducibility. Thus, as synthesized POA matrix is compatible for urease immobilization for fabrication of urea biosensor.

SYNTHESIS AND BIOSENSOR DEVELOPMENT
In the present investigation all chemicals are AR grade and used as without any further purification. Polyaniline doped oxalic acid (POA) immobilization matrix was prepared by in situ chemical oxidation method. For preparation of POA matrix aniline (0.2M) prepared in 100 ml distilled water with pouring 0.05 M oxalic acid in as prepared aniline solution and lastly oxidized by 0.05 M $fecl_3$ solution. The prepared POA matrix used for

cladding modification on 2 cm unclad portion from 1 meter optical fiber. Further enzyme-Urease immobilized on cladding modified portion by cross-linking method via glutarldehyde solution. After, as prepared sensing element was used for sensing experiment.

RESULT AND DISCUSSION
XRD
Fig.1 shows the XRD pattern of as synthesized cladding modified POA matrix. The XRD pattern not shown any sharp characteristic peaks like a crystalline materials thus, it confirms that it is in amorphous nature. Due to periodic vertical and parallel structure in the polymer main chain attributes two peaks at 22° and 34° [*Chuanyu et.al, 2014*].

UV-Vis.
Fig. 2 shows the UV-Vis. spectrum of POA cladding modified matrix recorded in the range 250 to 900 nm. The spectrum shows two absorption peaks at ~275 and ~750 nm. The peak at ~750 nm is attributed due to the POA quinone ring structure [*Chuanyu et.al, 2014*]. The peak at ~275 ensured the POA matrix is in the half-oxidized emeraldine form [*Botewad et.al, 2016*]. These absorption peaks confirms that the prepared POA matrix in half-oxidized emeraldine form.

FTIR
Fig.3 shows the FTIR spectrum of POA matrix and confirms the all characteristic frequency band. The strong absorption peak at 1717 cm^{-1} can be assigned to C=NH stretching. The absorption peaks at 1237 and 1341 cm^{-1} may confirms the C-N stretching of primary aromatic amines. The peak at 1508 cm^{-1} attributes to the absorption vibration peak of C=C in quinone ring and at 1465 and 1408 cm-1 attributes to the absorption vibration peak of C = C in benzene ring. The absorption peaks at 1084 and 1008 cm^{-1} stands for the C-H plane bending vibration [7]. The 827 cm^{-1} peak attributes to the plane bending vibration peak of C-H in disubstituted benzene [8]. This further illustrates that the oxalic acid has doped well into the polyaniline chain.
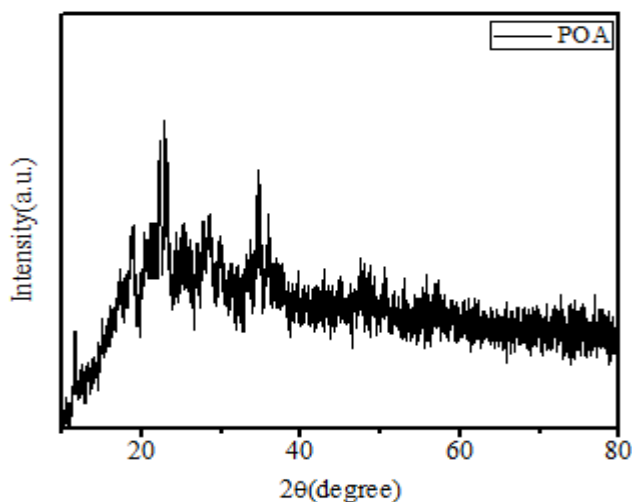
Fig-1: XRD pattern of POA matrix
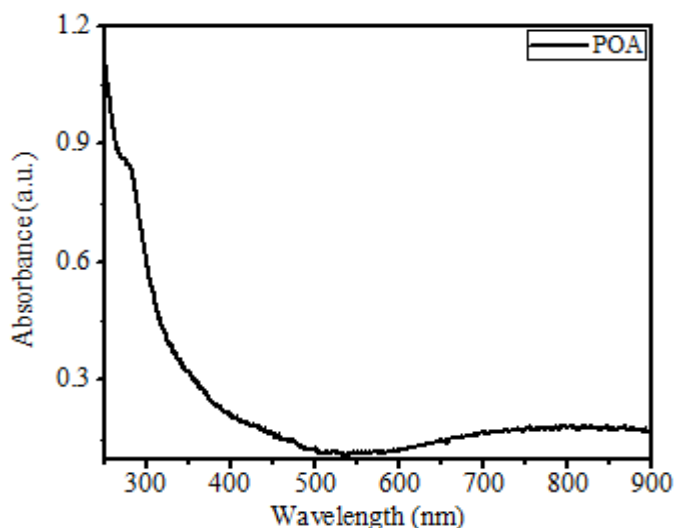
Fig-2: UV-Vis. pattern of POA matrix
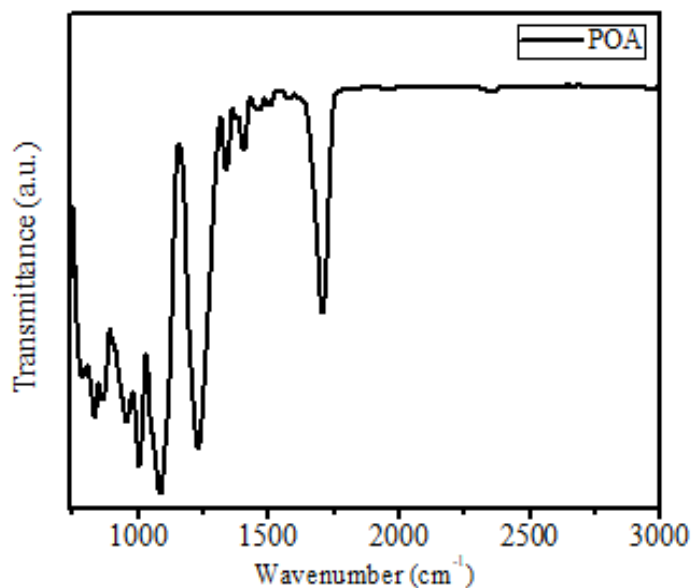
Fig-3: FTIR pattern of POA matrix

BIOSENSOR PERFORMANCE

The sensing performance of developed biosensor was analyzed by acquiring absorption spectrum from the UV-vis portable spectrometer (BLACK-Comet-SR, Stellar Net, USA). In the experiment SMA905 connectors connected both ends of sensing element attached between light source and spectrometer. Light passing from end through the sensing element by source and spectrometer recorded the modulated absorption spectrum by other end.
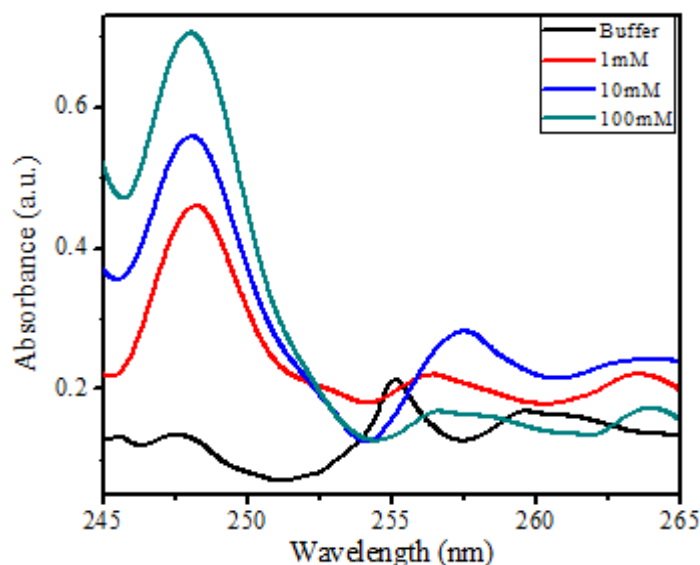
Fig-4: sensing response of urea biosensor

SENSITIVITY

Sensing study performed with urea concentration in the range 1mM to 100mM compared by buffer (Ph 7.4) solution. The fig 4 shows the sensing response of developed biosensor in the form of absorption spectra. It is clearly reveals that the absorption for urea concentration is high compared to buffer solution. The absorption is increased corresponding to increased urea concentration. The change in absorption is occurs due to the reaction between analyte-urea and enzyme-urease at sensing element. Reaction around the sensing element changes the microenvironment at modified cladding and because of this changes the refractive index. Due to the changing refractive index for each concentration occurs change in absorption intensity.

CONCLUSION

In present study we successfully developed the cladding modified urea biosensor using POA matrix. The developed biosensor gives the very good response towards the urea concentration in the range 1M to 100mM. Thus the cladding modified POA matrix proved the good immobilization matrix for enzyme urease in urea biosensor.

REFERENCES

1. Botewad S. N., Pahurkar V. G., Muley G. G. (2016), Development and Study the Performance of PBA Cladding Modified Fiber Optic Intrinsic Biosensor for Urea Detection, AIP Con. Proc.,1728, 020487

2. Botewad S.N., Pahurkar V.G., Muley G.G. (2018), Fabrication and evaluation of evanescent wave absorption based polyaniline-cladding modified fiber optic urea biosensor, Optical Fiber Technology (40) 8–12.

3. Choudhury P. K., Yoshino Toshihiko (2003), On the pH response of fiber optic evanescent field absorption sensor having a U-shaped probe: An experimental analysis, Optik 114(1) 13–18.

4. Chuanyu Sun, Rahman M. D. Farabi, Yu Wang (2014), Preparation and characterization of polyaniline nanostructures doped with oxalic acid, Optoelectronics And Advanced Materials – Rapid Communications Vol. 8(7-8) 810 – 813.

5. Pahurkar V.G., Tamgadge Y.S., Gambhire A.B., Muley G.G. (2015), Evanescent waveabsorption based polyaniline cladding modified fiber optic intrinsic biosensorfor glucose sensing application, Measurement 61 (9–15).

6. Pahurkar V.G., Tamgadge Y.S., Gambhire A.B., Muley G.G. (2015), Glucose oxidase immobilized PANI cladding modified fiber optic intrinsic biosensor for detection of glucose, Sensors and Actuators B vol. 210, 362–368.

7. Singh Minni, Verma Neelam, Garg Arun Kumar, Redhu Niha (2008), Urea biosensors, Sensors and Actuators B (134) 345–351

8. Sen Tanushree, Mishra Satyendra, Shimpi Navinchandra G. (2016), Synthesis and sensing applications of Polyaniline nanocomposites: a review, RSC Adv., 6, 42196.

Z-SCAN STUDIES OF TARTARIC ACID INFLUENCED AMMONIUM DIHYDROGEN PHOSPHATE (ADP) CRYSTAL

S. P. Ramteke[1], Mohd Anis[2], G. G. Muley[3]
[1,3]Department of Physics, Sant Gadge Baba Amravati University, Amravati
[2]Department of Physics and Electronics, Maulana Azad College of Arts, Science and Commerce, Aurangabad

ABSTRACT
The materials with promising nonlinear optical (NLO) features are widely needed for photonic device fabrication hence present investigation is aimed to explore the third order nonlinear optical (TONLO) properties of tartaric acid (TA) influenced $NH_4H_2PO_4$ (ADP) crystal. The TONLO properties of TA influenced ADP single crystal has been examined by means of Z-scan technique at 632.8 nm. The Z-scan technique has been configured to close and open aperture so as to examine the nature of TONLO refractive index and absorption. The magnitude of TONLO refraction (n_2), absorption (β) and cubic susceptibility (χ^3) of TA influenced ADP crystal has been determined and compared with pure ADP crystal.

1. INTRODUCTION
In recent technological progress ammonium dihydrogen phosphate (ADP) having d_{36} coefficient (1.38×10^{-9} esu) is an exclusive material for optical device applications [1]. The ADP crystal has potential credibility due to piezoelectric, ferroelectric and nonlinear optical (NLO) properties which suggests its advantage in designing monochromators for X-ray fluorescence analysis, harmonic generators, ultrafast communication and optical switching devices [2-7]. It is observed that various aspects of ADP crystal have been explored in literature. The properties of interest can be modified by several ways. It is observed that the properties such as morphology, XRD, second harmonic generation efficiency and luminescence of ADP crystal has been modified due influence of TA however, the its TONLO properties are yet not explored [8]. Hence present investigation is very firstly scripted to explore the TONLO properties of TA influenced ADP crystal by employing the Z-scan technique.

2. EXPERIMENTAL PROCEDURE
Ammonium dihydrogen orthophosphate (ADP) of 1 mole was dissolved in distilled water and stirred till the homogeneous solution was formed. L-tartaric acid (TA) of 0.5 mole was gradually added to the solution of ADP and then mixed well for four hours. The TA influenced ADP (TA-ADP) solution was filtered in the clear dust free rinsed beaker using the filtration unit (membrane filter paper, vacuum pump). This beaker was placed in a constant temperature water bath maintained at 35 °C. The grown TA-ADP crystal is shown in Fig. 1. The recrystallization was done to eliminate the impurity in the crystal material.

Fig-1: Crystal of TA-ADP

3. RESULTS AND DISCUSSION
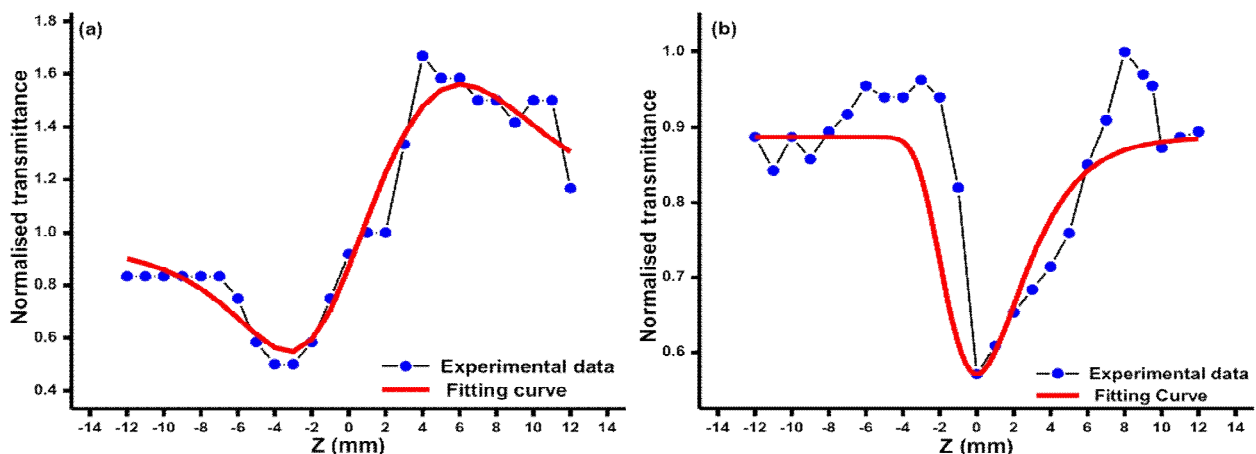
Fig-2a: Z-scan transmittance curve with aperture (a) close and (b) open

The TONLO properties of material play crucial role in designing three dimensional (3D) fluorescence imaging/optical data storage, ultrafast optical modulation, optical power limiting and microscopic lithography devices [9]. The He-Ne laser assisted Z-scan technique has been employed to determine the TONLO properties of TA influenced ADP crystal. The Z-scan setup includes the He-Ne laser operating at 632.8 nm, Gaussian filter, converging/convex lens (20 cm), sample translator and the photo detector placed at far distance (113 cm from laser source). As the components are optically aligned the polished crystal is placed at the sample holder and translated along the beam irradiated path. Firstly the close aperture Z-scan technique has been employed to determine the profile of TONLO refraction (n_2) and the Z-scan transmittance curve is shown in Fig. 2a. It is evident that the transmittance about the focus shifts from the pre-focus valley to post-focus peak which is signature of material having self-focusing ability [10]. This confirms the presence of positive nonlinear refraction [11] which attributes the occurrence of Kerr lens modelocking (KLM) ability desirable for laser alignment and shorter pulse generation system [12]. The phase change in profile of n_2 is due to localized irradiation of highly repetitive laser beam causing the thermal lensing effect [13]. The open aperture Z-scan transmittance curve is shown in Fig. 2b it is observed that the TA-ADP crystal offers the reverse saturable absorption (RSA) effect which is essential for optical limiting device applications. The RSA effect is governed by the two photon effect assisted by the excited state absorption [14]. The cubic susceptibility of TA-ADP crystal has been determined and it is found to be of order esu. It is notable that the ADP crystal itself attributes the positive n_2 and RSA effect as well [15]. The TONLO parameters of pure and TA-ADP crystal is tabulated in table 1.

Table-1: TONLO parameters

Crystal	n_2 (cm^2/W)	β (cm/W)	χ^3 (esu)
ADP	6.34×10^{-11}	9.55×10^{-6}	1.73×10^{-5}
TA-ADP	2.64×10^{-10}	3.73×10^{-4}	7.69×10^{-4}

4. CONCLUSION

The crystal has been grown by slow solvent evaporation technique. The Z-scan study has been employed using He-Ne laser to determine the TONLO properties of TA-ADP crystal. The close aperture Z-scan study confirmed the presence of positive nonlinear refraction in TA-ADP crystal. The magnitude of n_2 is found to be 2.64×10^{-10} cm^2/W. The open aperture Z-scan study revealed the inhabitance of reverse saturable absorption effect with the magnitude of β 3.73×10^{-4} cm/W. The TONLO susceptibility of TA-ADP crystal is found to be 7.69×10^{-4} esu. The promising TONLO parameters of TA-ADP crystal can find applications in photonics devices.

REFERENCES

1. G.E. Francois Phys. Rev. 143 (1966) 597-600

2. A. Moritani, Y. Okuda, J. Nakai Appl. Opt. 22 (1983) 1329-1336

3. M.J. Gunning, R.E. Raab, Piotr Gorski, Wlodzimierz Kucharczyk Ferroelectric Lett. 24 (1998) 63-68

4. R. Levitskii, I. Zachek, L. Korotkov, A. Vdovych, S. Sorokov Bull. Russian Academy Sci. Phys. 75 (2011) 1388-1393

5. S. Chaki, M.P. Deshpande, J.P. Tailor, M.D. Chaudhary , K. Mahato Cond. Matter Phys. 2 (2012) 22-26

6. Shaohua Ji, Fang Wang, Lili Zhu, Xinguang Xu, Zhengping Wang, Xun Sun Sci. Reports (2013) http://dx.doi.org/10.1038/srep01605

7. Xiue Ren, Dongli Xu, Dongfeng Xue J. Cryst. Growth 310 (2008) 2005-2009

8. W.J.P.V.Enckevort, R. Janssen-Van Rosmalen, W.H. Van Der Linden J. Cryst. Growth 49 (1980) 502-514

9. S.P. Ramteke, M.I. Baig, Mohd Shkir, S. Kalainathan, M.D. Shirsat, G.G. Muley, Mohd Anis Opt. Laser Technol. 104 (2018) 83-89

10. Changgui Lu, Yiping Cui, Bing Gu, Feng Wang J. Nonlinear Opt. Phys. Mater. 19 (2010) 327-338

11. Yu-Peng Tian, Ming-Liang Zhang, Zhang-Jun Hu, Han-Mei Hu, Jie-Ying Wu, Xuan-Jun Zhang, Sheng-Yi Zhang, Xu-Tang Tao and Min-Hua Jiang, He-Ping Chen, Suchada Chantrapromma, Hoong-Kun Fun Transact. Metal Chem. 30 (2005) 778-785

12. Mohd Anis, Mohd Shkir, M.I. Baig, S.P. Ramteke, G.G. Muley, S. AlFaify, H.A. Ghramh J. Mol. Struct. 1170 (2018) 151-159

13. V. Ganesh, L. Haritha, Mohd Anis, Mohd Shkir, I.S. Yahia, Arun Singh, S. AlFaify Sol. Stat. Sci. 86 (2018) 98-106

14. Mohd Anis, M.I. Baig, S.S. Hussaini, M.D. Shirsat, Mohd Shkir, H.A. Ghramh Chn. Phys. B 27 (2018) 47801-47807

15. J.H. Joshi, S. Kalainathan, D.K. Kanchan, M.J. Joshi, K.D. Parikh Arabian J. Chem. (2017) https://doi.org/10.1016/j.arabjc.2017.12.005

POLYPYRROLE–POLYVINYL ALCOHOL DOPED Al$_2$O$_3$ COMPOSITES AS AMMINE GAS SENSOR

D. B. Dupare[1] and M. D. Shirsat [2]
Head[1], Department of Chemistry, Shri. Dr. R. G. Rathod Arts and Science College, Murtizapur
Head[2], Department of Physics, Director of Academic Staff College, and Registrar, Dr. Babasaheb Ambedkar
Marathwada University, Aurangabad

ABSTRACT
Synthesis and characterization of polypyrrole films were deeply studied for application of ammine and other gas sensing properties in resent year but polypyrrole –polyvinyl alcohol doped Al$_3$O$_3$ films no deeply studied so here we are synthesis this doped films at room temperature by chemical bath deposition method. The uniform thin films formation was very difficult task.We are synthesised and characterization by U.V.,FTIR and SEM study. The suitable uniform thin films have studies for ammine gas sensing properties at room temperature. The sensing properties of film observe atlower 1-10 ppm level to higher level about500ppm level. The stability and gas sensing behaviour of films has observed for different temperature.

Keywords: Polypyrrole, polyvinyl alcohol,ammine, Al$_2$O$_3$ and sensor.

INTRODUCTION
In recent decay the much more attraction in the field of electro-active polymers to development of new materials that provides the large outputs in field electronic, opticaland sensor devices. The tremendous efforts have been devoted to the optimization of electroactive for enhanced electrochemical stability,mechanical strength and strain and stress (1).Conducting polymers, especially polypyrrole (PPy), are emerging as intelligent materials and they have a wide range of applications in the field of optical, electronic, electrochromic devices and sensors. The reasons for such widespread interest of polypyrrole (PPy) are its easy deposition from aqueous and non-aqueous media, adherence to many types of substrates, stability in air and aqueous media and high electrical conductivity.PPy has certain drawbacks like brittle film forming nature and poor mechanical strength. These limitation can be overcome by introducing PPy with another polymer matrix as host medium to form a strong inter chain interaction betweenthem (2).

Polypyrrole has attractive and interesting materials for achieving the conductivity as well as sensing propertiesand Polyvinyl alcohol as netural macromolecule has been incorporate into polypyrrole to improve their electrical and mechanical properties. PVA has been extensively used because of its availability with different molecular weight, its good film forming character, high hydrophilicity, easy processability, non-toxicity, biocompatibility, biodegradability and good chemical resistance. PVA has wider application because of its chemical, physical and most promising film forming properties.(3) To impart a high level of physical properties and durability against environment, different additives are added usually to PVA polymer in order to modify and improve its properties like electrical and mechanical properties, flexibility and thermal stability.TheControlling the materials properties of conducting polymers such as morphology, electroactivity and conductivity, which are strongly dependent on how conducting polymer are synthesized, is required for the successful implementation of conducting polymers in devices (4).

The study deal with to construction of ammine gas sensors with highly sensitive detection or a lower limit of detection for gas sensing application using Al$_2$O$_3$has become an attractive research work owing to its unique electrical properties, high surface-to-volume ratio, high electron transfer rate, high mechanical properties and outstanding flexibility. Even though the gas sensing response of Al$_2$O$_3$ is large and more rapid than pure polypyrrole films because they get strongly affected by relative humidity at room teperature, slow recovery, poor selectivity, detection limit and repeatability which limits their practical application.The main aim of this study is to information for sensor response measurements has been utilized for PPy/PVA /Al$_2$O$_3$ synthesis and characterization of these thin films. The synthesis uniform PPy/PVA /Al$_2$O$_3$ thin film was to pass the amminegas is turned on for 5 minutes (gas-on) and in the second step is turned off for 20 minutes (air-on) forming a 25 minutes cycle. Gas sensing measurements of PPy/PVA /Al$_2$O$_3$ were carried out at room temperatures.

2 EXPERIMENTAL METHODS
2.1. Materials
PVA of average molecular weight 85,000–124,000 g.mol^{-1} having degree of hydrolysis 87–89% and powder was purchased from Sigma-Aldrich, India. The pyrrole monomer (RankchemRanbaxy,India. sodium hydroxide (GR grade >99%, MERCK), HCl (GR grade, 37%, MERCK). Aluminium foil was purchased from Sigma-Aldrich, India.

2.2. Preparation of Ppy-PVA/ Al₂O₃ film

The composites thin films electrolyte Ppy-PVA/Al$_2$O$_3$films was prepared by mixing the desired amount of pyrrole monomer and HCl in a suitable concentration of acid aqueous solution. Before that, the aluminium foil was impregnated in 0.1N NaOH for 1 h to remove the native oxide film on the surface. The aluminium foil after pre-treatment was immediately placed in the electrolyte solution that had been purged with nitrogen to remove dissolved oxygen. To preparing of thin film on glass substrate by chemical bath deposition method the polyvinyl alcohol dissolved in conductivity water with continuous stirring the an appropriate molar concentration of pyrrole monomer of 0.5M, PVA additive (25mg) dopant Al$_2$O$_3$(0.05M)and oxidant FeCl$_3$(0.5M) was added. The resulting reaction mixture was kept for 2 hours in closed vessel along with glass substrate at 10 ^{0}C. The synthesized uniform films were selected for characterization and gas sensing behaviours.

2.3. Characterization

The structural and morphological characterization of PPY-PVA films and Ppy-PVA/Al$_2$O$_3$doped composites thin films was performed. Both types of the thin films UV-visible and FTIR spectra were recorded at room temperature in Dimethyl sulphoxide (DMSO) solvent. The surface morphology was characterized by using scanning electron microscopy (SEM) at different magnification range by (JEOL-JSM-6360 A). Synthesized PPY-PVA films and Ppy-PVA/Al$_2$O$_3$doped composites films composites were subjected to the Ammonia gas at room temperature by using indigenously developed computer controlled gas sensor system and electrical conductivity (I-V characteristics) of the films was recorded using four probe-methods computer control system.

3. RESULTS AND DISCUSSION

The synthesized Ppy-PVA/Al$_2$O$_3$composites doped thin films characterized by following analysis.

3.1. UV-Visible spectra of synthesized Ppy-PVA/Al₂O₃doped composites film

The UV-Visible absorption spectra of the polymer films were recorded by dissolving the polymer film in Dimethyl Sulfoxide (DMSO) solvent and the absorption spectra of,Ppy-PVA/Al$_2$O$_3$doped composites films in.The band observed at 272-298 nm samples corresponds to π -π* transition of Ppy-PVA/Al$_2$O$_3$ composites films. The bands appear at the 360-408 nm is due to n-π* in Ppy-PVA/Al$_2$O$_3$film due to lone pair on nitrogen in pyrrole ring, which is inter charge transfer band associated of benzenoid to quinoid ring .The transitions of quinone-imine groups, together with the extending tail at 940- 1100nm. The conducting emeraldine salt (ES) phase in the polymer is identified by broad peak at 950 nm. Thus from the UV-visible spectroscopic measurements it was observed that the polymer is composed of mixed phase i.e. conducting salt phase of the polymer. All these UV –visible spectral data clear that in these synthesized films Ppy-PVA/Al$_2$O$_3$doped composites formation take place.

3.2. FTIR of synthesized Ppy-PVA/Al₂O₃doped composites film

The molecular structure of synthesized Ppy-PVA/Al$_2$O$_3$composites films was characterized by FTIR spectroscopy. The Infrared spectra of all Ppy-PVA/Al$_2$O$_3$composites films are similar appear when dissolved in DMSO solvent. The bands related to N–H stretching of an aromatic amine (> NH stretching) normally appear in the region between 3210-3440cm^1. A broad band near at 3464 cm^{-1}for Ppy-PVA/Al$_2$O$_3$film, the same time NH region also shows dependence of the doping. The band appears at 2900 and 3000 cm $^{-1}$ due to CH$_3$ and CH$_2$ (C-H stretching). The two bands observed in the 1410–1426 cm^{-1} regions are related to the stretching of the C–N bonds of the benzonic and quinonic rings, respectively and are present due to the conducting state of the polymer. The bands corresponding to quinoid (N=Q=N) and benzenoid (N–B–N) ring stretching modes were observed at 1668 cm^{-1}for (C=N) Stretching and 1439 cm^{-1} for (C-N), respectively.We attributed the shoulder bands at 1048 cm^{-1} as the asymmetric and symmetric C-O stretching vibrations of polyvinyl group, and peaks at 730 cm^{-1}assigned to C-H bending. All these characteristic bands confirm the presence of conductingemeraldine salt phase of the polymer of Ppy-PVA/Al$_2$O$_3$composites material.

3.3. Morphology of synthesized Ppy-PVA/Al₂O₃doped composites film -

Scanning Electron Microscopy is concerned with the surface structure or (morphology) of polymer. The object of electron microscopy is to observe the relationship between adjacent particles and small group of particles. The microstructure and surface morphology of Ppy-PVA/Al$_2$O$_3$nanocomposite films was examined using scanning electron microscope. The surface morphology of the synthesized Ppy-PVA/Al$_2$O$_3$doped composites film was studied by using scanning electron microscope (SEM). The SEM images of the synthesized films are shown in Fig 3.3. We have observed better porous, granular and globular surface morphology with very good uniformity and adhesiveness for synthesized film samples suitable for sensor application.
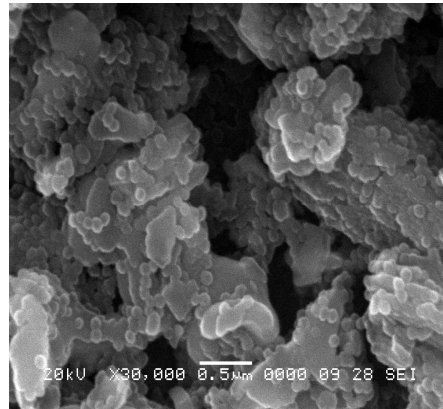
Fig-3.3: SEM of Ppy-PVA/Al$_2$O$_3$films

3.4. Conductivity control and doping

Due to its wide bandgap,-Al$_2$O$_3$is intrinsically aninsulator. However, it also exhibits very good p-typeconductivity when synthesized under reducing conditions. The p-type semiconductivity is commonlyattributed to oxygen vacancies which are ionizedand form donors. Conductivity of the Al$_2$O$_3$ grown by floating zone method can be controlled bychanging by doping.As reportedby Vu QuocTrungaetal (7). The conductivity of Ppy-PVA/Al$_2$O$_3$doped composites were studied by using four probe technique at different concentration dopant varies and its conductivity .
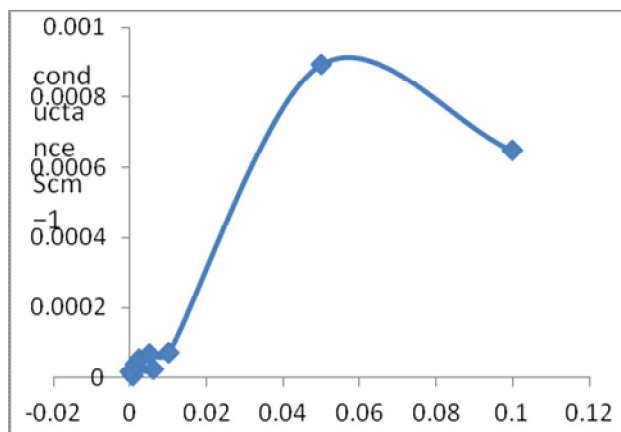
Fig-3.4: conductivity with molar concentration

3.5. I-V Measurement Ppy-PVA/Al$_2$O$_3$doped composites film

The I-V characterization measurement of the Ppy-PVA/Al$_2$O$_3$film was recorded by an indigenously developed computer controlled I-V measurement system using four- probe method at room temperature. The current–voltage (I-V) characteristics of the synthesized Ppy-PVA/Al$_2$O$_3$thin films were studied to ensure an ohmic behavior of the films. A linear relationship of the I-V characteristics shown in Fig.3.4 reveals that the Ppy-PVA/Al$_2$O$_3$doped composites filmshas an ohmic behavior.
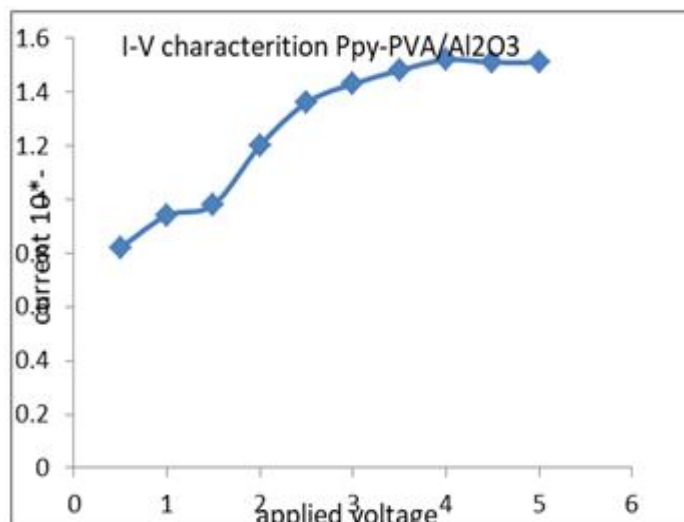
3.5. Ammonia Gas Sensing Characteristics

The ammonia gas-sensing characteristics of the synthesized Ppy-PVA/Al_2O_3dopant composites films at room temperature, we have used the Four-probe technique of resistivity measurement, The synthesized Ppy-PVA/Al_2O_3composites films were exposed to ammonia gas for 5 minutes response time. The recovery time was measured by exposing the film to the air for 20 minutes. The change in resistivity of the film was measured at an interval of 10 s. We have explored the ammonia gas-sensing curves of Ppy-PVA/Al_2O_3at different concentrations of ammonia gas 1 ppm to 500 ppm. The sensing properties of film observe at lower 1-10 ppm level to higher level about 500ppm level. It was observed that the resistivity of the Ppy-PVA/Al_2O_3composites thin film increases in the presence of ammonia gases and after a few minutes becomes saturated and the resistivity decreases steadily to a minimum value, when the ammonia gas was removed however, a drift from its original value was observed. The relationship between change in resistivity and time of the synthesized Ppy-PVA/Al_2O_3composites films when exposed to different concentration of ammonia gas are shown in (Fig. 3.5).
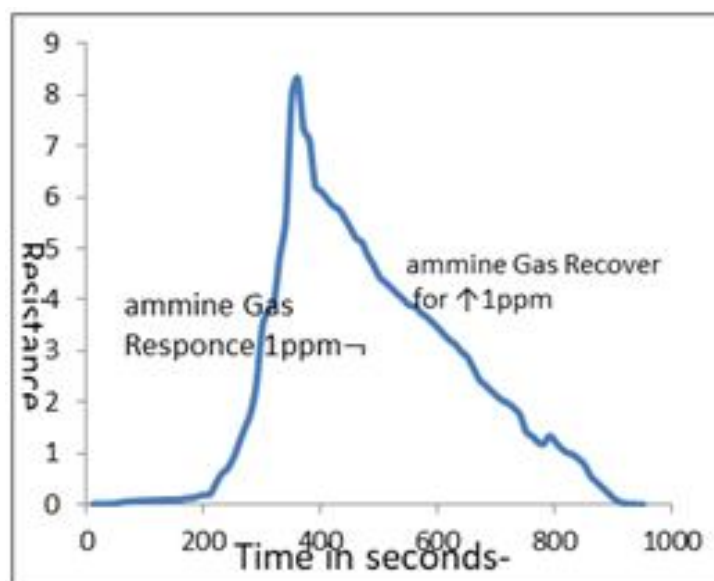
CONCLUSION

This study describes the synthesis of Ppy-PVA/Al_2O_3 composite films using chemical bathdeposition method and successful fabrication of chemiresistive ammine sensors based on Ppy-PVA/ Al_2O_3 composite films for ammine leakage detection at room temperature. Several characterization techniques such as FTIR and SEM analysis confirmed that Al_2O_3 were successfully incorporated into the Ppy/PVA blend matrix. Effect of different concentration of Al_2O_3 on structural, electrical and gas sensing properties of Ppy-PVA/Al_2O_3 composite films were studied. FTIR analysis showed good intermolecular interaction between Ppy/PVA matrix and Al_2O_3. The surface morphology of Ppy-PVA/Al_2O_3 composite films was examined using SEM analysis and the results confirm that Al_2O_3 are homogeneously dispersed in Ppy-PVA matrix. The synthesis composite films with Al_2O_3doping showed highest conductivity with a value of 8.23×10^{-4} Scm^{-1} among all the other Ppy-PVA/Al_2O_3composites. The results obtained in the present study for Ppy-PVA blend and Ppy-PVA/Al_2O_3composite films based for ammine gas sensors. Thissynthesis filmswere response at lower 1ppm level to higher 500 ppm concentration of ammine gases.

REFERENCES

1. Jaehwan K. ,DespandeS.D. , Yun S. and Qubo L. (2006). " a comparative study ofconductive polypyrrole and polyaniline coating on electro-active papers." Polymer journal 38 (7),659-668.

2. YanB.,   wu.Y.and Liang G.(2017)."Recent advance on polypuroleelecrtroactuators"mdpi .com /journal /polymer ppm 1-20.

3. ThangamaniJ. G., Deshmukh K.,   Sadasivuni K.K.,   Ponnamma4 D., Goutham S.,VenkateswaraRao K.. Chidambaram K., Ahamed B., Grace 6 A,M., Faisal M.,& PashaS. K.(2017) "White graphene reinforced polypyrrole and poly(vinyl alcohol) blend nanocomposites as chemiresistive sensors for room temperature detection of liquid petroleum gases" MicrochimActa

4. Thomas M. H., Moulton S.E., GilmoreK J., Gordon G. W., and Marc P.(2011)"Gellan gum doped polypyrrole neural prosthetic electrode coatings" Soft Matter, , 7, 4690–4695.

5. DunstK. J, CysewskaK., KalinowskiP., JasińskiP. (2015) "Polypyrrole based gas sensor for ammonia detection" Materials Science and Engineering, pp 102-108.

6. BradyS., LauK.T., MegillW., WallaceG.G., and DiamondD., (2005), "The development andcharacterization of conducting polymeric-based sensing devices" Synth. Met. 154(1–3)

7. TrungaV. Q., TungbD. N. and HuyencD. N. (2009) "Polypyrrole/Al2O3 nanocomposites: preparation, characterisation and electromagnetic shielding properties" Journal of Experimental Nanoscience Vol. 4, No., 213–219.

8. Mohammad A.S and Bashir I. M(2018)."Characterization of a Novel Polypyrrole (PPy) Conductive Polymer Coated Patterned Vertical CNT (pvCNT) Dry ECG Electrode" Chemosensors, 6, 27pp1-12.

SYNTHESIS AND CHARACTERIZATION OF L-VALINE CAPPED MgO NANOPARTICLES

Y. S. Tamgadge[1], V. G. Pahurkar[4], S. S. Talwatkar[3], G. G. Muley[4]
[1]Department of Physics, Mahatma Fule Arts, Commerce & Sitaramji Chaudhari Science Mahavidyalaya, Warud, Amravati
[3]Department of Physics, D. K. Marathe and N. G. Acharya College, Chembur, Mumbai
[4]Department of Physics, Sant Gadge Baba Amravati University, Amravati

ABSTRACT

We report synthesis, structural and linear optical properties of L-valine capped MgO nanoparticles (NPs). L-valine capped (5, 10 and 15 mol%) MgO NPs were obtained by chemical co-precipitation method. . X-ray diffraction (XRD) pattern shows major reflections at 2θ = 42.94°, 62.09° and 78.44° corresponding to (200), (220) and (222) planes of MgO with a face-centered cubic structure respectively and the average particle size was found to be 12 nm. Transmission electron microscopy (TEM) attests the formation of spherical like nanoparticles. Ultraviolet-visible (UV-vis) spectroscopy attests the formation of NPs and strong blue shift in the excitonic absorption has been observed.MgONPs exhibited strong absorption between 200 and 230 nm, and the absorption edge at 230 nm and 228 nm corresponds to the excitation of four-fold coordinated O_2^- anions in the edges and corners.

Keywords: MgO nanoparticles, L-valine, XRD, UV-vis, TEM.

1. INTRODUCTION
Nanotechnology is playing very crucial role in our day to day life. Materials at the nanoscale found potential applications in various fields e.g. photonics, sensors, optoelectronics, etc. owing to their enhanced properties due to high surface to volume ratio and quantum size effects [1-3]. Metal oxide semiconductors and its nanocomposites are known to possess peculiar nonlinear optical properties and materials like ZnO, CuO and their composites have been already investigated [4-9].Magnesium oxide (MgO) is gaining importance due to its broad applications, such as in catalysis, hazardouswaste treatment,antimicrobial activity, refractory materials, and superconductormaterials [10-15]. In this article, we report synthesis and characterization of L-valine capped MgO nanoparticles which could be further investigated for their nonlinear optical properties.

2. EXPERIMENTAL
All chemicals of analytical reagent grade were used as received without further purification. Magnesium chloride ($MgCl_2 6H_2O$),OxfordDiagnostics, Bombay, L-valine from Central drug house (P) Ltd. (CDH), New Delhi, sodium hydroxide pellets (NaOH, 99%) and ethanol were procured from SD-fine Chemicals, Mumbai, India. Hydrochloric acid (HCl), acetone, Nitric acid (HNO_3) etc have been purchased from SD-fine chemicals ltd, Mumbai, India.Stock solutions of 1M $MgCl_2.6H_2O$, 2M NaOH and 0.1M L-valine in double distilled water were prepared. Double distilled (d.d.) water was used as a solvent for synthesis of MgO nanoparticles. MgO nanoparticles were synthesized using L-valine as capping agent. For this, 10 ml stock solution of $MgCl_2.6H_2O$ was added into 150ml d.d. water and stirred continuously for 1h under constant heating at 80^oC. The temperature was maintained above 80^oC throughout the reaction. For the synthesis of sample MgV1, 5 ml L-Valine (5 mol%) from stock solution was added drop wise into above solution. The resultant solution was again stirred for another 30min. After this, 10-15 ml NaOH stock solution was added drop wise into this solution till the precipitate is formed. The precipitate then washed 2-3 times with d.d. water. The precipitate was then dried for 24h in hot air electric oven. Two more samples namely MgV2 and MgV5 were also synthesized in this manner by adding 10ml (10mol%) and 15ml (15mol%) stock solution of L-valine respectively. One sample (Sample name: MgO-pure) was also prepared without the use of L-valine as capping agent.

3. RESULT AND DISCUSSION
3.1 Structural Morphology using XRD and TEM
All samples of NPs were subjected to structural and morphological characterization by X-ray diffraction (XRD) using Rigaku diffractometer Miniflex II with nickel filtered CuK_α radiation (λ=1.5406 Å). Fig. 3.1 shows the XRD pattern of MgO nanoparticles. XRD pattern shows major reflections at 2θ = 42.94°, 62.09° and 78.44° corresponding to (200), (220) and (222) planes of MgO with a face-centered cubic structure respectively, which are in good agreement with the standard JCPDS card (No: 78-0430). No characteristic peaks of $Mg(OH)_2$, Mg or other impurities were detected in the XRD pattern, indicating the high quality of the synthesized products. The broad nature of the diffraction peaks clearly indicates that the crystallites are in nanometer regime. The mean crystallite size (D) of MgO nanoparticles was calculated for (2 0 0) and (2 2 0) planes using Debye

Scherrer's formula [16] $d = \dfrac{k\lambda}{\beta \cos\theta}$; where k is a constant (k=0.93) and β is width of the diffraction peak at half maxima. The average particle size was found to be 12 nm.
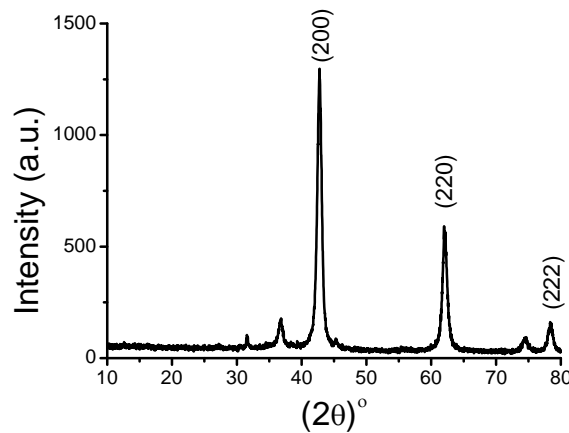
Fig-3.1: XRD spectrum of MgO NPs

TEM micrographs of MgO NPs are shown in Fig 3.2 (a and b) from which, information regarding morphology and size of MgO NPs are evident. Obtained size of NPs are in good agreement with XRD data.
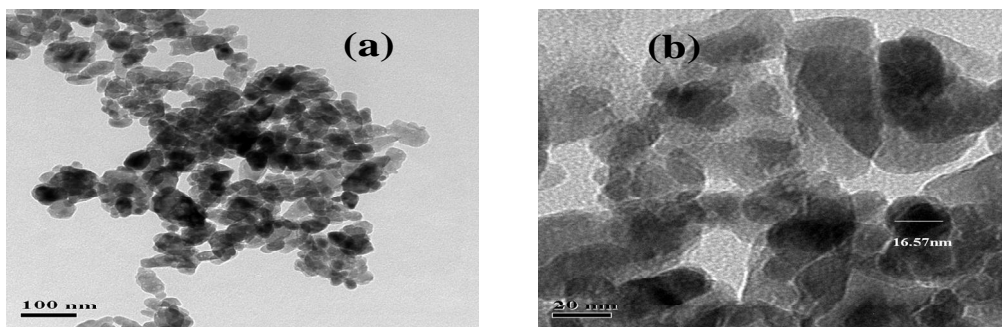
Fig-3.2: TEM images of Zn doped MgO NPs ((a) and (b)).

3.2 Ultraviolet-visible Spectroscopy

UV-vis spectroscopy was performed using UV-visible spectrophotometer (BLK-C-SR, Stellarnet, USA) in the wavelength range 190-900 nm. All samples of MgO NPs have been subjected to Ultraviolet-visible-near infra-red (UV-vis-NIR) spectroscopy and studied extensively.UV-vis spectra and optical band gap using Tauc' plots of MgO nanoparticles are shown in figure 3.3 (a & b). MgO nanoparticles exhibited strong absorption between 200 and 230 nm, and the absorption edge at 230 nm and 228 nm corresponds to the excitation of four-fold coordinated O2− anions in the edges and corners. Blue shifting of the maximum absorption wavelength is thus obvious. MgO NPs capped using highest concentration of L-valine shows strong blue shift and reduced particle sizes are obtained as indicated by quantum confinement effect. However, absorption intensity goes on decreasing and absorption bands become narrow as particle size decreases. This indicates that L-valine effectively modified the surface of MgO NPs by annealing surface states. Low density of surface states might have caused less and selective absorption.
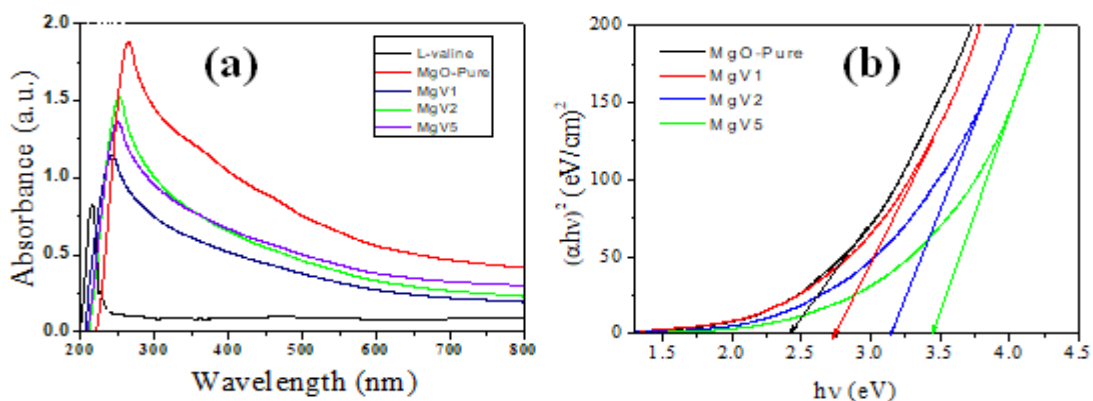
Fig-3.3 (a) UV-vis spectra and (b) Tauc' plots for MgO NPs

Table-3.1: UV-vis spectral details of all MgO NPs

Sample	Max Absorption (nm)	Optical band gap (eV)
MgO-pure	267	1.97
MgV1	244	2.02
MgV2	240	2.15
MgV5	235	2.20

4. CONCLUSIONS

PureMgO nanostructures passivated with L-valine were successfully prepared by soft chemical route. The XRD analysis confirms crystal structure of grown nanoparticles. TEM micrographs reveal the formation of uniformly spherical nanoparticles. UV-vis studies reveal the presence of excitons and absorption peaks appear at 200 and 240 nm for MgO NPs. Maximum optical band gap is witnessed for the sample MgV5 that result due to 15 mol% of L-valine as capping agent.

5. ACKNOWLEDGEMENTS

6. REFERENCES

1. H. Zhong, Y. Zhou, Y. Yang, C. Yang, and Y. Li, J. Phys. Chem. C 111, 6538 (2007).

2. C. Y. Zhang, H. C. Yeh, M. T. Kuroki, and T. H. Wang, Nature Mater. 4, 826 (2005).

3. R. Agarwal and C. M. Lieber, Appl. Phys. A: Mater. Sci. Process. 85, 209 (2006).

4. Y.S. Tamgadge, A.L. Sunatkari, S.S. Talwatkar, V.G. Pahurkar, G.G. Muley, Opt. Mater. 37, 42-50 (2014).

5. Y.S. Tamgadge, A.L. Sunatkari, S.S. Talwatkar, V.G. Pahurkar, G.G. Muley, Opt. Mater. 51, 175-184 (2016).

6. Y.S. Tamgadge, G.G. Muley, K.U. Deshmukh, V.G. Pahurkar, Opt. Mater. 86, 185–190 (2018).

7. Y.S. Tamgadge, P.P. Gedam, R.P. Ganorkar, M.A. Mahure, V.G. Pahurkar, G.G. Muley, AIP Conference Proceedings, 1953, 030003 (2018)

8. Y.S. Tamgadge, G.G. Muley, Materials Science Forum, 863, 85-89 (2016).

9. Y.S. Tamgadge, S.S. Talwatkar, A.L. Sunatkari, V.G. Pahurkar, G.G. Muley, Thin Solid Films 595, 48-55 (2015).

10. Yang PD, Lieber CM. Science 1996;273:1836.

11. Bhargava A, Alarco JA, Mackinnon ID, Page D, Iiyushechkin A. Mater Lett 1998;34: 133.

12. Choudary BM, Mulukutla RS, Klabunde KJ. J Am ChemSoc 2003;125:2020.

13. Kakkar R, Kapoor PN. J PhysChem B 2004;108:18140.

14. Huang L, Li DQ, Lin YJ, Wei M, Evans DG, Duan X. J InorgBichem 2005;99:986.

15. PiyaOuraipryvan, ThammanoonSreethawong ,SumaethChavadej, Materials Letters 63 (2009) 1862-1865.

16. B. D. Cullity, Elements of X-ray diffraction, 2nd ed. Addison-Wesley publishing company, Inc. Reading, Massachusetts (1956).

SPRAY PYROLYSIS DEPOSITION AND CHARACTERIZATION OF NANOCRYSTALLINE MnFe₂O₄ THIN FILM

Chikundre C. B.[1] and Dr. Birajdar A. P.[2]
[1]Department of Physics, Dr. Babasaheb Ambedkar Marathwada University, Aurangabad
[2]B. S. S. Arts Science & Commerce College, Makani Tq. Lohara, Dist Osmanabad

ABSTRACT
$MnFe_2O_4$ thin filmhas been deposited by chemical spray pyrolysis method on a glass substrate at a temperature of 350 ^oC. The deposited film was annealed at 550°C for 4 h. X-ray diffraction technique was employed to confirm theformation of single cubic phase nanocrystalline thin film. The crystallite size of the present thin film is of the order of 15 nm confirming the nanocrystalline nature of the film. The thickness of the film was measured by surface profiler meter and is found to be 289 nm. The formation of spinel ferrite phase is confirmed to active Raman mode peaks of bands in the thin film by using Raman spectroscopy. The energy band gap(E_g)is found to 2.01 allowed direct electronic transitions was observed through UV-vis studies.

Keywords: Spray Pyrolysis; $MnFe_2O_4$; XRD; UV-Vis; Thin film.

1. INTRODUCTION
Ferrites are the most important magnetic material due to their combined electrical and magnetic properties, which can be modified for thedesired application[1]. Now day's ferrite thin films are used in alot of applications, such as magnetic recording media, sensors, and microwave device[2-5]. The ferrite films are effectively utilized as magnetic core materials with thelow iron loss, opto-magnetic devices, and vertical recording magnetic material in surface magnetism study[6]. The spinel type refers to $M^{2+}M_2^{3+}O_4$, which attract great interest owing to their multipurpose practical applications. If M^{3+} = Fe, the resulting spinel ferrites can be represented by the general formula of MFe_2O_4 (M = Mg, Zn, Mn, Co, Cd) is extensively utilized as magnetic materials[7]. However, the presence of the two cations in the spinel structure leads to improved sensing behavior towards target gas/vapors. This motivated us to investigate the ethanol and acetone vapor sensing properties of manganese ferrite ($MnFe_2O_4$). The spinel nanostructure form of $MnFe_2O_4$ with Fd3m space group is commonly illustrated by its unit cell of cubic structure having eight formula units. The entire unit cell from the cubic structure has twenty four cations arranged in eight of the sixty four tetrahedral sites (Mn) and sixteen of the thirty two are arranged at the octahedral sites (Fe^2). In $MnFe_2O_4$ nanostructure, 80% have normal spinel structure and remaining 20% of Mn^{2+} cation arranged in octahedral site with Fe^{3+} cations[8]. The sensitivity of the sensing material highly depends on its size, composition and morphology along with its synthesis techniques[9]. Different preparation methods have been employed to produce nano-sized spinel ferrite $MnFe_2O_4$, such as co-precipitation, hydrothermal and solvethermal synthesis sol-gel, processing and microwave method[10-12]. The present investigation is to enhance the structural and optical properties of the $MnFe_2O_4$ nanoferrite thin film by spray pyrolysis technique.

2. EXPERIMENTAL PROCEDURE
The manganese ferrite ($MnFe_2O_4$) thin film was deposited on to preheated glass substrate (350 ^oC) by using spray pyrolysis technique. The solutions are prepared by using amixture of $Mn(No_3)_2.6H_2O$ (manganese nitrate hexahydrate) of 0.08 M and $Fe(No_3)_3.9H_2O$ (ferric nitrate nonahydrate) of 0.08 M in separately dissolving in double distilled water. The final solutions are prepared by mixing two initial solutions in 1:2 volumetric proportions.

The $MnFe_2O_4$ thin film was prepared by spraying solution on to glass substrate. The glass substrate was pre-heated with an ultrasonication for 30 min in distilling water before film deposition. Then after cleaning glass substrate was mounted on to asurface hot plate and set the substrate temperature to 300 °C. The temperature controller was used to control the temperature within ± 10 °C through a thermal couple connected to the surface of a hot plate. The other preparative parameter such as spray rate 5ml/min. the solution of total quantity 75ml. the parameters of thenozzle to substrate distance 28.5 cm was kept constant and thefreshly prepared solution was atomized in air 0.30 M pa. Compressed air was used as a carrier gas to atomize the spray. The atomized droplets were transferred on to the heated glass substrate for 10s intermittently[13].

In spray pyrolysis method, the precursor material is dissolved in a suitable solvent and then the solution is sprayed on to the preheated glass substrate maintained at a desired temperature. By the spraying of amixture of metallic nitrides, chlorides with a particular concentration and semiconducting film can be prepared. In this process, the precursor solution is atomized through a glass nozzle. The nozzle converts to the solution into small

droplets known as aerosols. These aerosols are allowed to travel through finally incident onto the heated glass substrates.

3. RESULTS AND DISCUSSION
3.1 Structural properties
The Fig. 1 shows that X-ray diffraction pattern of theMnFe$_2$O$_4$ thin film deposited on glass substrate at 300 °C temperature and annealed 550 °C for 4 hrs. The X-ray diffraction shows that some lower intensity peaks appeared in thenickel ferrite thin film due to the lower peaks as (220), (221) (311),(321), (421), (422), (511), (440) and (441) also the spinel cubic crystal structure of the deposited film. Average crystallite size of nanoparticles was calculated from the Debye-Scherrer's equation[14]. (1)

where, D is the crystalline size, $\lambda$is the wavelength of x-ray (1.5406 A), β the full-width of the diffraction line at half–maximum intensity and θ is the Bragg's angle. The crystalline size of themanganese ferrite was estimated to 15 nm in the **table 1**.The film thickness is one of the important physical parameters, its most of the properties depend upon a film thickness[15]. The grain size of film changes with thickness. The thickness of the film was measured using surface profiler and found to be 289 nm.
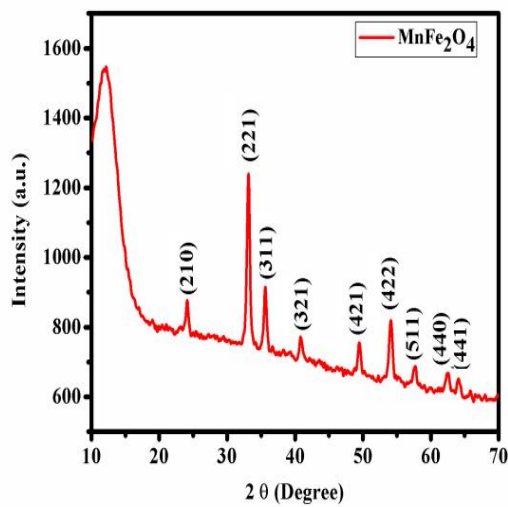
Fig-1: X-ray diffraction ofMnF$_2$O$_4$ thin film
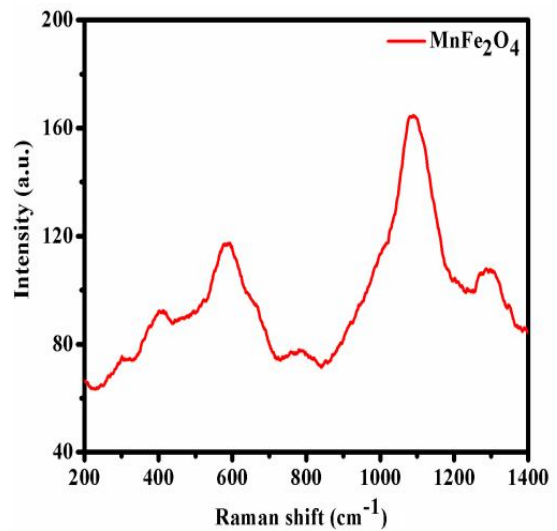
Fig-2: Raman spectra of MnFe$_2$O$_4$ thin film.

Table-1: Lattice constant (a), X-ray density (ρ_x), and crystallite size (T) and energy band gap (E_g) for MnFe$_2$O$_4$ thin film.

Lattice constant a (Å)	X-ray density ρ_x (gm/cm)	Crystallite D size (nm)	Energy band gap E_g eV
8.235	5.485	15	2.01

To have more information regarding the structure ofmanganese ferrite thin film analysis by using Raman spectra was recorded at room temperature are shown in Fig. 2.The Raman peak over the region 671.12 cm^{-1} represents the modes of tetrahedral group and 467.08 cm^{-1}region to the octahedral group of manganese ferrite thin film[16].

3.2 Optical properties
An optical property of manganese ferrite thin film on glass substrate was studied by using UV-VIS spectrophotometer. The optical absorptions spectrum of annealed MnFe$_2$O$_4$ thin film (550 °C) recorded at room temperature. The visible light absorptions a spectrum was examine using UV spectrophotometer having glass substrate. Fig. 3 shows the plot of absorption spectra of MnFe$_2$O$_4$ in 200-800 nm wavelength range. The direct optical band gap energy (E_g)of MnFe$_2$O$_4$thin film are determined by the relation between absorption coefficient (α) and energy (hν) of the incident photon[17].

Where A is a constant independent of hν, and(E_g) is the semiconductor band gap and n is a number equal to 1 for direct band gap. The plot of (αhν) versus (hν) is shown in Fig. 3. It is seen that the direct optical band gap (E_g) of mangnese ferrite thin film is 2.01 nm.The direct and indirect band gap energy ofMnFe$_2$O$_4$ thin films has been determined byTauc plot based on the above formula as shown in fig.3.The value of optical band gap is calculated by extrapolating the straight line portion of thegraph on 'hν' axis[18].
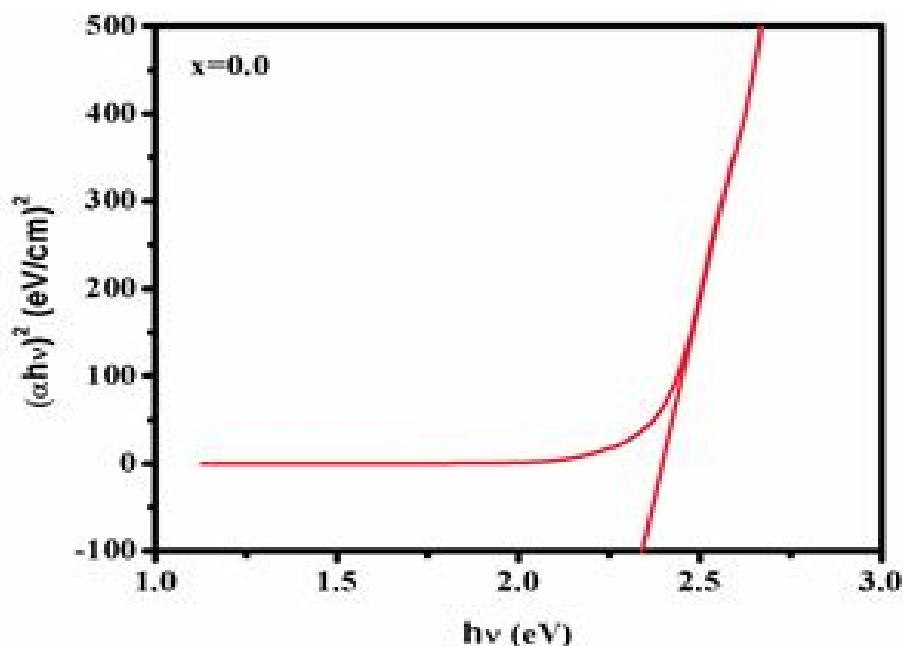
Fig-3: Direct band gap MnF_2O_4 thin film at annealed 550 ^{o}C

REFERENCE

1. C.R. Vestal, Z.J. Zhang, Effects of surface coordination chemistry on the magnetic properties of MnFe2O4 spinel ferrite nanoparticles, Journal of the American Chemical Society, 125 (2003) 9828-9833.
2. D.S. Mathew, R.-S. Juang, An overview of the structure and magnetism of spinel ferrite nanoparticles and their synthesis in microemulsions, Chemical engineering journal, 129 (2007) 51-65.
3. S.W. Lee, S. Bae, Y. Takemura, I.-B. Shim, T.M. Kim, J. Kim, H.J. Lee, S. Zurn, C.S. Kim, Self-heating characteristics of cobalt ferrite nanoparticles for hyperthermia application, Journal of Magnetism and Magnetic Materials, 310 (2007) 2868-2870.
4. R. Valenzuela, Novel applications of ferrites, Physics Research International, 2012 (2012).
5. Z. Sun, L. Liu, D. zeng Jia, W. Pan, Simple synthesis of CuFe2O4 nanoparticles as gas-sensing materials, Sensors and Actuators B: Chemical, 125 (2007) 144-148.
6. S. Bellad, C. Bhosale, Substrate temperature dependent properties of sprayed CoFe2O4 ferrite thin films, Thin Solid Films, 322 (1998) 93-97.
7. S. Kumar, S. Sharma, M. Knobel, R. Choudhary, C.G. Lee, B. Koo, R. Kumar, Structural and magnetic properties of bulk and thin films of Mg0. 95Mn0. 05Fe2O4, Current Applied Physics, 9 (2009) 1009-1013.
8. X.-Y. Long, Z.-J. Zhang, J.-Y. Li, D. Sheng, H.-Z. Lian, Controllable preparation of CuFeMnO4 nanospheres as a novel multifunctional affinity probe for efficient adsorption and selective enrichment of low-abundance peptides and phosphopeptides, Analytical chemistry, 89 (2017) 10446-10453.
9. C. Wu, P. Yin, X. Zhu, C. OuYang, Y. Xie, Synthesis of hematite (α-Fe2O3) nanorods: diameter-size and shape effects on their applications in magnetism, lithium ion battery, and gas sensors, The Journal of Physical Chemistry B, 110 (2006) 17806-17812.
10. K. Park, J. Son, H. Chung, S. Kim, C. Lee, H.-G. Kim, Synthesis of LiFePO4 by co-precipitation and microwave heating, Electrochemistry Communications, 5 (2003) 839-842.
11. J. Sczancoski, L. Cavalcante, M. Joya, J.A. Varela, P. Pizani, E. Longo, SrMoO4 powders processed in microwave-hydrothermal: Synthesis, characterization and optical properties, Chemical Engineering Journal, 140 (2008) 632-637.
12. D. Jugović, D. Uskoković, A review of recent developments in the synthesis procedures of lithium iron phosphate powders, Journal of Power Sources, 190 (2009) 538-544.
13. A.R. Chavan, S.D. Birajdar, R.R. Chilwar, K. Jadhav, Structural, morphological, optical, magnetic and electrical properties of Al 3+ substituted nickel ferrite thin films, Journal of Alloys and Compounds, 735 (2018) 2287-2297.
14. A.R. Chavan, J.S. Kounsalye, R.R. Chilwar, S.B. Kale, K. Jadhav, Cu2+ substituted NiFe2O4 thin films via spray pyrolysis technique and their high-frequency devices application, Journal of Alloys and Compounds, 769 (2018) 1132-1145.
15. O.I. Vinogradova, Drainage of a thin liquid film confined between hydrophobic surfaces, Langmuir, 11 (1995) 2213-2220.

16. G. Dixit, J. Singh, R. Srivastava, H. Agrawal, R. Chaudhary, Structural, magnetic and optical studies of nickel ferrite thin films, Adv. Mater. Lett, 3 (2012) 21-26.
17. A.R. Chavan, R.R. Chilwar, P.B. Kharat, K. Jadhav, Effect of Annealing Temperature on Structural, Morphological, Optical and Magnetic Properties of NiFe 2 O 4 Thin Films, Journal of Superconductivity and Novel Magnetism, (2018) 1-10.
18. N. Rezlescu, E. Rezlescu, C. Pasnicu, M. Craus, Effects of the rare-earth ions on some properties of a nickel-zinc ferrite, Journal of Physics: Condensed Matter, 6 (1994) 5707.

STUDIES ON LINEAR OPTICAL PROPERTIES OF ADP-KDP MIXED CRYSTAL FOR ELECTRO-OPTIC APPLICATIONS

R. N. Shaikh[1] Y. B. Rasal[2], M. D. Shirsat[3], S. S. Hussaini[4]

[1,4]Crystal Growth Laboratory, Department of Physics, Milliya Arts, Science and Management Science College, Beed
[2]Smt. S. K. Gandhi Arts, Amolak Science, P. H. Gandhi Commerce College Kada, Tal. Ashti, Dist. Beed
[3]RUSA Centre for Advanced Sensor Technology, Dr. Babasaheb Ambedkar Marathwada University, Aurangabad

ABSTRACT
In present work ADP-KDP mixed crystal (90:10) has been grown by slow evaporation solution growth technique. The UV-visible study confirms the wide optical transmittance window for electro-optic applications. The transmittance data has been used to evaluate the optical band gap of grown crystal. The optical band gap was found to be 4.95 eV. Theoretical calculations were carried out to determine the linear optical constants like refractive index, reflectance, extinction coefficient, optical conductivity, electrical conductivity, real and imaginary part of dielectric constant.

Keywords: ADP, Growth from solution, KDP, Optical properties, UV-Visible.

1. INTRODUCTION
KDP (Potassium dihydrogen phosphate) is well known hydrogen bonded ferroelectric and ADP (Ammonium dihydrogen phosphate) is also known for its antiferroelectric behavior. The mixing of ADP and KDP leads to significant change in the properties of crystal [1]. ADP and KDP are non linear optical (NLO) crystals with lower impurity which has been used as optical modulator, frequency converter, optical switching, optical data storage, telecommunication accessories [2-4]. Mixing of ADP and KDP is being carried out for many years by several researchers [1, 5]. However there is no report available in the literature on linear optical properties of ADP-KDP mixed crystal. In the present work we have grown ADP and KDP (AKDP) mixed crystal in the ratio (90:10) by slow evaporation solution growth method, characterized by UV Visible spectral analysis and its detailed optical parameters were reported for electro-optic applications.

2. EXPERIMENTAL PROCEDURE
The AR grade ADP and KDP salt was dissolved separately in deionized water with constant stirring to achieve supersaturated solutions. The supersaturated solutions of ADP and KDP was taken in the ratio 90:10 and allowed to stir at constant speed to achieve homogeneity throughout the volume. The prepared solution was filtered by Whatman filter paper and kept for slow evaporation in a constant temperature bath of accuracy ±0.01 ^{0}C at temperature 45^{0}C. The transparent seed crystals were harvested within 10-12 days.

3. RESULT AND DISCUSSION
3.1 UV-Visible Study
The AKDP grown seed crystal of 2 mm thickness was subjected to UV-visible study using the Shimadzu UV-2450 spectrophotometer to assess the optical transparency within the range of 200 to 900 nm and recorded transmittance spectrum is shown in Fig.1. The grown AKDP crystal exhibits high transmittance above 75% in entire visible region. The lower cutoff wavelength is found to be 220 nm indicating the wide optical transmission window favorable for second harmonic generation [6].
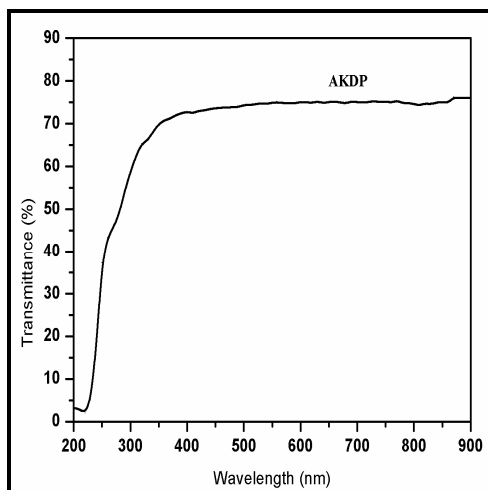
Fig-1: UV Transmittance Spectrum
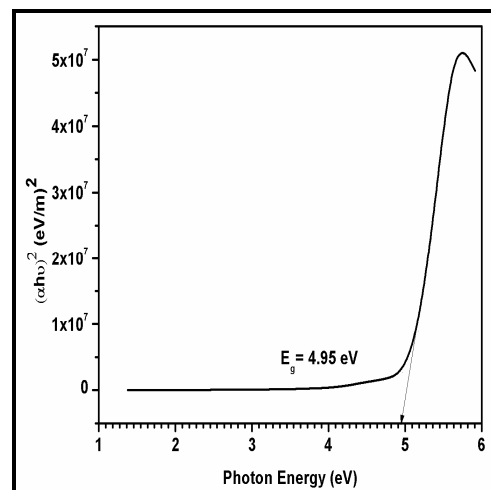
Fig-2: $(\alpha h\nu)^2$ vs. hν (eV)

3.2 Determination of optical constants

Optical parameters of material are important as they provide information on the electronic band structures, localized states and types of optical transitions. The transmittance (T) data was used to evaluate optical absorption coefficient (α) from the following relation [7]

$$\alpha = (1/t) \ln (1/T) \tag{1}$$

Where T is the transmittance and t is the thickness of the seed crystal.

Optical band gap was evaluated from the absorption spectrum and optical absorption coefficient (α) near the absorption edge is given by,

$$\alpha = A (h\nu - E_g)^{1/2} \tag{2}$$

Where E_g is the optical band gap of the crystal and A is a constant.

The band gap of AKDP crystal was estimated by plotting $(\alpha h\nu)^2$ vs. photon energy ($h\nu$). As shown in Fig.2 the value of band gap E_g is estimated by extrapolating the linear portion of the curve to the point $(\alpha h\nu)^2 = 0$. The band gap observed is 4.95 eV. The wide band gap makes it potential candidate for electro-optic applications [8].

The extinction coefficient K can be obtained in terms of absorption coefficient,

$$K = \frac{\alpha \lambda}{4\pi} \tag{3}$$

The reflectance (R) in terms of the absorption coefficient and refractive index (n) can be derived from the relations,

$$R = \frac{1 \pm \sqrt{\exp(-\alpha t) + \exp(\alpha t)}}{1 + \exp(-\alpha t)} \tag{4}$$

$$n = \frac{-(R+1) \pm 2\sqrt{R}}{(R-1)} \tag{5}$$
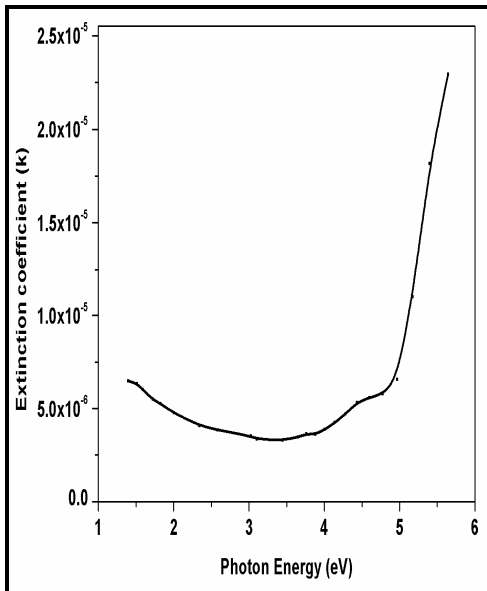
Fig-3: Extinction Coefficient vs. hν (eV)
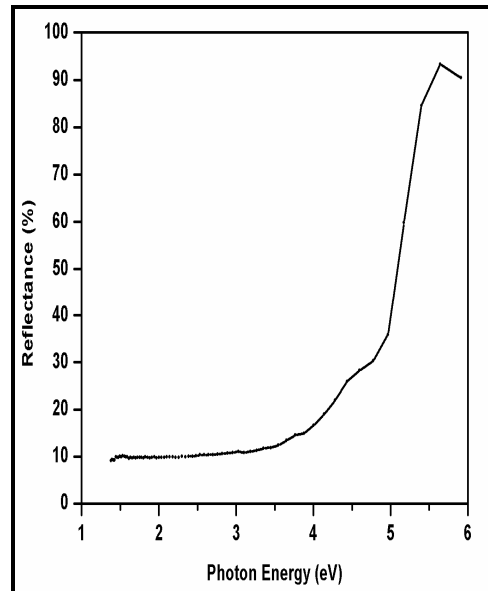
Fig-4: Reflectance vs. hν (eV)

The variations of extinction coefficient, reflectance and refractive index are sequentially shown in Fig. 3,4 & 5. From figures 3 and 4, it is clear that the reflectance and extinction coefficient depend upon the absorption coefficient. The least absorption and significantly lower index of refraction in entire visible region exhibited by AKDP crystal is most desirable property for antireflection coating in solar thermal devices [9].

The optical conductivity is a measure of frequency response of the material when irradiated with light.

$$\sigma = \alpha n C / 4\pi \tag{6}$$

where C is the velocity of light. The plot between optical conductivity against photon energy was depicted in Fig. 6. The high magnitude of optical conductivity confirms the presence of very high photo response nature of the material [9].
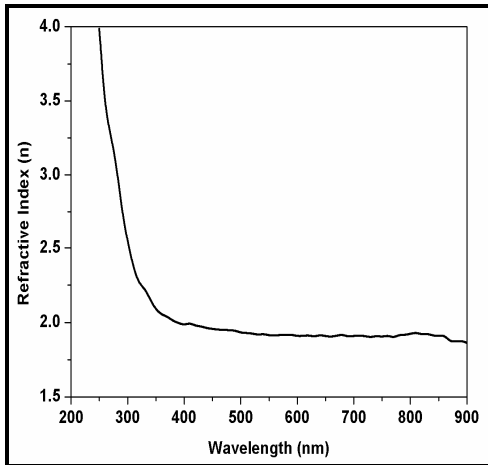
Fig-5: Refractive Index vs. Wavelength
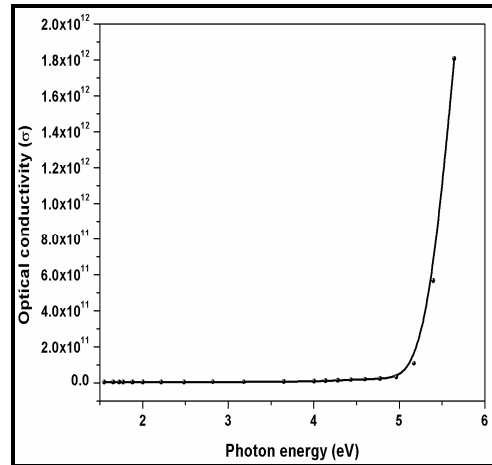
Fig-6: Optical Conductivity vs. hυ (eV)
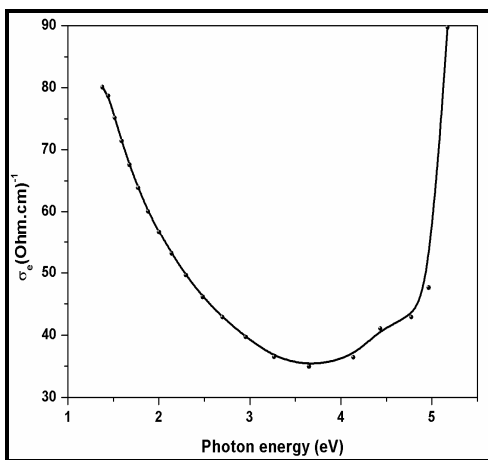
Fig-7: Electrical Conductivity vs. hυ (eV)
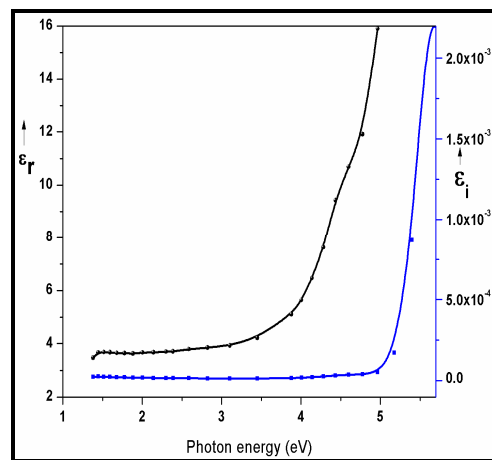
Fig-8: Real& imaginary dielectric const.vs. hυ (eV)

The electrical conductivity can be estimated by optical method using the relation

$$\sigma_e = \frac{2\lambda\sigma}{\alpha} \tag{7}$$

The plot between electrical conductivity against photon energy was depicted in Fig. 7.

The real and imaginary dielectric constants, ε_r and ε_i can be calculated from the following relations and it is depicted in Fig.8.

$$\varepsilon_r = n^2 - K^2 \quad and \quad \varepsilon_i = 2nK \tag{8}$$

CONCLUSIONS

The AKDP crystal has high optical transparency above 75% in entire visible region. The optical band gap is found to be 4.95 eV. The grown crystal has lower refractive index and high optical response which are vital for distinct optical applications. The grown AKDP crystal has encouraging optical properties which makes it potential candidate for electro-optic applications.

REFERENCES

1. Rajesh P., Ramasamy P.,& Bhagavannarayana (2013). Growth of ADP-KDP mixed crystal and its optical, mechanical, dielectric, piezoelectric and laser damage threshold studies. *Journal of Crystal Growth*, 362, 338-342.

2. Mohd Anis, Hussaini S. S., Shirsat M. D., Shaikh R. N., & Muley G.G. (2016). Analysis of the x-ray diffraction, etching, luminescence, photoconductivity, thermal and dielectric properties of an ADP crystal influenced by the bimetallic additive sodium metasilicate (Na_2SiO_3). *Journal of Mater. Res. Express,* 3, 106204.

3. Shaikh R. N., Mohd. Anis, Shirsat M. D., & Hussaini S. S. (2014). Study on optical properties of L-valine doped ADP crystal. *Journal of Spectrochemica Acta Part A: Molecular and Bimolecuar Spectroscopy*, 136, 1243-1248.

4. Shaikh R. N., Mohd Anis, Rabbani G., Shirsat M. D., & Hussaini S. S. (2016). Studies on optical, thermal, mechanical and dielectric properties of L-Cysteine doped KDP crystal to explore NLO device applications. *Journal of optoelectronics and Advanced Materials,*10 (7-8), 526-531.

5. Srinivasana K. Ramasamy P. Cantoni A., & Bocelli G. (1998). Mixed crystals of $NH_4H_2PO_4$–KH_2PO_4: compositional dependence of morphology, microhardness and optical transmittance. *Journal of Material Science and Engineering B,* 52, 129-133.

6. Shaikh R. N., Mohd. Anis, Shirsat M. D., & Hussaini S. S. (2014). Growth, Optical and Dielectric study of pure and Glycine doped Ammonium dihydrogen NLO Crystal: Potential Material for Optoelectronics Applications. *Journal of Material research Express*, doi:10.1088/2053-1591/1/1/015016.

7. Shaikh R. N., Mohd. Anis, Shirsat M. D., & Hussaini S. S. (2014). A study on Optical, dielectric and NLO Properties of L- alanine added ammonium dihydrogen phosphate single crystal. *Journal of optoelectronics and Advanced Materials*, 16 (9-10), 1147-1152.

8. Shaikh R. N., Mohd. Anis, Shirsat M. D., & Hussaini S. S. (2014). Investigation on the Linear and Nonlinear Optical Properties of L-Lysine Doped Ammonium Dihydrogen Phosphate Crystal for NLO Applications. *IOSR Journal of Applied Physics*, 6(1), 42-46.

9. Sabari Girisun T. C., & Dhanuskodi S. (200). Linear and nonlinear optical properties of tris thiourea zinc sulphate single crystals. *Journal of Crystal Research &. Technology*, 44(12), 1297-1302.

COMPARISON OF POTENTIAL ENERGY CURVES FOR THE GROUND STATES OF SiSe MOLECULE

Suchita Deshmukh

Department of Physics, Indraraj Arts, Commerce & Science College, Sillod

ABSTRACT

The diatomic SiSe molecule is spectroscopically studied by many workers. The accurate ground state constants of this molecule derived from latest Fourier Transform spectroscopic analysis are used to construct the RKRV curve. The Hulbert-Hirschfelder, extended Rydberg and Zavitsas potential energy functions are used and are compared with their respective RKRV curve. The error curves are also studied.

Keyword: Hulbert-Hirschfelder, extended Rydberg, Zavitsas, RKRV. RPC

1. INTRODUCTION

The knowledge of potential energy curves is of prime importance in the study of diatomic molecular spectra [1]. In the calculations of F.C. factors, dissociation energies and thermodynamic quantities etc, the studies of potential energy curves are necessary. The empirical potential energy functions like Hulbert-Hirschfelder [2,3], extended Rydberg [4,5] and Zavitsas function [6,7] are usually applied and the potential energy curves are drawn. For all these calculations the Rydberg Klien Rees- Vanderslice RKRV [8-11] curves are essential. Naturally to compute the turning points of various vibrational levels the accurate spectroscopic constants are required. The empirical potential functions also require these molecular constants. In the present study the potential energy curves for the ground electronic states are constructed for the diatomic molecule SiSe. There is one more technique through which the Reduced Potential energy curves (RPC's)[12] could be constructed. This method is also employed to construct the RPC's of these molecule.

2. CHOICE OF MOLECULE AND EXPERIMENTAL DETAILS

SiSe band assignment were established by isotopic and rotational structure studies. In SiSe, the $2450\text{-}2800A^0$ band involves the vibrational levels $4 \leq \upsilon \leq 14$ in the $E^1\Sigma^+$ state and the levels $0 \leq \upsilon \leq 7$ in the $X^1\Sigma^+$ state, while the $4000\text{-}6000A^0$ bands involve the $0 \leq \upsilon \leq 13$ levels in the $E^1\Sigma^+$ state and the $25 \leq \upsilon \leq 52$ levels in the $X^1\Sigma^+$ state [13-15]. For SiS, the $2100\text{-}2400A^0$ bands arise out of transitions from the $0 \leq \upsilon \leq 15$ vibrational levels of the $E^1\Sigma^+$ state to the $0 \leq \upsilon \leq 9$ vibrational levels of the $X^1\Sigma^+$ state, while the $3500\text{-}6600A^0$ bands involve transitions from the $0 \leq \upsilon \leq 17$ levels in the $E^1\Sigma^+$ state to the $20 \leq \upsilon \leq 51$ levels of the $X^1\Sigma^+$ state [16-19]. The unusual occarance of E-X bands of SiSe in two distinct regions is related to the relative positions of the potential energy curves involve in these transitions. Furthermore, since some of these radicals have been observed in the interstellar medium [20-22] the unusual intensity distribution among the E-X bands may be expected to have a bearing on the population distribution among high-lying vibrational levels in the ground electronic state ($X^1\Sigma^+$). The molecular constants derived from these studies are reported in Table 1.

3. THE POTENTIAL ENERGY FUNCTIONS

3.1. The Hulbert-Hirschfelder potential function: This function [2,3] is an extension of a Morse function and is defined as follows.

$$U_{H\text{-}H}(r) = D_e \{ [1\text{- exp}(\text{-}x)]^2 + cx^3(1 + bx)e^{-2x} \} \qquad \ldots\ldots\ldots\ldots \text{(1)}$$

Where $\quad x = x_1(r - r_e)$; $x_1 = (\omega_e x_e / B_e)^{1/2} / r_e$

$c = 1 + a_1(D_e/a_o)^2$; $b = 2 - \{[(7/12) - (D_e - (a_2/a_o))]/c\}$

$a_o = \omega_e^2 / 4B_e$; $a_1 = -1 - \{\omega_e x_e / (6B_e)^2\}$ $\quad$ and

$a_2 = (5/4)a_1 - (2/3)(\omega_e x_e/B_e)$

This function employees the spectroscopic constants like ω_e, $\omega_e x_e$, B_e and D_e etc. The potential energies $U_{H\text{-}H}$ could be calculated by substituting the values of the constants and r values obtained from the RKRV data and the relevant parameters.

3.2. The extended Rydberg Potential function

Murrell and Sorbie [4] and Huxley and Murrell [5] have suggested a potential function, which is based on the force field parameters and is similar to Rydberg potential function. It has the form

$$U_{exR} = D_e - D_e \{ 1 + a_1\rho + a_2\rho^2 + a_3\rho^3]e^{-a/\rho} \qquad \ldots\ldots\ldots\ldots \text{(2)}$$

Where $\quad \rho = r - r_e$; a_1, a_2 and a_3 are the constants defined through following discussions. These constants should not be confused with the constants appearing in H-H function. The constant a_1 is determined from the solution of the following quartic equation :

$D_e a_1^4 - 6 f_2 a_1^2 - 4 f_3 a_1 - f_4 = 0$ ……….…….. (3)

The parameters f_2 , f_3 , f_4 are called force field parameters and are defined as :

$f_2 = 4 \pi^2 \mu \omega_e^2 c^2$

$f_3 = - (3 f_2/r_e) [1 + (\alpha_e \omega_e / 6 B_e)^2]$

$f_4 = (f_3 /r_e)^2 \{15[1 + (\alpha_e \omega_e / 6B_e^2)] - (8\omega_e x_e / B_e)\}$

Usually the largest positive root of equation (3) is selected as a_1. The other parameters a_2, a_3 and a_4 appearing in equation (2) could be calculated from following equations:

$a_2 = (1/_2) [a_1^2 - (f_2 /D_e)]$

$a_3 = (a_1 a_2 - (a_1^3/3) - (f_3/6D_e)]$

This potential function was studied further and was compared with Dimitreva– Zenevich [35] potential function by Bhartiya and Behere[36]. This potential was applied by Birajdar [23] to a large number of molecules and found to give satisfactory results.

3.3. The Zavitsas potential energy function
This recently suggested potential function by Zavitsas [6,7] is based on

electronegativities of the constituent atoms forming a diatomic molecule. This function is also a modification of Morse function but the constant β appearing in Morse function is no more a constant in this function. The function is

$U_z (r) = D_e [\exp (-2 \beta_\pm x) - 2 \exp (\beta_\pm x)]$ ……….…….. (4)

$\beta_M = 8.486 (k_N)^{1/2}$; $x = r - r_e$, Where $k_N = k_e/ D_e$.

The variables $\beta_\pm$ are calculated separately for $r < r_e$ and $r > r_e$.

For $r < r_e$ $\beta_- = \beta_M\{1 + m u^{1/2} \}$

For $r > r_e$ $\beta_+ = \beta_M\{1 + a_1 u^{1/2} + a_2 u^n + a_3 u^{3n} + a_4 u^{5n}\}$

Where, $u = \exp (-2 \beta_M x) - 2 \exp (-\beta_M x) + 1$

For all species $a_1 = -0.32m$; $a_2 = 0.15$; $a_3 = 0.2 - 0.6m$ and $a_4 = (0.21-3m) (\Delta \chi)^{2.}$

m and n are calculated as follows :

$m = - 0.025 r_e + [0.70 \exp (- 7.41 \times 10^3 k_N r_N) / z_1 z_2] + 0.042 |\Delta \chi|$

And

$n = 0.70 - 0.03 r_e + 0.096 / (10^3 \times k_N r_N - 0.3) + [0.55 (\Delta \chi)^2 / r_e^{1/2}]$

Where $r_N = r_e / D_e$

Zavitsas has taken D_e in kcal /mol , bond length in A^o and ω_e in cm^{-1} , μ is in amu the electronegativity difference $|\Delta \chi|$ is from Pauling scale[31]. We also retained same units but finally converted the energies in cm^{-1} which otherwise come in kilocalories .

4. THE REDUCED POTENTIAL ENERGY CURVES
The method suggested by Jenc [12] uses the RKR data. The reduced potential energy curves are drawn between two parameters namely ρ on X axis and u +1 on Y axis

$u = U/D_e$ where $U = \Sigma C_i (v+ \frac{1}{2})^i$ … (5)

C_i are vibrational constants like $C_1 = \omega_e$, $C_2 = - \omega_e x_e$, $C_3 = \omega_e y_e$ etc. De is dissociation energy.

$$\rho = \frac{r - [1-\exp (-r / \rho_{ij})] \rho_{ij}}{r_e - [1-\exp (-r / \rho_{ij})] \rho_{ij}}$$ … (6)

Where r_e is equillibrium internuclear separation and ρ_{ij} can be calculated as follows,

$$\rho_{ij} = \frac{r_e - [(3.96) D_e / \kappa_e]^{1/2}}{1 - \exp(-r_e / \rho_{ii})}$$

... (7)

Where κ_e is a force constant.

The reduced quantities fulfill following conditions.

i) $\rho \geq 0$

ii) $\rho = 0$ for $r = 0$

iii) $\rho = 1$ for $r = re$

iv) $\rho \to \infty$ for $r = \to \infty$

v) $u \leq 0$ for $U \leq 0$

vi) $u = 0$ for $U = 0$

vii) $u \to \infty$ for $U \to \infty$

viii)$u = -1$ for $U = -De$

4.1 Properties of RPC

a) The RPC's of different molecules never intersect.

b) The RPC's of diatomic molecules slightly differing in both atomic numbers coincide.

c) While keeping one atomic number constant a considerable change in the values of other effect than a relatively small change in the values of both atomic numbers. This fact is clear in the RPC's of heavy hydrides.

d) In general the shape of RPC turns slowly to the right around the minimum while becoming broader.

e) Rare gas molecules does not follow the rule number 2, 3 and 4. The RPC's of rare gas molecules coincide approximately to each other and form a right hand boundary of the admissible RPC region.

f) All RPC's including excited state lie in RPC region.

g)The approximate coincidence mentioned in rule 2 and 5 is very accurate in repulsive limb.

It was found that deviations from the above rule in the RPC's of the diatomic molecules might appear suggesting the possible existence of perturbation in the state or because of erroneous extrapolation of the RKR potential.

The applications of RPC could be as follows
i)   It can detect the errors in the construction of RKR.

ii)   It can be used to detect errors in molecular constants.

iii) It can detect the errors in analysis of a spectrum due to perturbations or otherwise.

5. COMPUTATIONAL PROCEDURE
The data of turning points i.e. r_{min} and r_{max} values obtained from RKRV curves of these molecules are substituted in equations 1, 2 and 4 respectively for H-H, extended Rydberg and Zavitsas potential functions along with the corresponding parameters shown in Table 2. The potential energies obtained plotted against r values yield a potential energy curve for that potential for that particular molecule. For comparison purposes all the potential energy curves of each molecule are drawn on same scale along with RKRV curve. These curves are shown in Fig 1 to 4 along with their error curves i.e. the % deviation from RKRV energies.

6. RESULTS AND DISCUSSION
For the study of potential energy curves the molecule is chosen SiSe. The purpose will be clear when we will discuss the Reduced Potential energy Curve (RPC). The PE curves are drawn which shows PE's around 60% of the D_e. Specifically SiSe(58) The Zavitsas Potential energy curves distinctly deviate from RKR. As per discussion with Zavitsas, the potential is mainly suitable for covalent molecules rather than ionic molecule. Moreover the electro negativity values of the atoms forming a diatomic molecule also can cause deviations. The H-H and Extended Rydberg potential functions almost overlap on each other and fall in between the Zavitsas

and RKR curves. The error comparison shows that nearly 3 to 4% deviations occur in the potential energies from RKR values.

The RPC of ground states of SiSe are constructed. The RKR turning points were calculated by the programmes used earlier and latest molecular constants were used and along with the molecular parameters which are presented in Table 2. The corresponding graphs of RKR and RPC are shown in Figures 6(a) and 6(b) These RPC curves show similarity with the corresponding RKR curve, which is one of the criteria obeyed by RPC and show minima at (1,1) i.e. $\rho = 1$ and $u + 1 = 1$.

REFERENCES

1. Hertzberg G., *Spectra of diatomic molecules*, Van Nostrand Reinhold Company, New York, (1950)

2. Hulbert H. M. and Hirschfelder J. O., *J . Chem. Phys.* **9**, 61 (1941)

3. Hulbert H. M. and Hirschfelder J. O., *J . Chem. Phys* **35**, 1901 (1961)

4. Murrell J N and Sorbie K S, *Faraday, Tranjections,* **70**, 1152 (1974)

5. Huxely P and Murrell J N, *J. Chem. Soc. Faraday*, **7A**, part 2, 323 (1983)

6. Zavitsas A. A., *J. Amer. Chem. Soc.* **113**, 13, 4755 (1991)

7. Zavitsas A. A., *J. Mol. Spectros.* **221**, 67, (2003)

8. Rydberg R*., Phys.* **73**, 376 (1931)

9. Klien O., *Z. Phys.* **76**, 226 (1932)

10. Rees. A. L. G., *Proc. Phys. Soc. London Sect. A,* **59,** 998 (1947).

11. Vanderslice. J. T, Mason E. A., Maisch W. G and Lippincott E. R., *J .Mol. Spectros.* **5**, 83 (1960)

12. Jenc F., *International Reviews in Physical Chemistry* **15**, 2, 467 (1996)

13. E.E. Vago and R.F.Barrow, Proc. Phys. Soc. 58, 538 (1946).

14. H.Bredohl, R.Cornet, I. Dubois, and D. Wilderia, J. Phys. B8, L259 (1975).

15. G.Lakshiminarayana and B.J.Shetty, J. Molec. Spectrosc. 130, 155 (1988).

16. S.J.Q.Robinson and R.F.Barrow, Proc. Phys. Soc. A 67, 95 (1954)

17. R.F.Barrow, J.L.Deutsch, A. Lagerqvist, and B.Westerlund, Proc. Phys. Soc. 78, 1307 (1961)

18. S.Gopal, G. Laximinarayana, and N.A.Narasimham, J. Phys. B8, 3781 (1980).

19. G.Lakshiminarayana and B.J.Shetty, S.Gopal, J. Molec. Spectrosc. 112, 1 (1985).

20. M.Morris, W. Gilmore, P. Palmer, B.E. Turner, and B. Zuckermann, Astrophys. J. 199, L47 (1975)

21. N.Kaifu, D.Buhl, and L.E.Snyder, Astrophys. J. 195, 359 (1975).

22. D.Buhl, L.E. Snyder, F.J. Lovas, and D.R.Johnson, Astrophys. J. 201, L29 (1975).

23. Dimitreva J. K and Zenevich V. A *Chem. Phys . Lett* **96**, 228 (1983)

24. Huber K P and Herzberg G, *Constants of diatomic molecules*, Van Nostrand Reinhold Company, New York (1979).

25. Sunande K, Sheila G, Shetty B J and Lakshminarayana G, *J. Quant.*

Table-1: Spectroscopic constants of the ground states of SiSe molecule

Molecule/ Constants	M	ω_e	$\omega_e x_e$	$\omega_e y_e$	B_e	α_e	D_e	r_e	References
SiSe	20.7224706	574.87	1.659	--	0.1920	0.0007	46021.2145	2.058324	24,25

Note: All constants are in cm^{-1} except r_e, which is in Å and μ is in amu

Table-2: Parameters of H-H, extended Rydberg, Zavitsas and RPC potentials for the ground state of SiSe molecule

Parameters		Zavitsas Parameters	
H-H Parameters		Bm	1.499285
a_0	430306.656	κ_e	4.107545
a_1	-2.81934022	κ_n	0.031224
a_2	4.175432205	r_n	0.015647
c	7.798819243	Z_1	3.8
b	0.246225029	Z_2	5.4
x_1	1.485584139	e_1	1.9
Extended Rydberg Parameters		e_2	2.55
a_1	1.281205	M	-0.02324
a_2	-1.388649	N	1.309356
a_3	0.546090	a_1	0.007438
		a_2	0.15
		a_3	0.213947
		a_4	0.118188
		RPC Parameter	
		ρ_{ij}	1.478062
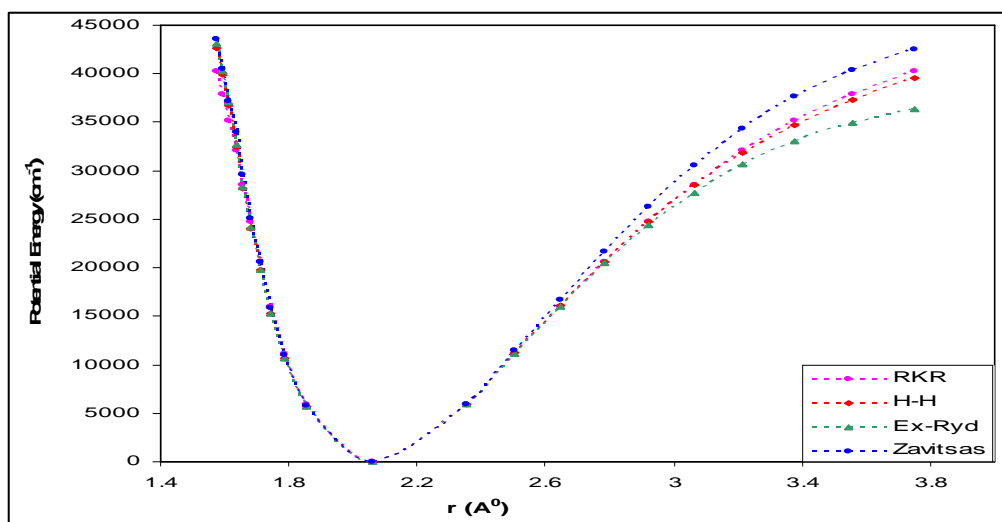
Figure-1 (a): RKR, H-H, Extended- Rydberg & Zavitsas Potential energy curves for the ground state of SiSe molecule
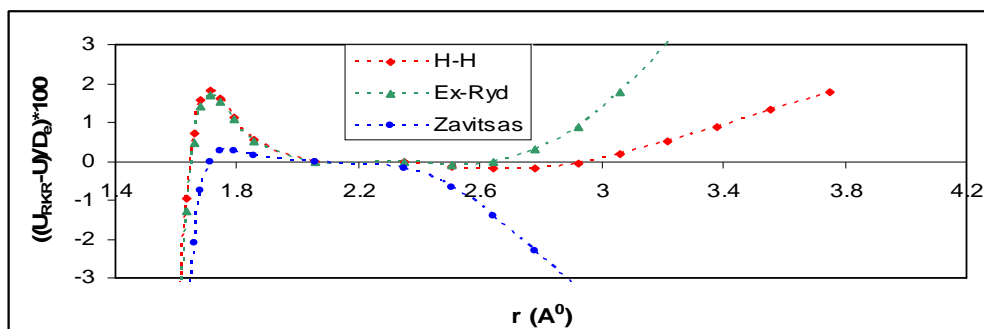
Figure-1 (b): % Deviation of H-H, Extended- Rydberg & Zavitsas Potential energy curves for the ground state of SiSe molecule
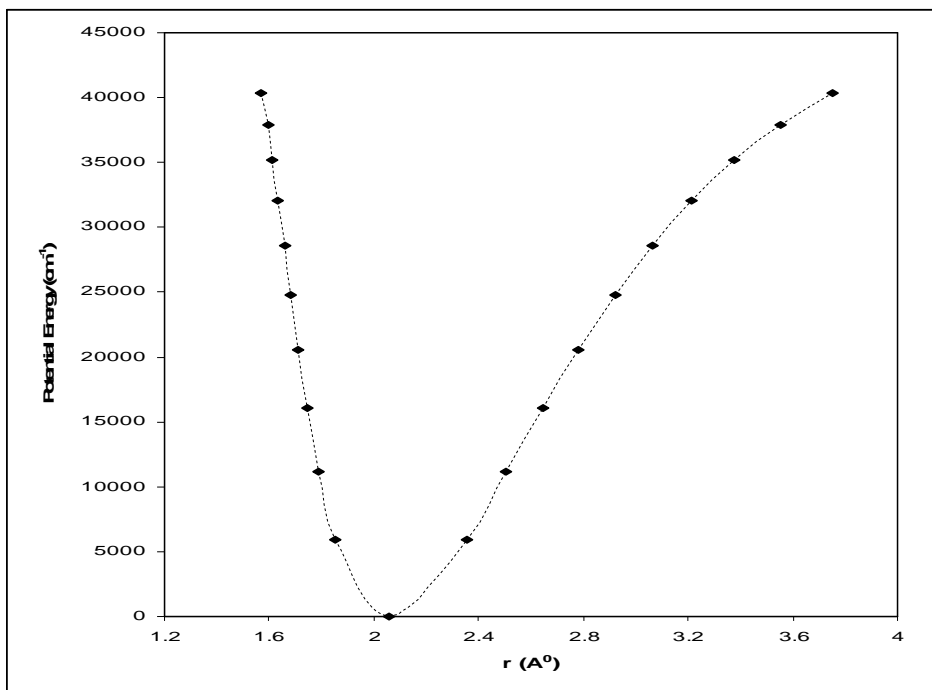
Figure-2 (a): RKR Potential energy curve for the ground state of SiSe molecule
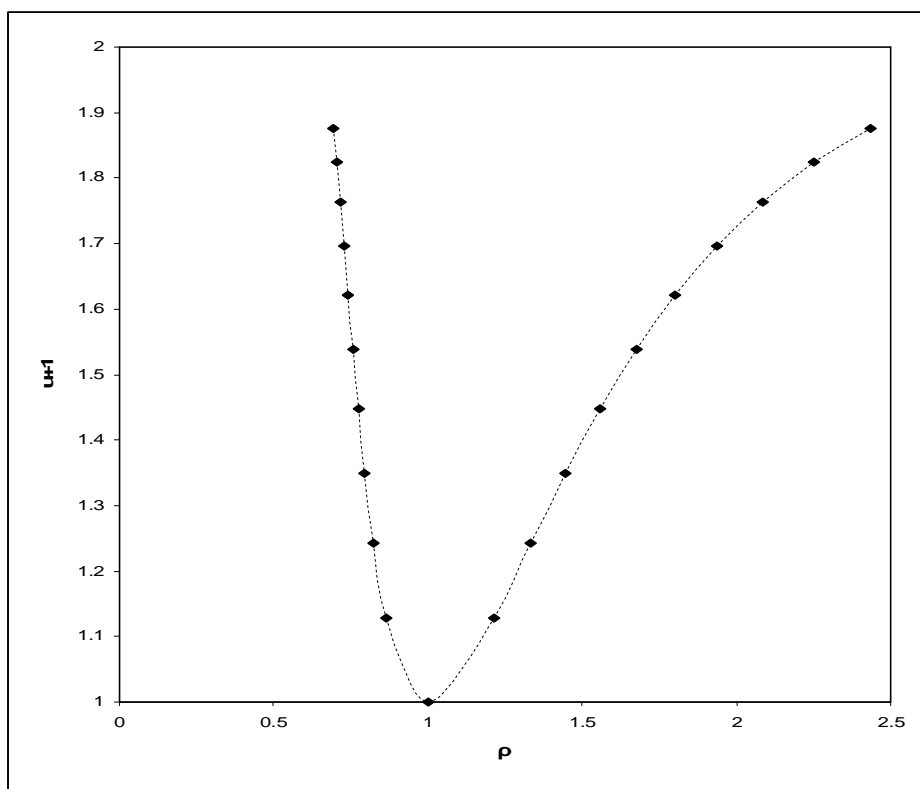
Figure-2 (b): RPC of the ground state of SiSe molecule

ELECTRICAL PROPERTIES OF M-TYPE HEXAGONAL FERRITE SYNTHESIZED BY SOL GEL METHOD

G. B Todkar[1] and R.H. Kadam[2]
[1]Dayanand Science College, Latur
[2]Shrikrishna Mahavidyalaya Gunjoti, Osmanabad

ABSTRACT

Hexagonal ferrites have attracted special attention due to their interesting electrical and magnetic properties. Strontium hexaferrites lie among the M-type class of hexaferrites which possesses a general formula $M\text{-}Fe_{12}O_{19}$. The general formula of present prepared ferrite were $BaCe_xDy_xFe_{12-2x}O_{19}$ in which the x=0.00,0.25, 0.50, 0.75 and 1.The ferrite material were doped with some quantity of Ce-Dy and these hexagonal ferrite were synthesized by sol-gel method using chelating agent as a citric acid. The preparation techniques as well as the structural doping of Ce-Dy ions influence the properties of this compound. The formed phases in the sample were characterized by X-ray diffraction using Philips X-ray diffraction with Cu-Kα radiation source. The variation of DC resistivity with temperature measured using two probe methods.

Keywords: Ferrite, Hexagonal material, Magnetic material, Sol-gel, X-ray diffraction.

1. INTRODUCTION

Ferrites are the magnetic ceramics consisting of iron (Fe^{3+}) as their main component. These materials have number of applications in various fields because they possess both electrical as well as magnetic properties[1-4]. Basically ferrites are ferrimagnetic materials as suggested by L. Neel. Ferrite compounds are very important because of their optical, electrical and magnetic properties. Ferrites are chemical compounds, ceramic with iron (III) oxide Fe_2O_3 as their principal components. Ferrites are usually non-conductive ferrimagnetic ceramic compounds derived from iron oxides such as hematite (Fe_2O_3) or magnetite (Fe_3O_4) as well as oxides of other metals. The magnetic and electrical properties of the spinel ferrites are strongly dependent on their physical structure, known by the general formula AB_2O_4, consisting of an almost perfect interstices cubic closed-packed oxygen arrangement, in which the cations reside on tetrahedral and octahedral inter-sites. The unit cell is obtained by doubling the approximately face-centered cubic oxygen sub-lattice along each of three directions. Of the resulting 64 tetrahedral or (A) sites and 32 octahedral or (B) sites, only 8 and 16 are occupied, respectively, by cations in stoichiometric spinel [5].

Due to the structural varieties like spinel ferrites, garnet and hexagonal ferrite the cations of different sizes can be accommodated at the available sites and thereby exhibit interesting electrical and magnetic properties. The electrical and magnetic properties of ferrite depend upon method of preparation, amount and type of dopants, preparative parameters etc. Hexagonal ferrites are classified on the basis of their chemical composition and crystal structure. It exist in six crystallographic forms i.e. M type ($AFe_{12}O_{19}$), X type ($A_2Me_2Fe_{28}O_{46}$), Y type ($A_2Me_2Fe_{16}O_{27}$), W type ($AMe_2Fe_{16}O_{27}$), U type ($A_4Me_2Fe_{36}O_{60}$) and Z type ($A_3Me_2Fe_{24}O_{41}$) type. Where A represents ions like Ba, Sr, Pb, and Me represents divalent metal ions like Mg or Zn[6].

Mixed metallic oxides are designated as an important class of compounds and among them ferrites are most prominent by virtue of their high electrical resistivity, thermodynamic stability, electro-catalytic activity and resistance to corrosion. Ferrites are regarded as better magnetic materials than pure metals because of their high resistivity, lower cost, easier manufacture and superior magnetization properties[7, 8]. Substitutions of magnetic/non-magnetic ions in simple and mixed ferrites have received a great deal of interest over the past few years. The presence of these ions in ferrites is found to alter their structural, magnetic and electrical properties. We have proposed the present study by keeping the importance of pure and substituted M-type hexagonal Barium ferrite in mind. There are various methods used to prepare sample like spray pyrolysis [9],sol-gel method [10, 11] and hydrothermal synthesis method [12]. Sol-gel method is adopted to synthesize the ferrite samples. The prepared samples are characterized by X-ray diffractometer and D.C. resistivity by two probe method and studied its structural and electrical properties.

2. EXPERIMENTAL

In this work the sol–gel method was adopted for synthesizing Ce-DY substituted barium ferrite samples. Iron nitrate, barium nitrate, cerium nitrate, dysprosium nitrate and citric acid were taken and weighted according to the stoichiometric ratio. The iron nitrate, barium nitrate, dysprosium nitrate and cerium nitrate were dissolved in distilled water under stirring to form an aqueous solution. Citric acid added as a chelating agent. The pH of the solution was adjusted around 7 adding ammonia solution. The solution stirred continually at 90° C until auto

combustion takes place and ash is formed. The ash is grounded to obtain fine powder and then prepared powder sintered at 1000°C. The flow chart of preparation of M-type hexagonal ferrite by sol-gel method is shown in Fig. 1.
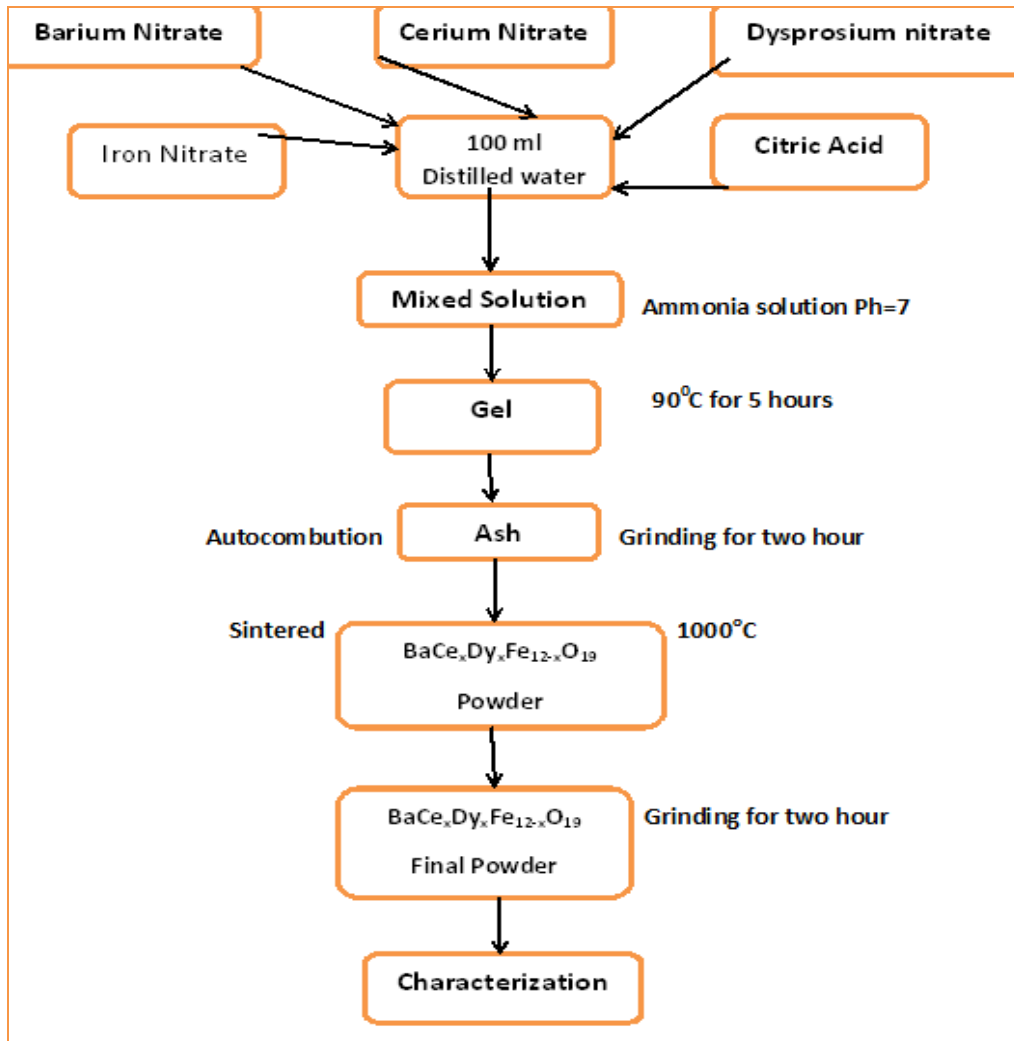
Fig-1: Flow chart of synthesis of ferrite sample by sol-gel method.

3. CHARACTERIZATION
The crystal structure was analyzed using X-ray diffractometer with Cu–kα (λ=0.154nm) radiation. The DC electrical resistivity is measured for all the samples as a function temperature in the temperature range 300–800K.

4. RESULT AND DISCUSSION
4.1 X-Ray Diffraction:
Fig. 2 shows the X-ray diffraction pattern of hexagonal ferrite. The Bragg reflection peaks of sample are sharp, narrow, and intense, indicating high crystallinity and fine grain size in the produced samples. All of the diffraction peaks for the sample well indexed. The crystal structure of sample is hexagonal magnetoplumbite crystal unit cell. Using X-ray diffraction, the lattice parameter, c/a ratio is calculated. The values of lattice parameter for pure $BaFe_{12}O_{19}$ is a=5.8871A° and c=23.182A° for x=0.00 sample. As reported earlier an examination of c/a parameter (ratio of height to width) may be used to quantify the structure type. The M-type hexagonal structure can be assumed if the observed ratio is lower than 3.98. Here in present series c/a ratio is 3.9378,this value is below 3.98 hence it confirm M-type hexagonal structure of prepared sample. The crystal size determined by using Scherrer formula [13],

$$D = \frac{k\lambda}{\beta \cos\theta}$$

(1)

Where D is the average size of the crystallites, k the Scherrer constant its value is 0.9, λ the wavelength of radiation, β the peak width at half height, and θ corresponds to the peak position. The crystal size is found to be D=43.9086 nm for x=0.00 of pure barium ferrite sample.
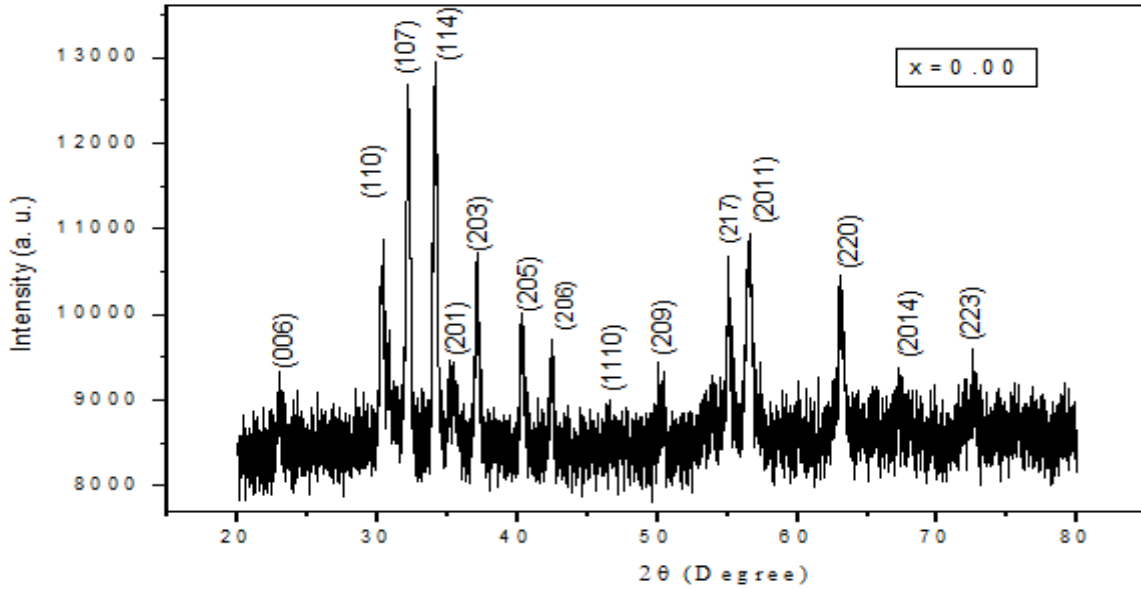
Fig-2: X-Ray diffraction of ($BaCe_xDy_xFe_{12-x}O_{19}$) with X=0.00

4.2 D.C. Resistivity

DC electrical resistivity is one of the useful characterization techniques to understand conductivity mechanism. The DC resistivity of the samples is estimated by two probe methods. Sample made in the form of pellet. A thin layer of silver paste was applied on both the flat surface of the pellets for good electrical contact. The sample holder along with the sample is placed in an electric furnace. The temperature of the furnace was varied using dimmer. A suitable thermocouple (Chromel- Alumel) was used to measure the temperature of the sample. The resistance of a sample was measured at the regular interval of temperature (5 K).

The values of resistivity were calculated using the following equation,

$$\rho = \frac{RA}{t} \quad \Omega \cdot cm \tag{2}$$

Where R: Resistance of the sample; A: Surface area of the sample = πr^2; r: Radius of the sample;

D.C. resistivity is studied as a function of temperature and the plot of log ρ vs 1000/T for all the compositions is shown in Fig.3. Fig.3 shows that for all sample resistivity decrease with the increase of temperature. Increase of temperature generally increases the mobility of conduction charge species and, therefore, the resistivity decreases [14]. The ferrites show semiconducting behavior.

From the Fig.3, DC electrical resistivity of the samples was found to be decreased with increasing the doping composition of Ce-Dy in barium ferrite. For pure barium ferrite with x=0.00 has higher value of resistivity and for highly Ce-Dy doped sample with x=1the value of resistivity is minimum.
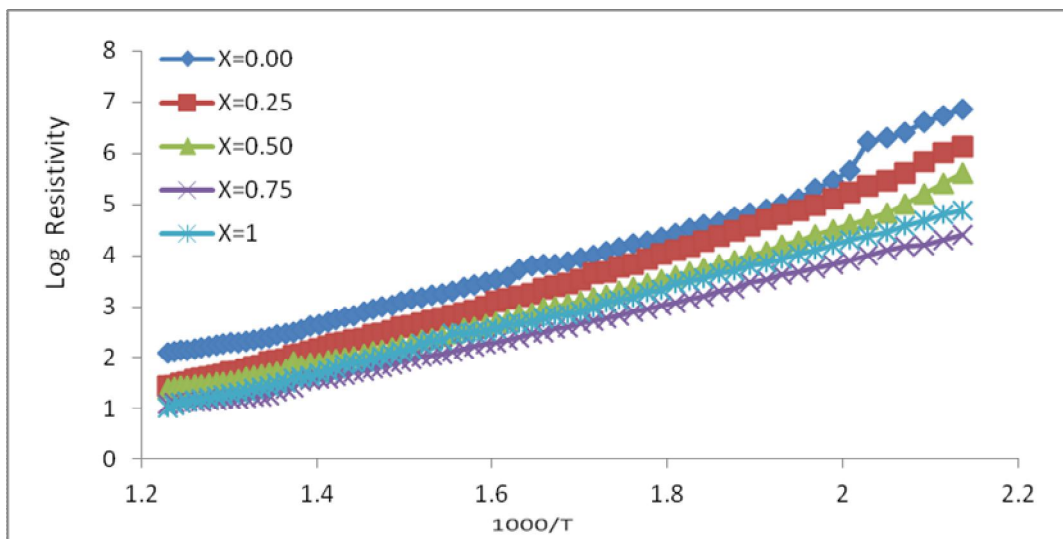
Fig-3: Variation of D. C.Resistivity with temperature of ($BaCe_xDy_xFe_{12-x}O_{19}$) with X=0.00,0.25,0.50,0.75,1.

5. CONCLUSION
The M-type hexagonal ferrites are synthesized successfully by sol-gel autocombustion methods. The formation of ferrite phase is confirmed by X-ray diffraction. From X-ray diffraction the structure of sample is hexagonal magnetoplumbite crystal with crystal size D=43.9086 nm for x=0.00 sample of pure barium ferrite. The measurement of resistivity with temperature shows highest value of resistivity is obtained for x=0.00 sample. The value of resistivity decreases with increase in doping composition of cerium and dysprosium.

REFERENCES
1. Iqbal M. J., Ashiq M. N., Hernandez-Gomez P., Munoz J. M., Cabrera C.T, (2010). Influence of annealing temperature and doping rate on the magnetic properties of Zr–Mn substituted Sr-hexaferrite nanoparticles, J. Alloys Compd. 500,113–116.

2. GhasemiA, Liu X., MorisakoA. (2009), Effect of additional elements on the structural properties, magnetic characteristics and natural resonance frequency of strontium ferrite nano particles/polymer composite, IEEE Trans. Magn.45 (10), 4420–4423.

3. Kim S. G., etal. (2007). Low temperature crystallization of barium ferrite nanoparticles by a sodium citrate-aided synthetic process, J. Phys. Chem. C 111(28), 10175–10180.

4. SozeriH., MehmediZ., Kavas H., Baykal A.(2015). Magnetic and microwave properties of $BaFe_{12}O_{19}$ substituted with magnetic, non-magnetic and dielectric ions, Ceram. Int. 41, 9602–9609.

5. Lewis L.H., Jiménez-VillacortaF. (2013).Perspectives on permanent magnetic materials for energy conversion and power generation, Metallurgical and Materials Transactions A, 44, 2-20.

6. Sami MahmoodH., MunaZaqsawD. Mohsen Osama E., AwadallahA., BsoulI., AwawdehM., MohaidatQ. (2016). Modification of the Magnetic Properties of Co2Y Hexaferrites by Divalent and Trivalent Metal Substitutions,Solid State Phenomena Vol. 241, 93-125

7. SrivastavaM., ChaubeyS., OjhaA.K. (2009). Investigation on size dependent structural and magnetic behavior of nickel ferrite nanoparticles prepared by sol–gel and hydrothermal methods, Materials Chemistry and Physics, 118 (2009) 174-18O

8. Li F.,Liu J., Evans D.G., Duan X.(2004). Stoichiometric synthesis of pure MFe_2O_4 (M= Mg, Co, and Ni) spinel ferrites from tailored layered double hydroxide (hydrotalcite-like) precursors, Chemistry of materials, 16, 1597-1602.

9. Kim M. H. etal. (2009). Nano sized barium ferrite powders prepared by spray pyrolysis from citric acid solution, Ceram. Int. 35(5), 1933–1937.

10. Auwal I., Baykal A. B., GunguneşH., Shirsath S.E (2016). Structural investigation and hyperfine interactions of $BaBi_xLaxFe_{12−2x}O_{19}$ ($0.0\leq x\leq 0.5$) hexaferrites, Ceramics International, 42, 3380-3387.

11. HossainM. S. , AlamMd. B., ShahjahanM.,Ara Begum H.,HossainM. M.,IslamS.,Khatun, M. Hossain, M. S. Alam, Al-MamunMd. (2018), J. of Adv. Dielectric, Vol. 8, 1850030.

12. KoseogluY., Alan F., Tan M., YilginR.,OzturkM(2012). Low temperature hydrothermal synthesis and characterization of Mn doped cobalt ferrite nanoparticles, Ceramics International, 38, 3625-3634.

13. Langford J.I. and Wilson A.J.C.(1978). Scherrer after Sixty Years: A Survey and Some New Results in the Determination of Crystallite Size," J. Appl. Cryst. 11, 102-113.

14. MaisnamM., PhanjoubamS. (2014). Higher d.c. resistivity of Li–Zn–Cd ferrites prepared by microwave sintering compared with conventional sintering, Bull. Mater. Sci., Vol. 37(6), 1227–1232.

MAGNIFICENT TRANSMUTATION IN OPTICAL TRAITS DUE TO METHIONINE DOPING ON ZINC THIOUREA SULPHATE (ZTS) METAL COMPLEX CRYSTAL

Siddique Aneesa Fatima[1], Rupali B. Kulkarni[2], Mahendra D. Shirsat[3], S. S. Hussaini[4]
[1,4]Crystal Growth Laboratory, Milliya Arts, Science & Management Science College, Beed
[2,3]RUSA Centre for Advanced Sensor Technology, Department of Physics, Dr. Babasaheb Ambedkar Marathwada University, Aurangabad

ABSTRACT

Present investigation explores the change in properties of Zinc Thiourea Sulphate (ZTS) crystal due to amino acid Methionine addition. Superior quality Methionine Zinc Thiourea Sulphate (M-ZTS) crystal with 0.1 M% concentration of Methionine was grown from aqueous solution by the slow evaporation method. Shimatzu make spectrophotometer was used to confirm the UV-visible spectral analysis in the range of 200–900 nm which affirmed the 88% transmittance, enhanced band gap value, lower cut off and lower optical constants viz. extinction coefficient, , refractive index, and reflectance of M-ZTS crystal. The obtained linear optical constants parameters showed the superiority of M-ZTS for application in distinct optoelectronics and laser stabilization systems.

Keywords: Crystal growth, Extinction coefficient, Refractive index

1. INTRODUCTION

Nonlinear optical materials like thiourea metal complexes offering improved optical, electrical and non-linear optical (NLO) coefficient has been sustained for past few decades due to their wide applications **[1-4].** Nonlinear optical (NLO) material Zinc tris (thiourea) sulphate (ZTS) is a best alternative for potassium dihydrogen phosphate crystals in frequency-doubling and laser fusion due to their properties high optical transparency, low refractive index, low reflectance low extinction coefficient ,widened band gap, Second harmonic generation efficiency 1.2 times of KDP, growth from solution by slow evaporation **[5-15].**

The impressive and significant influence of amino acid on the optical and electrical response of ZTS crystal **[16-24]** has attracted the attention of authors **[25-27].** As an output of literature study, authors want to acknowledge that authors are firstly elaborating the optical studies of Metheonine doped ZTS confirming its superiority for optical device applications.

2. EXPERIMENTAL PROCEDURE

Zinc Thiourea Sulphate (ZTS) metal complex salt was prepared by taking Zinc Sulphate and thiourea in 1:3 molar concentration. Prepared salt was further purified by repetitive recrystallization. 0.1M% Methionine was doped in ZTS supersaturated solution and the prepared solution was filtered in a sterilized beaker and kept for slow solvent evaporation in a constant temperature bath at 37°C. After UV-visible study, it was evident that 0.1M% Methionine doped ZTS express high prominent and good crystal planes and higher transmittance The 0.1 M% Methionine doped ZTS crystal is shown in **Fig. 1.**
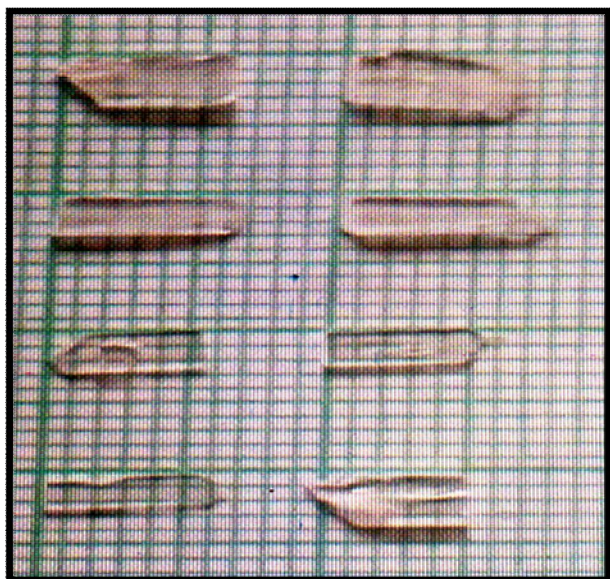
Fig-1: Metheonine doped ZTS crystals

3. RESULTS AND DISCUSSION
3.1. Optical study
3.3.1 UV-visible study
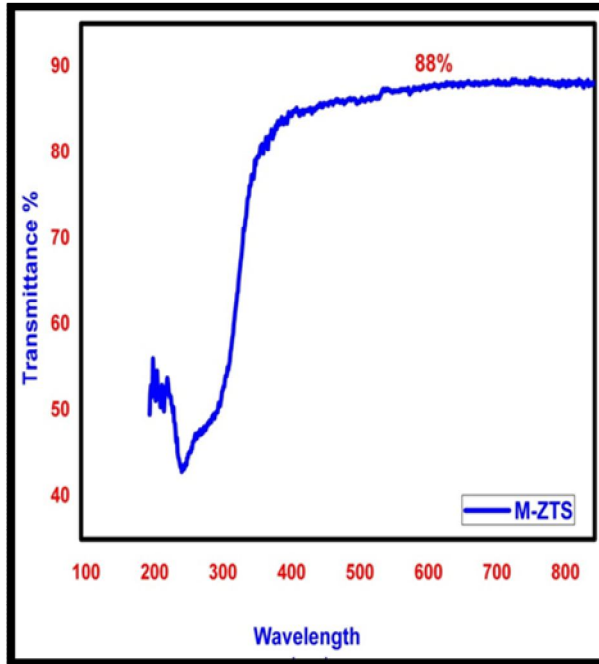
Fig-2: Transmittance Curve
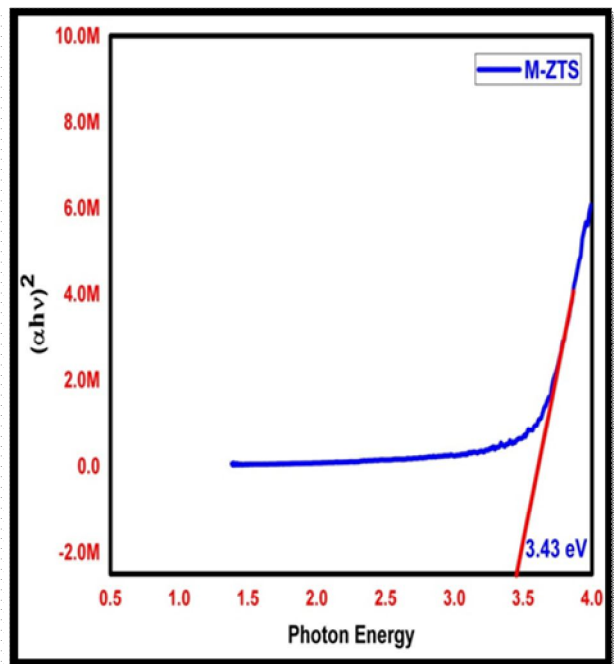
Fig-3: Tauc's Plot of band gap

Shimadzu make UV-2450 spectrophotometer was used in the range 200-900 nm to ascertain the optical transmittance of M-ZTS crystals and plotted in **Fig.2** showed maximum transmittance 88% in the visible region. The enhancement in optical transmittance may be attributed due to a decreased scattering effect **[28]**. The high transmittance has shifted the cut-off wavelength towards the lower wavelength **[29]**.

3.3.2 Band Gap

Tauck's plot demonstrated the optical band gap shown in **Fig.3.** The optical band gap of M-ZTS crystal is 3.43 eV. Widened band gap is added advantage for optoelectronics device fabrication **[30-33]**.

3.3.3 Linear Optical constants
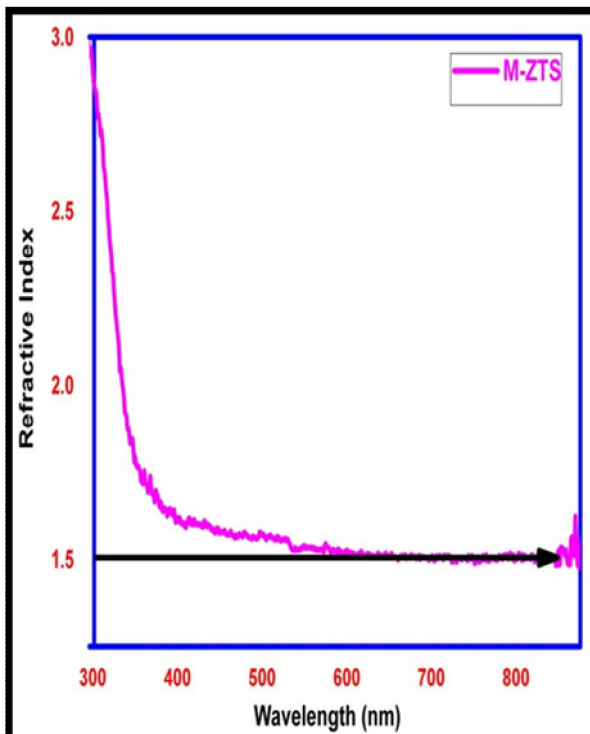
Fig-4: Refractive Index
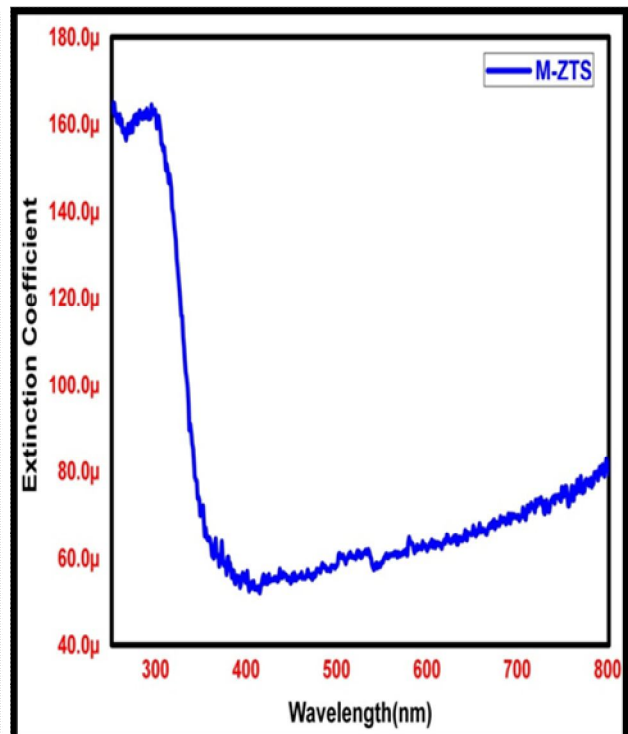
Fig-5: Extinction coefficient
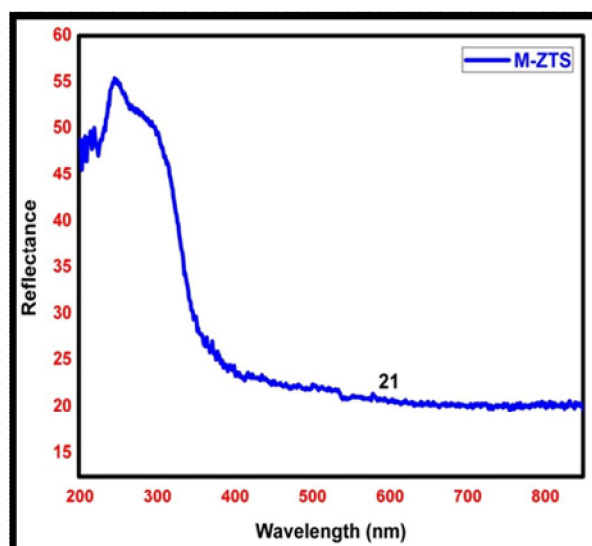
Fig-6: Reflectance of Metheonine doped ZTS crystal

The transmittance data was used to determine the linear optical constants. The variation of refractive index, extinction coefficient, and reflectance is shown in **Fig.4, Fig.5, Fig.6** respectively. The obtained optical constants viz. lower reflectance, lower extinction coefficient and refractive index near 1.5 of M-ZTS crystal in entire visible region favors suitability for antireflection coating applications. The optical fabrication field demands low refractive index materials for calibration **[30-34].**

4. CONCLUSION

Methenonine doped ZTS crystals have been grown by slow solution evaporation technique at 37˚C. The optical studies revealed 88 % higher and wider transmission, lower cut-off (303 nm), widened band gap (3.43eV) and improved lower values of extinction coefficient, reflectance, and refractive index of M-ZTS favoring its suitability for solar thermal device fabrication, nonlinear optical and laser applications.

REFERENCES

1. R.Uthrakumar,C.Vesta,C.Justin Raj,S.Krishnan,S.Jerome Das (2010) "Bulk crystal growth and characterization of non-linear optical bisthiourea zinc chloride single crystal by unidirectional growth method", Curr. Appl. Phys. 10**,**548-552.

2. N. N. Shejwal, Mohd Anis, S. S. Hussaini, M. D. Shirsat(2014),"Optical, thermal and electrical properties of pure and doped bis-thiourea cadmium formate (BTCF) crystal", Phys. Scr. 89, 125804-125810.

3. Mohd Anis, S. S. Hussaini, M.D. Shirsat (2016), "A systematic study on electrical and physical properties of calcium bis-thiourea chloride crystal",OPTIK,127, 9734-9737.

4. Rupali B. Kulkarni, Mohd Anis, S.S. Hussaini, M.D. Shirsat (2018) ,"Transfiguring structural, optical and dielectric properties of cadmium thiourea acetate crystal by the addition of L-threonine for laser assisted device applications"**,**Materials Research Express ,5,036204 .DOI: 10.1088/2053-1591/aab2f8

5. Kanganapathy, G.Gowri (2016), Indian J. of pure and applied physics, 54, 193-198.

6. Sweta Moitra, Tanusree Kar (2007) "Growth and characterization of nonlinear optical crystal zinc tris (thiourea) sulphate in presence of L-arginine", Optical Materials,30,508–512.

7. S. Moitra , S. Bhattacharya , T. Kar, A. Ghosh (2008) "Dielectric properties and phase transition of zinc tris(thiourea) sulfate single crystal", Physica B, 403,3244–3247.

8. T. C. Sabari Girisun,and S. Dhanuskodi (2009) " Linear and nonlinear optical properties of tris thiourea zinc sulphate single crystals", Cryst. Res. Technol., 441297-1302.

9. J. Felicita Vimala , J. Thomas Joseph Prakash (2013) " Growth and Characterization of Pure and Potassium Sulfate - Doped Zinc (tris) Thiourea Sulfate (ZTS) Single Crystals" Elixir Crystal Growth, 56,13350-13354.

10. Kiran T. Rathod, I.B. Patel, C.F. Desai, Y.H. Gandhi, (2015)," Growth and Investigation of LCysteine Doped Zinc (Tris) Thiourea Sulphate Single Crystals" Inter. J. of Luminescence and Applications, 5 , 86-88.

11. S. K. Kushwaha, K. K. Maurya, D. Haranath and G. Bhagavannarayana (2011), " The effect of Cr 3+ doping on the crystalline perfection and optical properties of zinc tris(thiourea)sulfate, a nonlinear optical material The effect of Cr 3+ doping on the crystalline perfection and optical properties of zinc tris(thiourea)sulfate, a nonlinear optical material" , J. Appl. Cryst., 44 ,1054–1061.

12. C. Krishnan and P. Selvarajan (2010) " Growth and Characterization of Zinc–Magnesium Tris(Thiourea) Sulphate (ZMTS) Single Crystals ", Journal of Experimental Sciences, 123-26.

13. Sonia Bhandari , Nidhi Sinha , Geeta Ray , Binay Kumar (2014) " Enhanced optical, dielectric and piezoelectric behavior in dye doped zinc tris-thiourea sulphate (ZTS) single crystals", Chemical Physics Letters, 591, 10–15.

14. V.N. Praveena, N.Vijayan, C.K.Mahadevan (2012) " Dielectric measurements on urea added ZTS single crystals", OPTIK, 123,1617.

15. Sunil Verma, M.K.Singh,V.K.Wadhawan,C.H.Suresh,Pramana (2000) " Growth morphology of zinc tris(thiourea) sulphate crystals", Indian Academy of Sciences, 54, 879–888.

16. N.R.Dhumane,S.S.Hussaini,V.G.Dongre,MahendraD.Shirsat (2008), "Influence of ... of zinc (tris) thiourea sulfate (ZTS) single crystal ",Optical Materials, 31, 328-332.

17. M.Lawrence, J.FelicitaVimala, Inter. J. of Engineering Science and Innovative Tech. 4(2015) " M. Lawrence , J. Felicita Vimala.,(2015)" Growth and characterization of pure and L-Alanine doped Zinc Tris-thiourea Sulphate (ZTS) single crystals", International Journal of Engineering Science and Innovative Technology IJESIT,4,208-214.

18. N. Balasundari , P.Selvarajan (2017) " Studies on Nucleation, Growth and Characterization of L-Leucine Doped ZTS Crystals", IOSR Journal of Applied Physics ,39-45.

19. J. Thomas J.Felicita, M. Lawrence(2010)," Growth and Characterization of Pure and L-lysine Doped Zinc (TRIS) Thiourea Sulphate Crystals, Inter. J. Computer Applications, 8.

20. K.Senthil Kannan , S.Gunasekaran1 Seethalakshmi. KA, Inter. J. of Scientific & Engineering Research 4(2013)." NLO, fluorescence, xrd & morphological studies of a new semi organic single crystal:lithium para nitrophenolate tri hydrate" , ISSN 2229-5518.

21. K.Kanagasabapathy,R.Rajasekaran (2012) " Growth, structural, optical and thermal studies of L-Threonine added Zinc(Tris) Thiourea Sulphate single crystals" , optoelec. and advanced materials – rapid comm., 6,218-224.

22. N.N. Shejwal, Mohd Anis, S.S. Hussaini, M.D. Shirsat (2016) " Monocrystal growth, X-ray diffraction, photoluminescence, thermal and dielectric studies of cadmium thiourea acetate complex doped with L-cystine" , OPTIK 127,6525-6531.

23. N.N. Shejwal, Mohd Anis, S. S. Hussaini, M. D. Shirsat (2016) " Investigation on structural, UV-visible, SHG efficiency, dielectric, mechanical and thermal behavior of LL-cystine doped zinc thiourea sulphate crystal for NLO device applications", Inter. J. of Modern Physics B, 30, 1650159.

24. F. Helena, G.Kanchana (2014) " Investigation on the properties of L- serine doped Zinc tris thiourea sulphate crystaol for NLO applications",Indian Journal of pure and applied physics,52,821-828.

25. D. Jaikumar, S. Kalainathan (2008) " Optical and mechanical properties of a new second order nonlinear optical crystal urea l□threonine", Cryst. Res. Technol.,43,565-571.

26. Mohd. Shakir, V. Ganesh, B. Riscob, K.K. Maurya, K. Kishan Rao, M.A. Wahab, G. Bhagavannarayana (2011) " Effect of L-Threonine Doping on Structural, Optical, Mechanical, Surface and Dielectric Properties of KDP Single Crystal", Int. J. Pure Appl. Phys. ,7, 13-24.

27. Mohd. Shkir, V. Ganesh, S. AlFaify, H. Algarni, G. Bhagavannarayana, K.K. Maurya, M.M. Abutalib, I.S. Yahia (2017) " Bulk growth, structural, vibrational, crystalline perfection, optical and dielectric properties of L-threonine doped KDP single crystals grown by Sankaranarayanan-Ramasamy (SR) method" , Mater. Res. Innov. ,21,106-114.

28. M.S. Pandian, P. Ramasamy (2010) " Conventional slow evaporation and Sankaranarayanan–Ramasamy (SR) method grown diglycine zinc chloride (DGZC) single crystal and its comparative study", J. Cryst. Growth, 312,413-419.

29. G. Ramesh Kumar,S. Gokul Raj,R. Mohan, R. Jayavel (2006) " Influence of Isoelectric pH on the Growth Linear and Nonlinear Optical and Dielectric Properties of l-Threonine Single Crystals", Crystal Growth and Design, 6,1308-1310.

30. M.S. Pandian, P. Ramasamy (2010) " Conventional slow evaporation and Sankaranarayanan–Ramasamy (SR) method grown diglycine zinc chloride (DGZC) single crystal and its comparative study" , , J. Cryst. Growth ,312,413-419.

31. G. Ramesh Kumar,S. Gokul Raj,R. Mohan, R. Jayavel (2006) " Influence of Isoelectric pH on the Growth Linear and Nonlinear Optical and Dielectric Properties of l-Threonine Single Crystals", Crystal Growth and Design ,6,1308-1310.

32. Mohd Shkir, Shabbir Muhammad, S. AlFaify,(2015) " Experimental and density functional theory (DFT): A dual approach to study the various important properties of monohydrated L-proline cadmium chloride for nonlinear optical applications",Spectrochem. Acta A, 143 ,128-135.

33. Rupali B. Kulkarni, Mohd Anis, S. S. Hussaini and Mahendra D. Shirsat(2018) "Tuning optical properties of cadmium thiourea acetate nonlinear optical crystal exploiting organic ligand of L-proline" ,Modern Physics Letters B, 32,1850424. DOI: 10.1142/S0217984918504249

34. R.B. Kulkarni, M.Anis, S. S. Hussaini, and M. D. Shirsat,(2019) "Illustrious influence of amino acid L-threonine(LT) on structural and optical insights of Zinc Thiourea Sulphate (ZTS) crystal", Inter. J. of Modern Physics B,33,1950010. DOI: 10.1142/S0217979219500103

OPTICAL AND STRUCTURAL PROPERTIES OF Dy^2O^3 DOPED ALUMINIUM ZINC BORATE GLASSES

S. R. Dagdale[1], M. N, Rode[1], Anil B. Naik[2], Anil B. Gambhire[3], G. G. Muley[4]

[1]Department of Physics, Vaidyanath College, Parli-Vaijnath, Dist. Beed
[2]Department of Chemical Technology, Sant Gadge Baba Amravati University, Amravati
[3]Department of Chemistry, Shri Anand College, Pathardi, Ahemadnagar
[4]Department of Physics, Sant Gadge Baba Amravati University, Amravati

ABSTRACT

The pure and doped aluminium zinc borate glass of system (x) Dy_2O_3-(1-x) Al_2O_3-ZnO-B_2O_3 with x = 0 (AZB), 0.03 (Dy:AZB) have been prepared by melt quench technique. The amorphous nature of the glass sample has been confirmed using powder X-ray diffraction study. Optical properties of Dy:AZB glass has been studied by recording emission and excitation spectra. The photoluminescence study of Dy:AZB reveals the two emission bands in the visible range present at 482 and 575 nm corresponding to transitions $^4F_{9/2} \rightarrow ^6H_{15/2}$ and $^4F_{9/2} \rightarrow ^6H_{13}$. Excitation spectrum presents absorption at 325, 350, 365, 387 and 426 nm corresponding to transitions $^6H_{15/2} \rightarrow ^4D_{7/2}$, $^6H_{15/2} \rightarrow ^6P_{7/2}$, $^6H_{15/2} \rightarrow ^4P_{3/2}$, $^6H_{15/2} \rightarrow ^4I_{7/2}$, and $^6H_{15/2} \rightarrow ^4G_{11/2}$.

Keywords: AZB, Dy:AZB glasses, powder X-ray diffraction, photoluminescence Properties

1. INTRODUCTION

In past few years, scientific investigation reveals that rare earth doped materials is important due to their potential applications in fields of laser technology, fiber optic amplifiers, optoelectronic devices, infrared to phosphors and visible up-converters [1-4]. The glasses which are formed by doping with rare earth ions are found to be luminescent materials as they have high emission efficiencies. In recent years, glasses doped with rare earth ions have drawn a lot interest due to their potential applications in solid state lasers, three-dimensional displays and optical amplifiers [5-8]. The various glassy materials such as fluoride, phosphate, fluorophosphates, borate, flouroborate and tellurite have been widely investigated with the purpose to know their utility for luminescence applications [9, 10]. There are many papers available in literature about the glasses having good optical studies [11]. The compounds containing aluminium elements are of particular importance as they can be partially replaced by the dysprosium ion in its trivalent state (Dy^{3+}) which is an efficient emitter in the visible region. It is the only ion that emits two intense colors which on mixing in suitable proportions yields white light [12-14]. Recently, few researchers were investigating the Dy^{3+} doped borate glasses study optical and luminescent properties of rare-earth ions. The Dy^{3+} doped such as lithium sodium bismuth borate glasses [15] zinc bismuth borate glasses [16] heavy-metal oxide and oxyhalide borate glasses [17] sodium aluminium phosphate glasses [18] lithium borate glasses [19].

The present work reports the investigations on luminescent properties of pure and Dy^{3+} doped aluminum zinc borate glasses prepared by melt-quench technique. The phase purity and photoluminescence study of pure and Dy^{3+} ion doped glasses has been reported in this report.

2. EXPERIMENT METHOD

Analytical reagent grade materials- aluminium oxide (Al_2O_3, Central Drug House (CDH), India), zinc oxide (ZnO, Fisher Scientific), dysprosium oxide (Dy_2O_3, LOBA Chemie, India) and boric acid (B_2O_3, sd Fine Chemicals, India) were used as a starting elements to prepare desire glasses.

An alkali borate glasses of system (x) Dy_2O_3-(1-x)Al_2O_3-ZnO-B_2O_3 with x = 0 (AZB), 0.03 (Dy:AZB) were prepared by the melt-quenching method. Appropriate amount of the chemicals Al_2O_3, ZnO, Dy_2O_3 and H_3BO_3 of 99.99% purity were taken together, mixed and crushed in a mortar with the help of pestle to make the homogeneous mixture. The mixtures were calcined at 550 ^oC for 5 h to remove moisture. The materials were removing from the crucible and once again crushed and heated at 950 ^oC for 900 minutes. This process was repeated two times to get polycrystalline powders of AZB and Dy:AZB compounds. Then powder samples were melted in a platinum crucible in an electric furnace for 120 minutes at 1000 ^oC. The obtained melt was poured on a stainless steel plate and immediately pressed with second one for immediate quenching to form amorphous phased solid. The formed glass sample was allowed to cool gradually to room temperature. The obtained glass was cut into rectangular slabs of dimensions 4x2x1 mm^3 and polished to use for further characterization.

Powder XRD patterns of powder glass sample was recorded on a X-ray diffractometer (Rigaku, Miniflex-600, Japan) using Cu-Kα (λ=1.504 Å) radiation to check the amorphous state of the prepared glass sample at the

scanning rate of 8 deg/min and 2θ varied from 10–90°. And photoluminescence study has been done using fluorescence spectrophotometer FL-7000 Hitachi, Japan.

3. RESULT AND DISCUSSION

3.1. X-ray diffraction study

X-ray diffraction patterns were recorded to confirm amorphous nature for all the glass samples. The typical XRD profile of the AZB and Dy:AZB glasses are shown in Fig. 1. The patterns exhibit a few broad peaks rather than sharp peaks that reflect amorphous nature of the material.
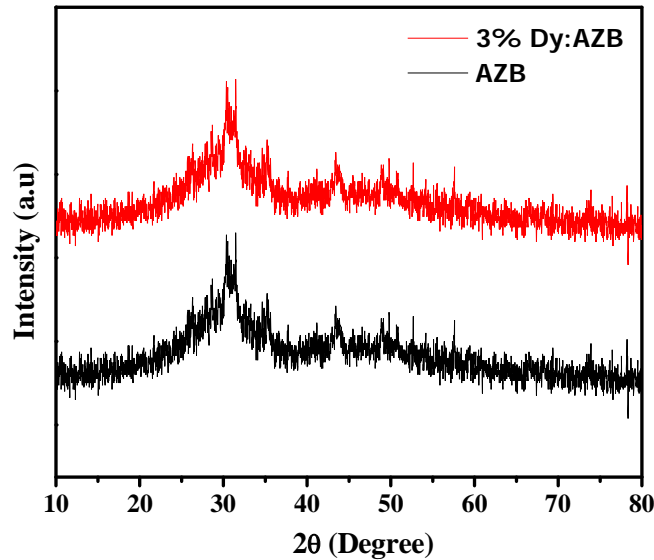
Fig-1: XRD pattern of pure and 3% Dy doped AZB

3.2. Photoluminescence Study

Photoluminescence is light emission from any form of matter after the absorption of photons. Dy:AZB glass was subjected to the photoluminescence study by recording emission spectrum by excitation with 388 nm, which gives two emissions at 482 nm and 575 nm. The blue emission band (at 470 nm) is a typical emission of Dy^{3+} ions corresponding to transition from $^4F_{9/2}$ to $^6H_{15/2}$ ground state, while the yellow emission (at 575 nm) corresponds to the $^4F_{9/2} \rightarrow ^6H_{13/2}$ optical transition of Dy^{3+} as shown in Fig. 2 [17, 20]. The transition from $^4F_{9/2} \rightarrow ^6H_{15/2}$ is a magnetic dipole transition which possess most intense blue emission band at wavelength 470 nm. The transition from $^4F_{9/2} \rightarrow ^6H_{13/2}$ is electric dipole transition which possess moderate intense yellow emission band at 575 nm [18]
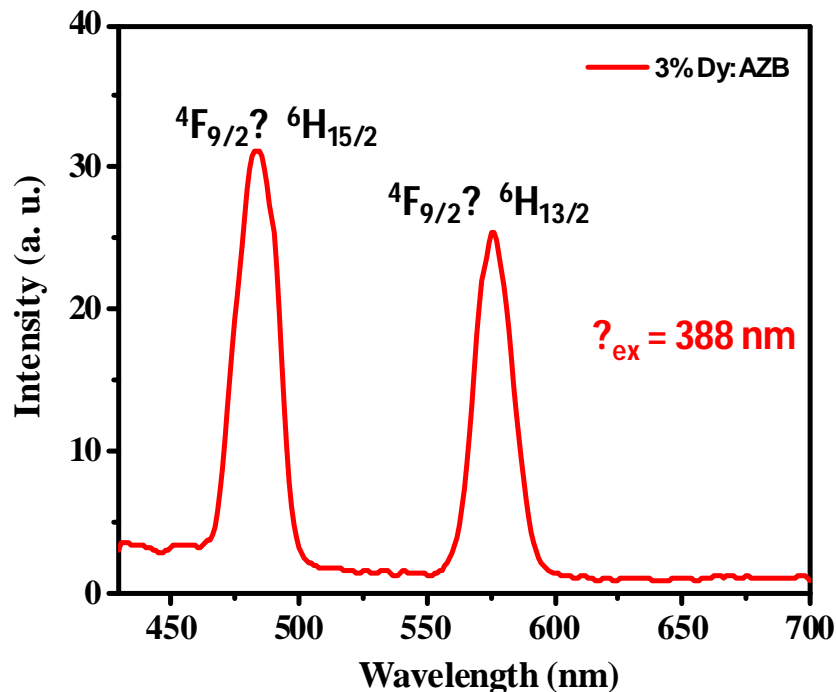
Fig-2: Emission spectra of Dy: AZB glass.

The excitation spectrum of Dy:AZB glass recorded by monitoring emission at 482 nm shows five absorption peaks at 325, 350, 365, 387 and 426 nm [5, 20]. The corresponding transitions $^6H_{15/2} \rightarrow ^4D_{7/2}$, $^6H_{15/2} \rightarrow ^6P_{7/2}$, $^6H_{15/2} \rightarrow ^4P_{3/2}$, $^6H_{15/2} \rightarrow ^4I_{7/2}$, and $^6H_{15/2} \rightarrow ^4G_{11/2}$ are as shown in the Fig. 3. The energy level diagram of Dy:AZB glass is shown in the Fig. 4. When the Dy^{3+} ions are excited to any level above $^4F_{9/2}$ level, there is a fast non-radiative decay to $^4F_{9/2}$ level and the emission takes place from $^4F_{9/2}$ level to lower levels $^6H_{13/2}$ (at 575 nm) and $^6H_{15/2}$ (at 470 nm) [21].
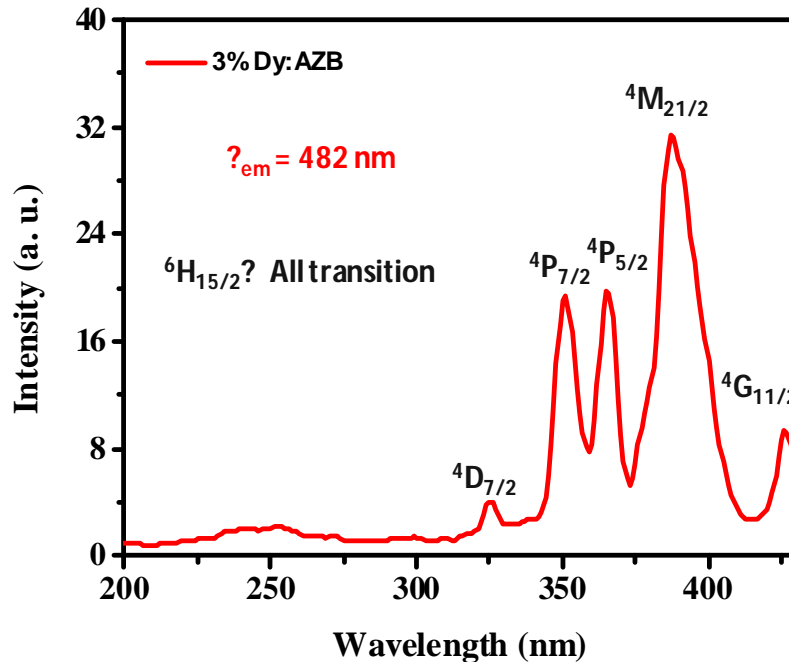
Fig-3: Excitation spectrum of Dy:AZB glass.
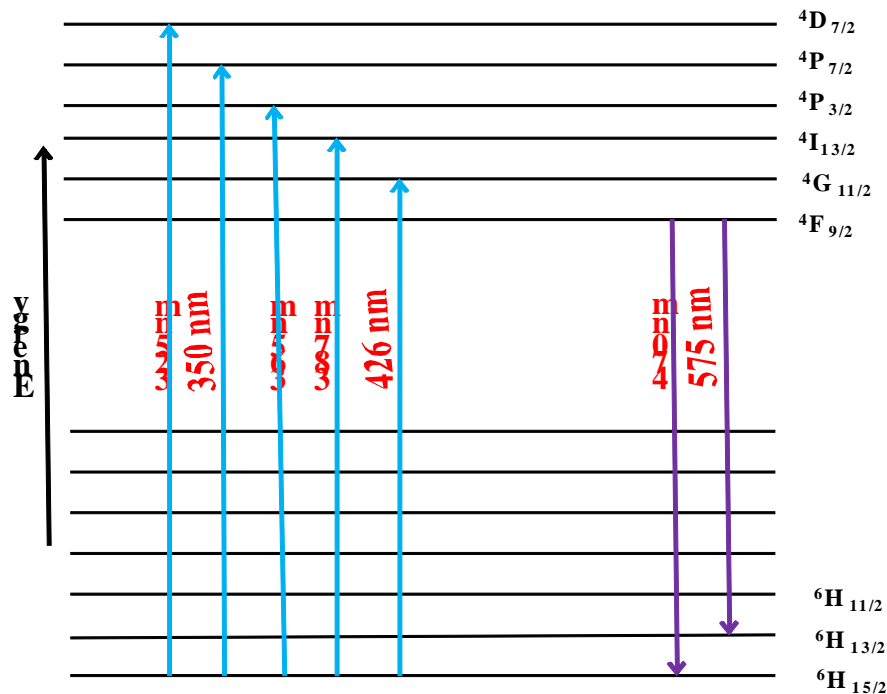
Fig-4: The energy levels diagram of Dy:AZB glass

4. CONCLUSIONS
The AZB and Dy:AZB glasses are successfully prepared by melt quenching method. The amorphous nature of the glasses was confirmed by XRD technique. Prepared borate glass, Dy:AZB, has been subjected to the photoluminescence study to know optical properties. It is clear that there are two emission bands $^4F_{9/2} \rightarrow ^6H_{15/2}$ and $^4F_{9/2} \rightarrow ^6H_{13/2}$ when excitation used at wavelength of 388 nm. These bands correspond to the electron transitions from the discrete levels $^4F_{9/2} \rightarrow ^6H_{15/2}$ and $^4F_{9/2} \rightarrow ^6H_{13/2}$ transitions for Dy^{3+} that confirm the presence of trivalent rare-earth ions in the glass matrix.

REFERENCE

1. Malchukova E., Boizot B., Ghaleb D., Petite G. (2005). Optical properties of pristine and γ-irradiated Sm doped borosilicate glasses. *Nuclear Instruments, Meth Phys Res*, **537**, 411–414.

2. Vetrone F., Boyer J. C., Capobianco J. A., Sepghini A., Bettinelli M. (2002). 980 nm excited upconversion in an Er-doped ZnO–TeO$_2$ glass. *Appl Phys Lett*, **80,** 1752–1754.

3. G. Lakshminarayana, R.Y. Mengfei and J. Qiu. (2009). Spectral analysis of RE^{3+} (RE = Sm, Dy, and Tm): P$_2$O$_5$-Al$_2$O$_3$-Na$_2$O glasses", *Optical Materials*, Vol. 31, 1506-1512.

4. Rajesh D., Ratnakaram Y. C., Seshadri M., Balakrishna A. and Krishna T.S. (2012). Structural and luminescence properties of Dy^{3+} ion in strontium lithium bismuth borate glasses. *Journal of* Luminescence, 132, 841-849.

5. Babu S., Reddy Prasad V., Rajesh D., and Ratnakaram Y. C. (2015). Luminescence properties of Dy^{3+} doped different fluoro-phosphate glasses for solid state lighting applications. *J. Mol. Struct.*, Vol.1080, 153-161.

6. Vijaya N., Upendra Kumar K. and Jayasankar C. K. (2013). Dy^{3+}-doped zinc fluorophosphates glasses for white luminescence applications. *Spectrochimica Acta Part A: Molecular and Biomolecular Spectroscopy*, 113, 145–153.

7. Vijayakumar R., Venkataiah G., Marimuthu K. (2015). Structural and luminescence studies on Dy^{3+} doped boro-phosphate glasses for white LED's and laser applications. *J. Alloys Compd.*, Vol. 652, 234-243.

8. Dagdale S. R., Harde G. B., Pahurkar V. G. and Muley G. G. (2017). Synthesis and optical properties of borate glass of system 3Li$_2$O-2K$_2$O-5B$_2$O$_3$, *ISCA-Research Journal of Chemical Sciences,* Vol. 7(3), 1-3.

9. Xie W., Wang Y. H., Hu Y. H., Luo L., Wu H.Y., Deng L.Y. (2010). Preparation and Red Long-Afterglow Luminescence of Y$_2$O$_3$: Eu, Dy. *Acta Phys. Sin.*, 59, 3344–3349.

10. Kirdsiri K., Kaewkhao J., Kim H. J. (2016). Luminescence Properties of Dy^{3+} doped Lutetium-Calcium-Silico-Borate Glasses for White Light Emitting Applications. *International Conference on Industrial Application Engineering*, 550-555.

11. Dagdale S. R., Muley G. G. (2015). Optical study of neodymium doped lanthanum calcium borate glasses of La$_2$O$_3$-8CaO-3B$_2$O$_3$ system. *Bionano frontier*, Vol. 8(3), 265-268.

12. Shanmugavelu B. and Ravi Kanth Kumar V. V. (2014). Luminescence studies of Dy^{3+} doped bismuth zinc borate glasses. *Journal of Luminescence*, 146, 358-363.

13. Liu H., Yu L., Li F. (2013). Photoluminescent properties of Eu^{3+} and Dy^{3+} ions doped MgGa$_2$O$_4$ phosphors. *Journal of Physics and Chemistry of Solids*, 74: 196.

14. Sun X. Y., Wu S., Liu X., Gao P., Huang S. M. (2013). Intensive white light emission from Dy^{3+}-doped Li$_2$B$_4$O$_7$ glasses. *Journal of Non-Crystalline Solids*, 368 51–54.

15. Parandamaiah M., Naveen Kumar K., Babu S., Venkatramana Reddy S. Ratnakaram Y.C. (2015). Dy^{3+} doped Lithium Sodium Bismuth Borate Glasses for Yellow Luminescent Photonic Applications. *Int. Journal of Engineering Research and Applications*, 5(8), 126-131.

16. Yasaka P., Boonin K. and Kaewkhao J. (2015). Structural and photoluminescence properties of dy^{3+} ion in zinc bismuth borate glasses. *Suranaree J. Sci. Technol.* 23(1), 69-75.

17. Pisarska J., Zur L., and Pisarski W. A. (2012). Structural and optical characterization of Dy-doped heavy-metal oxide and oxyhalide borate glasses. *Phys. Status Solidi A*, 1–7.

18. Amarnath Reddy A., Chandra Sekhar M., Pradeesh K., Surendra Babu S., Vijaya Prakash G.. (2011). Optical properties of Dy^{3+}-doped sodium aluminum phosphate glasses. *J Mater Sci*, 46, 2018-2023.

19. Ramteke D. D. & Gedam R. S. (2015). Spectroscopic properties of dysprosium oxide containing lithium borate glasses. *Spectroscopy Letters*, 48: 417–421.

20. Marzouk M. A., Ouis M. A., Hamdy Y. M. (2012). Spectroscopic studies and luminescence spectra of Dy$_2$O$_3$ doped lead phosphate glasses, *Silicon*, 4, 221–227.

21. Suthanthirakumar P., Marimuthu K. (2016). Investigations on spectroscopic properties of Dy^{3+} doped zinc tellurofluoroborate glasses for laser and white LED applications. *Journal of Molecular Structure*, 1125, 443-452.

DIELECTRIC STUDY OF CESIUM CHLORIDE DOPED L-THREONINE SINGLE CRYSTAL

Pratik M. Wankhade[1], Vikas Pahurkar[2], Anil G. Gacche[3], Prakash S. Ambhore[4] and Gajanan G. Muley[5]

[1]Department of Physics, Late Rajkamalji Bharti Arts, Commerce and Smt. Sushilabai R.Bharti Science College, Arni

[2]Department of Enginnering Physics, Prof. Ram Meghe Institute of Technology and Research, Badnera

[3]Department of Physics, Vasantrao Naik College, Vasarni, Nanded

[4]SMD High school, Hingoli

[5]Department of Physics, Sant Gadge Baba Amravati University, Amravati

ABSTRACT

Crystal of an amino acid L-threonine doped with cesium chloride (LTCC) was grown by low temperature slow solvent evaporation solution growth method. In the present communication, the grown nonlinear optical (NLO) single crystal LTCC has been subjected to the dielectric and ac conductivity studies. The variation of dielectric constant and dielectric loss with frequency at a constant temperature has been presented. Dielectric constant and loss of LTCC is decreases with increase in frequency of an applied electric field at constant temperature. The dielectric constant of LTCC is slightly more than pure L-threonine at low frequency region. The dielectric constant of LTCC was found to be 53 for 1MHz at 50°C. The major difference in dielectric constant of LTCC at different constant temperature is observed in low frequency region only. In low frequency region, dielectric constant and dielectric loss of LTCC increase with increase in temperature. Small variation of ac conductivity with temperature is observed in LTCC crystals. The activation energies of LTCC have been found to be 0.0658 and 0.0155 eV at 100 kHz and 1 MHz respectively.

Keywords: ac conductivity, activation energy, dielectric constant, dielectric loss.

1. INTRODUCTION

Second order nonlinear optical (NLO) material gains much importance because of their wide range of applications in the field of optoelectronics. These applications have in optical elements such as optical switching, optical data storage, optical communication, harmonic generator, etc. To realize these applications, information of materials properties such as optical transparency, band gap, second harmonic generation efficiency, dielectric constant, dielectric loss, and ac conductivity etc. has require[1-3]. The dielectric study gives the useful information about the possible distribution of electric field with mechanism of polarization within the solid. The quality of the grown crystal can be judge from the dielectric loss study. Electrical ac conductivity of crystals especially ionic crystals yields important information about mobility of charge and production of defects in the crystal.

L-threonine is family member of amino acid. It crystallizes in orthorhombic crystal system with non-centrosymmetric $P2_12_12_1$ space group having lattice parameter a=13.6111 Å, b=7.738 Å, and c=5.144 Å [2]. Kumar et al. have studied crystallization kinetics, growth parameters and, effect of pH, deuteration on different properties of L-threonine crystal in detail [3-4]. L-threonine can form variety of complexes enhancing nonlinear optical properties [5-6]. We had done optical and thermal study of LTCC single crystal [7]. An exciting thermal and optical property of grown crystal urges us to study electrical properties of grown crystal for application point of view. In the present communication, we study electrical properties such as dielectric constant, dielectric loss, ac conductivity and activation energy of LTCC single crystal.

2. EXPERIMENTAL

2.1 Material synthesis and crystal growth

L-threonine (S D Fine-Chem Ltd. India) and cesium chloride (Loba Chem Ltd. India) of analytical grade were procured and used as it is without any purification. They were dissolved in equimolar ratio in double distilled water. The solution was kept at a constant temperature 40°C and stirred continuously using magnetic stirrer for four hours to form homogeneous solution. The homogeneous solution was filtered using membrane filter and kept for spontaneous crystallization in the constant temperature water bath maintained at a constant temperature 35°C. The seed crystals were obtained after a period of three days by slow solvent evaporation method. The material was purified by re-crystallization and used for growth of single crystal. Good quality single crystal was grown within 12-15 days.

2.2 Characterization

The grown single crystal of LTCC was first cleaned and then lapped. The grown crystal was subjected to the electrical studies. Capacitance was measured using an impedance analyzer (Agilent, 4284A) equipped with programmable heating furnace.

3. RESULTS AND DISCUSSION
3.1 Dielectric study
The crystal was cut in the form of rectangular slab of thickness 1.5 mm. The two opposite faces of the crystal was silver pasted to have good electrical contact. They can act as parallel plates of capacitor. The capacitance and dissipation factor (D) of thus formed capacitor was measured as a function of frequencies and temperatures. The dielectric constant of the grown crystal material (ε_r) was calculated using the formula [8].;

$$\varepsilon_r = \frac{Ct}{\varepsilon_0 A} \tag{1}$$

Where 't' is the thickness of the crystal, 'A' is the surface area, and 'ε_o' is the permittivity of free space and 'C' be the capacitance at various frequency keeping temperature constant.
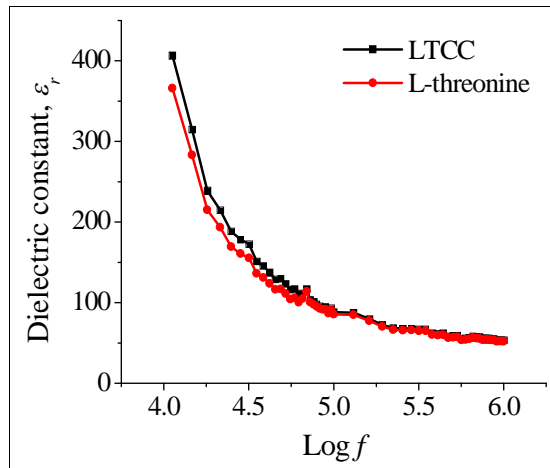
Fig-1: Dielectric constants (ε_r) of L-threonine and LTCC measured at 35°C.
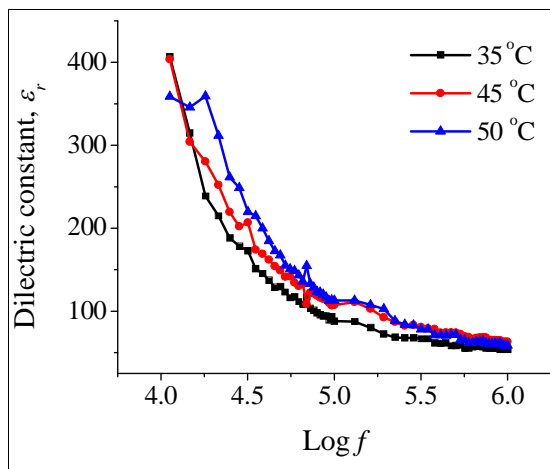
Fig-2: Dielectric constants (ε_r) of LTCC measured at 35, 45 and 50 ^{o}C.
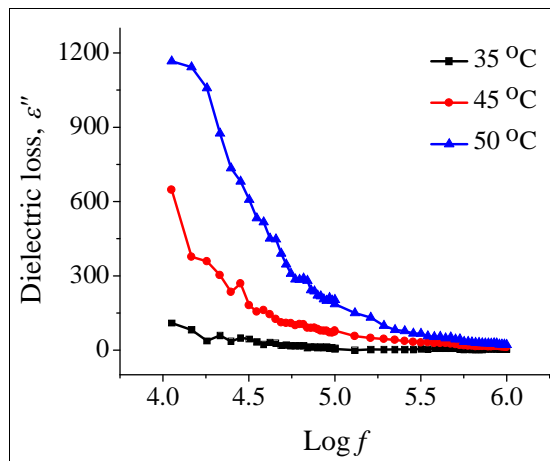
Fig-3: Dielectric loss ($\varepsilon_{''}$) of LTCC measured at 35, 45 and 50 ^{o}C.
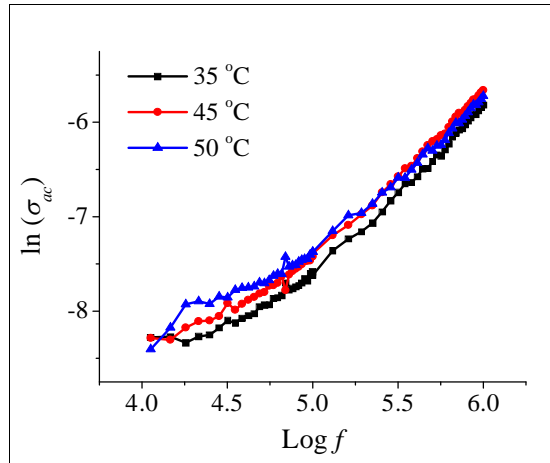
Fig-4: Variation of ac conductivity of LTCC with temperature measured at different frequencies.
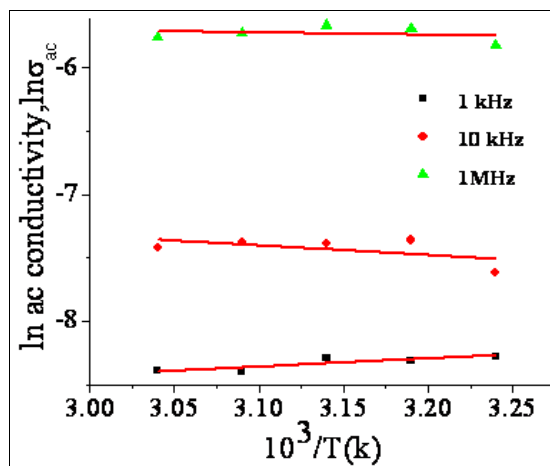
Fig-5: 1000/T(k) vs lnσ_ac for LTCC single crystal

Fig. 1 shows a variation of dielectric constant with frequencies for L-threonine and LTCC crystal. It is clearly evident that the dielectric constant of LTCC crystal at a lower frequency is slightly higher than that for L-threonine crystal and at higher frequencies the difference is no considerable. The increase in the dielectric constant of LTCC is may be due to increase in polarization in the presence of Cs^+ and Cl^- ions. The variation of dielectric constant with frequency at different constant temperature for LTCC crystal is depicted in the Fig. 2. The dielectric constant of the crystal decreases with increase in frequency. The high value of dielectric constant at low frequencies may be due to the contribution of all the polarizations namely; space charge, orientation, ionic and electronic significantly. As the frequency increases contribution of the above polarization decreases gradually. It attributes to dipole does not follow the alternating field beyond a certain frequency of the electric field confirm from the shape of the curve of graph. The dielectric constant of LTCC was found to be 53 for 1MHz at 50^oC and that of pure 175 for 1MHz at 100^oC respectively [3]. It is important to note that, LTCC show low dielectric constant at high frequency region independent of temperature. Thus, the LTCC crystal may be used in low frequency region for charge storage and in high frequency region for electro-optic applications. According to Miller rule, the low value of dielectric constant at high frequency is a suitable parameter for the enhancement of second harmonic generation coefficient (SHG) [8].

The dielectric loss (ε'') was calculated from the dissipation factor by using equation;

$$\varepsilon'' = \varepsilon_r D \tag{2}$$

The variation of dielectric loss with frequency at different temperature is shown in Fig. 3. The graph indicates, decrease in dielectric loss with increasing frequency at constant temperature. In low frequency region, dielectric loss is high at high temperature. The large value of dielectric loss in low frequency region at all temperature is observed. This behavior may be due to the resonance occurring between the applied ac field and natural frequency of the molecules result into large dissipation of energy in the form of heat. It is to be noted that, there is large effect of temperature on the dielectric loss in low frequency region. In high frequency region the dielectric loss is almost independent of temperature. The low value of dielectric loss suggests good optical quality crystal with lesser defects, which is the desirable property for NLO applications [8].

3.2 ac conductivity study

ac Conductivity (σ_{ac}) of the crystal as a function of frequency (f) of the applied field was calculated using a relation [8];

$$\sigma_{ac} = \frac{2\pi fCt}{A} \qquad (3)$$

The variation in ac conductivity with the applied frequency and temperature for the LTCC crystals is shown in Fig. 4. As shown in Fig. 4, ac conductivity increases with increase in the frequency of applied field across the grown crystal and also with temperature. There was no major observe change in the ac conductivity with temperature with high frequency. ac conductivity in low temperature region is known as extrinsic region. It is defect sensitive region. Mostly, in extrinsic region conductivity takes place due to presence of defect or by addition of impurity creates defects [9]. Larger value of ac conductivity in crystal at high frequency may be due to polaron hopping process present along with other defect process [10]. Small variation of ac conductivity with temperature in low frequency region is observed in LTCC crystals. Thus, thermally created vacancy defect may play an important role in LTCC crystal.

3.3 Activation energy

Arrhenius relationship using ac conductivity is given by $\sigma_{ac} = \sigma_0 \ exp \ (-E_{ac}/kT)$ [10]. Here, E_{ac} is the activation energy of conduction at temperature T and k is Boltzmann constant. Fig. 5 is a plot of ln σ_{ac} versus $1/T$ is straight line with slope equal to $-E_{ac}/k$. Therefore, the sample exhibits Arrhenius type conductivity behavior in the temperature range of investigation. Activation energies are estimated using the slopes of the lines ($E_{ac} = -(slope)k \times 1000$). The activation energies of LTCC for the conduction process, calculated from the plot, are found to be 0.0658 and 0.0155 eV at 100 kHz and 1 MHz respectively. The low activation energies confirm that the trapping levels originating probably from the defect states that are responsible for conduction in the region [9-10].

4. CONCLUSIONS

Dielectric constant and dielectric loss of LTCC decreases with frequency of an applied electric field. LTCC show low value of dielectric constant at high frequency region. The dielectric constant of LTCC was found to be 53 for 1MHz at 50°C. There is no influence of temperature on dielectric constant value in high frequency region. The dielectric loss values were also found to be negligible at higher frequency. Small variation of ac conductivity with temperature is observed in LTCC crystals in low frequency region. The activation energies of LTCC have been found to be 0.0658 and 0.0155 eV for 100 kHz and 1 MHz respectively. Owing to above electrical properties LTCC crystal may be used in NLO applications in high frequency region.

5. REFERENCES

1. Kumar G. R., Raj S. G., Saxena A., Karnal A. K., Raghavalu T., Mohan R., (2005), "Growth, structural and spectral analyses of nonlinear optical l-threonine single crystals", Journal of crystal growth, 275 (1-2), e1947-1951.

2. Shoemaker D. P., Donohue J., Schomaker V., Corey R. B., (1950) "The Crystal Structure of L-Threonine", Journal of American Chemical Society, **72(6),** 2328-2349.

3. Kumar G.R., Raj S.G., Raghavalua T., Mathivanan V., Kovendhan M., Mohan R., Jayavel R., (2007), "Effect of pH, thermal, electrical and thermomechanical properties of nonlinear optical L-threonine single crystals", Spectrochimica Acta Part A: Molecular and Biomolecular Spectroscopy, **68,** 300-304.

4. Kumar G.R., Raj S.G., (2009), "Growth and PhysioChemical Properties of Second-Order Nonlinear Optical L-Threonine Single Crystals", Advances in Materials Science and Engineering, 2009, Article ID 704294.

5. Ramesh K., Gokul S., Mohan R., Jayavel R., (2005), "Growth and characterization of new nonlinear optical l-threonium acetate single crystals", Journal of crystal growth, 283(1-2),193-197.

6. Natarajan S., Umamaheswaran M., Kalyana S. J., Suresh J., Martin Britto Dhas S.A., (2010), "Structural, spectroscopic and nonlinear optical studies on a new efficient organic donor–acceptor crystal for second harmonic generation: l-Threoninium picrate", Spectrochimica Acta Part A: Molecular and Biomolecular Spectroscopy ,77(1), 160–163.

7. Wankhade P.M., Muley G.G., (2016)," Optical and thermal study of cesium chloride doped L-threonine single crystal for nonlinear optical applications" , Material Research Innovations, 20(2), 128-132.

8. Wankhade P.M., Gambhire A.B., Muley G.G., (2016) "Influence of urea doping on optical, thermal and dielectric properties of L-arginine phosphate monohydrate single crystal", optik, 3322-3328.

9. Akhtar F., Podder J., (2011) "A Study on Structural, Optical, Electrical and Etching Characteristics of Pure and L-Alanine Doped Potassium Dihydrogen Phosphate Crystals"J. Crystall, Process and Technol., 1(3), 55-62.

10. Kumari A., Chandramani, (2003),"Electrical conductivity and dielectric measurement of in Au^+ doped and undoped KDP", Indian Journal of Pure and Applied Physics, 43, 123-128.

NANO MATERIALS FOR AGRICULTURE

Dhanyakumar Kurmude[1], Rajendra Yannawar[2], Rahul Waghmare[3] and Achyut Munde[4]
Associate Professor[3], Department of Physics, Milind College of Science, Aurangabad
Associate Professor[2], Department of Electronics, Milind College of Science, Aurangabad
Associate Professor[3,4], Department of Chemistry, Milind College of Science, Aurangabad

ABSTRACT
Nano materials are important class of materials mainly characterized by its size. Due to nano size large surface area, modified energy levels and quantum effects play crucial roles in modifying materials' properties. Nano materials exhibits novel and enhanced physical, chemical, electrical, magnetic and optical property. Nano materials are useful in various applications such as storage media, sensing devices, communication means, health care systems, medical diagnostic - treatment tools, defence systems, forensic investigation, crime control and even food security and agriculture. This paper briefly reviews the agriculture industry related applications of nano materials having power to revolutionize the entire agricultural industry.

Keywords: Nano materials, synthesis, properties, characterization, agricultural applications

1. INTRODUCTION
Materials constituted of nano particles/grains are nano materials. Anything of size less than 100 nm is regarded as nano particle. Nanotechnology deals with materials, systems and processes that operate at a scale of 100 nano meters (nm) or less. Aspects such as with synthesis, characterization, visualization, organization and manipulation of nano particles so as to build various devices for desired applications are taken care of in the area of nano technology.

In general chemical routes of nano particles' synthesis are efficient and widely followed. These includes sol gel auto combustion, hydrothermal, micro emulsion etc. Among microbes, prokaryotes have received the most attention for biosynthesis of nanoparticles. Bacteria have been used to biosynthesize mostly silver, gold, Fe-S and magnetite nanoparticles and quantum dots of cadmium sulphide (CdS), zinc sulphide (ZnS) and lead sulphide (PbS). The C-containing and/or inorganic nanoparticles are synthesized using biogenic, geogenic, atmospheric and pyrogenic processes.

Characterization of nano structures usually calls for sophisticated characterization tools. Different methods of characterization are employed to determine phase, structure and properties of the nano materials using equipments such as X-ray diffractometer, Scanning electron microscope, transmission electron microscope, scanning tunneling microscope, atomic force microscope etc. Device fabrication technique mainly involves top down (lithographic processes, etching techniques) and bottom up (growth, assembly and chemical vapor deposition) approaches. Fabrication of flexible electronics is fast progressing field today.

Apart from efficient and successful use of nanotechnology in storage media [**Masud Mansuripur**], healthcare [**Shavi**], medical diagnosis [**K. Rajasundari**], medical treatment [**Mohammad Abu**] etc. the nanotechnology has its role to play in the field of agricultural industry at various stages right from crop production, processing, storing, packaging and transport of agricultural products. Nanotechnology has potential to revolutionize agriculture and food industry with its emerging techniques namely, precision farming, increasing of plants' nutrients absorption ability, effective and targeted inputs, early detection and control of diseases. After years of green revolution and turn down in the agricultural products ratio to world population growth, it is obvious the necessity of employing new technologies in the agriculture industry more than ever. Food security has always been the major issue of the mankind. Nano materials that offer safe and efficient administration of pesticides, herbicides, and fertilizers are being developed. Smart sensors and smart delivery systems help to combat viruses and other crop pathogens. [**Sayed Roholla Mousavi**].

Present paper is focused on various nano particles and related technologies used in agriculture and food industry for improving crop yield, disease detection and control, collection, storage and distribution of agriculture yields.

2. NANO MATERIALS FOR AGRICULTURE AND PROPERTIES:
Nanoparticles in various forms find its applications related to agriculture industry. Nanoparticles for protection from various plant diseases, for yield enhancement, for quality growth, targeted delivery of DNA and other chemicals to plants etc. are discussed briefly in the following lines.

2.1 Silver (Ag): In most of the bio - systems silver nanoparticles due to large surface area and surface atoms are placed at top as it exhibits strong inhibitory and bactericidal effects and broad spectrum of antimicrobial

activities. A wide range of horticultural crops gets badly affected with powdery mildew, a serious fungal disease and reduces the crop yield and quality. The affected crops lead to distortions in leaf, early defoliation and reduced flowering.

Instead of using anhydrous milk fat and soybean oil emulsions colloidal solution of silver nanoparticles of about just one and half nano meter average diameter, is effective against rose powdery mildew caused by *Sphaerotheca pannosa* Var *rosae*. Double capsulated silver nanoparticles prepared by reaction of silver ion with aid of physical method, reducing agent and stabilizers are highly stable and highly dispersive in aqueous media. It eliminates unwanted microorganisms in planter soils and hydroponics systems. Colloidal nano silver is in use as foliar spray to stop fungi, moulds, rot and several other plant diseases. In addition, silver is known to stimulate the plant-growth.

2.2 Alumino-silicate (Al_2SiO_5): Nano tubes of alumino-silicate with active ingredients are used in pesticides for making it biologically more active, eco friendly and safe. These pesticides when sprayed on plant surfaces are easily picked up in insect hairs. Insects actively groom and consume nano tubes filled with pesticide. Targeted delivery of DNA and chemicals into plant cells is possible with mesoporous silica nano particles.

2.3 Titanium dioxide (TiO_2): Titanium dioxide (TiO_2) is a non-toxic, powerful disinfectant its use in food products up to 1% of product final weight. Its photo catalyst technique free from generation of toxic and dangerous compounds can protect plant and possesses great pathogen disinfection efficiency and research to enhance the phytopathogenic disinfection efficiency of TiO_2 thin films by dye doping etc.

2.4 Carbon (C): Carbon nano tubes filled with plant protecting chemicals when functionalized with magnetic nano particles allows control nano carriers' movement inside the plant system [**Saurabh Singh**]. Recently, fluorescent nanoparticles (NPs) or quantum dots (QDs) have been developed for labelling the plant proteins. There is need of systematic study of effects carbon nano materials in plants as increased use and exposure to carbon could cause environmental concerns.

2.4 Nickel Ferrite ($NiFe_2O_4$): Nickel ferrite nanoparticles can work as potential adsorbent for removal of dipyrone from aqueous solution. It is low cost alternative adsorbent for removal of polar pharmaceutical compounds from water samples [**Springer Valeria**].

2.5 Silicon Oxide (SiO_2): Application of nano-SiO_2 (up to 8 g per litre) as fertilizer significantly improves seed germination of tomato, seed germination index, seed vigour index, seedling fresh weight and dry weight resulting effective growth and high yield. Under salinity stress, nano-SiO_2 improves leaf fresh and dry weight, chlorophyll content and proline accumulation, free amino acids, nutrients, antioxidant enzymes activity thereby improving the tolerance of plants to abiotic stress.

2.6. Zinc Oxide (ZnO_2): Zinc oxide nanoparticles increase plant growth and development such as peanut, wheat and onion. Lower concentration of nano-ZnO exhibited a beneficial effect on seed germination of cucumber. Nano-ZnO (up to 200 mg per litere) supplemented with Murashige and Skoog (MS) media improved tolerance to biotic stress [**Shalaby Tarek**].

3. CONCLUSION

Nanoparticles have emerged as a versatile platform, which could provide cost effective, efficient and environmentally acceptable solutions to the global sustainability challenges facing society. Nanoparticles have a significant influence on the economy and the environment by improving both fertilizers and energy. So, these nanoparticles have a high potential for achieving sustainable agriculture. Nanoparticles can have both positive and negative effects on plants depending on several factors such as plant species, nanoparticles and environmental factors. It has to be verified still whether essentialities of nanoparticles for plants in various ways. Biochemical, physiological and molecular mechanisms of nanoparticles in plants are to be analyzed in more details. The agricultural nanotechnology might take a few decades to move from laboratory to land.

4. REFERENCES

- **K. Rajasundari** and K. Ilamurugu, Nanotechnology and Its Applications in Medical Diagnosis, J. Basic. Appl. Chem., 1(2)26-32, 2011

- **Masud Mansuripur,** The role of nanotechnology in data storage devices and systems, DOI: 10.1364/ISOM_ODS.2011.OMA2, Conference: Joint International Symposium on Optical Memory and Optical Data Storage

- **Mohammad Abu** & Moshed, Azmal & Khairul, Mohammad & Sarkar, Mohammad Khairul & Khaleque, Abdul & Author, Corresponding & Morshed, Abu Mohammad Azmal. (2017). The Application of

Nanotechnology in Medical Sciences: New Horizon of Treatment. American Journal of Biomedical Sciences. 2017. 1-14. 10.5099/aj170100001.

- **Saurabh Singh**, Bijendra Kumar Singh, S.M. Yadav and A.K. Gupta, 2015. Applications of Nanotechnology in Agricultural and their Role in Disease Management. *Research Journal of Nanoscience and Nanotechnology, 5: 1-5.*

- **Sayed Roholla Mousavi,** Maryam Rezaei, Nanotechnology in Agriculture and Food Production, *J. Appl. Environ. Biol. Sci.*, 1(10)414-419, 2011

- **Shalaby Tarek**, Bayoumi Yousry, Abdalla Neama, Taha Hussein, Alshaal Tarek, Shehata Said, Amer M, & domokos - szabolcsy Eva & El-Ramady, Hassan & A Shalaby, T & Bayoumi, Yousry & Abdalla, N & H Taha, bullet & H El-Ramady, bullet & Shehata, Sami. (2016). Nanoparticles, Soils, Plants and Sustainable Agriculture. 10.1007/978-3-319-39303-2_10 Chapter from book Nanoscience in Food and Agriculture 1

- **Shavi**, Gopal and Deshpande, Praful & Nayak, Usha & Gurram, Aravind Kumar & Averineni, Ranjith Kumar & Sreenivasa Reddy, M & Udupa, Nayanabhirama & Koteshwara, K. (2010). Applications of Nanotechnology in Health Care: Perspectives and Opportunities. International Journal of Green Nanotechnology: Biomedicine. 2. B67-B81. 10.1080/1943085x.2010.532072.

- **Springer Valeria**, Pecini Eliana, Avena Marcelo (2016). Magnetic nickel ferrite nanoparticles for removal of dipyrone from aqueous solutions. Journal of Environmental Chemical Engineering. 4. 3882. 10.1016/j.jece.2016.08.026

SYNTHESIS AND CHARACTERIZATION OF COMPOSITE THIN FILMS OF CONDUCTING POLYMER, GALLIUM ARSENIDE AND THEIR APPLICATIONS FOR SOLAR CELL

S. D. Nimbalkar, P. P. Bhosale, S.S.Arsad, M. D.Shirsat and Madhav. N. Rode
Optoelectronics and Advanced Sensors Research Laboratory, RUSA,
Department of Physics, Dr. B.A.M.U, Aurangabad,
Department of Physics, M.F.M. Warud, Dist.Amravati
Department of Physics, Vaidyanath College, Parli-Vai., Dist. Beed

ABSTRACT
The rapid development and progress of science and technology in the field of energy and material has been illuminated the significance of conducting polymer. During the last decade researcher have been struggling to rise up the power conversion efficiency of solar cell by developing new material and structure. In the present work a composite films of conducting polymer and GaAs with attractive feature have been synthesized by Electro deposition method and drop casting method respectively. The structure and morphology of the prepared films were studied from XRD and AFM pattern. And optical characteristics of the prepared films were studied from UV spectrometer it shows that the band gap of the prepared thin films of GaAs material is 1.39 ev and voltage current characteristics of the composite films shows the suitability of materials for photovoltaic application.

Keywords; conducting Polymer, GaAs, Solar cell, thin films, PEDOT: PSS.

INTRODUCTION
In earlier days, the most common solar cells were designed using single p-n junction silicon crystal. But the cost of the single silicon crystalline substrate was high and hence new absorbing materials and cheap technologies were under sought. The main advantage of the thin film technology is the material can be spread on to the large area of wafer or substrate by any suitable method in order to produce high volume.

GaAs is one of the most influential III-V semiconducting materials, which possesses high mobility and direct band gap of 1.43ev.this properties of GaAs material makes them suitable for an optoelectronics and photovoltaic application. different growth techniques are used for the synthesis of GaAs thin films, these methods are spray paralysis[11],liquid phase epitaxial[7],molecular beam epitaxial[12],electrode position, metal organic chemical vapor deposition[15],chemical vapor deposition[15].these all techniques are expensive and complicated .among all various techniques, electro deposition techniques offer several advantages [8,17], means it is simple ,powerful and inexpensive. In this technique films thickness, structure and composition can be controlled by voltage or current, here the optimization of parameter for the deposition of single metal is easy but for binary compound is difficult [9] .we studied the characteristics of photo electrochemical solar cell designed using GaAs thin film acts as photo electrode and graphite as counter electrode in 2M polysulphide. D.K.Ferry reported the successful deposition of GaAs from an electrolyte whose ph was 0.7[15], Mahalinga reported the deposition of GaAs from an electrolyte of GaCl$_3$ and As$_2$O$_3$ for various pH and temperature [6]. K.R.Murali, have synthesized GaAs by varying duty cycle from aqueous solution of GaCl$_3$ and As$_2$O$_3$ [14]. Andreoly have reported the synthesis of GaAs thin films by deposing Ga on Ti substrate and As, layer was electrodeposited on Ga layer [19]. M.Chamekh Have reported that the co deposition of GaAs metal at 279k and pH was 1 from gallium metal and As$_2$O$_3$ dissolved in dilute HCL [1]. In the literature.V.M.Zozlov, S.Chandra [17, 9] has been reported that large effort had been made by researcher for the deposition of GaAs thin films from acidic and alkaline solution with limited fruitful output. In this paper we present the co-deposition of gallium and arsenic metal at room temperature from a electrolyte contain gallium metal and As$_2$O$_3$ dissolved in concentrated HCL and the pH was maintain at 1.2

Before 30 year it was considered that polymers were used as an insulator but by simple modifications in the conjugated polymer their electrical conductivity has been raised[18] the first remarkable feat in the field of conducting polymers has been taken around 1978, explained by Shirakawa[18,3]he showed that the oxidation and reduction reaction in the conjugated polymer and enhance their conductivity and turn as p doping and n doping respectively[3] Conducting polymer have found large applications in the manifold fields of Electronics, Optics, Energy devices and Medicine .study on polymer solar cell reveals a positive effect on the efficiency and hence, the structure of inorganic –organic hetrojunction solar cell have been allured much more attention.

Generally hetrojunction solar cells are fabricated from Donar and Acceptor layers.Donar materials absorb light and generate excitons and Acceptor layer transports electrons [25, 24] efficiency of solar cell depends upon

several factors. In the present work PEDOT: PSS layer was form on GaAs substrate by Drop casting method. And demonized water was used as solvent, in the PEDOT: PSS conducting polymer PEDOT is a polycation and PSS is a polyanion [26, 27]

EXPERIMENTAL DETAILS

Thin films of GaAs material have been electrodeposited from an electrolyte containing Ga metal and As_2O_3 dissolved in concentrated HCL. Gallium metal (99.99% pure purchased from Sigma Aldrich) and As_2O_3(99.99% pure purchased from Sigma Aldrich) were separately dissolved in concentrated 10ml HCL,1M Gallium metal was separately dissolved in concentrated HCL and 0.1M As_2O_3 was dissolved in another 10 ml HCL. After adding two solutions in appropriate ratio, the resulting solution was stirred for 3 hours, the solution was diluted by adding double distilled water and the pH value of the electrolyte was set to 1.2 by adding concentrated KOH solution in such a way that the final volume of the electrolyte should be 40ml. ITO coated glass substrate were commercially available and it is purchased from sigma Aldrich and the size of the substrate was 2.5 cm× 2.5cm which has a resistance of 10 Ω /cm^2 ITO coated glass substrate were initially cleaned ultrasonically in order to remove surface contamination, dust particle and then rinsed thoroughly with double distilled water, and dried at 400 C^o for 5 min.

Electrolytic cell consisted of two electrodes in contact with electrolyte, ITO coated glass substrate used as working, platinum plate acts as counter electrode and $Ag/Agcl_3$ was used as reference electrode. During the electrolysis process Ga, and As, ion attracted toward cathode and gets deposited on ITO substrate. The Stoichiometric ratio of Ga and As ions depends on the pH of the electrolyte, temperature, concentration, current or voltage parameter and electro deposition time. There is no clear cut method discussed in the previous literature for the fixing of deposition parameters for binary metal. And hence failure rate in co-deposition of metal was high. In the present work, we performed our experiment by applying a potential between 0.6 to 1.1volt.during the experiment we prepared number of samples for various deposition times while other growth parameters kept constant. Then prepared samples were removed and rinsed thoroughly with double distilled water and annealed in air for 10 min. Here, we prepared two samples of photovoltaic cells, the first sample prepared by using GaAs thin film deposited by electro deposition techniques and second was prepared by GaAs substrate (100) purchased from U.S.A the substrates were cleaned in ultrasonic bath, isopropyl alcohol and demonized water for 5 min. and in dil. HCL solution for 2 min. in order to remove the surface contamination and annealed at temp. 100^0 Si doped n –type GaAs substrate (100) with doping concentration (0.4-4) $* 10^{18}$ and thickness of 350 micrometer purchased from Precision Micro Optics (USA) are used for device fabrication. Thermally evaporated aluminum was used as cathode, ITO used as Anode, PEDOT: PSS (Clevious PH1000) dissolved in demonized water, and (P3HT) poly-3 hexythiophene was used hole transport layer as shown in figure below.
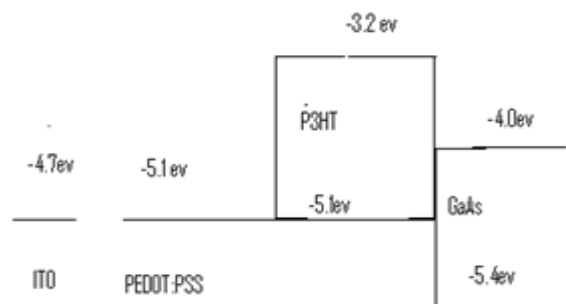
Fig-1: Band alignment diagram in Planner hetrojunction solar cell
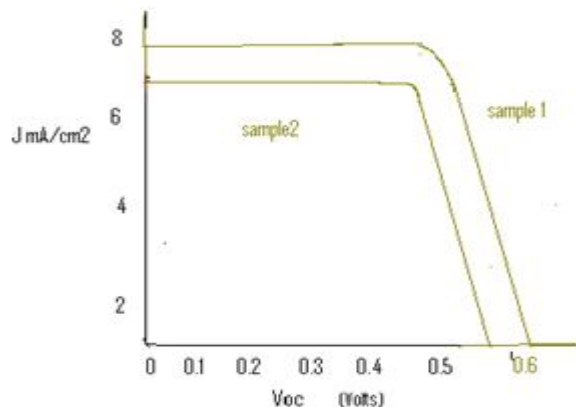
Fig-2: Voltage –current characteristics of the prepared composite thin films shown in fig. above.

CHARACTERIZATION

GaAs thin films deposited on ITO coated glass substrate were characterized by keithely XRD diffractometer Operating in θ-2θ geometry XRD pattern used to identify crystalline phases ,XRD pattern shows that films are polycrystalline in nature and peaks intensity corresponding to single phase GaAs .UV absorption spectral characteristics of the prepared samples were studied at room temperature.
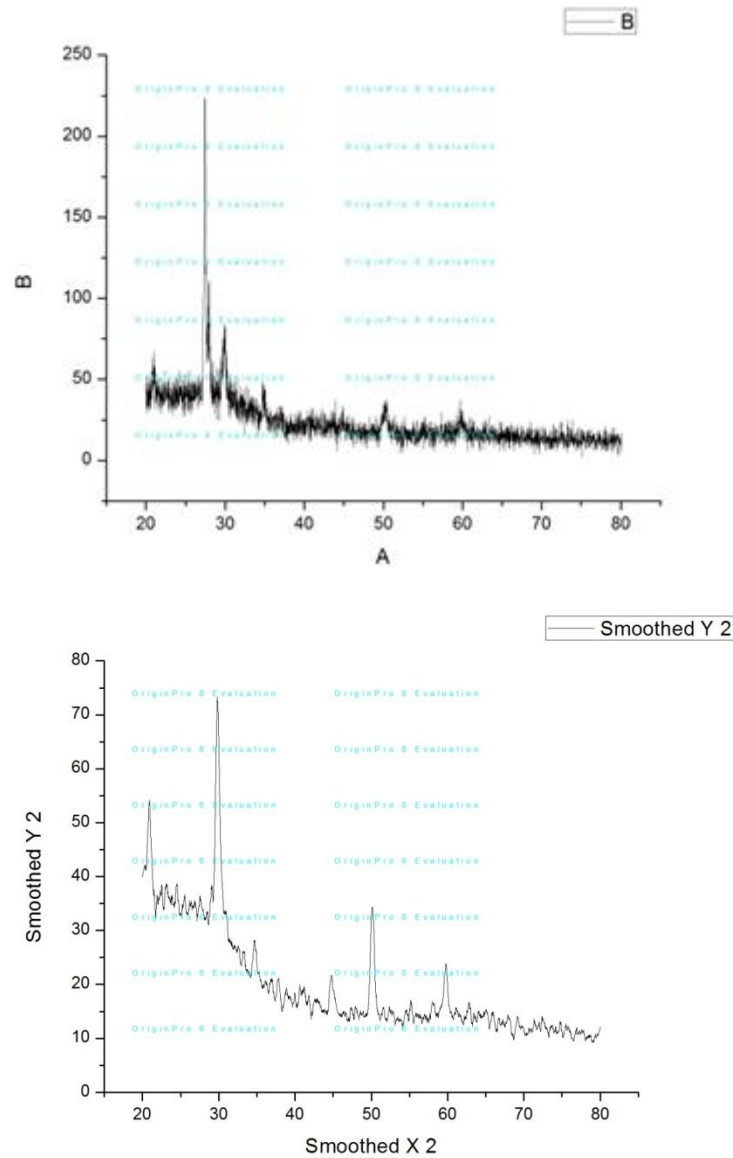
Fig-3: XRD of the prepared thin films
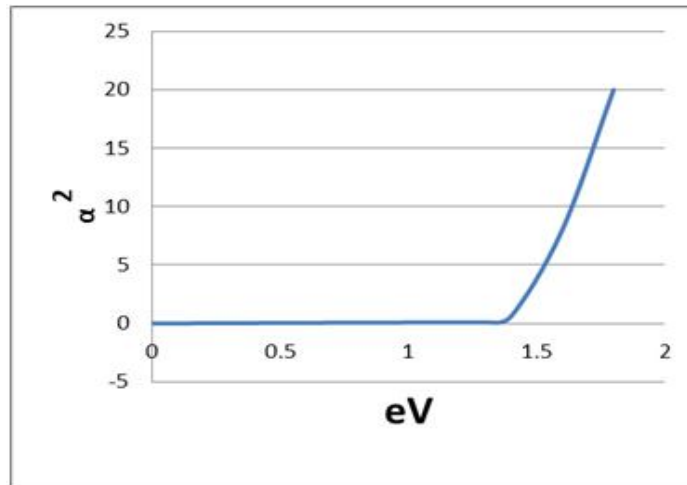
RESULT AND DISCUSSION

The sharp diffraction peak in the XRD pattern reveals that the films are crystalline in nature. Figure show that if the deposition time of the prepared film is less than 10 minute then it exhibit cubic and orthorhombic structures. (16,17) where as the film deposited at deposition time greater than 10 min shows predominantly of orthorhombic structure (19,20) .by applying Debye-Scherer formula (18), to XRD pattern we can calculated the average grain size of the prepared films.

$$D= k\lambda \ /B\cos \theta \ \text{------------------------ (1)}$$

Where- k is the shape factor, λ is the X-ray wavelength and θ is the diffraction angle.

The three dimensional surface scan of the prepared GaAs thin film is analyzed by AFM technique. This study reveals that as the deposition time was increased then the average particle sizes of the surface were found to increase.

The absorption coefficient of the films is given by $\alpha E = C (E - Eg)^{n}$.

Where, C is constant E is the photon energy and E_g is the band gap energy n is the constant which value is depend upon the types of transition and which may be assigned the value 2, 1/3, 1/2 for allowed indirect transition, forbidden direct transition ,allowed direct transition respectively.

GaAs is a direct semiconductor materials and hence for this materials n=1/2.the absorption coefficient α can also be calculated from the following equations which shows the relationship between the sample thickness ''d ''and transmittance'' T'' this equations is valid for high absorption when the reflectivity dispersion and interference effect are negligible (23)

$$\alpha =2.303 \ Log \ (1/T)/d$$

Where T is transmittance and d is thickness

Linear nature of the graph between α and E indicate that this is direct band gap semiconductor and the straight line intercept at x axis gives the value of band gap energy. Band gap is in good agreement with the values reported for GaAs thin films prepared by Galvanostatic technique. (6,14).

Under 110 mw/cm^2 illumination power, voltage current characteristics of prepared hybrid solar cell are measured in this case open circuit voltage, current density, fill factor and efficiencies are Voc=0.610 v, J=7.10 mA/cm2 ,FF=0.71 ,η=4.72 % but the performance of the another solar cell which was designed by electrodeposited GaAs layer on ITO substrate was poor .in this case open circuit voltage, current density, fill factor and efficiency are Voc=0.57 v ,J=8.10 mA/cm2 ,FF=0.61, η=2.72% as shown in figure above.

CONCLUSION

GaAs material is useful for optoelectronic devices and sensors. We can increase the efficiency of solar cell with heterojunction structure accompanied with conductive polymer which has tremendous applications in the field chemical, electrical and medical. But still there are some challenges in the field of development and implementation; co deposition of conducting polymer and metal is very complicated.

REFERENCES

1. Chiang C K Finchee C R,Park Y W ,Heeger A J,Lewis E J, Gan S , C and Mac Diarmid A G, electrical conductivity in doped polyacetelene, Phys Rev Lett,39 (1977)1098

2. B.D. Cullity, *Elements of X-ray Diffraction* (Addison-Wesley, USA, 1978)

3. Chiang C K,Drug M A, Gan S C,Heeger A J,Lewis E J, Mac . Diarmid A G,Park Y W And Shirakawa H, synthesis of highly, conducting polymer Am Chem soc, 10(1978)1013

4. I.G.Dioum, J.Vedel, B.tremillion J.Electroanal.chem.139, 329, 1982

5. D.K.Ferry, Gallium Arsenide theory H.W.Sams and company 1985.

6. S.Chandra, N khare, semi. Science Technol.2 1987(214,215)

7. M.J.Howes, D.V.Morgan, Gallium Arsenide materials devices and circuit 1985

8. S.Chandra, N.Khare, Semiconductor science technology 2, 214, 215, 1987.

9. S.Chandra and Neeraj Khare, semiconductor sci. technology2, 214- 219 1987.

10. S.Chandra, N.Khare and H.M. Upadhyaya Bull. Matter, Sci., Vol10, no.4, Jully 1988

11. G. Casamassimma, T. Ligonzo, R Murri, N. pinto, L. schiavulli and valentine, matter. Chem. ...physics 21,313,314, 1989

12. N.Koguchi, K.Ishige, S.Takahashi, J.Vac.sci.technol.B 11, 13,799-1993.

13. Y.Gao, A.Han, Y.Lin, Y.Zhao, J.Zhang, J.Appl.physics 75, 547, 1994.

14. Y.Gao, A Han, Y .Lin, Y.Zhao, J.Zhang, journal of app. Physics, (1994), 75,546

15. S.Okamoto, Y.Kanemitsu, K.S.Min, H.A.Atwater, Appli.Phy.Lett.73, 75, 1998.

16. J.Nayak, S.N.Sahu, Applications surf science 182,83,2001.

17. V.M.Zozlov, B.Bozzini, L.P.Bicelli, J.Alloys compound.379, 209, 2004.pp323, 332.

18. A, K, Bakshi, Geetika Bhalla, Journal of scientific and industrial research, vol63, 2004 Pp715-728

19. T.Mahalingam, soonil Lee, Hanto Lim, Hosun, Moon, Youg Deak Kin .solar energy Material and solar cell, 90, 2006.

20. K.R.Murali and D.C.Trivedi Phys.stat.sol (9)203, no.5, 875-877-2006.

21. P. Prathap, N. Revathi, Y.P. Venkata Subbaiah, K.T.Ramakrishna Reddy, J. Phys. Condens. Matter **20**, 2008

22. J. Nayak, S.N. Sahu, Physica E **41**, 92 (2008)

23. M.Chamekh, M.Lajnef, L.Zerroual and R.Chtoourou, Eur.phys.J.Appl. Phys. 52, 2010

24. H.C.Chen, C.W.Lai, I.C.Wu, H.R.Pan, I.W.P.Chen, Y.K.Peng, C.L.Liu, C.H.Chen and P.T.Chou, Adv.Mater, 2011, 23, 5451-5455

25. Jhih-Fong Lin, Wei Che Yen, Chun-Yu Chang, Yang-Fang Chen and Wei-Fang Su, J.Mater.Che.A, 2013, 1,665.

26. S.Xiao, S.Abreu Fernandes, C.Essen, A.Ostendorf, and Picosecond Laser Direct Patterning of PEDOT: PSS.

27. J.Weszka.M.M.Szindler, P. Jarka, Journal of Achievements in materials and Manufacturing engineering, vol.59, issue 2, Aug 2013.

PROPERTIES CHARACTERIZATION AND EFFECT OF CLINOPTILOLITE ZEOLITE ON GROWTH AND YIELD OF MUSHROOM.

G S Duthade

[1]Department of Physics, Yeshwant Mahavidyalaya, Nanded

ABSTRACT

Zeolites are crystalline hydrated aluminosilicates of alkali and earth metals. Properties of the aluminosilicates, framework and presence of well defined channel systems make it possible a variety of application such as agricultural, industrial, and medicinal etc. Zeolites have many more useful properties with high ion exchange and retention capacity. Due to such fascinating properties of zeolites the plant growth, yield of crop have been increased by the application of zeolites and work has been reported in many national and international journals. Taking this fact in to consideration, we have planned to concentrate on the characterization, properties of natural zeolite Clinoptilolite and to study their application on the growth and yield of Mushroom.

Natural zeolite Clinoptilolite were collected from Fardapur, near Ajanata cave, District Aurangabad from the Marathwada region of Maharashtra state, India. Characterization IR and XRD of Clinoptilolite were carried out. The powdered form of Clinoptilolite were applied in various proportions to study the growth and yield of Mushroom. On the application of Natural zeolite Clinoptilolite we found the considerably growth and yield of Mushroom.

Keywords: Clinoptilolite, Zeolites, Mashroom, Fardapur, Ajanta caves.

INTRODUCTION

Zeolites are crystalline hydrated aluminosilicates of alkali and earth metals that possess infinite, three dimensional structures. These crystals are further characterized by an ability to lose and gain water reversibly and to exchange some of their constituent elements without major change of structure[1]. Now a days soilless culture is the modern cultivation system of plants is used for organic or inorganic substrate through nutrient solution nourishment[2]. Soilless growing media are easier to handle with compared to soil culture and it may provide better growing environment.

Zeolites are having potentiality as soilless media for its unique properties. Zeolite crystals alumina-silicates have negative charges, which is balanced by one or two valence of positively charged cations[3]. It has high water absorption, retention and releasing capacity. It has high cation exchange capacity with high buffering ability of ph change[4]. Zeolites are microporous crystalline materials that have a high internal surface area[5]. It has been reported that due to its higher cation exchange capacity, nutrient and water holding capacity yield of tomato, carrot, wheat etc increased greatly. Tomato plants grown in perlite and zeolite mixture substrate increases yield. Taking this fact of the references in to consideration, we have planned to apply different proportions of the zeolite Clinoptilolite, a platy variety of zeolite crystal to check growth and yield of eatable mushroom.

MATERIALS AND METHODS

Clinoptilolite a platy variety of natural zeolite crystal was collected from Fardapur near Ajanta caves Dist. Aurangabad of Maharashtra state, India. Collected sample were characterized by IR and XRD. IR spectra was recorded on Perkin IR instrument and X-ray diffraction patterns were recorded on a JEOL X-ray Diffractometer

TIFR Mumbai between the scan range 5° to 60° to confirm the zeolitic nature and phase structure of the collected sample Clinoptilolite. The culture(seeds) of oyster mushroom variety P. Sajor Caju ware obtained from Vasantrao Naike Agriculture Marathwada University Parbhani (MS). Soybean straw is used as substrate ware collected from village Gour Tq. Purna(Jn.) Dist. Parbhani (MS) for cultivation purpose.

Dry Soybean straw was soaked in a cold water for 14 hours and separated from water. The substrate soybean straw was pasteurized in a autoclave under 15Ibs pressure for 22 minutes and discharged from autoclave and cooled down to room temperature. After cooling down,1kg quantity of straw per bag filled into the polythene bags with addition of powdered form of a platy variety of zeolite crystal Clinoptilolite, in different proportions i.e 1, 3, 5,7 and 10gms. After this process polythene bags tightly packed and transferred to the Mushroom house for soil less cultivation of mushroom. Temperature and humidity conditions are maintained at $18\text{-}24^0$C and 75-85 % respectively. Time period recorded for the formation of fruiting bodies in addition of different proportions of Clinoptilolite. The data of experiment is recorded for the yield and germination period of the of mushroom.

Figure-(01) : IR Spectrum of Clinoptilolite zeolite
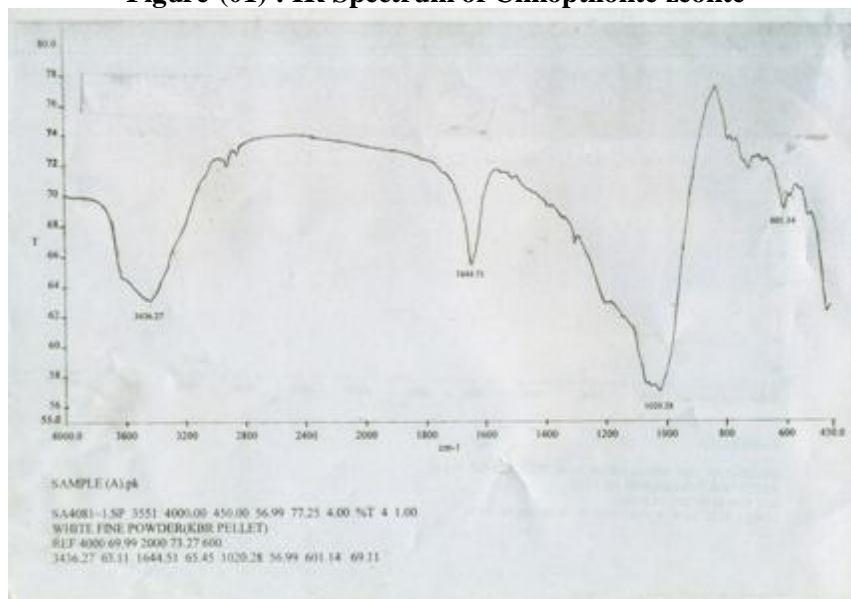
Figure-(02): X-RD Pattern of Clinoptilolite zeolite
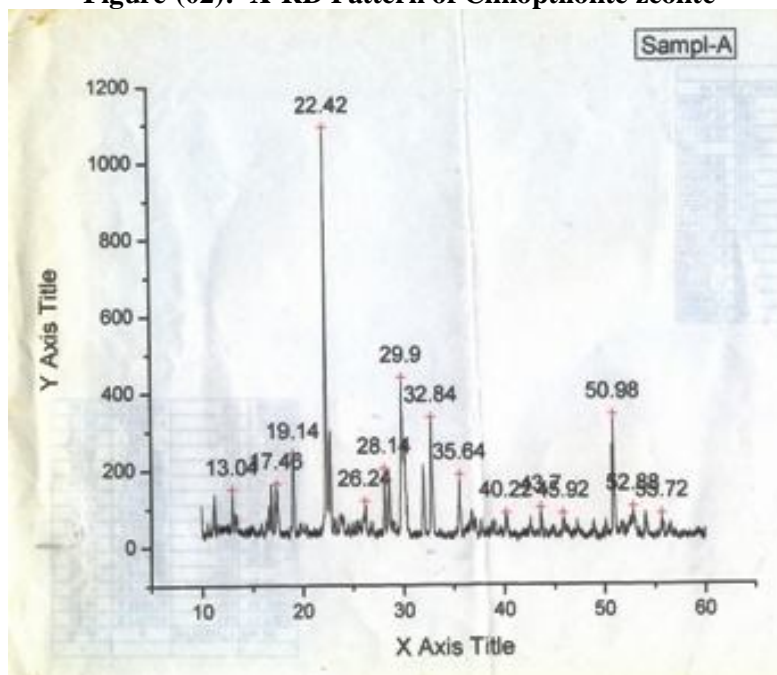
RESULT AND DISCUSSION
Experimental data presented in table(01), from the analysis of the data it is clear that, on the addition of zeolite Clinoptilolite in different proportions, the yield of the *P.sajor caju* mushroom have been increased considerably. The time period required for formation for fruiting bodies were reduced by 1 to 2 days with the addition of a platy variety of zeolite Clinoptilolite. Also we have observed growth rate for the germination period of mushroom culture(seeds) was reduced by 4 hours.

Table-1: Effect of Clinoptilolite zeolite on Mushroom growth.

Substrate	Days for formation of fruiting bodies	Fresh wt. of Mushroom (gm/kgm of straw)	Dry wt. of Mushroom (gm/kgm of straw)
Soybean straw (Control)	17	122.10	11.91
Soybean straw + 1gm Zeolite	16	198.72	12.13
Soybean straw + 3gm Zeolite	16	238.55	12.41
Soybean straw + 5gm Zeolite	15	255.3	12.65
Soybean straw + 7gm Zeolite	15	269.04	13.03
Soybean straw + 10gm Zeolite	15	278.00	13.90

YIELD OF MUSHROOM

The fruiting bodies (mushroom) were harvested in three slots. From experimental data presented in table -01, the yield (Fresh and dry wt.) of mushroom increased relevantly with the addition of different proportions of zeolite Clinoptilolite. We found that the maximum yield of mushroom obtained 278.00 gm/kgm of straw with the addition of 10 gm of Clinoptilolite and the ratio of the increase in the yield is 1: 2.27 as compared to control.

From the above result, it can be concluded that, the productivity increases with decrease in germination period of mushroom on the application of zeolites.

ACKNOWLEDGE

REFERENCES

1. Fedrick A Mumptora, State university college, Brockport, Ny 14420.

2. Md. Asaduzzaman, Md. Saifullah, AKM Salim Reza Mollick, Md. Mokter Hossain, GMA Halim and Toshiki A Sao : Influence of soilless culture substrate on improvement of yield and produce quality of horticulture crops. 2015.

3. Mumpton FA, Uses of natural zeolites in agriculture and industry, Proceding of natural academy of science, USA: 19999,96, 3463-3470.

4. Allen ER, Ming DW, Recent progress inthe use of natural zeolites in agronomy and horticulture, Nature of zeolite. 1995, 93, 477-490.

5. Amir Zaman Khan, H. Khan, R. Khan, S. Nigar, B. Saeed, H. Gul, Amanullah, S.Wahab, A.Muhammad, M. Ayub, T. Henmi, Morphology And Yield Of Soybean Grown On Allophanic Soil Asinfluenced By Synthetic Zeolite Application. Pak. J. Bot., 43(4): 2099-2107, 2011.

ACOUSTIC STUDY OF *OFFICINALE ZINGIBER* AND ZINC CHLORIDE AT VARYING CONCENTRATION BY ULTRASONIC INVESTIGATION

Pallavi B. Nalle[1], Sangita U. Shinde[2] and K. M. Jadhav[3]

[1]Department of Physics, Shivchhatrapati College, Aurangabad
[2]Department of Physics, Pratishthan Mahavidyalay, Paithan, Aurangabad
[3]Department of Physics, Dr. Babasaheb Ambedkar Marathwada University, Aurangabad

ABSTRACT

Ultrasonic investigation is donefor the ethanolic extract of Officinale Zingiber in ZnCl₂with varying concentration and at constant temperature 303.15K. From experimental data the acoustic parameters such as intermolecular free length (L_f), adiabatic compressibility (β) and specific acoustic impedance (Z) have been obtained. Investigated parametersare used to calculate acoustic parameters.Obtained experimental and acoustic parameters are used to investigate the molecular association between Officinale Zingiber and Zn⁺⁺ ions. The results are helpful for pharmacological applications of drugs.

Keywords: Acoustic Parameters, Officinale Zingiber Extract, Pharmaceutical Applications

INTRODUCTION

As ultrasound is a nondestructive technique it is widely used in pharmaceutical science. Intermolecular and intramolecular association between atoms and molecules are basically identified by ultrasonic velocity.*Officinale Zingiber* is mainly used as a spice in every kitchenof India, and in other countries[Purseglove, J. W., 1981, Zingiber officinale. 1976].It is also used as a food preservative. *Officinale Zingiber*is a underground rhizome which belongs to Zingiberaceaefamily [Schulick, P. 1994]. Medicinal properties of drug are decided from its constituents. Official Zingiber is a non-toxic and natural antioxidant compound.Its biological functions aresuch as antioxidant, antimicrobial, anti-inflammatory, immunomodulatory, anticarcinogenic. This is 5-hydroxy-1-(4-hydroxy-3-methoxyphenyl) decan-3-one;pyridine-3-carboxylic acid IUPAC name of officinal zingiber. Its molecular formula $C_{23}H_{31}NO_6$.*OfficinaelZingiber*is well known antioxidant herbal medicine. It has a very few side effects (Ali et al., 2007) [Ali, B. H., 2007]. A very few physicochemical studies of antioxidant herbal drug*OfficinaleZingiber*have been studied so far. We have undertaken a systematic study on the ultrasonic investigation of an antioxidant ethanolic extract of *Officinale Zingiber*with zinc chloride to investigate interactions present in that system.

EXPERIMENTAL
Preparation of the extract from Officinal Zingiber
Good quality dried*OfficinaleZingiber* were purchased from the local market and used after cleaning with water. Official Zingiber were ground to a coarse powder. 100 gm. powdered Official Zingiber added in 1 lit. Ethanol kept on magnetic stirrer for 30 min. boiled it and then cooled at room temperature for decantation. Zinc chloride is added in ethanol and prepared molar solution of zinc chloride. Then known numbers of moles of drug (Official Zingiber) were added into a fixed volume of solvent.

METHODS
Ultrasonic velocity
Single frequency (frequency 2 MHz) ultrasonic interferometer model no F-81 is used to determine ultrasonic velocity of *Officinale Zingiber*extract with Zn⁺ion.Density of experimental liquid is determined by using digital balance and Specific gravity bottle with capacity 25 ml. Viscosity of experimental liquid is calculated with the help of Ostwald Viscometer and stop watch. All parameters are measured at temperature 308.15 K.

THEORY AND CALCULATIONS

Acoustic parameters are calculated from experimental investigation (ultrasonic velocity (U), density(ρ) and viscosity (η)) byusing following standard equations.

1. **Adiabatic compressibility:** $\beta = \frac{1}{U^2 \rho}$ ....(1)

2. **Specific Acoustic Impedance:** $Z = \rho U$ ....(2)

3. **Intermolecular free length:** $L_f = K_T \sqrt{\beta}$ ....(3) Where $K = (2.075 \times 10^{-6})$

RESUTS AND DISCUSSINS

Ultrasonic Velocity: Table 1 and fig. 1 (a) represents the values and nature of graph of acoustic parameters for *Officinale Zingiber*ethanolic extract at different concentrations and at temperature 303.15K. Values of ultrasonic velocity increases with increasingconcentration. When solute is added in liquid there is molecular association occurs. Increasing trend of ultrasonic velocity shows presence ofinteraction between solute-solvent[Aswale S., 2013].

Density(ρ): Density (ρ) is association ofmolecular association. Density of various concentration of *Officinale Zingiber*with Zn+ is listed in Table 1 and represented in fig. 1 (b). It is observed from Table 1 that as concentration of *Officinale Zingiber*with Zn+ ions increases the value of density decreases. Graphical representation reflect that there is interactions between solvent - solvent and solute- solvent and shrinkage in the volume [Ramteke, S., 2015].

Viscosity(η): It is observed from Table 1 and fig. 1 (c) that the value of viscosity goes on decreasing with increase inconcentration of *Officinale Zingiber*except 1.4018 mol concentration.Graphical representation shows that the molecular association becomes strong with increasing concentration except at 1.4018 molvalue.

Adiabatic Compressibility (β): Adiabatic compressibility and ultrasonic velocity shows reverse trend to each other.Adiabatic compressibility decreasesas with increases in concentration of *Officinale Zingiber*as shown in table 1 and fig. 1 (d). Values of adiabatic compressibility decreases with increase in metal ion concentration, this reflects electron donor and acceptor capacity/nature same behavior was observed by SunandaAswale and et.al. [Aswale, S., 2012].

Intermolecular Free Length (L_f): Table 1 and Fig. 1 (e) shows the values and graphical presentation of intermolecular free length (L_f). It is seen that due to increasing concentration of Zingiber Officinale the values of intermolecular free length (L_f) decrease.Decreasing trend indices predominance ofsolvent-solute interactions in this system. It reflects that there is presence of molecular association which is similar for system cetrizine, loratidine and chlorpheniramine [Baluja, Sh., 2007].

Specific Acoustic Impedance (Z): Table 1 and fig. 1 (f) show values and graphical presentation of specific acoustic impedance (Z) against concentration which is found to be increases. Variation in specific acoustic impedance occurs due to molecular associationpresent in the system [Jamankar, G., 2015].

CONCLUSIONS

It can be concluded from the above study that the interferometer technique requires minimum efforts. It is a direct method and has its own identity and significance in material science, which can give an idea about effectiveness of solvent. Variation inacoustic parameters shows there is presence of molecular association in liquid mixtures and solutions. Thus, the conclusion drawn from all the studies is that the studied drug *Officinale Zingiber*when added in ethanolic Zn+ mixtures there is formation of molecular association. Such kind of study is helpful for pharmacological study of drugs which is used to understand formokinetic processes (transport of drug across biological membranes, drug action and physicochemical properties).

Table 1: Ultrasonic velocity (U), density (ρ) and viscosity (η) adiabatic compressibility (β), intermolecular free length (L_f), specific acoustic impedance (Z), relaxation amplitude (α/f^2) and relaxation time (τ) for *Officinale Zingiber* + $ZnCl_2$ system at 303.15 K.

No. of moles	(U) ms^{-1}	(ρ) Kg/m^3	(η) / 10^{-3} N S/m^2	(β) $\times 10^{-10}$ $Kg^{-1} ms^2$	(L_f) /10^{-11} m	(Z) $\times 10^5$ $Kgm^{-2} s^{-1}$
0.7009	1251	895.6	5.688	7.13463	5.543812	11.20396
1.4018	1260	888.4	6.022	7.09007	5.526472	11.19384
2.1027	1276	882.2	5.894	6.96196	5.476316	11.25687
2.8036	1285	879	5.7001	6.88977	5.447849	11.29515
3.5045	1297	881.8	5.4687	6.7414	5.388871	11.43695
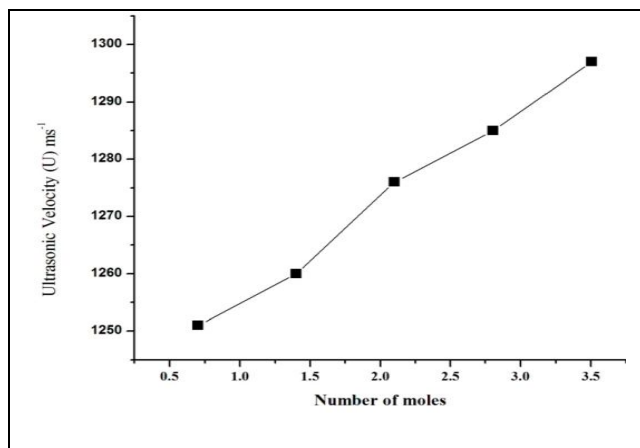
Fig-1 (a) Ultrasonic velocity (U) for *Officinale Zingiber* + Zn⁺ at 303.15 K.
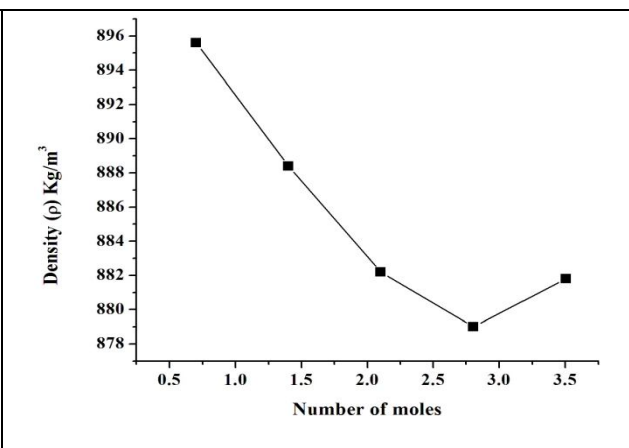
Fig-1 (b) Density (ϱ) for *Officinale Zingiber* + Zn⁺ at 303.15 K.
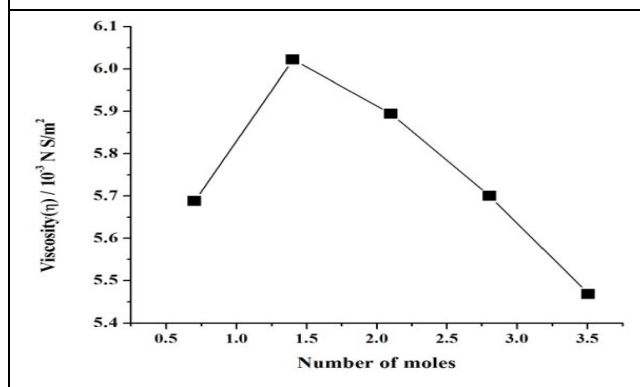
Fig-1 (c) Viscosity (η) for *Officinale Zingiber* + Zn⁺ at 303.15 K.
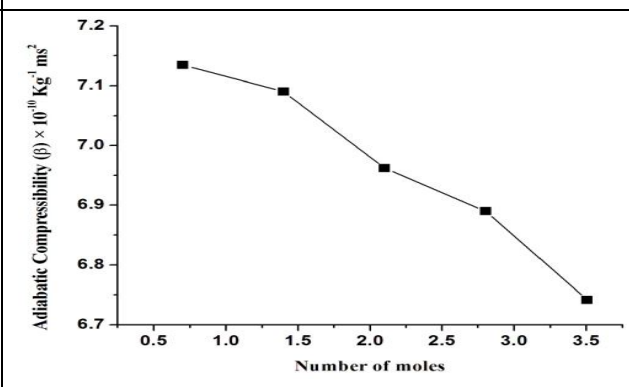
Fig-1(d) Adiabatic Compressibility (β) for *Officinale Zingiber* + Zn⁺ at 303.15 K.
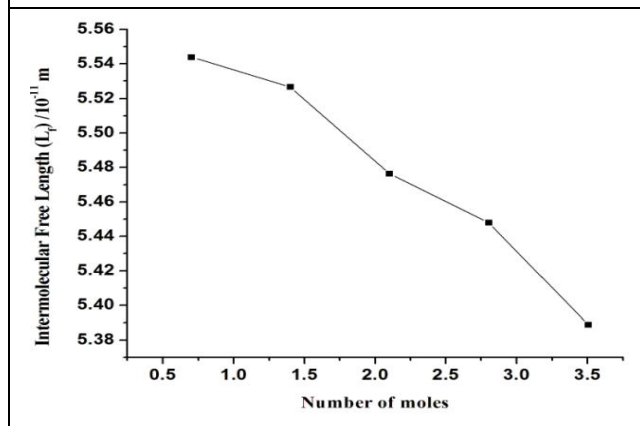
Fig-1 (e) Intermolecular Free Length (L_f) Officinale Zingiber + Zn⁺ at 303.15 K.
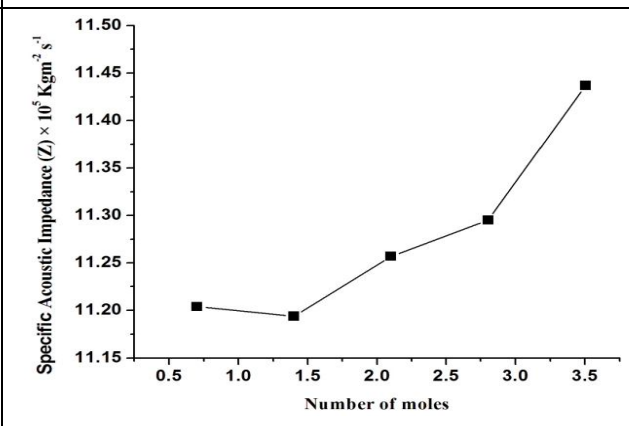
Fig-1 (f) Specific Acoustic Impedance (Z) for *Officinale Zingiber* + Zn⁺ at 303.15 K.

REFERENCES

- Purseglove, J. W., Brown, E. G., Green, C. L., Robbins, (1981). SRJ. Longman Inc:New York.

- Zingiber officinale.(1976). The Wealth of India. CSIR Publications andInformation Directorate, New Delhi.

- Schulick, P. (1994), *Ginger-common spice and wonder drug*. Edn 2. HerbalFree Press Ltd. Brattleboro Vermont USA.

- Ali, B. H., Blunden, G., Tanira, M. O., Nemmar, A. (2007).*Somephytochemical, pharmacological and toxicologicalproperties of ginger Zingiber officinalis Roscoe: a reviewof recent research*: Food ChemTox.

- AswaleS., S., AswaleS., R.,DhoteA., B.,,, (2013).*Adiabatic compressibility, free length and acoustic impedanceof aqueous solution of paracetamol*:Journal of Natural Sciences.

- Ramteke, S. P., Chimankar, O. P.,Mandal, R. A.,Tabhane, V. A., (2015).*Investigation of Acoustical Behavior of Dichlofenacsodium drug in Ethanol at Different Temperature*: International Journal of Science and Research.

- Aswale, S., S., Aswale, S., R., Hajare, R., S: (2012).*Adiabatic compressibility, intermolecular free length and acoustic relaxationtime of aqueous antibiotic cefotaxime sodium*: Journal of Chemical and Pharmaceutical Research.

- Baluja, Sh.,Solanki, A., Kachhadia, N., (2007): *An Ultrasonic Study of Some Drugs in Solutions:*Russian Journal of Physical Chemistry A.

- Jamankar, G., M,.andDeshpande, M., S.,(2015):*Ultrasonic studies of molecular interaction of gallic acid with ethanol:*Pelagia Research Library Der ChemicaSinica.

INVESTIGATION OF FLUORESCENCE SPECTROSCOPY AND KINETICS OF PLANT LEAVES FOR THE STUDY OF EFFECT OF STRESSES

A. D. Suryawanshi[1], V. B. Sanap[2], A. S. Padampalle[3], D. D. Suryawanshi[4] and B. H. Pawar[5]
[1]Department of Physics, B. J. College, Ale, Pune
[2]Department of Physics Y.C.College, Sillod, Aurangabad
[3]Department of Physics S.C.S.College, Omerga, Osmanbad
[4]Department of Chemistry Dr. B.A.M.University Aurangabad
[5]Ex.Head, Dept. of Physics, S. G. B. A. U. Amravati

ABSTRACT

The rate of photosynthesis is determined by the intensity of incident radiation, the temperature in the neighborhood of the plant, the water contents and the density of the pigments present in plant leaves. The excess or deficient quantity of these parameters has direct influence on the photosynthesis rate. The excess or deficient quantity of the parameters responsible for the plant metabolism may be called as stress. It is very important to detect the stresses because they have direct influence on the plant health.We have studied combined effect of water and nutrient stresses in the plant Clitoria ternatea (Papilionaceae) by using fluorescence spectroscopy.

Keywords: Photosynthesis, He-Ne laser, Photomultiplier tube, Clitoria ternatea (Papilionaceae)

INTRODUCTION

One of the powerful techniques to detect the stress in the plant is the laser induced fluorescence kinetic method It is necessary to analyze the physiological state of plants growing over wide surfaces such as agricultural areas, forest and oceans. For biochemical analysis a collection of plants sample is necessary and it is also essential to know about the early detection of stress condition so that proper precaution may be taken and the plants may be saved from the unwanted damage. .(1-3)

SAMPLE PREPARATION

We selected the plants Clitoria ternatea (Papilionaceae) for performing experiment to study the fluorescence kinetics. The plants were developed under the condition of natural light and temperatures. Plants were well watered and regularly nourished and developed thoroughly in the washed river sand condition. After one month of the planting in the green house the plants were transferred in the open top chamber so that they get fresh air. A leaf is detached from the plant and immediately transferred to the laboratory for performing the experiment related to fluorescence. The flow of water and minerals from roots of the plants get stopped and the process of photosynthesis is also terminated and hence the plant leaf is under combined water, nutrient stress.

EXPERIMENTAL SET UP

For the study of the effect of short term combined effect of water and nutrients stress in the plant leaves, the experimental arrangement for recording fluorescence kinetics and fluorescence spectra are shown in fig.1 A He-Ne laser delivering 2 mw output power at 632.8 nm was used as an excitation source. An aluminium tube was fixed at the output end of the fiber to maintain a constant leaf area illumination. The light source illuminants 0.4 – 0.5cm2 area on the leaf and the observations are recorded at normal angle of incidence at a distance 0.1 cm from the leaf surface. The laser induced chlorophyll fluorescence spectra were analyzed using a jobin – Yvon H10DUV scanning monochromator. Fluorescence emission collected by the optical fiber was focused onto the entrance slit of the monochromator and detected by Hamamamstu R928 photomultiplier tube. (4-5)
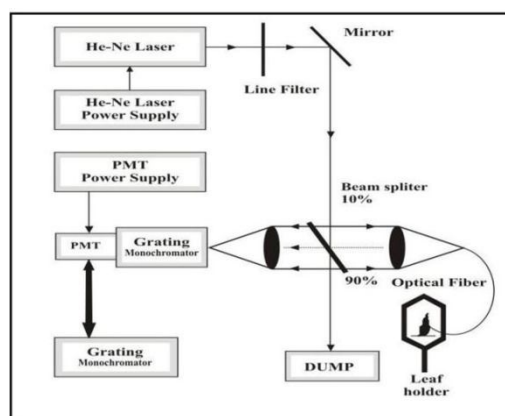
Figure-1: Experimental arrangement of He-Ne laser based system for recording LIF spectra of plant leaves.

RESULTS AND DISCUSSION

The experiment is carried out by He-Ne laser as an excitation source. Here the study of combined water and nutrient stress has been carried out by recording the fluorescence kinetics and fluorescence spectra of leaves. The fluorescence spectra and fluorescence kinetics of adaxial and abaxial surfaces are recorded at different timing by keeping plant leaf as it is in darkness immediately after detaching from the plant. When leaf is detached from the plant it will be under combined water and nutrient stress. The shapes of He-Ne laser induced chlorophyll fluorescence emission spectra are characterized by two maxima at about 685 and 730nm. The spectra delivered by both the surfaces of the leaf are recorded. Fluorescence kinetics at 685 nm and 730 nm and the fluorescence spectrum after immediately achieving steady state fluorescence. It is seen from the Fig. 2 that the intensity of fluorescence kinetics at 685 nm is more than that at 730 nm. It is observed that the steady state fluorescence condition reaches within about 5 min. After reaching steady state also the fluorescence spectrum exhibits the peaks at 685 and 730 nm. Peak height of the fluorescence spectrum of the fluorescence kinetics and fluorescence spectra after 20, 40, 60, 80 and 100 hours emitted by the upper surface are recorded. The comparison of the spectra clearly shows that the shape of the fluorescence kinetics changes with time. As the stress increases it will take more time for reaching steady state fluorescence. The observations clearly indicate that the time required for achieving steady state condition that could be used to measure the stress factor. It is obvious that by recording the time for reaching steady state fluorescence, we may remotely detect the stress stage condition of whole plant. [6-10]

CONCLUSION

In our study of short term combined water and nutrient stress it is concluded that peak height at 685 and 730 nm in the fluorescence spectra are the indicators of stress factors. As the shape of fluorescence kinetics takes horizontal form, it is said to be in the stress condition. The observations also shows that the steady state fluorescence is suitable tool for nutrients related stress in plants. The results also show that the laser induced fluorescence technique is very useful in vegetation. Further, it also shows that the laser induced fluorescence technique is very useful in vegetation remote sensing experiments.

Fig. 2 (a) Fluorescence kinetics at 685 and 730 nm (Time 0 hr)

Fig. 2 (b) Fluorescence kinetics at 685 and 730 nm (Time 20 hr)

Fig. 2 (c) Fluorescence kinetics at 685 and 730 nm (Time 40 hr)

Fig. 2 (d) Fluorescence kinetics at 685 and 730 nm (Time 80 hr)
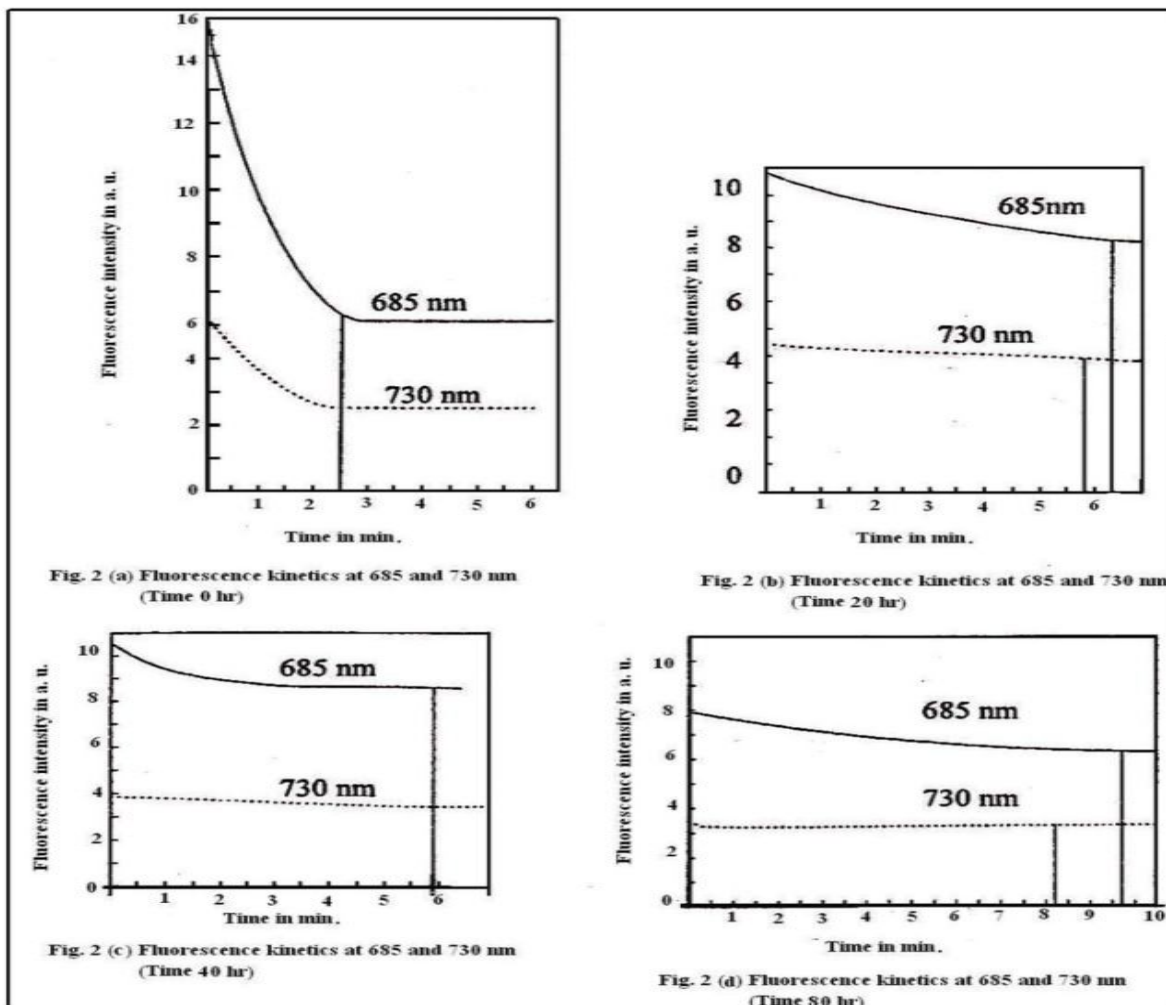
Figure-2: Comparative Characteristics of fluorescence kinetics at 685 and 730 nm upper surface of leaf.

REFERENCES

1. Subhash N. and Motianan c., " Remote detection of Nutrient stress in Groundnut plants by Deconvolution of laser induced Fluorescence spectra", IEEE, pp2323-2325, 1995.

2. Subhash N. et al. " Air pollution stress detection in plants by laser induced chlorophyll fluorescence." project report submitted to state council of science, technology and Enviorment, government of Kerala, Thiruvanthapuram, 2003.

3. Marinella Broglia, "Blue Green laser induced Fluorescence from intact leaves Actinic light sensitivity and subcelluar origin" , Applied optics, vol. 1, 32, no. 3, 1993.

4. Chappelle E. W. et al. " Laser induced Fluorescence green plants". Applied optics, 23, 134-138 1984.

5. Chappelle E. W. et al. " Laser may help in Remote assignment of vegetation " , Laser focus, 25(6), 123-132, 1989.

6. Subhash N. and Mohanan C., "Curve fit Analysis of chlorophyll fluorescence spectra": Application of Nutrient Stress Protection in sunflower Remot sens. Enviorn, 60, 347-350, 1997.

7. Lichtenthaler H. K.. "Laser induced chlorophyll fluorescence and blue fluorescence of green vegetation", proceedings 10th EP Sel symposium Toulouse, 1990.

8. Burtoskova H. et al., "The arrangement of chloroplasts in cells Influences the Reabsorption of chlorophyll fluorescence emission", The effect of Desiccation on the chlorophyll Fluorescence Spectra of Rhizominium punctatum leaves, vol.62 no. 2-3, 251-260, 1999.

9. Stresser R. J., Schwarz b., Eggenberg P., "Fluorescence Routine tests to describe the behavior of a plant in its environment. Application of chlorophyll fluorescence." Kluwer Acad. Publisher's pp. 181-187, 1988.

10. Chappelle E. W. et al., "Laser induced blue fluorescence in vegetation.", CH2825-8/90, pp. 1919-1922, 1990.

EFFECTS OF GAMMA RADIATION ON THE PROPERTIES OF POLYMETHYL ACRYLATE

R. R. Bhosale[1], P. S. Kore[2], D. V. Meshram[3], P. P. Pawar[4] and M. N. Rode[5]
[1]Department of Physics, Deogiri College, Aurangabad
[2,4]Department of Physics, Dr. Babasaheb Ambedkar Marathwada University, Aurangabad
[3,5]Department of Physics, Vaidyanath College, Parli-V, Beed

ABSTRACT
Mass attenuation coefficient (μ_m), effective atomic numbers(Z_{eff}), electron densities(N_{eff}),total cross-section(σ_t) & electronic cross-section(σ_e) have been computed for poly methyl acrylate using NaI (Tl) detector. Results of gamma radiation parameters such as μ_m, σ_t, σ_e, decreases with increasing gamma ray energy. Z_{eff} values of the polymethyl acrylate almost constant as a function of energy.It is clearly observed from the results that the polymethyl acrylate have good absorption capability of gamma photons in low energy region. We believe that some high Z elements dope with polymethyl acrylate may have potential applications in the shielding against gamma rays. An experiment has been done to investigate the new gamma ray shielding material that can be used at large scale and available easily having non-toxic.

INTRODUCTION
Since last few decades as the use of ionizing radiation increases in many fields such as medical field, structure modification, agriculture industry etc. The study on the effects produced by ionizing radiation on new materials for the dosimetry and radiation shielding is increased. As we know ionizing radiations are harmful for living tissues thus there is need to study and investigate a new gamma ray shielding material which can be used at large scale are nonhazardous and are inexpensive. Traditionally used lead shows neuro-toxicity. Many researchers studied and investigated the effects and properties produced by gamma-ray using various research methods [1-6]. Radiation damage in many materials studiedand investigated the results produced by it [9-10]. The poly methyl acrylate is C, H and O based low-Z material, which is tissue equivalent material and can be used as phantom to understand the radiation attenuation.

To study gamma-ray attenuation properties of materials the mass attenuation coefficient (μ_m) is the fundamental parameter to derive other parameters as atomic cross-sections (σ_t), electronic cross-sections (σ_e), effective atomic numbers (Z_{eff}) & effective electron densities (N_{eff}).

An attempt is made in the present work to check the availability of poly methyl acrylate as gamma ray shielding material and to find out its interaction properties using NaI (Tl) detector. The investigated results in the present work could be useful in the dose rate measurement and radiation shielding against gamma radiation.

EXPERIMENTAL
Radioactive sources having energies 122, 279, 320, 364, 637, 1115, 1408 keV were used for irradiation. The gamma ray photons were detected using NaI (Tl) detector with resolution of 0.101785 at 662 keV. Signals from the detector were enlarged and analyzed with 8K multichannel analyzer. The effectiveness of NaI (Tl) detector is higher at low source energy (Mohamed Abd-elzaher). The uncertainty in determined experiment is found to be 1-4 % (Mustafa RacepKacal) Topoly methyl acrylate as radiation target we use KBr press machine to prepare tablets having same thickness (0.13 g/cm2) and then filled in a cylindrical plastic container having the same diameter as that of sample tablets. To determine the diameters of these samples we use a traveling microscope. We done some experiment with the empty sample container and found that attenuation of photons of the empty containers were negligible. The experimental part is discussed in [8]. In this work mass attenuation coefficient (μ_m) , atomic cross-sections (σ_t), electronic cross-sections (σ_e), effective atomic numbers (Z_{eff}) & effective electron densities (N_{eff}).were calculated from formulas reported elsewhere [7-8, 11].

RESULTS AND DISCUSSION
The values of μ_m (cm2/g) are shown in figure 1, the values of μ_m from energy range 122 keV to 1170 keV decreases but from energy range 1115 to 11408 keV the values are constant. The σ_e, σ_t, Zeff, and Neff, values for poly methyl acrylate are shown in the table1.The values of all parameter studied initially decreased and then reached a constant value at higher photon energies as seen in table1. The experimental values were in good agreement with the XCOM values. From the values for effective atomic number of poly methyl acrylate depends on the number of elements in the materials.

Table-1: Gamma-ray parameters for poly methyl acrylate

PMA	122 keV		279 keV		320 keV		364 keV		637 keV		1115 keV		1408 keV	
	Exp.	The.	Exp.	The.	Exp.	The.	Exp.	The.	Exp.	The.	Exp.	The.	Exp.	The.
μ_m	0.1575	0.1564	0.1226	0.1219	0.1084	0.1071	0.1022	0.1031	0.0866	0.0850	0.0640	0.0649	0.0563	0.0571
σ_t	22.5054	22.3482	17.5185	17.4184	15.4894	15.3037	14.6035	14.7321	12.3772	12.1458	9.1450	9.2736	8.0448	8.1591
σ_e	5.8710	5.8300	4.5700	4.5439	4.0407	3.9923	3.8096	3.8432	3.2288	3.1685	2.3857	2.4192	2.0986	2.1285
Z_{eff}	3.8333	3.8264	3.8333	3.8231	3.8333	3.8219	3.8333	3.8213	3.8333	3.8204	3.8333	3.8194	3.8333	3.8191
N_{eff}	3.2192	3.2134	3.2192	3.2106	3.2192	3.2097	3.2192	3.2092	3.2192	3.2084	3.2319	3.2075	3.2192	3.2073
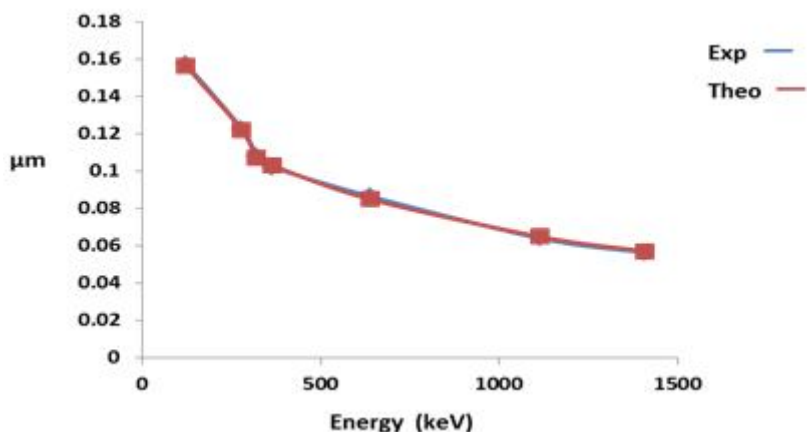
Fig-1: Variation of μ_m with photon energy

CONCLUSION

It can be concluded from the present work that the poly methyl acrylate used in this investigation shows significant attenuation of low energy photons and can find use as gamma ray shielding material in electronics industry, construction, plastic industry, and agriculture. The calculated and investigated values of poly methyl acrylate are useful in medical field.

REFERENCES

1. Chen, S.; Bourham, M.; Rabiei, A. Radiat. Phys. Chem. 2012, 96, 59–69.

2. D. Rezaei- Ochbelagh, S. Azimkhani. Applied radiation physics 70 (2012), 2282-2286.

3. Gaikwad, D.; Pawar, P.; Selvam, T. Pramana J. Phys. 2015.

4. H E Hassam, H M Badran, AAydarous and T Sharshar, NIM B 360 (2015) 81-89.

5. J. Zsigrai, Tam C N, Andrev B. NIM B. 2015. 359, 137-144.

6. Jean M, Francois B, W J Weber, Journal of Nuc. Materials. 2013, 440, 508-514.

7. R R Bhosale, D K Gaikwad, P P Pawar, M N Rode, Rad effects & defects in solids. DOI:10.1080/10420150.2016.119448

8. R R Bhosale, D K Gaikwad, P P Pawar, M N Rode. Nuclear technology & Rad. Protection. 2016, 31(2), PP. 135-141.

9. Singh, T.; Kaur, P.; Singh, P.S. Asian J. Chem. 2009, 21 (10), s225–228.

10. Singh, V.P.; Medhat, M.E.; Badiger, N.M.; SaliqurRahman, A.Z.M. Radiat. Phys. Chem. 2015, 106, 175–183.

11. Zhuo L, Luy, Zhao W, Yang C,Jiang J. polymer degradation & stability. (2016), doi: 10:1016/j. polymdegradstab.2015.12.015.

ELECTROCHEMICAL HYDROGEN EVOLUTION OF Ni DOPED ZINC FERRITE NANOPARTICLES PREPARED BY TAMARIND-MEDIATED SOL-GEL AUTO COMBUSTION

Ajinkya R. Phale[1], Ravindra Kamble[2], Amol Pansare[3], Vaishali Bambole[4]
[1]Department of Physics, University of Mumbai, Mumbai
[2, 3]Molecular electronics Lab, Department of Physics, Mumbai
[4]Department of Physics, University of Mumbai, Mumbai

ABSTRACT
M doped zinc ferrite (M= Ni)Zn0.5Ni0.5Fe2O4 nanoparticles have been green synthesized by tamarind-mediated sol- gel auto combustion technique and The structural and morphological properties of the prepared samples were characterized by X- ray diffraction (XRD), Field emission scanning electron microscopy (FEG-SEM), Field emission gun transmission electron microscopy (FEG-TEM) and Electrochemical properties of the nanoparticle at room temperature were studied by CH 660 Instrument.X-ray patterns confirmed the formation of single phase cubic structure with space group Fd-3m. The average crystallite size of Zn0.5Ni0.5Fe2O4 ferrite nanoparticles are found to be 27.8 nm. Further, the material was tested for hydrogen production through electrochemical hydrogen evolution. HER activity of nanocomposites was tested for hydrogen evolution at an applied potential of 0 to 2 V in acidic electrolyte. It shows themaximum current value is $1.27 \times 10\text{-}2A$ and also shows good exchange current density of 47.8 mAcm-2at over potential of 238.7mV and a Tafelslope of 114.7mVdec-1 for Zn0.5Ni0.5Fe2O4 ferrite nanoparticles.

Keywords: Tamarind-mediated synthesis, voltammetry, current charge density, Tafel Plot.

INTRODUCTION
In today's state of affairs, the most supply of energy throughout the planet principally depends on the fossil fuels like coal, gas and crude oil, however use of an equivalent ends up in atmospheric phenomenon so deteriorating theatmosphere. to cut back the greenhouse and environmental effects, hydrogen is taken into account joined of the foremost vital energy supply having blessingslike top quality, high energy density, clean energy fuel for many devices, environmentally friendly, made from An well-endowed renewable energy sources and is definitely a promising energy carrier for the long run. Mechanics of HER isn't straightforward because it depends on electrochemical conditions, wherever in multiple pathways will at the same time occur. Cathodic hydrogen evolution in acidic liquid media is accepted to take place in 3 steps.

$$\text{Tafel step} \quad : \quad H_2 \rightarrow 2Had$$

$$\text{Heysrovsky step} \quad : \quad H_2 \rightarrow Had + e- + H^+$$
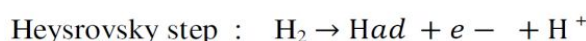
$$\text{Volmer step} \quad : \quad Had \rightarrow H^+ + e-$$

Hydrogen evolution reaction has been found out on various electrode materials in sight of effective ways of hydrogen production viz. lower potential and good kinetic characteristics. The overall reaction mechanism of the above fast reaction depends on several imperative kinetic parameter such as rate, exchange current density io (A/cm2) at a given temperature/pressure, its corresponding activation energy Ea(KJ/mol), anodic to cathodic transfer coefficients viz. tafel slope (mVper decade). All these parameter analysis would confirm the sort of the reaction viz. Tafel, Volmer and Heyrovsky and these reactions depend upon the over potential of H_2 production, that may be a key factor governing the reaction. An electrode for the electrochemical hydrogen evolution reaction (HER) should have basic properties such as massive active surface area,low over potential, electrochemical stability, selectivity, low cost, simple in use and sensible electrical conduction. The hydrogen evolution reaction [HER] could be a cathode based reaction via water electrolysis employing a catalyst albeit high-priced and therefore the value will be decreased with the employment of low-cost and affective catalysts. Thus, non-platinum active metals like Fe, Ni, Cu, Co further their alloys and composites are received an enormous as electrocatalyst for HER due to their value cost and smart activity. Glassy carbon electrodes (GC) are most commonly used in electrochemistry in aqueous acid-base medium compared to metallic electrode because it features along life time.

RGO-magnetic hybrids are developed for wide selection of applications, iron-basedspinel oxides like Fe_3O_4 and ferrite with general formula AFe_2O_4 (A = Zn, Ni, Co, Mn) with low price have been extensively studied as anode materials as electro catalysts. Spinel transition metal oxides with two metal elements provide the

practicability to tune the energy density and dealing voltage by changing the metal content MFe_2O_4 (M =Co, Ni, Cu, etc.) Represent a very importantcategory of spinel oxides that exhibit a broad range of fascinating physical and chemical properties, giving several intriguing merits such as the rich redox chemistry, excellent biocompatibility, high electronic conductivity, good superparamagnetic properties, low toxicity, easy preparation, high adsorption ability, low price, and abundant resources has potential applications in super capacitor, Li ions batteries, semiconductor photo catalysts, biosensor devices and medical applications. Such spinel ferrites possess vitalelectrocatalytic activity and stability in high pH however its low electrical conductivity restricts its application in a catalyst. In general, the sensible applications of ferrites chiefly rely on electronic conductivity, as a result of thermal activation of electrons or positive holes along the chains of neighbouring cations in the ionic lattice. Potential application energy storage Studies have mention that the charge transfer happened via hopping processes between cations of variousvalencies, which needs comparativelylower activation energies, wherein O forms the face centered cubic (fcc) packing with M(II) occupying the octahedral (O) interstitial site and Fe(III) distributed equally within the O and tetrahedral (T) sites. Such a structure has shown smart electrical conductivities because of the electron hopping between completely different valence states of metals in O-sites and additionally provides necessary surface redox active metal centers for the adsorption and activation of electroactive species. In view of all the above factors, this report has been targeted on the development of M doped ferrites as composite materials and further been tested as an electro catalyst towards hydrogen evolution reaction (HER). The developed materials was investigated by FESEM, XRD, and TEM to grasp its structural features and further exploited by various electrochemical tests like cyclic voltammetry, linear sweep voltammetry, electrochemical impedance spectroscopy and tafel analysis to review the impact of the ferrite composites towards HER reaction.

2. EXPERIMENTAL DETAILS
2.1 Synthesis of $Zn_{0.5}Ni_{0.5}Fe_2O_4$ Ferrite Nanoparticles
All of the chemical reagents were purchased from business suppliers and used withoutfurther purification. These reagents enclosed iron nitrate $[Fe(NO_3)_3 \cdot 9H_2O]$ and nickel nitrate $[Ni(NO_3)_2 \cdot 6H_2O]$, Zinc nitrate $[Zn(NO_3)_2 \cdot 6H_2O]$, that were purchased from Sigma Aldrich. The extremely pure tamarind juice is used as a part of green synthesis, stoichiometric amounts of $Ni(NO_3)_2.6H_2O$, $Zn(NO_3)_2 \cdot 6H_2O$ and $Fe(NO_3)_3.9H_2O$ were dissolved in distilled water to obtain a mixed solution. The molar quantitative relation (ratio) of $Ni(NO_3)_2.6H_2O$ and $Zn(NO_3)_2 \cdot 6H_2O$ to $Fe(NO_3)_3.9H_2O$ was 1:2. The metal nitrates were dissolved together with the minimum quantity of double-distilled water required to get a transparent solution. An aqueous solution of lime water was then mixed with the metal nitrate solution. The mixed solution was placed on a hot plate with continuous stirring at $100^{o}C$. Throughout evaporation, the solution formed a viscous gel. The gel was then heated to $350^{o}C$ to start a self-sustaining combustion reaction and to produce an as-burnt ferrite powder. The important constituents of tamarind juice, i.e. citric acid. Oncethe metal zinc ferrite gel precursor was heated at a temperature of $350^{o}C$, the decomposition the release of nitrogen and carbon dioxide gases, and the final product comprising $Zn_{0.5}Ni_{0.5}Fe_2O_4$ ferrite nanoparticles powder was formed. Finally, the as-burnt powders were annealed in a furnace underneath an air atmosphere at $1200^{o}C$ for 2 hrs.
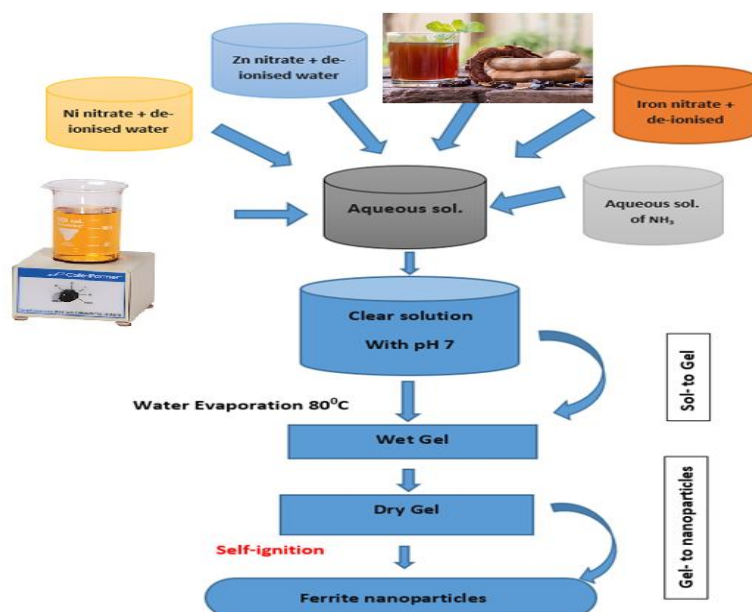
Fig-1: Flow chart for the synthesis of $Zn_{0.5}Ni_{0.5}Fe_2O_4$ Ferrite Nanoparticles

3. CHARACTERIZATION
3.1 X- ray Diffraction Analysis
Figure 2 (a) shows the XRD pattern of $Zn_{0.5}Ni_{0.5}Fe_2O_4$ Ferrite Nanoparticles and XRD analysis confirmed the formation of a spinel structure in the synthesized samples. All of the diffraction peaks agreed well with the standard JCPDS data (54-0964) for MFe_2O_4 (M = Ni, Co, Zn, Mn). The Average crystallite size (D) of $Zn_{0.5}Ni_{0.5}Fe_2O_4$ was determined from the full width at half maximum of the (220), (311), (222), (400), (422), (511), and (440) XRD peaks using the well-known Debye–Scherer equation

$$D = \frac{k\lambda}{\beta cos\theta} \qquad (1)$$

Where k is the grain shape factor (0.9) and λ, θ, and β are the X-ray wavelength, Bragg diffraction angle, and full-width at half-maximum of the diffraction peak, respectively. The value of average crystallite size of $Zn_{0.5}Ni_{0.5}Fe_2O_4$ ferrite nanoparticles was found to be **27.8 nm**respectively.
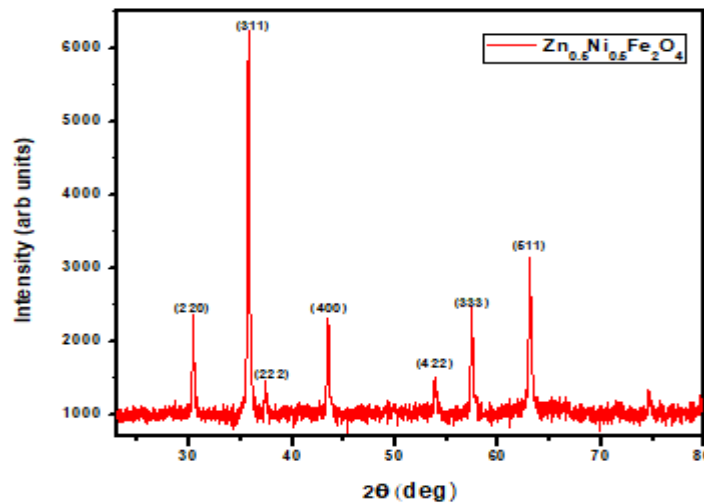
Fig-2 a) XRD Patterns of $Zn_{0.5}Ni_{0.5}Fe_2O_4$

3.2 Morphology Investigation
Fig.3shows the cuboidal structure of $Zn_{0.5}Ni_{0.5}Fe_2O_4$ ferrite nanoparticles of size is about 12-56 nm. Recently, reported the octahedron morphology of $Zn_{0.5}Ni_{0.5}Fe_2O_4$ ferrite nanomaterial synthesized employing the single gentle hydrothermal method at 160^oC without any surfactant. Moreover, found that ferrite nano-octahedrons will be ready employing a cost-efficient and facile hydrothermal method. In the present study, we have a tendency to find out the nano-octahedron morphology of $Zn_{0.5}Ni_{0.5}Fe_2O_4$ ferrite nanomaterial synthesized using a tamarind-mediated sol-gel combustion method. Figures 3 show FE-SEM images of the $Zn_{0.5}Ni_{0.5}Fe_2O_4$ spinel ferrite octahedron nanoparticles synthesized by tamarind-mediated sol-gel combustion and those subsequently annealed at 1200^oC. Histograms of the size distributions are shown as insets in Figures The as-synthesized $Zn_{0.5}Ni_{0.5}Fe_2O_4$ spinel ferrite octahedron nanoparticles measured 12-56 nm, The size distributions obtained were consistent with the crystallite size determined in the XRD study. In general, the kinematics of the crystal growth along different crystal directions determines the morphology of the final product.
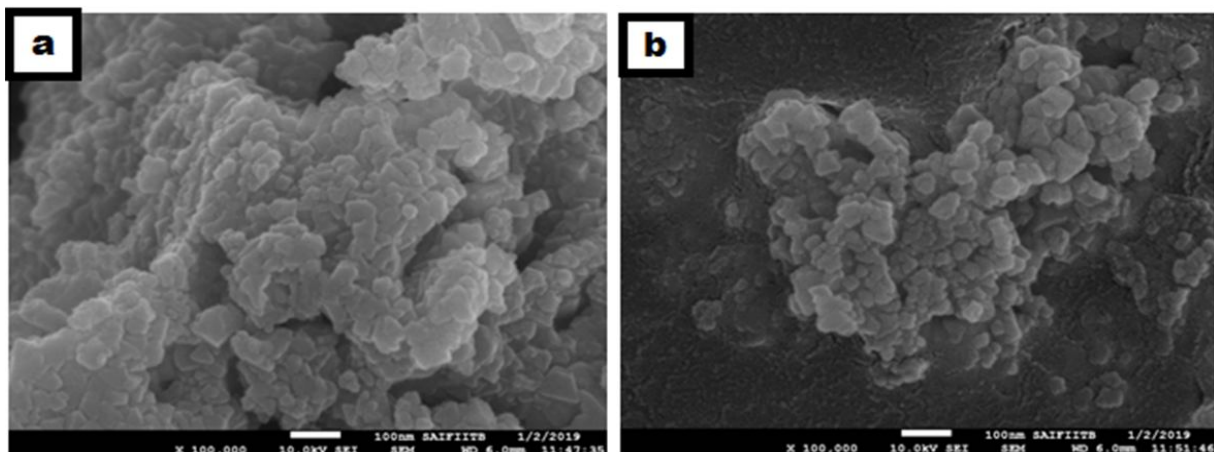
Fig-3(a & b)FEG-SEM images$Zn_{0.5}Ni_{0.5}Fe_2O_4$ ferrite nanoparticles

The average particle size of the $Zn_{0.5}Ni_{0.5}Fe_2O_4$ ferrite nanoparticles were calculated using FEG-TEM images, which are shown in fig.4 The average particle size were found in the range of **21-58 nm**, which is calculated using Image-J software and matched with XRD and SEM images.
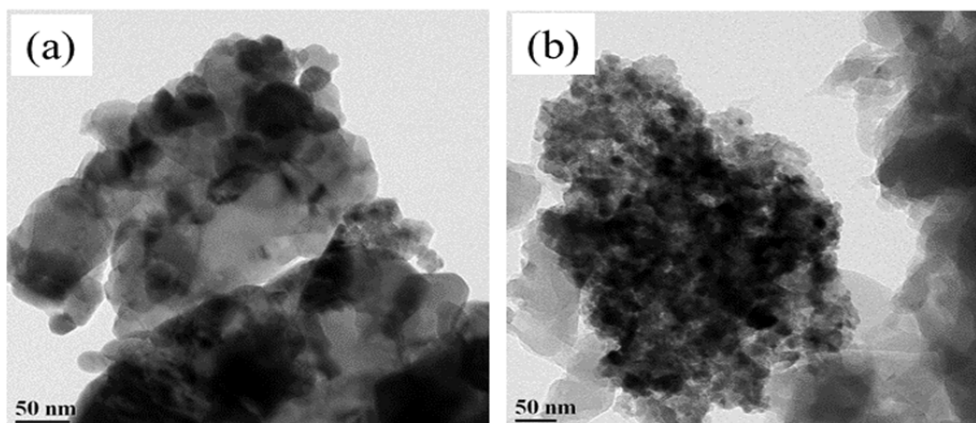
Fig-4: (a& b)FEG-TEM images of $Zn_{0.5}Ni_{0.5}Fe_2O_4$ ferrite nanoparticles.

3.3 Electrochemical Properties

CHI 660C electrochemical workstation is employed for electrochemical measurements. All the experiments were performed at normal room temperature with a conventional there electrode electrochemical cell setup; Pt electrode employed as counter electrode, Ag/AgCl as reference and $Zn_{0.5}Ni_{0.5}Fe_2O_4$ nanocomposites as operating electrodes respectively. The electrochemical measurements were carried out in aqueous solutions, where analytical reagents and deionised water was always used. Freshly prepared 0.5M H_2SO_4 solution employed as a test electrolyte. The polarization experiments viz. cyclic voltammetry, linear sweep voltammetry and electrochemical impedance measurements were carried out as test experiments. The potentials were measured against and referred to RHE electrode. The impedance was recorded in the frequency domain of 0.1Hz to 10^5 Hz at an applied voltage of 0.1V. To achieve reproducibility, each experiment was carried out at least thrice and average values are reported.

3.3.1 Preparation for Electrochemical Measurements

We are using glassy carbon electrode as a working electrode and for better electrochemical performance we add sodium borohydride as a reducing agent,so we are preparing $Zn_{0.5}Ni_{0.5}Fe_2O_4$ Nanocomposite operating electrode.

3.3.2 Preparation of $Zn_{0.5}Ni_{0.5}Fe_2O_4$ **Nanocomposite were sodium borohydride as a reducing agent.**

We are taking 0.3 gm of $Zn_{0.5}Ni_{0.5}Fe_2O_4$ Nanocomposite and add it into 100 ml de-ionized water and sonicate the solution for 30 minutes or up to well dispersed. Once the nanocomposite is completely dissolved we add 3 gm of sodium borohydride $NaBH_4$ and allow the solution 12 hrs. for stirring in magnetic stirrer after stirring filter the solution 3 to 4 times by de-ionized water up to we get clear water. Once we get the clear water wash or filter the composite with ethanol and dry the composite by keeping it in a vacuum Owen. Our $Zn_{0.5}Ni_{0.5}Fe_2O_4$ / $NaBH_4$ Nanocomposite is ready to use it as working electrode in the electrochemical measurements.

3.3.3 Preparation of $Ni_{0.8}Mn_{0.2}Fe_2O_4$ or $Co_{0.7}Ni_{0.3}Fe_2O_4$ Nanocomposite operating electrode.

We are taking Glassy carbon electrode as a working electrode, now applying the $Zn_{0.5}Ni_{0.5}Fe_2O_4$ Nanocomposite on a glassy carbon electrode and use the Nafion as a binder. First apply the sufficient amount Nafion on glassy carbon electrode with the help of dropper and keep it in front of IR lamp for dry take care that Nafion will not spared outer side of glassy circle of electrode similarly apply the stoichiometric amount of $Zn_{0.5}Ni_{0.5}Fe_2O_4$ Nanocomposite on a glassy carbon electrode and again keep it in front of IR lamp for dry take care that Nanocomposite will not spared outer side of glassy circle of electrode.

3.3.4 Electrochemical hydrogen evolution

1. Voltammetric studies

Cyclic voltammetry (CV) test was picked for characterization of the prepared composite materials towards hydrogen evolution reaction and the relating plots are given in Fig.5. Cyclic Voltammetry curves were recorded from 0 to 2 V at a scan rate of 100 mV/s. As saw from the figure, the fast increment in the cathodic current was related with the oxide reduction followed by H+ intercalation and the corresponding anodic current peak was due to the DE intercalation process. In this manner cyclic voltammetry results showed the best catalytic activity of the ferrite based composites for HER reaction. Both the modified electrodes clearly showed an increment in magnitude of current and positive potential shift with respect to the bare electrode, which affirms the electro catalytic activity of $Zn_{0.5}Ni_{0.5}Fe_2O_4$ Nanocomposite towards HER.
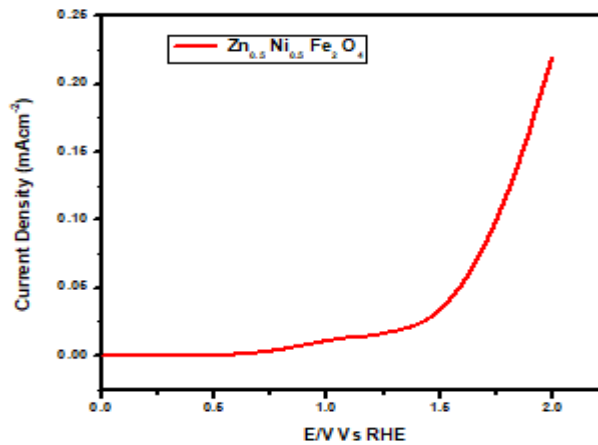
Fig-5: Cyclic voltammetry of $Zn_{0.5}Ni_{0.5}Fe_2O_4$ Nanocomposite at a scan rate of 100 mV/S in 0.5 M H_2SO_4
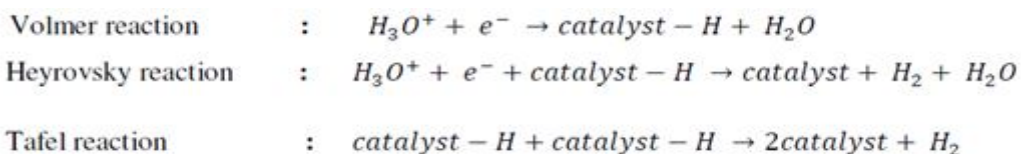
2. Polarization test analysis

To methodically study the electrochemical activity of the catalyst, steady state polarization curves of HER for the catalyst were measured. Polarization is a technique used for the investigation of hydrogen evolution reaction, (HER) which is the generation of H_2 gas through water electrolysis. The electro catalytic activities of $Zn_{0.5}Ni_{0.5}Fe_2O_4$ nanocomposites were assessed in 0.5M H_2SO_4utilizing a three probe electrode framework and the relating polarization curves of the composites are given in Fig. 5 estimated at a scan rate of 100mV/s. As determined from the analysis, the **maximum current** value is $\mathbf{1.27 \times 10^{-2}}$ **A** for $Zn_{0.5}Ni_{0.5}Fe_2O_4$ and the **onset potential** (initial potential for H_2 evolution) of $Zn_{0.5}Ni_{0.5}Fe_2O_4$ is **0.516 V**, which are relatively higher than observed for general ferrites (-1.01 V) and bare GC electrode (-1.06 V). The composites exhibited a rather completely different catalytic activity, which could be due to the electron transfer capability of the nanocomposites. When we go ahead and extrapolate of the Tafel plot to the current axis gives the **exchange current density47.8 mAcm^{-2}**. Subsequently the outcomes uncovered that both the nanocomposites demonstrated a low onset potential and a quickly increasing current density within the applied potential [-1.2 to 2 V]. Therefore the great electro catalytic behavior of the composite materials may emerge from the synergetic impact of the exposed active sites given by the ferrite/graphene composites and graphene, which in turn could promote quick electron transport.Tafel plots got from over potential versus log current density (η vs. log j) are appeared in Fig.6 which could be exploited for the quantitative kinetics analysis of HER. The linear regions of the Tafel plots were fitted into the Tafel equation.

$$\eta = a + b \log j$$

$$\eta = \frac{2.3}{\alpha F} \log j_o - \frac{2.3}{\alpha F} \log j$$

In which we have η is the overpotential, j_o is exchange current density, R is the ideal gas constant (8.314 J mol^{-1}K^{-1}), T is the absolute temperature and F is the Faraday constant. The value of Tafel slope (b), J_o and transfer coefficient (α) are shown in Table 1. It is commonly acknowledged that there are three principle steps for converting named H+ to H_2 for HER in acidic medium, usually named as Volmer, Heyrovsky and Tafel reaction. The previous includes the electrochemical reduction steps, the second either an ion or atom reaction and the third is the atom combination reaction. Inside a specific arrangement of conditions, when the Volmer reaction is the rate deciding step of HER, the Tafel slope is may be in the range of 120 mV/dec^{-1} (with α, charge transfer coefficient value being around 0.5). At the point when the rate-limiting step is the Heyvosky or the Tafel-step, the slope would be in the vicinity of 40 mVdec^{-1} and 30 mVdec^{-1} with α value being 1.5 and 2.0 respectively.

Volmer reaction	:	$H_3O^+ + e^- \rightarrow catalyst - H + H_2O$
Heyrovsky reaction	:	$H_3O^+ + e^- + catalyst - H \rightarrow catalyst + H_2 + H_2O$
Tafel reaction	:	$catalyst - H + catalyst - H \rightarrow 2catalyst + H_2$

On account of ferrite based composites, the **Tafel slope** values were determined to be **114.7 mVdec^{-1}**for $Zn_{0.5}Ni_{0.5}Fe_2O_4$ with cathodic **transfer coefficient (α)** value being **0.16** respectively and subsequently it could be concluded that the HER mechanism of ferrite catalyst follows the Volmer reaction. The determined values are given in Table 1.
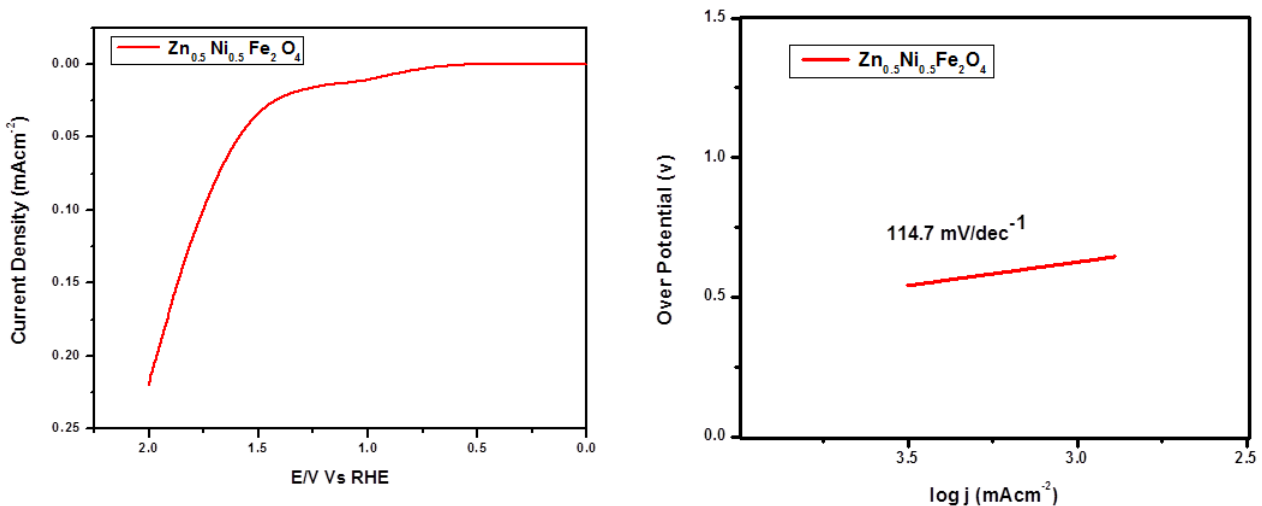
Fig-6: Linear sweep voltammetry&Tafel plot of $Zn_{0.5}Ni_{0.5}Fe_2O_4$ Nanocomposite

Table-1: Tafel slopes and Exchange current density values for HER using $Zn_{0.5}Ni_{0.5}Fe_2O_4$Nanocomposite

Catalyst	$-logj_o$mA/cm^{-2}	b mV/dec^{-1}	A	η (mV)
$Zn_{0.5}Ni_{0.5}Fe_2O_4$	47.8	114.7	0.16	238.7

3. Cycle stability test for Nanocomposite

The long term stability test for nanocomposite was performed and the outcomes are shown in Figure 7(a)$Zn_{0.5}Ni_{0.5}Fe_2O_4$ catalysts based electrodes were constantly cycled for 1000 cycles in 0.5M H_2SO_4 at a scan rate of 100 mV/s .The current density remained unchanged even after 1000 cycles for $Zn_{0.5}Ni_{0.5}Fe_2O_4$, there was a minor decrease though it was marginal. This slight difference is because of H+ or H2 bubbles on the surface of the electrode that delays the reaction in both nanocomposites indicating greatdurability of this catalyst in acid solution.

4. Electrochemical impedance spectroscopy

To additionally sanction the electrode kinetics, electrochemical impedance spectroscopy (EIS) was recorded for ferrite composites. EIS was performed at a potential of 0.1 V vs. Ag/AgCl and the equivalent is given in Fig.7 (b) In the Nyquist plot, the X and Y axes symbolizes the real and negative imaginary parts of impedance. The **charge transfer resistance (Rct)** for hydrogen evolution of $Zn_{0.5}Ni_{0.5}Fe_2O_4$ is**22.4** which is attributed to the semicircle recorded at the indistinguishable over potential at 0.1 V in the frequency range 0.1 Hz to 10^5 Hz. From the frequency (f*) corresponding to the maximum of the imaginary component (– Im Z'') of the semicircle, the time constant (T) is calculated by using the equation In this experiment modified electrode/electrolyte interface of the nanocomposite is lower in double layer capacitance and hence subsequently increased the charge transfer resistance of hydrogen evolution.

T = 1/2πf*

The **time constant** was less, and was calculated to be **3.13×10^{-5}s** for $Zn_{0.5}Ni_{0.5}Fe_2O_4$ nanocomposite.
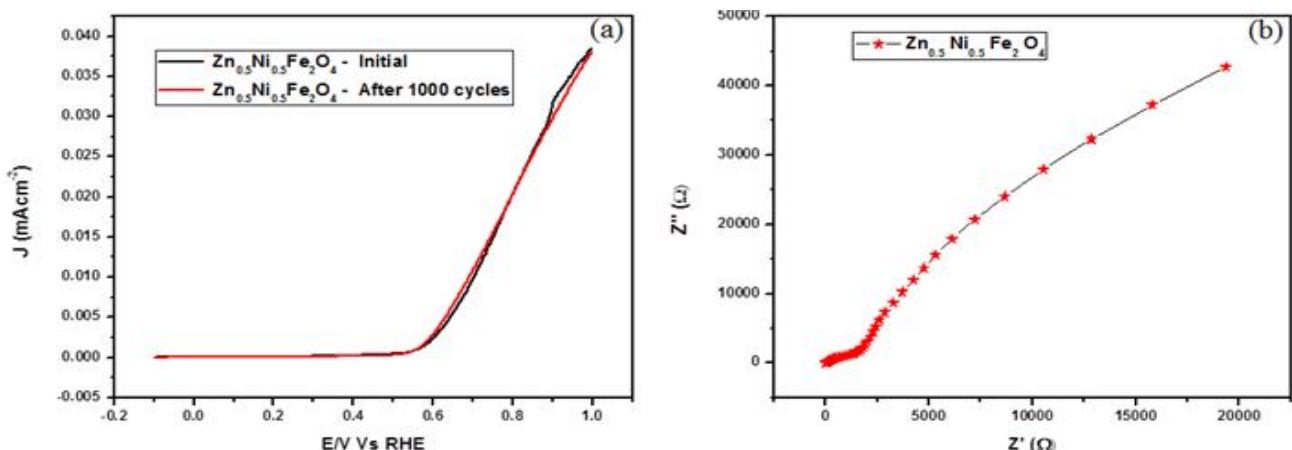
Fig-7 (a) Cyclic stability test for $Zn_{0.5}Ni_{0.5}Fe_2O_4$ in 0.5M H_2SO_4 at a scan rate of 100 mV/s

(b) Nyquist plot of $Zn_{0.5}Ni_{0.5}Fe_2O_4$ electrodes by applying a sine wave with amplitude of 0.1 V over the frequency range from 0.1 Hz to 10^5Hz.

5. CONCLUSION

Taking everything into account, $Zn_{0.5}Ni_{0.5}Fe_2O_4$ nanocomposite was synthesized by a green synthesis method and further examined for their electrochemical action towards hydrogen evolution reaction (HER). Outcomes demonstrated that both the nanocomposites exhibited highly electrocatalytic activity towards HER in acidic medium. As observed from the analysis, the **maximum current** value is $\mathbf{1.27 \times 10^{-2}A}$, **An exchange current density** of **47.8mAcm^{-2}** at an **over potential** of **238.7 mV** observed for $Zn_{0.5}Ni_{0.5}Fe_2O_4$. A Tafel slope of **114.9 mV/dec^{-1}** showed that the reaction followed Volmer mechanism.

Further EIS measurements demonstrated a less charge transfer resistance for $Zn_{0.5}Ni_{0.5}Fe_2O_4$ composite and hence overall outcomes indicated that M doped Zinc ferrite $Zn_{0.5}Ni_{0.5}Fe_2O_4$ based composite is a better electrocatalyst towards HER. Thus $Zn_{0.5}Ni_{0.5}Fe_2O_4$ nanocomposites as electrocatalyst could be proposed as a good candidate for HER.

REFERENCES

1. S .Lewis **"Light work with water"** *Nature* vol: 414,**Pg: 589-590, (2001).

2. R .Solmaz, G. Kardas." Fabrication and characterization of NiCoZn-M (M: Ag, Pd and Pt) electrocatalysts as cathode materials for electrochemical hydrogen production". *IntJHydrogen Energy v*ol: 36, pg.: 12079-87, (2011).

3. R.M .Navarro, M.A. Pena, J.L.G. Fierro," Hydrogen production reactions from carbon feedstocks: fossil fuels and biomass", *Chem. Rev*,vol :107, pg:3952–3991,(2007).

4. M.H. Miles, "Evaluation of electrocatalysts for water electrolysis in alkaline solutions", *J.Electroanal. Chem. Interfacial Electrochem*. vol:60,pg: 89–96,(1975)**.

5. C . Lupi, A,DellEra,M . Pasquali, "Nickel-cobalt electrodeposited alloys for hydrogen evolution in alkaline media", Int. J. Hydrogen Energy vol:34, pg:2101–2106,(2009).

6. Y.R. Dar, P .Vijay, M.O. Tadé, R .Datta.," Improved Tank in Series Model for the Planar Solid Oxide Fuel Cell" *J. Electroanal. Chem*. vol: 50,pg: 1056–1069, (2012).

7. N.S.Lewis, D.G.Nocera," A Perspective on Forward Research and Development Paths for Cost-Effective Solar Energy" *Chemsuschem* ,vol : *2*, pg: 383-386 (2006).

8. AA. Abdul, BH. Hanaa., MA. Abdul Rahim." Nanostructured Ni/P/TiO$_2$ composite coatingsforelectrocatalytic oxidation of small organic molecules". *J ElectroanalChem*vol; 620, pg: 517-526, (2008).

9. T.Y.Chen, Y.H Chang, C.L .Hsu, K.H .Wei., C.Y. Chiang, L.J. Li," Comparative study on MoS$_2$ and WS$_2$ for electrocatalytic water splitting", *Int. J. Hydrogen Energy*vol :38, pg:12-32,(2013).

10. RL. Creery. "Advanced carbon electrode materials for molecular electrochemistry". *ChemRev*vol: 108, pg: 2646–87, (2008).

11. 11.J.L. Tang, Y. Zuo, "Study on corrosion resistance of palladium films on 316Lstainless steel by electroplating and electro less plating", *Corros. Sci.*vol:50, pg.: 2873–2878, (2008).

12. R. S. Sai Siddhartha**, "**Spot-free catalysis using gold carbon nanotube & gold graphene composite For hydrogen evolution reaction". *Journal of power Sources*vol: 288,pg:441-450,(2015).

13. S. Wirth, F. Harnisch, M. Weinmann and U. Schroder, "Electrocatalytic H$_2$ production from seawater over Co, N-codopednanocarbons" *Nanoscale*, , vol:7,pg: 2306-2316,(2015).

14. M. H. Tang, C. Hahn, A. J. Klobuchar, J. Wellendorff, T. Bligaard, andT. F. Jaramillo, "Nickel– Silver alloy electrocatalysts for hydrogen evolution and oxidation in an alkaline electrolyte",Phys*Chem. Phys.*,vol :16**,**pg:19250-19257,(2014).

15. J. R. Kitchin, J. K. Norskov, M. A. Barteau and J. G. Chen," Modification of the surface electronic and chemical properties of Pt(111) by subsurface 3d transition metals" *J. Chem.Phys*.vol**:**120**,**pg: 10240 (2004).

SYNTHESIS AND TSDC STUDY IN PURE AND DOPED POLYSULFONE FOILS

Pooja Devi Sahu and P. K. Khare

Department of Post Graduate Studies and Research in Physics and Electronics, Rani Durgavati Vishwavidyalaya, Jabalpur

ABSTRACT

The polymer used in the present work was PSF, while the dopant malachite green was dye. Foils prepared by isothermal immersion technique.Thermally stimulated depolarization currents(TSDCs) in short circuit mode in pure and doped malachite green (MG) Polysulfone (PSF) foils have been recorded. TSDC measurements have been considered to be helpful to understand the effect of space charge behavior, relaxation behavior in polymers.TSDC measurements were carried out on such samples at temperature range in 45, 55, 65, and 75^oC at various field 60, 90, 120, 150 $kVcm^{-1}$ by monitoring the current from 45^oC -160^oC.PSF and MG used for the present study were supplied by Glexo Leb. Bombay.

Keywords: TSDC, CTC, polarization, Polysulfone, malachite green.

INTRODUCTION

Polymer films which are polarized in strong electric field at an elevated temperature and are cooled with the field on, show semipermanent electric polarization which persists for years at room temperature, they are called polymer electrets (1). One of the most widely used method for investigating the parameters of localized energy levels in dielectric materials is the technique of thermally stimulated current (TSC) (2) .Polymer materials have been considered to be good insulators, because their predominant covalent bonds exhibit law electroconductivity. The compounds so obtained are colourless (the luco compounds) and are converted on oxidation into the colour base which gives malachite green. Both strong acid and base cause the colour of malachite green (3).

EXPERIMENTAL PROCEDURE

The solution cast technique was utilized for preparing pure and malachite green doped Polysulfone (PSF) samples. The solution was prepared in a glass beaker by dissolving PSF (3gm) and malachite green (3mg and 5mg by weight respectively) in chemically pure dimethyl formamide (DMF). The solution was kept for 24 h to get a homogeneous and transparent solution. The solution thus prepared was then poured onto an optically plane cleaned glass plate floating on mercury. The solvent was allowed to evaporate in an oven at 600 ^0C for 24 h to yield the desired samples.

RESULT AND DISCUSSION

The experimental condition under which the thermally stimulated discharging current were measured are summarized below.

Polarizing field (Ep)	-	60, 90, 120 and 150kV
Polarizing temperature (Tp)	-	45^0C
Heating rate	-	3^0C/min
Electrodes	-	Aluminium (both side)

The thermally stimulated discharge current (TSDC) spectra for pure and doped Polysulfone (PSF) foils polarized with polarizing temperature 45^oC at different polarizing voltages 60, 90, 120 and 150kV are illustrated in figure 1and 2 for similar electrodes (i.e. Al -Al).
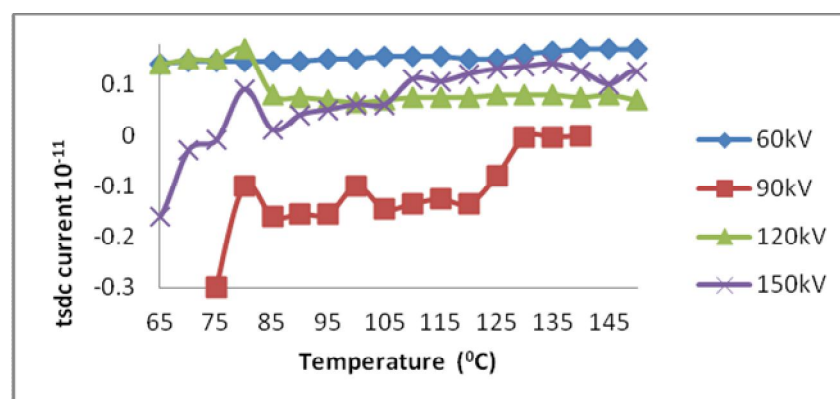
Figure-1: Thermally stimulated depolarization current of Polysulfone (PSF) sample with a 45^oC at various voltages 60, 90, 120 and 150kV**.**
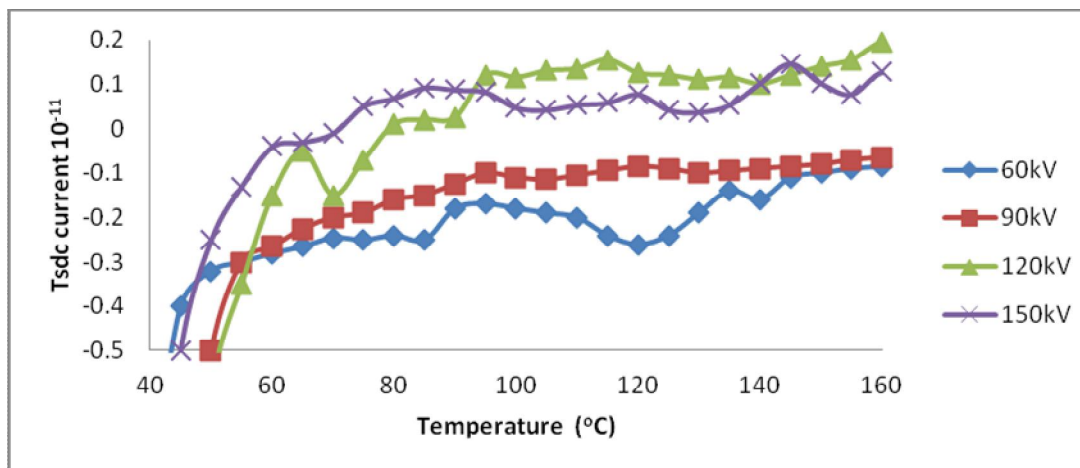
Figure-2: Thermally stimulated depolarization current of malachite green doped Polysulfone (PSF) sample with a 45°C at various voltage 60, 90, 120 and 150kV.

In figure 1 are showing two TSDC peaks, one at low temperature (β peak) at 80° C, which is associated with dipolar relaxation and other at higher temperature (α peak) at 130 – 145° C that appears due to space charge relaxation (4). Further, TSDC curves are characterized by a high value of initial current. The peak position is independent of the polarizing field. However, the TSD current as well as the peak current initially decreases with increase in the polarizing field, then increases for high values of polarizing field but finally again decreases for still higher values of polarizing field.

The TSDC studies on malachite green sensitized films weremade in usual manner as that of pure PSF.The effect of sensitizer on the polymer matrix was studied.Khare et al have reported TSDC studies on pure andsensitized films, the peak temperature and charge retainingcapacity was found to alter with different sensitizers [5].The addition of sensitizer has a strong effect on the temperature, (peak) is shifted towards the lower temperature is60 - 65°C to the discharging process. The peak angle is decreases upon sensitization with malachite green in PSF matrix (6).

CONCLUSIONS
The results are explained in terms of the energy levelscreated by the sensitizers and charge transfer through atunneling mechanism.The peaks values evaluated in the present investigations are found to be lower for the pure films. Formation of CTC results in the reduction of the crystalline amorphous interface and provides conducting paths through the amorphous regionsby interconnecting the crystallites.

REFERENCES
1. J Van Turnhout Thermally Stimulated Discharge ofPolymer Electrets (Amsterdam : Elsevier) (1975).

2. P. K. Khare , Gautama bangre, Pankaj Mishra and Joyti mishra Indian J. Phys. 82 (10) 1301-1308 (2008).

3. F. Gutman, and L. E. Lyons, Organic Semiconductors. John Wiley And Sons, NewYork, (1967), 434-484**.**

4. Pooja. Saxena,, M. S. Gaur, Prashat Shukla, and P. K. Khare; Journal of Electrostatics **66** (2008) 584 – 588.

5. Khare, P. K., Indian J. Pure Appl. Phys. 32, 160 (1994).

6. P. K. Mishra, J. Mishra, R. Kathal, H. Pandeyand P.K.Khare AIP Conference Proceedings **1512**, 792 (2013).

TSDC STUDY OF PURE AND DOPED POLYVINYL ACETATE

Pooja Devi SahuO[1]. P. Bagri[2] and P. K. Khare[3]
[1,3]Department of Post graduate Studies and Research in Physics and Electronics, Rani DurgavatiVishwavidyalaya, Jabalpur
[2]Pt. Deendayal Upadhayay Govt. College, Begumganj, Raisen

ABSTRACT
Thermally stimulated discharge current (TSDC) in pure and malachite green doped polyvinyl acetate (PVA$_C$) were studied as a function of the voltage (250, 400, 550 and 700 volts), temperature of polarization 40^0C and the amount of doping 5mg respectively. For pure PVAc and 5 mg malachite green sensitized PVAc samples two relaxation processes are observed around at $50 – 70\ ^0C$ and $110 – 125\ ^0C$ respectively and they are designated as β and α relaxation and have been attributed to the motion of the dipole under the effect of external electric field. The β relaxation accompanied with small activation energy is due to the rotational motion of the long flexible side groups/dipoles.

Keywords: Polyvinyl Acetate (PVAc), malachite green, thermally stimulated depolarization current, dipolar polarization.

INTRODUCTION
The thermally stimulated discharge current (TSDC) has become one of the most powerful tools for investigating electric properties of polymers and other dielectric materials (1-3).One of the most widely used method for investigating the parameters of localized energy levels in dielectric materials is the TSDC technique (4). Gross (5)put forward two charge theory which explains the effect in polar dielectric in terms of the orientation of electric dipoles under the influence of electrical and thermal activation however in the case of non-polar dielectrics additional factors such as trapping and accumulation of charge carries have to be taken into account. The method involves heating a polarization temperature, the release of charges is gradually speed up and when the half-life of this process become comparable with the time scale of the experiment (determined by the heating rate) discharge becomes measurable and gives rise in the external circuit to a current which first increases with increasing temperature and then decay when the supply of charge is depleted. A current peak thus will be observed at a temperature where dipolar disorientation ,ionic migration or carrier release from traps is activated and as the total polarization usually arise from a combination of several individual effects with various relaxation times a complete picture of the temperature-dependent relaxations will in principle be obtained. The TSDC method is however more sensitive and owing to its low equivalent frequency the resolution is usually much better.The process taking place during TSDC is similar to those occurring during charging but they behave in an opposite way. The charge of a thermo-electret arises from aligned dipoles and trapped excess charges (6).

Poly Vinyl Acetate (PVAc) is rubbery synthetic polymer and it is prepared by polymerization of vinyl acetate monomer, exhibiting piezoelectric, pyro-electric and ferroelectric properties. The typical advantages of PVAc are its flexibility, formability and low density.

Malachite green (7) is an azo-dye. Azo-dyes are the largest class of synthetic dyes. Their chromophore is an aromatic system joined to the azo-group. These dyes are obtained by the introduction of NH_2: NR_2 or OH groups into the rings. The compounds so obtained are colourless (the luco compounds) and are converted on oxidation into the colour base which gives malachite green. Both strong acid and base cause the colour of malachite green.This paper describes the TSDC study of polyvinyl acetate films doped with malachite green.

EXPERIMENTAL PROCEDURE
The isothermal immersion technique was utilized for preparing pure and malachite green doped polyvinyl acetate (PVA$_C$) samples. The solution was prepared in a glass beaker by dissolving PVA$_C$ (4 gm) and malachite green 5 mg by weight respectively in chemically pure dimethyl formamide (DMF). The solution was kept for 24 h to get a homogeneous and transparent solution. The solution thus prepared was then poured onto an optically plane cleaned glass plate floating on mercury. The solvent was allowed to evaporate in an oven at $40\ ^0C$ for 24 h to yield the desired samples. This was followed by room temperature out gassing at 10^{-5} torr for a further period of 12 h to remove any residual solvent. The plate was then drawn slowly out of the solution, leaving a uniform film on the plate. Samples thus obtained were uniformly smooth and could be easily peeled from the glass surface. The preconditioned samples were sandwiched between aluminized electrodes over a central circular area of 36 mm diameter. The thickness of the sample was of the order of 30 µm which was estimated by

measuring the capacitance of the fabricated sandwiched The various TSDC data e.g. activation energy, relaxation time, attempt to escape frequency and charge released for pure and malachite green doped PVA_C samples are calculated and listed in Tables 1- 2.

RESULTS AND DISCUSSION

The electric polarization of solid dielectrics can be produced by dipole alignment, migration of ions within the material or charge injection form the electrodes (8,9). The trapping centers originate in the transition of the crystalline state into amorphous regions, in the rearrangement of molecules in the polymer chain and form the presence of impurities and defects in the materials. The various defects, in addition to giving rise to their own characteristic trapping levels, can also combine with other trapping centers present around them, and thus they can modify qualitatively as well as qualitatively the TSDC spectra observed under different conditions. It is therefore difficult to it is correlate a peak with a particular configuration of defects in the material. Thus we find not only that the original trapping levels corresponding to the TSDC peaks at are quantitatively affected by the addition of impurity but also that new peak appear which depend upon the amount of doping used. The low temperature peak can be attributed to the shallow trapping of mobile charge carriers. On incorporation of an impurity these carriers are bound to the impurity sites.
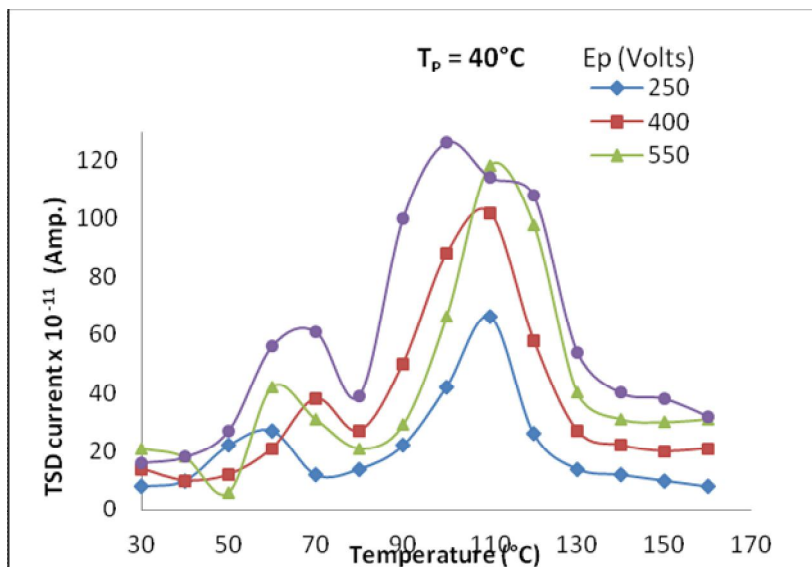

Figure-1: TSDC thermograme of pure PVAc samples poled at 40°C with different polarizing field (i.e. 250, 400, 550 and 700 volts)
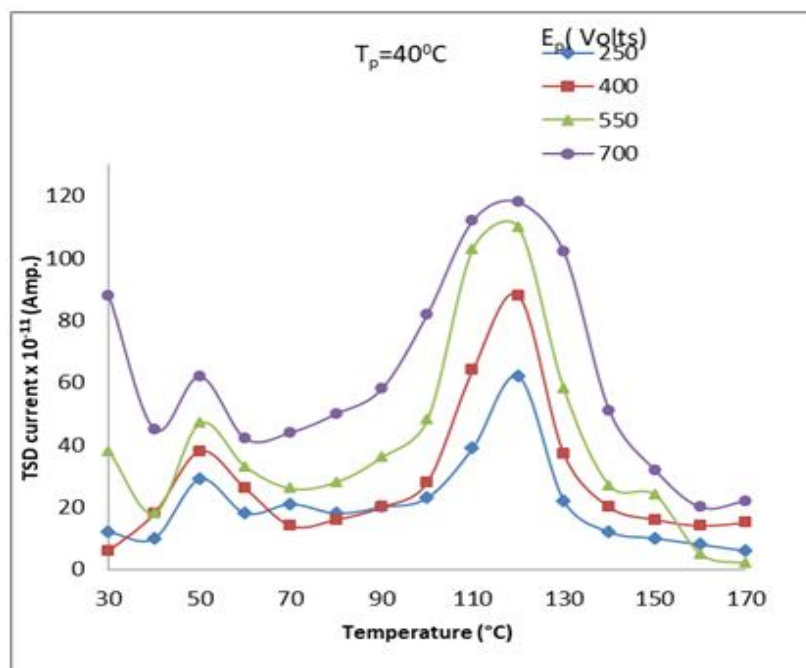

Figure-2: TSDC thermograme of PVAc doped malachite green (A1) samples poled at 40°C with different polarizing fields (i.e. 250, 400, 550 and 700 volts)

Table–1: Depolarization kinetic data of pure polyvinyl acetate (PVA$_C$) thermoelectres

S.N.	Polarizing Temperature (°C)	Polarizing Voltage (Volts)	Attempt to escape Frequency υ (s^{-1})	Activation Energy (eV)
1.	40	250	6.759×10^9	0.225, 0.336
		400	4.378×10^{11}	0.212, 0.309
		550	5.379×10^{10}	0.203, 0.298
		700	5.437×10^6	0.199, 0.290

Table–2: Depolarization kinetic data of malachite green (5 mg)doped (PVA$_C$) samples

S. N.	Polarizing Temperature (°C)	Polarizing Voltage (Volts)	Attempt to escape Frequency υ (s^{-1})	Activation Energy (eV)
1.	40	250	7.538×10^7	0.210, 0.293
		400	5.678×10^9	0.207, 0.289
		550	6.666×10^7	0.197, 0.278
		700	7.753×10^8	0.176, 0.260

Two relaxation peaks in the TSDC thermogram for PVA$_C$ and sensitized with malachite green 5mg have been observed at around 45-60^0 C to 120 ± 5^0 C and designated as β and α relaxations respectively at constant temperature by varying polarizing voltage (Figs 1-2) The β relaxation, accompanied with small activation energies, is due to the rotational motion of the long flexible side groups/dipoles and α relaxation, having large activation energies, is associated with a change in the dipolar orientation due to the segmental rotations or translations of the main chain. Dipolar β relaxation peak arises due to local motions of polar side groups which take place in glassy state of the polymer below T$_g$. The total charge released associated with this peak was also found to increase linearly with the forming field these characteristics further support our argument that the low temperature peak observed in the present investigation may be considered to arise due to dipolar motions with distribution in relaxation frequencies.

According to the two charge theory advanced by Gross(5), net apparent charge density of an electret is the combined effect of two charges, homo-charge and hetero-charge. The hetero-charge is the volume charge produced by either the rotation of dipoles or the separation of the ions. The homo-charge, on the other hand, is the space charge consisting of ions or electrons and is considered to be produced by the discharge in the minute air gaps between the electrode and the surface of the sample. An imperfect contact between the poling electrode and the surface of the sample increases the possibility of discharge in minute air gaps and thereby producing the homo-charge. It appears that the opposite side is associated with the injection of charge carriers from the electrode in the presence of higher charging field. The neutralization of these injected charge carriers caused by the increased conductivity at higher temperature will result in a peak in the same direction as the charging current. Peak in the positive direction may also be attribute to the fast detrapping rate of charge carriers, exceeding the charge exchange rate of the injecting electrode, thus resulting in partial blocking of the electrode during depolarization , resulting in shift of the position of zero field plane towards non-injecting electrode Charge reversals were also observed by Wiseman and Lindon(10), in case of polyvinyl acetate thermoelectret. According to them, the observed initial charge changes its sign due to slow decay of dipolar polarization. Also, it was shown that the final charge was homo-charge, after the second transition. Hashimotoet al (11), have also observed peak of opposite polarity in polyethylene electrets and attributed them to hetero- and homo-charge trapping.

The appearance of a peak with polarity opposite suggests that, in addition to the normal mechanism of polarization described earlier, some other mechanism must be operative which traps the mobile charge carriers responsible for the negative polarity of the thermally stimulated current. This necessitates some form of potential barrier which will have a built in electric field opposite to that due to the applied polarizing voltage (12).

In the segments, mobility may be increased after the complete phase transition and thus the possibility of injection of charge carriers near the electrodes and their drift seem to be possible by self motion of charge carriers/ions above the T$_g$ range. Above T$_g$ of the polymer, a sudden change in its volume may occur and thus structural rearrangements of chains (segments) may be possible due to sufficient mobility of segments (13).

REFERENCE

1. Perlman, M.M. , J. Appl. Phys. 42, 2545 (1971).

2. Perlman, M.M. , J . Electrochem. Soc. 119, 892 (1972).

3. Wintle, H.J. , J. Appl. Phys. 42. 4724 (1971).

4. Randall J.T. and Wilkins M H F 1945 Proc. Ray. Soc. A 184, 365-90.

5. Gross B, J Chem Phys. (USA), 17 (1949) 866.

6. Gross B , and Perlman M. M., J. Appl. Phys. (USA) , 43 (1972) 853.

7. K. Amakawa and Y.Inuishi, in M. M. Perlman (ed.),Electrets, Charge Storage and Transport in Dielectrics, The Electrochemical Society, Princeton, New Jersey, 1973,p.114.

8. A. Van RoggenAnnu. Rep., Conf. Electr. Insul., National Research Council Publ.1336 Ottowa, Canada, 1965

9. J. Van Turnhout. Polym. J., 2. 173 (1971).

10. Wiseman G G and Lindon E G ,Electr. Eng. (Australia), 72 Ed (USA), 13,12 (1975)2401.

11. Hashimoto T, Shiraki M and Sakai T, J. Polym. Sci. Polym. Phys. Ed (USA), 13,12 (1975) 2401.

12. W.W.Piper and F.F.Williams, B.J. Appl. Phys., 6 (1955)539

13. Turnhout J. Van (Ed.), Thermally stimulated discharge in Polymer electrets (Elsevier, Amsterdam) 1975.

FABRICATION AND I-V CHARACTERISTICS STUDY OF HETEROJUNCTION DIODE COMPOSED OF LANTHANUM SELENIDE AND CADMIUM SULPHIDE

C. T. Londhe, A. G. Bagde, K. N. Shivalkar and G. D. Bagde
Thin Film Laboratory, Department of Physics, Mahatma Gandhi Mahavidyalaya, Ahmedpur, Dist. Latur

ABSTRACT
The p-n heterojunction diode fabricated by the depositing of lanthanum selenide on fluorine-doped tin oxide coated glass substrate by spray pyrolysis technique and cadmium sulphide deposited by successive ionic layers and adsorption and reaction (SILAR) method successfully. The current – voltage (I-V) characteristics study at room temperature reveal excellent current rectification behavior. The ideality diode factor is calculated and is about 6.5 and it confirms the presence of high density recombination centers in space charge region.

Keywords: Hetrojunction diode, p-Lanthanum Selenide, n-Cadmium Sulphide, spray pyrolysis, SILAR

INTRODUCTION
Rare earth chalcogenides have been largely investigated because of their good physical properties such as superconductivity, mixed valences, strong electron correlations, magnetic, optical and thermoelectric properties [1]. Its sharp luminescence band has increased its investigation in the field of optoelectronics. These have also shown good semiconducting properties at high temperature application [2]. In order to maximize the utilization of the semiconducting property of rare earth material, a p-n junction is formed between the lanthanum Selenide (La_2Se_3) and the well known and widely used n-type material cadmium sulphide (CdS). P-N heterojunction forms the basic building block of semiconductor devices like diodes, transistors [3], light emitting diodes [4], solar cells [5]etc. Thus for any new material system, a proper characterization of p-n junctions is crucial for the development of electronic devices [3].

Among the various techniques used for fabrication, spray pyrolysis and successive ionic layer adsorption and reaction (SILAR) process offers many advantages. Spray pyrolysis has a less possibility of inclusion of contaminants in the deposited films. It also prevents the formation of metal hydroxide precipitates in the solution [2]. Similarly, SILAR method has also been vastly explored for the deposition of thin films [5-7]. SILAR technique is one of the inexpensive methods for the large scale deposition of high quality thin films [8]. In the present investigation, we report the synthesis of formation of p-n type heterojunction using two different processes. First lanthanum selenide was deposited using the spray pyrolysis method on the FTO glass. Then CdS, n-type material was deposited over it using successive ionic layer adsorption and reaction (SILAR) technique. Later, the electrical properties of the p-n junction diode formed have been undertaken using the current-voltage (IV) characteristic.

EXPERIMENTAL DETAILS
The fluorine doped glass (sheet resistance $\approx$ 10-20 Ω cm^{-2}) of dimensions 7.5 cm x 2.5 cm x 0.1 were used as a back contact. The substrate were initially cleaned with dilute HCl acid followed by detergent solution labolene and then with double distilled water (DDW) in order to remove the contaminants which later increases the adhesion of the material. In order to remove the acidic contaminants, the FTO substrates were kept in 1 M NaOH solution and later ultrasoniated in DDW for 15 min. Finally, the substrates were dried in alcohol vapors.

DEPOSITION OF LANTHANUM CHALCOGENIDES
Lanthanum trichloride ($La_2Cl_3.7H_2O$), thioactemide ($CH_3-CS-NH_2$) and selenium dioxide (SeO_2) powders were used as precursors in order to synthesis lanthanum selenide (La_2Se_3) [2, 9,10]. The solutions of 0.05 M $La_2Cl_3.7H_2O$ and the chalcogenide precursors were mixed in 2:3 volume ratios. The mixed solutions were sprayed on the preheated, cleaned substrate maintained at a temperature of 275 °C and 250 °C for sulphide and selenium respectively, with spray rate 4 cm^3 min^{-1}. In spray pyrolysis technique, fine drops of solution were sprayed on the heated substrate. Due to the pyrolytic decomposition of the solution a continuous and well adherent film is formed on the substrate. The chemical reaction for deposition of La_2Se_3 can be expressed as follows

LANTHANUM SELENIDE
$$La_2Cl_3 + 3\ SeO_2 \xrightarrow[250^\circ C]{\Delta} La_2Se_3 + 3Cl_2\uparrow + 3O_2\uparrow \qquad (1)$$
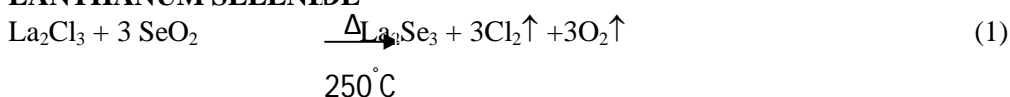
where Δ denotes pyrolytic decomposition temperature,

DEPOSITION OF CADMIUM SULPHIDE
The cationic precursor for CdS was 0.06 M cadmium acetate (CH$_3$-COO)$_2$Cd H$_2$O) complexed with ammonia in order to maintain the pH~11. The anionic precursor was prepared from 0.1 M thiourea solution whose ph was maintained at 5. The adsorption and reaction time for the growth of CdS were optimized to be 15 s each and the rinsing time was optimized to be 40 s. One total SILAR cycle was thus: 15 s adsorption in cationic precursor solution, 40 s rinsing in ample amount of double distilled water, 15 s in thiourea solution and 40 s rinsing in double distilled water by repeating such 30 SILAR cycles. We obtained a film of thickness 0.7 μm. The films were deposited at room temperature (27°C).

Cadmium ions are adsorbed on the surface of the substrate when it is immersed into the cadmium acetate precursor. The unadsorbed ions are removed through rinsing in the double distilled water. Next, the substrate was immersed in the cationic source of sodium sulphide. Sulphide ions react with the adsorbed cadmium ions to form a single layer of CdS. The unreacted ions are separated out by rinsing the substrate in DDW.

RESULTS AND DISCUSSIONS
Current-voltage characteristic
A detailed analysis of the morphology, structure and phase has been studied [2, 9, 10]. Figure 1 shows the schematic representation of the setup used for evaluating the current-voltage (I-V) characteristic. The I-V characteristic of n-CdS / La$_2$Se$_3$ junction has been shown in figure 2. The current rectifying behavior of the junction formed is similar to a pn-junction diode indicating the presence of depletion layer [11]. The graph shows a resemblance with the diode property which indicates that a p-n junction is formed between the La$_2$Se$_3$ layer and the CdS layer. Importantly an ideality factors n$_1$ and n$_2$ were derived. The achievement of ideality factor indicates the excellent diode behavior of our automatically sharp hetrojunction p-n diodes. The exponentially decreases curve with negative voltage represent reverse bias and the increasing current with increasing voltage represent forward bias. The figure 2 shows that the knee voltage for La$_2$Se$_3$ is approximately 0.5 V. This also confirms that the films of La$_2$Se$_3$ act as a p-type material [12]. The ideality factor was calculated from the I-V characteristic by using the formulae

$$I=I_0 (e^{qv/nkT} -1) \tag{2}$$

where I_0 is the reverse saturation current, q is the elementary charge, k is the Boltzmann constant, T is the absolute temperature and n is the ideality factor. Based on this equation a graph has been plot between log I vs V. It was observed that the curve shows two distinct regions one at low (< 1V) and another at high (1-2V) bias ranges. The linear behavior of the semi logarithmic I-V characteristics at low and high region shows a double exponential relationship between current and voltage. The e diode equation (2) can be modified into following form

$$I=I_{01} [e^{qv/n_1 kT} -1]+I_{02} [e^{qv/n_2 kT} -1] \tag{3}$$

The first and second terms describe the diffusion and recombination generation components respectively. The ideality factor calculated with the flat band potentials is 6.5. The ideality factors were much higher than the theoretically expected values of 1.0 to 2.0 [13]. The increase in the ideality factor has been suggested to be due to the trap-assisted tunneling and the carrier leakage [14]. The junction ideality factor values indicate that the p-n junction formed between the La$_2$Se$_3$ and CdS are non-ideal in nature.
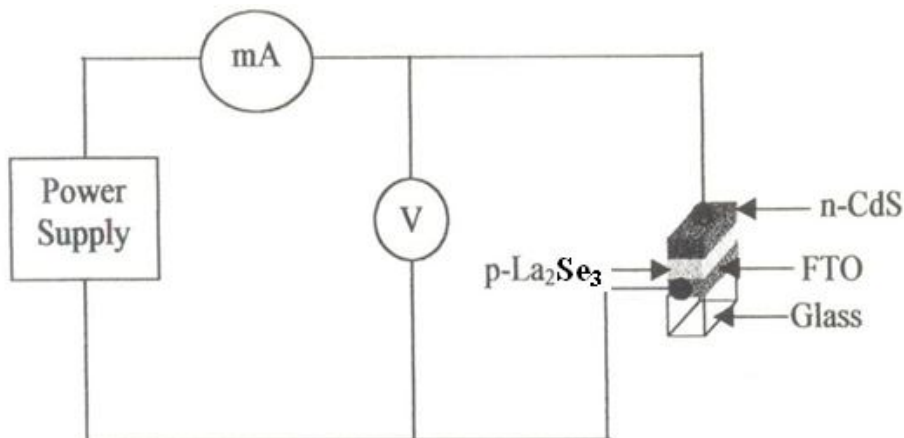

Figure-1: Circuit diagram for current-voltage (I-V) characterization study of p-La$_2$Se$_3$/n-CdS heterojunction device.
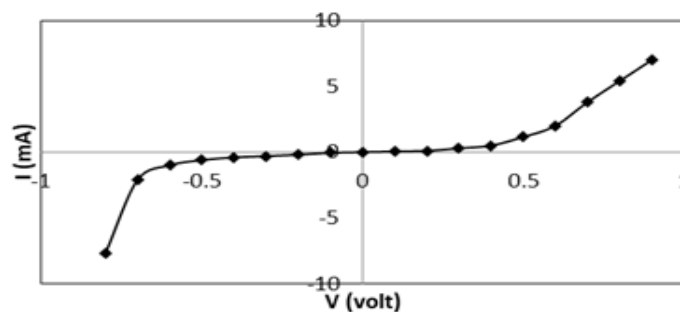
Figure-2: Current-voltage (I-V) characteristics of p-La$_2$Se$_3$/n-CdS heterojunction

CONCLUSION

We have successfully fabricated p- Lanthanum Selenide (La$_2$Se$_3$) and n-Cadmium sulphide (CdS) diode using simple spray pyrolysis and SILAR method which also help in reducing the contaminants on the deposited film. A diode I-V characteristic has been obtained in this structure. An ideality factor much greater than 1 has been obtained for each diodes formed. The I-V characteristics represent hetrojection formed.

REFERENCES

1. Viennois, R., Niedziolka, K., & Jund, P. (2013). Physical properties of the thermoelectric cubic lanthanum chalcogenides La3−yX4 (X = S, Se, Te) from first principles *Phys. Rev. B*, 88, 174302.

2. Bagde, G. D., Sartle, S. D., & Lokhande, C. D. (2003). Deposition and annealing effect on lanthanum sulfide thin films by spray pyrolysis. *Thin Solid Films*, **445**, 1-6.

3. Lee, J. U., Gipp, P. P., & Heller, C. M. (2004). Carbon nanotube p-n junction diodes. *App. Phys. Lett.*, **85**, 145-147.

4. Chena, X. A., Ng, M. C., Djurišić A. B., Chan, W. K. Fong, P.W. K., Lui, H. F. Surya, C., Cheng, C. C. W., & Kwok, W. M. (2013). GaN/MgO/ZnO heterojunction light-emitting diodes. *Thin Solid Films*, **527**, 303-307.

5. Pathan, H. M., Sankapal, B. R., Desai, J. D., & Lokhande C. D. (2003). Preparation and characterization of nanocrystalline CdSe thin films deposited by SILAR method. *Mater. Chem. Phys.*, **78**, 11-14.

6. Lokhande, C. D., Sankapal, B. R., Pathan, H. M., Muller, M., Giersig M., & Tributch, H.(2001). Some structural studies on successive ionic layer adsorption and reaction (SILAR)-deposited CdS thin films. *Appl. Surf. Sci.*, **181**, 277-282.

7. Sankapal, B. R., Ennaoui, A., Guminskaya, T., Dittrich, Th., Bohne, W., Röhrich, J., Strub E., & Lux-Steiner, M. Ch. (2005). Characterization of p-CuI prepared by the SILAR technique on Cu-tape/n-CuInS$_2$ for solar cells. *Thin Solid Films*, **480**, 142-146.

8. Garole, D., Tetgure,S. R., Borse,A. U., Toda, Y. R., Garole,V. J., Sankapal B. R. & Baviskar, P. K. (2015). The first report on SILAR deposited nanostructured uranyl sulphide thin films and their chemical conversion to silver sulphide. *New J. Chem.*, **11**, 8695-8702.

9. Bagde, G. D., Sartale S. D., & Lokhande, C. D. (2003). Spray deposition of lanthanum selenide (La2Se3) thin films from non-aqueous medium and their characterizations. *Mater. Chem. Phys*, **80**, 714-718.

10. Bagde, G. D., Sartale,S. D., & Lokhande, C. D.(2005). Spray pyrolysis deposition of lanthanum telluride thin films and their characterizations. *Mater. Chem. Phys*, **89**, 402-405.

11. Singh, B., & Ghosh S. (2013). Zinc oxide and metal phthalocyanine based hybrid P-N junction diodes. *App. Phys. Lett*, **103**, 133301-133304

12. Aoki, T., Hatanaka, Y., & Look, D.C. (2000). ZnO diode fabricated by excimer-laser doping *App. Phys. Lett*, **76**, 3257-3258.

13. Shah, J. M., Li, Y. L., Gessmann, Th., & Schubert, E. F.(2003). Experimental analysis and theoretical model for anomalously high ideality factors (n >> 2.0) in AlGaN/GaN p-n junction diodes. *J. Appl. Phy.*, **94**, 2627-2630.

14. Zhu, D., Xu, J., Noemaun, A. N., Kim, J. K., Schubert, E. F., Crawford, M. H. & Koleske, D. D.(2009). The origin of the high diode-ideality factors in GaInN/GaN multiple quantum well light-emitting diodes. *App. Phys. Lett.*, **94**, 081113.

DEVELOPMENT AND MPD SENSING STUDY OF FIBER OPTIC POA/GOX MODIFIED BIOSENSOR FOR THE DETECTION OF GLUCOSE

V. G. Pahurkar[1], Y. S. Tamgadge[2], P. M. Wankhade[3], A. B. Gambhire[4] and G. G. Muley[5]
[1]Department of Physics, Prof. Ram Meghe Institute of Research & Technology, Amravati
[2]Department of Physics, Mahatma Fule Mahavidyalaya, Warud
[3]Department of Physics, Late R. Bharti Arts, Commerce & Smt. S. R. Bharti Science College, Arni
[4]Department of Chemistry, Shri Anand College, Pathardi, Ahemadnagar
[5]Department of Physics, Sant Gadge Baba Amravati University, Amravati

ABSTRACT

The design, development and characterization of polyaniline doped with oxalic acid/glucose oxidase (POA/GOx) cladding modified fiber optic intrinsic glucose biosensor (FOIGB) have been proposed. The sensor has been used to sense the analyte-glucose in solutions. The sensing response of the sensor in the form of novel modal power distribution (MPD) technique and selectivity in the form of power vs. time was studied. The POA matrix material prepared by polymerization technique for cladding modification was analysed using various optical and surface morphological studies.

Keywords: Biosensor; MPD, Optical fiber; Polyaniline; Selectivity.

1. INTRODUCTION
Diabetes is a complicated disease and exact care is needed for its prevention [1, 2]. It has been realized that fiber optic biosensor is very effective for early detection and prevention of diabetes as compared to traditional sensors [3]. Fiber optic biosensors have small and compact size, high sensitivity, reliability, fast, ability to be multiplexed, remote sensing, ability to be embedded into textile structures, immunity to electromagnetic interference, non-conducting and intrinsically safe for patients [4]. The composition of sensing element is important for designing and development of fiber optic intrinsic biosensor (FOIB). The cladding modification approach is very much useful, convenient and inexpensive for FOIB development. Its principle is based on change of optical power or intensity induced in modified region [4, 5]. Conducting polymers provide a suitable matrix for the immobilization of biomolecules [6]. However, polyaniline (PANI) is reported as highly accommodating surface behaviour and biocompatible. In addition, it has low oxidation potential, environmental stability, sensitivity and good matrix quality. In various polymers polyaniline has been found a suitable matrix material to bind biomolecules [6, 7]. Jiang *et al.* [3] and Binu *et al.* [8] have designed and studied the properties of fiber optic biosensors for glucose detection.

In the present investigation, a PANI doped with oxalic acid (POA) cladding modified fiber optic intrinsic glucose biosensor (FOIGB) is developed and studied [9]. GOx was used for immobilization through cross-linking via glutaraldehyde solution and further used to detect glucose-analyte. The sensing responses in the form of novel modal power distribution (MPD) technique for 1, 10 and 100 mM glucose solutions along with buffer solution have been determined. The selectivity of the prepared sensor toward glucose was also determined in the form of optical power. The suitability of deposited POA material was characterized using field emission scanning electron microscopy (FE-SEM), optical microscopy and energy dispersive X-ray spectroscopy (EDS).

1. EXPERIMENTAL
1.1 Materials and method
Aniline (monomer) and ferric chloride (oxidant) of analytical grade were purchased from Fisher Scientific, USA. Glucose oxidase (GOx, 125 units/mg) was procured from Sisco Research Laboratories (SRL), India. Oxalic acid, glucose, glutaraldehyde solution (25%), urea, potassium dihydrogen orthophosphate and sodium hydroxide were purchased from SD Fine chemicals, India. All the chemicals were used as received without further purification. The necessary synthesis processes were carried out in aqueous medium. The stock solutions of GOx in proportion 2 mg/ml and glucose were prepared in 0.1 M phosphate buffer of pH 7.4 and kept at the temperature 4°C for 24 hrs [10, 11].

The surface morphology and elemental analysis were confirmed through field emission scanning electron microscopy (FE-SEM) equipped with energy dispersive X-ray spectroscopy (EDS) (S-4800, Hitachi, Japan). Optical microscope (AxioCam ERc 5s, Germany) was used to record image of optical fiber to confirm the thin layer of POA matrix. The sensing responses in the form of MPD and selectivity using power vs. time have been studied with the help of CCD camera beam profiler (BC106-VIS, Thorlabs, USA).

1.2 Construction of sensor

About half meter long plastic cladded silica core multimode optical fiber (core/cladding-425/320μm) was taken to prepare POA-FOIGB. Both the ends of optical fiber were fine polished to couple laser beam at input and CCD camera at the output as shown in Fig. 1. The original cladding of optical fiber (2 cm) portion was removed mechanically. The removed surface was cleaned several times and cladding modification of desired sensor was done using simple chemical polymerization method. The sensing element was submerged in polymerization vessel to deposit a thin layer of POA matrix as an active cladding. For the purpose, 0.2 M aniline and 0.05 M $FeCl_3$ solutions were prepared in separate beakers using double distilled water. In a beaker, 0.2 M solution of aniline monomer was mixed homogeneously with oxalic acid while constant stirring with dropwise addition of HCl solution. $FeCl_3$ solution was then added drop by drop with constant stirring. After preparing the sensing element, the solution of enzyme-GOx was immobilized on it through cross-linking via 1% glutaraldehyde solution using layer by layer technique [9-11].
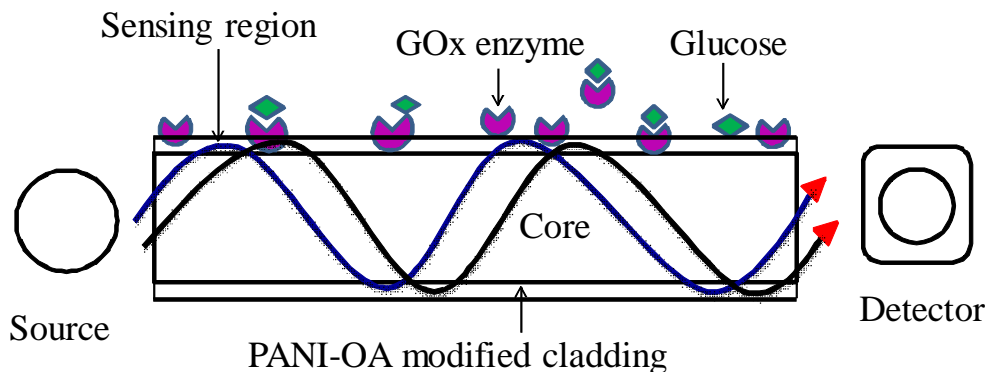

Fig-1: Experimental arrangement of POA-FOIGB for glucose determination.

2. RESULTS AND DISCUSSION

2.1 Surface morphology

Fig. 2(a) shows the FE-SEM image of surface morphology of POA film deposited on the optical fiber core. It confirms new aspect of morphological growth, demonstrating that when oxalic acid is used as doping agent, it guides the formation of PANI structure. It looks porous having cauliflower like structure. This type of morphology is very useful for the immobilization of biomolecules and found suitable for sensing applications. Inset of Fig. 2(a) shows optical microscope image of FOIGB sensing element deposited with POA thin film, confirms a desirable thickness around 1.655 μm. The purity and presence of necessary basic elements in POA polymeric matrix have also been confirmed using EDS spectrum as shown in Fig. 2(b). Since, the deposited POA has amorphous nature and merely useful for enzyme-GOx immobilization [11, 14, 15].
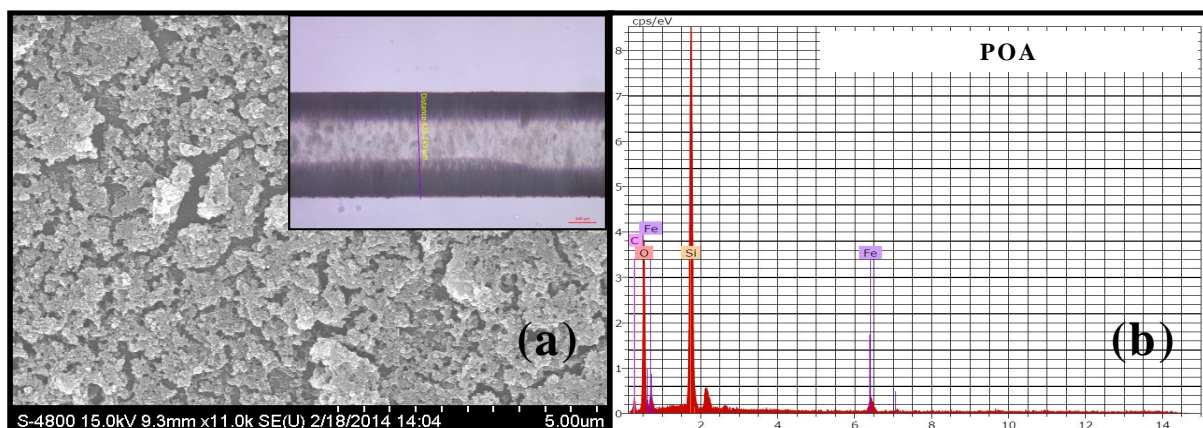
Fig-2 (a): FE-SEM with OM image and (b) EDS of POA matrix

2.2 Sensing response-MPD study

In the present study, the sensing response was measured in the form of MPD for 1, 10 and 100 mM glucose solutions as compared to the buffer solution as shown in Fig. 3. It has been achieved by off-axis illumination. It is an easy and convenient technique to study the intensity distribution among various modes and even more sensitive for a little change in refractive index of modified cladding. An active layer of POA/GOx acts as the primary layer having lower refractive index than core. While reaction between GOx and glucose, the number of leaky modes get coupled back the core, and help to improve the optical properties of the sensor [6, 11].

Fig. 3(a-d) clearly shows the discrete pattern of MPD in 2D for buffer solution, 1, 10 and 100 mM glucose solutions respectively with their respective intensity x-profiles. It can be easily seen that inner modes becoming more intense with the increasing concentrations as compare to buffer solution by diffusing outer mode. Moreover, this scenario can also be seen in their relative x-profiles with increasing concentration i.e. the merging of outer mode in inner mode with the increased area. More precisely, it can be said that there is an increase in total power at the output with increasing glucose concentration through the coupling of outer leaky modes in inner one [11].
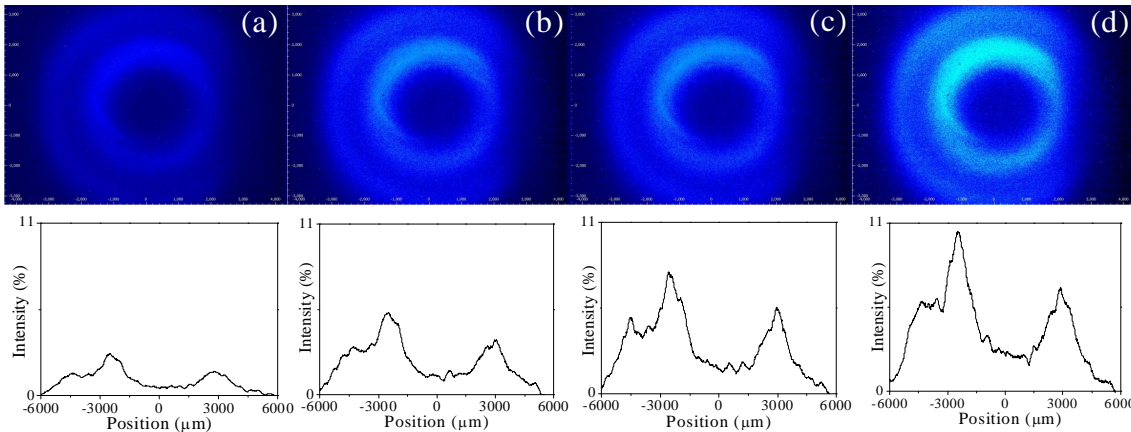

Fig-3: MPD pattern of POA-FOIGB for (a) buffer solution, (b) 1, (c) 10 and (d) 100 mM glucose solutions with corresponding intensity x-profiles.

2.3 Selectivity

The prepared sensor should be specific with its aim of selectivity, beacause the real samples also have other interfering species with glucose. Therefore the present sensor was also examined for its selectivity towards glucose, along with buffer solution and urea (100 mM) as shown in Fig. 4. It is observed that there is slight change in the output power in case of urea as compared to buffer solution suggesting variation of refractive index in both solutions. However, the observed large variation for glucose measurement may not due to the refractive index, but due to reaction between GOx and glucose on the sensing element region which modifies the optical properties. Thus it can be concluded that the reported sensor is highly selective for glucose meaurement [11].
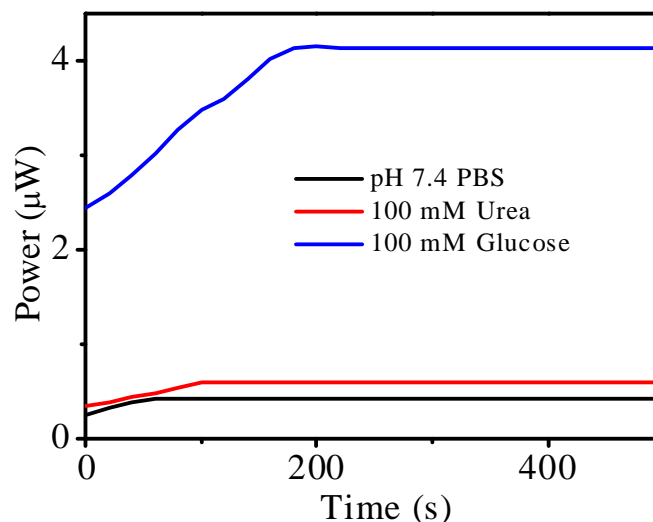
Fig-4: Selectivity of POA-FOIGB toward glucose.

3. CONCLUSIONS

The cladding modified FOIGB has been successfully developed and studied for the detection of glucose. The cladding was modified with POA/GOx/glutaraldehyde thin film through cross-linking. MPD study confirmed the power distribution with increasing concentration of glucose, which directly attributed to redirecting leaky modes to the core. The prepared sensor also found to be highly selective towards glucose. As-synthesized POA matrix has been found suitable for enzyme-GOx immobilization as confirmed from FE-SEM, optical microscopy and EDS studies. Finally, it can be concluded that the present POA-FOIGB may find potential applications in medical and other important fields.

REFERENCES

1. J. D. Newman, A.P.F. Turner, Home blood glucose biosensors: a commercial perspectiveBiosens. Bioelectron. 20 (2005) 2435-2453.

2. J. Wang, Glucose biosensors: 40 years of advances and challenges, Electroanal. 13(12) (2001) 983-988.

3. D. Jiang, E. Liu, X. Chen, J. Huang, Design and properties study of fiber optic glucose biosensor, Chinese Opt. Lett. 1(2) (2003) 108-110.

4. A. Leung, P. M. Shankar, R. Mutharasan, A review of fiber-optic biosensors, Sens. Actuators, B 125 (2007) 688-703.

5. M. E. Bosch, A.J.R. Sanchez, F. S. Rojas, C. B. Ojeda, Recent Development in Optical Fiber Biosensors, Sensors 7 (2007) 797-859.

6. M. El-Sherif, L. Bansal, J. Yuan, Sensors 7 (2007) 3100-3118.

7. B. Kuswandi, R. Andres, R. Narayanaswamy, Optical fibre biosensors based on immobilised enzymes, Analyst 126 (2001) 1469-1491.

8. S. Binu, V.P.M. Pillai, V. Pradeepkumar, B. B. Padhy, C. S. Joseph, N. Chandrasekaran, Fibre optic glucose sensor, Mater. Sci. Engi. C 29 (2009) 183-186.

9. V. Pahurkar, S. Dagdale, Y. Tamgadge, V. Nagale, G. Muley, Cladding Modified with PANI-Oxalic Acid Composite Glucose Oxidase Immobilized Fiber Optic Intrinsic Glucose BiosensorMacromol. Symp. 362 (2016) 149-151.

10. V. G. Pahurkar, Y. S. Tamgadge, A. B. Gambhire, G. G. Muley, Evanescent wave absorption based polyaniline cladding modified fiber optic intrinsic biosensor for glucose sensing application, Measur. 61 (2015) 9-15.

11. V. G. Pahurkar, Y. S. Tamgadge, A. B. Gambhire, G. G. Muley, Glucose oxidase immobilized PANI cladding modified fiber opticintrinsic biosensor for detection of glucose, Sens. Actuators, B 210 (2015) 362-368.

12. N. Thummarungsan, D. Pattavarakorn, Electrochromic Performances of Conductive Polyaniline Copolymer, Inter. J. Chem. Eng. Appl. 5(2) (2014) 176-180.

13. V. Rajasekharan, T. Stalin, S. Viswanathan, P. Manisankar, Electrochemical Evaluation of Anticorrosive Performance of Organic Acid Doped Polyaniline Based Coatings, Int. J. Electrochem. Sci. 8 (2013) 11327-11336.

14. M. R. Saboktakin, A. Maharramov, M. A. Ramazanov, Synthesis and characterization of hybride polyaniline / polymethacrylic acid/ Fe3O4 nanocomposites, J. of Nat. Sci. 5(3) (2007) 67-71.

15. V. B. Chanshetty, K. Sangshetty, G. Sharanappa, Surfacemorphology studies and thermal analysis of V_2O_5 doped polyaniline composites, Int. J. Eng. Res. Appl. 2(5) (2012) 611-616.

SEMICONDUCTIVE PROPERTIES OF CHROMIUM DOPED Cu-FERRITE

S. R. Bainade[1] and C. M. Kale[2]

[1]Research Center, Jijamata Mahavidyalaya, Buldhana

[2]Department of Physics, Indraraj Arts, Commerce and Science College, Aurangabad

ABSTRACT

Samples of type $CuCr_xFe_{2-x}O_4$ (x = 0.0, 0.2, 0.4, 0.6, 0.8, and 1.0) were prepared by the self propagating sol-gel autocombustion technique. Using X-ray diffraction (XRD) pattern, the prepared samples confirm the formation of single phase cubic spinel structure. The lattice constant determined at different Cr substitutions and it decreases with increase in Cr^{3+} concentration x. The observed behavior of lattice constant can be explained on the basis of the relative sizes of ionic radii.The temperature dependence of D.C. electrical resistivity (DCR) studied in the temperature range of 300-800K by two-probe method. The values of DCR show the semiconducting bahaviour of the samples. The Arrhenius plots exhibit a kinck point at which the Curie temperature measured. Curie temperature decreases at Cr content increases.The Curie temperature is dividing the curve in two regions explain the activation energy in ferrimagnetic and paramagnetic region increases with increase in Cr content.The values of Curie temperature measured by DCR and Loria technique are close to each other.

Keywords: Activation energy, Arrhenius plots, Curie temperature, DCR, XRD.

1. INTRODUCTION

Ferrites plays a useful role in many magnetic applications because of their electrical conductivity is relatively low in comparison with that of magnetic metals. Nanoferrites are important components in the latest electronic products, such as cell phone, computers, video cameras, memory devices etc. They require small dimensions and all light weights and have better functions. The soft ferrites exhibit two antiferromegnetically coupled sub-lattices namely tetrahedral (A) and octahedral [B] site [1, 2]. The electrical resistivity was studied on the system $Cu_xCd_{1-x}Fe_2O_4$ [3], to illustrate the effect of Cu^{2+} substitution. The results showed that the activation energy increases with Cd content up to 50%, beyond which it decreases and the Curie point decreases with increasing Cd content. The results showed that the annealing changes the sign of conduction from p-type to n-type. The electrical resistivity of the system $Cu_xMg_{1-x}Fe_2O_4$ was measured [4]. The results showed that the activation energies are lower for higher conductivity samples.The results showed that the conductivity is due to compensation of electrons and holes. The aim of the present work is to study the effect of Cr substitution instead of iron atoms in Cu ferrite on its physical properties of $CuCr_xFe_{2-x}O_4$ (where, x = 0.0, 0.2, 0.4, 0.6, 0.8, and 1.0) were prepared by the self propagating sol-gel autocombustion technique. The substitution of Cr (nonmagnetic with the same valence) instead of Fe (magnetic) in $CuFe_2O_4$ ferrites is of much interest because this may leads to the decrease of the hopping conduction in the B-sites, thus change in electrical properties can be expected.

EXPERIMENTAL

A series of multicrystalline nanoferrite having the chemical formula $CuCr_xFe_{2-x}O_4$ (where, x = 0.0, 0.2, 0.4, 0.6, 0.8, and 1.0) were synthesized by using self propagating sol-gel autocombustion method. The starting materials having high purity (99 %, S. D. fine, India) were copper nitrate: $Cu(NO_3)_2 \cdot 6H_2O$, ferric nitrate: $Fe(NO_3)_2 \cdot 9H_2O$, chromium nitrate: $Cr(NO_3)2 \cdot 9H_2O$, citric acid: $C_6H_8O_7 \cdot H_2O$ and ammonia: NH_3 all of 99% pure AR grade. Calculated quantities of metal nitrates were dissolved together in a 100ml of distilled water to get clear solution. An aqueous solution of citric acid was then added to the metal nitrate solution. The molar ratio of citric acid to the total moles of nitrate ions was adjusted to 1:3. A small amount of NH_3 was added drop wise into the solution so as to adjust pH value to about 7 so the sample becomes neutral. A continuous stirring and heating at 90^0C to solution on hot plate with magnetic stirrer until it becomes a very viscous gel. The process from mixing of materials to the final burnt powder is as shown in stepwise formation of $CuCr_xFe_{2-x}O_4$ nanoferrite in **Fig.1**.The powder was annealed in air at temperature 500°C for six hours with heating rate 50^0C per min to obtain a spinel phase. The final product is then grinded and subjected to further study.
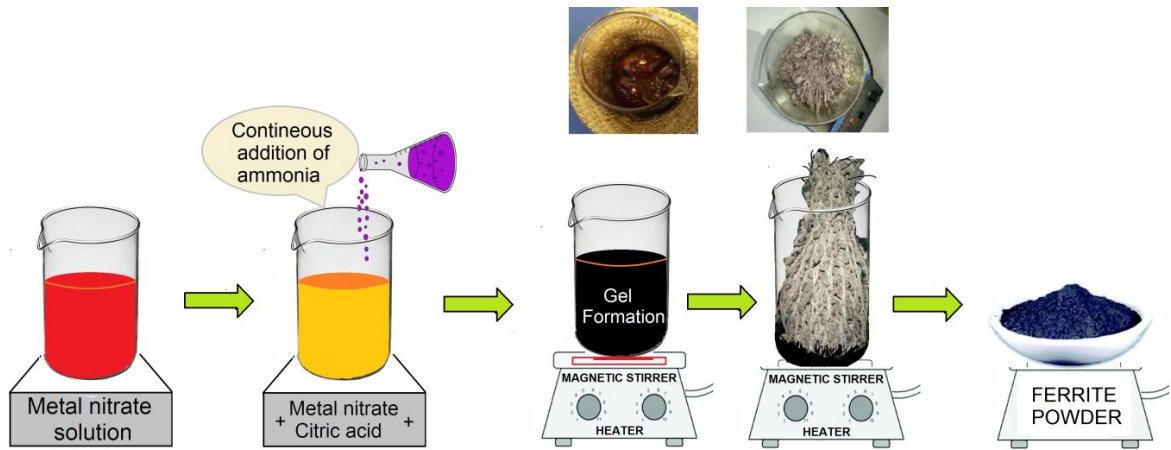
Fig-1: Steps of formation of $CuCr_xFe_{2-x}O_4$ nanoferrite

3. RESULTS AND DISCUSSION

XRD technique is used to confirm the single nano-phase formation of $CuCr_xFe_{2-x}O_4$ system where, x= 0.0 to 1.0 in the step of 0.2. The XRD patterns of all the composition show that all the peaks corresponding to cubic spinel structure without any extra impurity peak. Due to the random orientation of the crystallites in the sample, a reflection at the particular position is due to a set of atomic planes which are satisfying Bragg's diffraction law. In the XRD patterns of ferrites all the Braggs reflections are allowed peaks have been indexed. The strongest reflection has come from (311) plane that indicates spinel phase.

Using XRD data, the lattice parameter has been determined using the method of least squares to an accuracy of ± 0.002 Å and the variation of lattice parameter 'a' with increase in chromium content 'x' is shown in **Fig.2**, and it indicates the lattice parameter decreases with increase in Cr^{3+} concentration x. The observed behavior of lattice constant can be explained on the basis of the relative sizes of ionic radii. The ionic radius of Cr^{3+} (0.63Å) ions is smaller than the ionic radius of Fe^{3+} (0.64 Å) ion. Replacement of larger Fe^{3+} cations by smaller Cr^{3+} cations in the copper ferrite causes decrease in lattice parameter. Similar variation of lattice parameter was observed for other Cr^{3+} substituted spinel ferrites [5, 6].
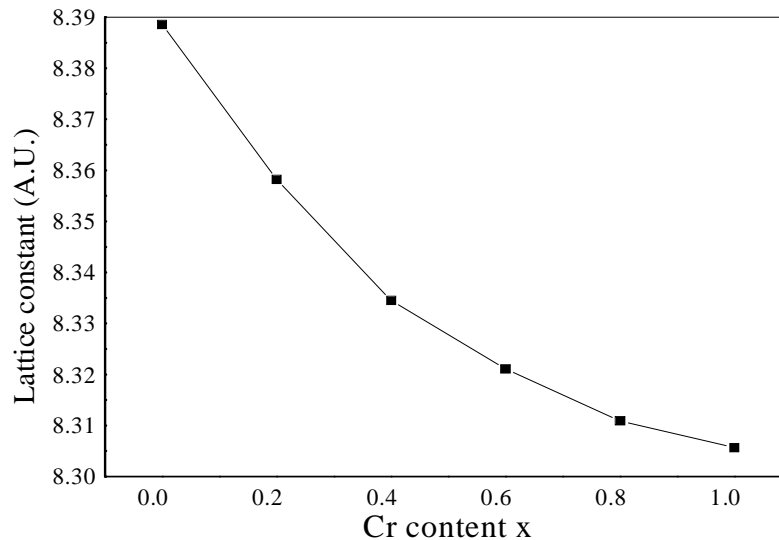
Fig-2: Lattice constant of the $CuCr_xFe_{2-x}O_4$ (x = 0.0 to 1.0 in the step of 0.2) nanoparticles

D.C. Electrical Resistivity (DCR)

The temperature dependence of DCR of all the samples of the series $CuCr_xFe_{2-x}O_4$ was studied in the temperature range of 300-800K studied by two-probe method. The DCR was calculated by measuring from dimensions and resistance of the pellet by using the relation,

$$\rho = \left(\frac{\pi r^2}{t}\right) R \quad \Omega cm$$

Where, r is radius of the pellet, t is thickness of the pellet, R is resistance of the pellet.

Table-1: Variation of Resistance, D. C. resistivity, activation energy in ferrimagnetic and paramagnetic region and Curie temperature of $CuCr_xFe_{2-x}O_4$ system

Cr content X	Resistance (R) Ω	D.C. Resistivity (ρ) Ω-cm	Activation energy (eV)			Curie temperature	
			E_F	E_P	ΔE	DCR	Loriea
0.0	1332570	235468	0.228	0.326	0.098	753	710
0.2	1356398	238132	0.256	0.364	0.108	702	682
0.4	1355132	239856	0.264	0.374	0.110	653	623
0.6	1363458	241345	0.269	0.398	0.129	604	565
0.8	1374201	243036	0.301	0.443	0.142	553	510
1.0	1391242	245987	0.312	0.475	0.163	423	415

Table 1, gives the values of D. C. resistivity as a function of composition shows that resistivity increases with chromium content x. To understand the DCR behavior of the samples, the variation of logarithm of resistivity versus reciprocal of temperature has been studied**. Fig. 3** displays the plots of logarithm of resistivity versus reciprocal of temperature of typical samples x=0.2, 0.4, 0.6, and 0.8. The plots exhibit a break near Curie temperature dividing the curve in two regions namely ferrimagnetic and paramagnetic region.

The variation of resistivity as a function of temperature is also studied. **Fig. 3** shows the variation of logρ versus 1000/T for all the composition x. It can be seen from **Fig. 3** that D.C. resistivity decreases with the increase in temperature, indicating the semi-conducting nature of the ferrite system. The resistivity - temperature behavior obeys the relation [7],

$$\rho = \rho_0 \exp\left(\frac{-\Delta E}{kT}\right) \quad Ohm\text{-}cm$$

Where, ρ is the resistivity at absolute temperature T, ΔE is the activation energy and k is the Boltzmann constant. Each sample shows a break near the Curie temperature which is attributed to the transition from ferrimagnetic region to paramagnetic region. Using above equation and the resistivity plots, the activation energy in ferrimagnetic and paramagnetic region was calculated and the values of activation energies are tabulated in **Table 1**
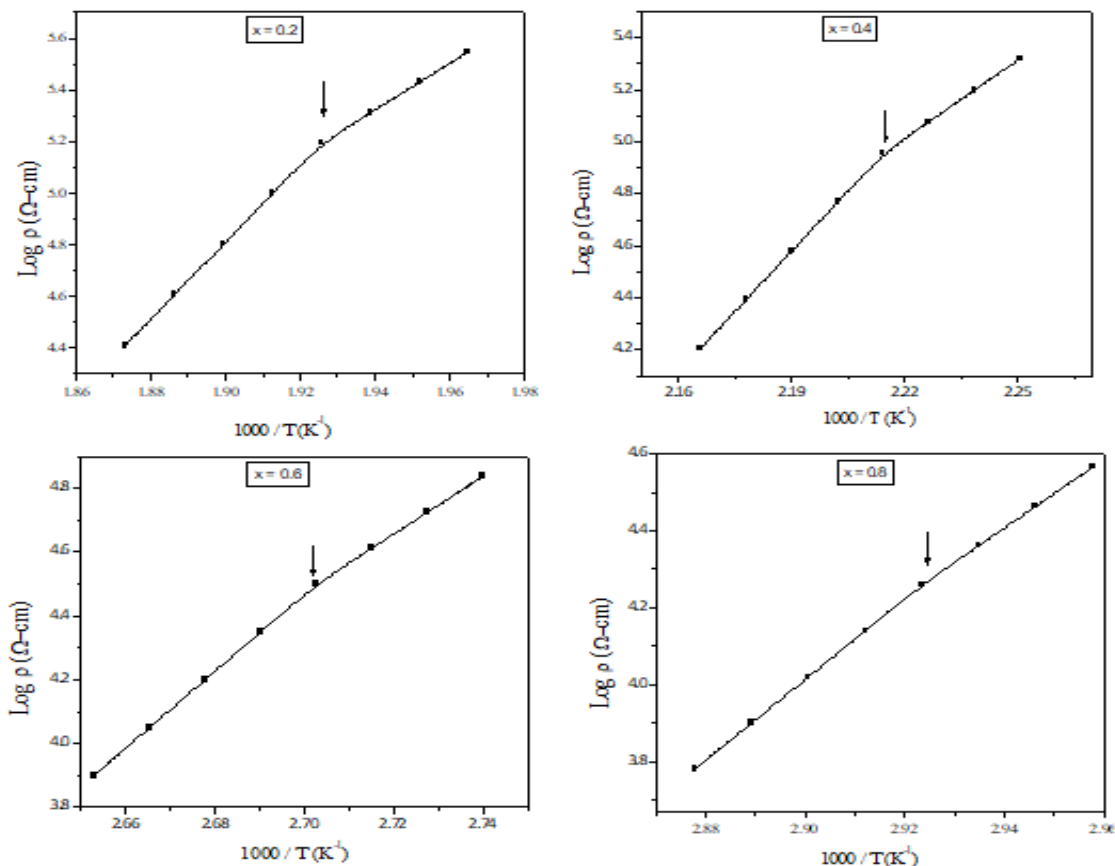

Fig-3: Logρ versus 1000/ T of $CuCr_xFe_{2-x}O_4$ (typical samples x=0.2, 0.4, 0.6, and 0.8) nanoferrite system

In the present study Fe^{3+} ions are replaced by Cr^{3+} ions. The substitutional ions (Cr^{3+}) have strong preference to octahedral B-site which leads to Fe^{3+} ions at B-site. These chromium ions do not participate in the conduction process but it limits the degree of $Fe^{2+}\square Fe^{3+}$ conduction by blocking of Fe^{2+} to Fe^{3+} ions [8]. This results in increase in resistivity with increasing chromium concentration. Similar behaviour was also reported in chromium substituted nickel zinc ferrite [9] and other well known ferrites [10, 11]. These plots obey Arrhenius relation indicating semiconducting behaviour of the samples. Using Arrhenius relation and resistivity plots, activation energy of all the samples has been obtained and the values are presented in **Table1**. It can be seen from table that activation energy in paramagnetic region is more as compared to the values of activation energy in ferrimagnetic region which is shown in **Fig.4**.
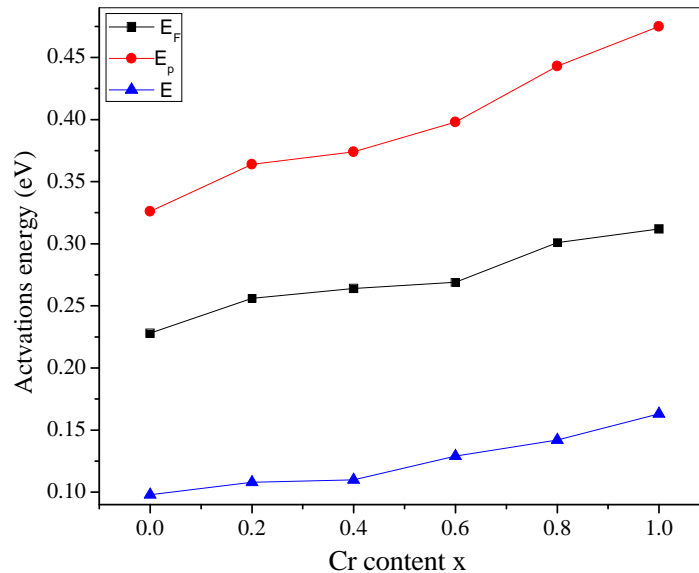
Fig-4: Activation energy in ferrimagnetic (E_F), paramagnetic (E_P) region and change in activation energy (ΔE) of $CuCr_xFe_{2-x}O_4$ ($0.0 \leq x \leq 1.0$) ferrite system
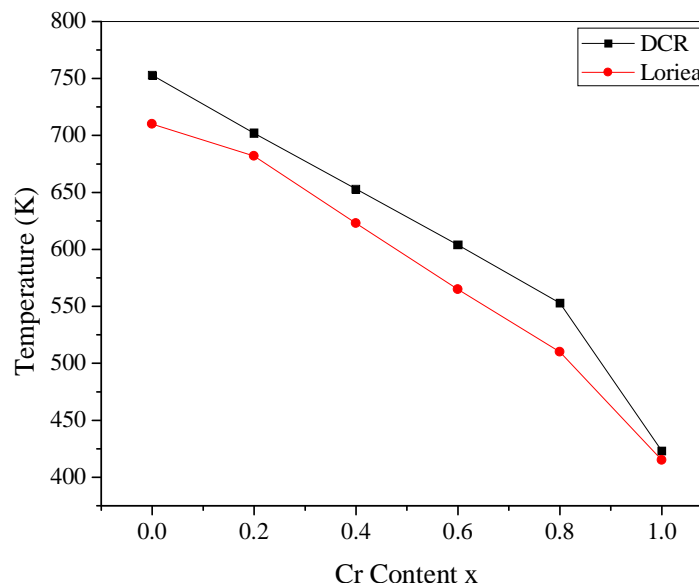
Fig-5: Curie temperature with Cr content x of $CuCr_xFe_{2-x}O_4$ nanoferrite system

The **Fig.5** shows that, the variation of Curie temperature 'Tc' using DC electrical resistivity and Loria technique with different Cr content x. It is clear from the graph that the values of Curie temperature from the both methods are very close to each other. The value from DCR method is slightly greater than the values obtained from Loria method. This change is due to the surrounding variation in room temperature.

4. CONCLUSIONS

The present investigations lead on the conclusions that, the chromium substituted copper ferrite system is successfully prepared by sol-gel autocombustion technique. The prepared chromium substituted copper ferrite system shows single phase cubic spinel structure. The lattice constant decreases with Cr^{3+} ions substitution. The

experimental data of electrical properties leads electrical resistivity measurements show that the resistivity increases with composition for chromium substituted copper ferrite. The electrical resistivity decreases with increase in temperature as can be seen from logarithm of resistivity versus temperature plots for chromium substituted copper ferrite. The values of Curie temperature obtained from the DCR method and Loria technique are very close agreement to each other. The conduction mechanism can be explained on the basis of hopping of polaron as activation energy values are found to be less than 0.2 eV.

REFERENCES

1. Mostafa, A. A., El-Shobaky G. A. & Girgis E. (2006), Effects of ZnO-doping on structural and magnetic properties of $CdFe_2O_4$. *Journal of Physics D: Applied Physics10(39)* 124-130.

2. Normura, T. and Nakano, A. (1992), New Evolution of Ferrite for Multilayer Chip Components, Ferrites. *6th International Conf. on Ferrites, Tokyo.* 1198

3. Mossad, M.M., Ahmed, M. A., Eil-Hiti, M.A. & Attia S. M. (1995), Semiconductive properties of Cu-Cr ferrites. *Journal of Magnetism and Magnetic Materials*, (150) 51-56

4. A.A.Sattar, (2003),Temperature Dependence of the Electrical Resistivity and hermoelectric Power of Rare Earth Substituted Cu-Cd ferrite, *Egyption Journal Sol-gel., 2(26)113-121*

5. Shinde, B. L., Suryavanshi, V. S. & Lohar, K. S. (2017), structural and magnetic properties of Cr3+ substituted Nickel Zinc Copper Nano ferrites *Internationa journal of material science,* 12(3) 433-442

6. Imran, S., Amin, N., Arshad, M. I., Islam, M.U., Anwar, H., Azam, A., Ahmad, M., Fakhar- E-Alam, M., Murtaza, G. & Mustafa, G. (2016), Structural and Optical properties of Cr substituted Mg ferrite synthesis by co-precipitation method. *Digest journal Nanomaterials and Biostructures.* 11(4) 1197-1204

7. Phanjoubam, & Prakash, C. (2002), Magnetic properties of vanadium substituted lithium zinc titanium ferrite. *Modern Physics Letters* B. (16) 1027

8. S.S. Ata-Allah, M.Yehia, (2009) Transport properties and conduction Mechanismsin $CuFe_2O_4$ and $Zn_xGa_{0.3}Fe_{1.7}O_4$; with(0.0rxr0.5) compounds. Physica- B (404) 2382-2388

9. Monica Sorescua, Diamandescua, L., Peelamedub, R., Royb, R. & Yadojic, P. (2004), structural and magnetic properties of NiZn ferrites prepared by microwave sintering method , *Journal of Magnetism and Magnetic Materials* (279) 195–201

10. Abdeen, A. M., Hemeda, O.M., Assem, E.E., & El-Sehly, M.M., (2002), structural, electrical and transport phenomena of Co ferrite substituted by Cd. *Journal of Magnetism and Magnetic Materials,* (238) 75

11. P.B.C.Rao, S.P.Setty Yattinahalli, (2010) Electrical properties of Ni-Zn nano ferrite Particles. *International Journal of Engineering Science and Technology*, 2(8), 3351-3354

NONLINEAR REFRACTIVE INDEX, ABSORPTION COEFFICIENT AND THIRD ORDER NONLINEAR SUSCEPTIBILITY OF GOLD NANO COLLOIDS

A. L. Sunatkari[1], S. S. Talwatkar[2], Y. S. Tamgadge[3] and G. G. Muley[4]
Assistant Professor[1], Department of Physics, N. G. Aacharya and D. K. Maratha College of A. S. C., Chembur
Associate Professor[2], Department of Physics, Siddhartha College of Arts, Science and Commerce, Mumbai
Assistant Professor[3], Department of Physics, Mahatma Phule Arts, Commerce & S.R.C. Science College, Warud
Assistant Professor[4], Department of Physics, Sant Gadge Baba Amravati University, Amravati

ABSTRACT
Nonlinear optical responses of gold nanocolloidal suspension were investigated using single beam Z-scan technique using He-Ne laser beam in CW regime operated at 632.8.8 nm as an excitation source. The nonlinear refractive index estimatedas large as $n_2 = (2.30 - 1.6) \times 10^{-6} cm^2 W^{-1}$, absorption coefficient $\beta = (3.80 - 1.80) \times 10^{-6} cmW^{-1}$ and third order nonlinear optical susceptibility $\chi^3_{eff.} = (3.29 - 2.21) \times 10^{-6} esu$ for colloidal GNPs suspension. The sign of nonlinear refractive index (n_2) was found negative, suggesting self-defocusing nature of samples. The Nonlinear refractive index, absorption coefficient and third order nonlinear susceptibility have found decreasing with the concentration of L-arginine used as stabilizer. The huge nonlinearity is attributed to the thermally induced thermo-optic phenomenon.

Keywords: Gold nanoparticles, L-arginine, nonlinear refractive index, nonlinear optical susceptibility, Z-scan technique, thermo-optic effect.

1. INTRODUCTION
The dependence of nonlinear properties of MNPs as function of size, shape, Surface Plasmon Resonance (SPR) band and refractive index of surrounding matrix is attracted great attention due to their applicability in sensors, photonics, LEDs etc. [1-7]. Under the illumination of strong electric field such as laser light, refractive index of material or/and medium vary as highly intense light passes through it. The intensity- dependant refractive index is called nonlinear refractive index (n_2) [8-12]. It is also associated absorption that changes with intensity.

Theany change in n_2 and in absorption, originates important nonlinear optical phenomenon such as self-focussing and defocussing, second- harmonic generation, four wave mixing and optical switching [13-14].

The objective of this work is to prepare GNPs in colloidal form stabilized with various concentration of L-arginine. The effect of L-arginine concentration on SPR, size of GNPs as well as on nonlinear refractive index (n_2), nonlinear absorption (β) and third order NLO susceptibility (χ^3_{eff}) of colloidal GNPs using Z-scan technique is studied.The underlying mechanism for NLO responses is discussed.

2. CHEMICALS AND EXPERIMENTAL PROCEDURE
2.1 Materials
Gold (III) chloride hydrate (HAuCl$_4$, 99.999 % purity), sodium borohydride (NaBH$_4$, 98% purity), L-arginine (99% purity) and PVP (MW 10000) purchased from Sigma-Aldrich and used without further purification. De-ionised water was used in synthesis process. L-arginine acid was used as capping agent and NaBH$_4$ was used as a reducing agent.

2.2 Synthesis Of L-Arginine Protected Colloidal GNPs Suspension
GNPs stabilized in various concentration of stabilizer (L-arginine) were synthesized by chemical reduction method. Stock solutions of 0.005 M HAuCl$_4$, 0.010 M NaBH$_4$ were prepared. L-arginine solutions with 0.001 M, 0.0025 M, and 0.005 M concentration were prepared by dissolving appropriate amount in de-ionised water. All solutions were kept in ice-bath for 20 min. In 200 ml volumetric flask, 30 ml de-ionised water and 10 ml NaBH$_4$ and 20 ml L-arginine solutions were taken and stirred at 50° c for 20 min to remove any excess NaBH$_4$. GNPs colloidal solution was obtained by drop wise addition of 20 ml gold precursor into the above mixture. Solution was turned light pink (stable colour) in colour in 10 min indicating formation of GNPs. As-synthesized GNPs colloidal suspension was purified by repeated centrifugation and washing, and were stable for long duration of 3 months.

2.3 Nonlinear Optical Measurements
Nonlinear optical studies such as third-order nonlinear susceptibility, nonlinear refractive index and nonlinear absorption were determined for L-arginine stabilized (at various concentrations) GNP colloid and GNPs-PVP

thin film by Z-scan technique. Standard Z-scan set up, as shown in the fig.1, is used for the measurements executed with low power 10 mW He-Ne Laser beam of wavelength 632.8 nm in CW regime.GNP Colloid samples were taken in the 1 mm path length quartz cuvette. In the present experimental set up laser beam is focussed using lens of 20 cm focal length. The beam waist is found 22 μm and Rayleigh length is $Z_0 = 2.4$ mm. Thin film samples were mounted on the sample holder placed at Z_0 position and moved to and fro along Z-axis. At each position on Z-axis, input beam energy and transmitted beam energy is measured with the help of detector. The experiment is carried out for open aperture as well as closed aperture configuration to estimate intensitydependent nonlinear refraction, nonlinear absorption and third order nonlinear susceptibility of GNP colloids
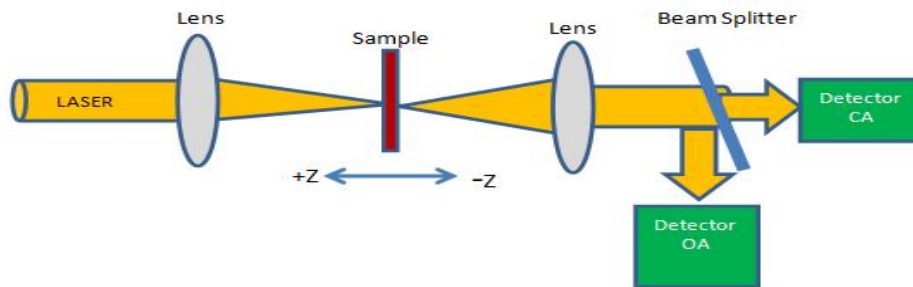

Fig-1: Schematic diagram of Z-scan setup

3. RESULTS AND DISCUSSION
3.1 Linear Optical Studies Of Colloidal GNPs
Linear optical properties of colloidal gold nanoparticles are studied.As we increased the concentration of L-arginine from 1 to 5 mM, the resonance absorption peak is found shifted from 520 to 512 nm for GNPs colloidal suspension indicating the blue shift. The XRD study reveals that average size of GNPs is found about 11.5 nm, 10 nm, 8 nm for 1, 2.5 and 5 mM L-arginine concentration respectively.The average sizes found from TEM images are 11 ± 0.4, 9 ± 0.6 and 7.5 ± 0.3 nm for 1, 2.5, and 5mM L-arginine concentration respectively. All these results are published in the [15].

3.2 Nonlinear Optical Studies Of Colloidal GNPs
The intensity of transmitted beam is recorded with OA configuration as well as CA configuration. The variation of transmittance experienced by thin films is shown in the **fig.2.**
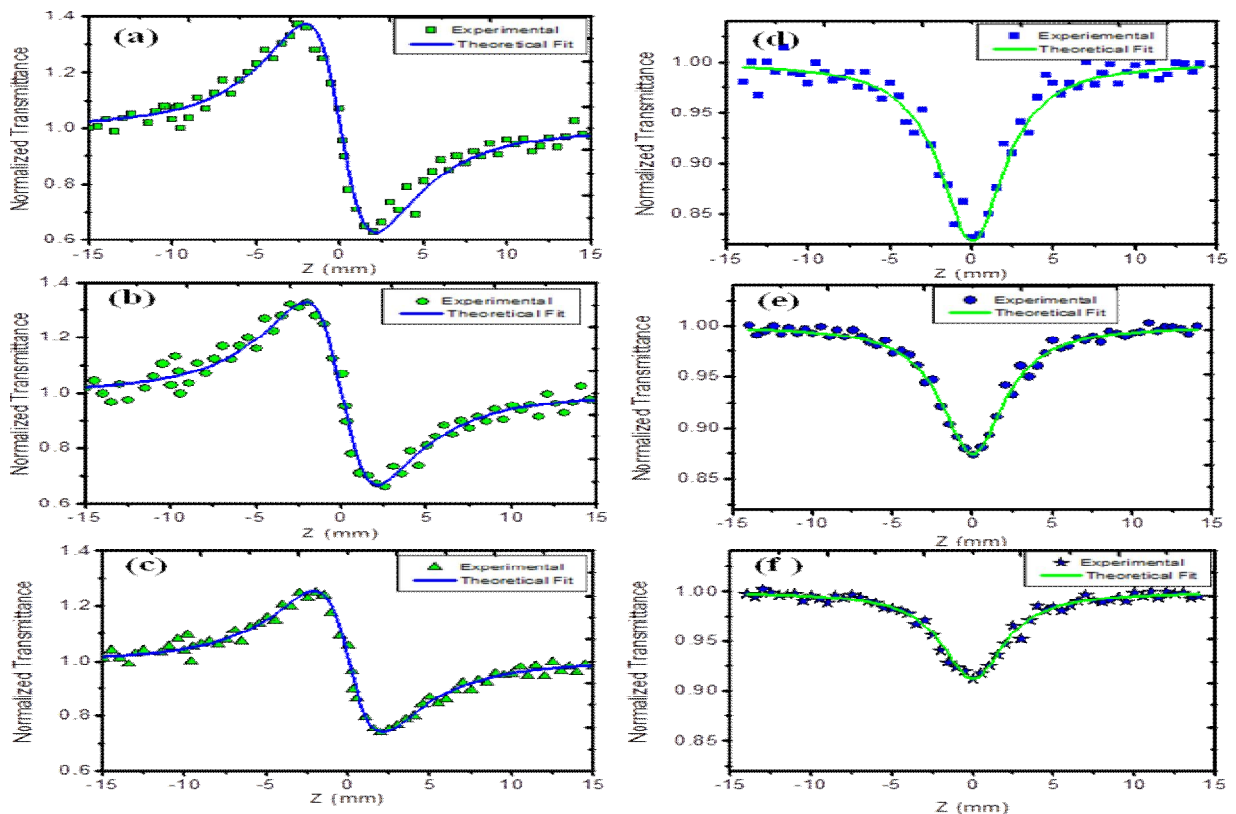

Fig-2 (a), (b), (c) are CA transmittance curves and (d), (e), (f) are OA transmittance curves of the colloidal GNPs stabilized in 1, 2.5 and 5 mM L-arginine concentration respectively.

The estimated values for nonlinear refractive index (n_2) and third order nonlinear susceptibility (χ^3) are listed in **Table 1.**

Table-1: Measured values of NLO parameters of colloidal suspension of GNPs stabilized in 1, 2.5 and 5 mM L-arginine

Sample	Stabilizer (L-arginine) concentration	GNPs Size (nm)	ΔT_{P-V}	$\lvert\Delta\phi_0\rvert$	n_2 cm^2/w 10^{-6}	β cmw^{-1} 10^{-6}	Re. χ^3 esu 10^{-6}	Im χ^3 esu 10^{-10}	χ^3_{eff} esu 10^{-6}
				Colloidal GNPs					
GNP1	1.0 mM	11	0.65	1.84	-2.3	3.80	3.29	2.70	3.29
GNP2	2.5 mM	9	0.57	1.63	-2.1	2.71	3.03	1.93	3.03
GNP3	5.0 mM	7.5	0.45	1.27	-1.6	1.80	2.21	1.28	2.21

We have noticed decrease in the magnitude of nonlinear refractive index (n_2), and third order NLO susceptibility (χ^3) and nonlinear absorption (β) with the increase of L-arginine concentration. It may be because of the formation of smaller size GNPs by L-arginine. The closed aperture z-scan curves for all samples show a peak-valley separation of more than 1.7 times Rayleigh Range Z_R. A peak-valley separation of more than 1.7 times the Rayleigh range is clear indication of thermal nonlinearity and indicates that the observed nonlinear effect is the third-order process [16-21].

3.3 CONCLUSION

In summary, the nonlinear optical parameters of colloidal GNPs stabilized in the various concentrations of L-arginine were estimated. We found huge enhancements in GNP-PVP matrix compared to the colloidal GNPs. The magnitude of n_2 and $\chi^{(3)}$ was found decreasing in with increase in concentration of L-arginine. The negative sign of n_2 indicates self-defocussing phenonmenon of ollidal GNPs. The enhancement of n_2, β and $\chi^{(3)}$ is due to the combined effect of SPR and thermo-optical phenonmenon attributed to the Kerr optical nonlinearity and local field factor.

3.4 REFERENCES

1. Daniel M. C. &AstrucD.,(2004)"Gold Nanoparticles: Assembly, Supramolecular Chemistry, Quantum-Size-Related Properties, and Applications toward Biology, Catalysis, and Nanotechnology**"** *Chem. Rev.*104, 293-346.

2. Shahriari E., Yunus W. M. M., Saion E., (2010)"Effect of particle size on nonlinear refractive index of Au nanoparticles" ,*Braz.J. Phys.*, 40, 256-260**.**

3. Tamgadge Y. S., Talwatkar S. S., Sunatkari A. L., Pahurkar V. G., & Muley G. G. (2015) "Studies on nonlocal optical nonlinearity of Sr–CuO–polyvinyl alcohol nanocomposite thin films", *Thin Solid Films*, 595, 48-55.

4. Aryal S., Remant B., Dharmaraj N., Bhattarai N., Kim C., Kim H., (2006)"Spectroscopic identification of S-Au interaction in cysteine capped gold nanoparticles",*SpectrochimicaActa Part A,* 63, 160-163 .

5. Joshi H., Shirude P. S., Bansal V., Ganesh K. N., Sastry M., (2004)"Isothermal titration Calorimeter studies on the binding of Amino acids to gold nanoparticles" ,*J. Phys. Chem. B. ,* 108, 11535-11540.

6. Loo C., Lin A., Hirsch L., Lee M., Barton J., Halas N,West J., (2004) "Nanoshell enabled photonic based imaging and therapy of cancer", *Technol. Cancer Res. Treat,* 3, 33-40.

7. Murray C., Sun S., Doyle H., Betley T., (2001) "Monodisperse 3d transition metals nanoparticles and their assembly in to nanoparticle superlattices", *MRS Bull.,* 26, 985-991**.**

8. Talwatkar S. S., Sunatkari A. L., Tamgadge Y. S., Muley G. G. (2018), "Nonlinear optical properties of Nd^{3+}-Li^+ co-doped ZnS-PVP thin films", *AIP Conference Proceedings* 1942 (1), 080060

9. Uchida K., KanekoS., Omi S., HataC., TanjiH., AsaharaY., &IkushimaA.,(1994) **"**Optical nonlinearities of a high concentration of small metal particles dispersed in glass: copper and silver particles"*J. Opt. Soc. Am. B* 11 1236-1243

10. Cotter D., Manning R. J. , Blow K. J., Ellis A. D., Kelly A. E., NessetD., Phillips I. D., PoustieA. J., & Rogers D. C., (1999) "Nonlinear Optics for High-Speed Digital Information Processing" *Science,* 286, 1523-1528

11. Talwatkar S. S., Sunatkari A. L., Tamgadge Y. S., Muley G. G. (2018), "Nonlinear optical properties of Nd^{3+}-Li^+ co-doped ZnS-PVP thin films", *AIP Conference Proceedings* 1942 (1), 080060

12. Hirsch L. R., Stafford R. J., BanksonJ. A., SershenS. R., Price R. E., HazleJ. D., Halas N. J., & West J. L., (2003) Proceeding of the Academy of Sciences (USA) PNAS 100 13549-13554.

13. KreibigU. &VollmerM., Optical Properties of Metal Clusters,Springer, Berlin, 1995.

14. Chen H., Kou X., Yang Z., Ni W., & Wang J., (2008),"Shape- and size-dependent refractive index sensitivity of gold nanoparticles",*Langmuir,* 24, 5233-5237.

15. Sunatkari A. L., Talwatkar S. S., Tamgadge Y. S, & Muley G. G. (2015). "Enhanced nonlinear optical properties of L-arginine stabilized gold nanoparticles embedded in PVP polymer", *AIP Conference Proceedings,* 1953 (1), 100008.

16. ShreejaR., AneeshP. M., ArvindA., ReshmiR., Philip R., &JayarajM. K., (2009) "Size-dependent optical nonlinearity of Au nanocrystals*" J. Electrochem. Soc.*,156 K167-K172.

17. Sunatkari A. L., Talwatkar S. S., Tamgadge Y. S, Muley G.G. "Synthesis, characterization and properties of L-arginine-passivated silver Nanocolloids", *AIP Conference Proceeding,,* 1728 (1), 020663

18. ShalaevV. M., PoliakovE. Y.,&Markel V. A. (1996), "Small-particle composites. II.

Nonlinear optical Properties" *Phys. Rev.B*, 53, 2437-2449.

19. StepanovA. L., (2011), "Nonlinear Optical Properties Of Implanted Metal NanoparticlesIn Various Transparent Matrixes: A Review" *Rev. Adv. Mater. Sci.* ,27, 115-145.

20. House J. W., Zhou H. TakamiS., HirasawaS., M.,Honma I., & Komiyama H., (1993) "Enhanced optical properties of metal-coated nanoparticles,"*J. Appl. Phys*,. 73, 1043-1048.

21. Sunatkari A. L., Talwatkar S. S., Tamgadge Y. S, & Muley G.G (2015) "Influence of SurfacePassivation by L-Arginine on Linear and Nonlinear Optical Properties of Ag-PVP Nanocomposite", *American Journal of Materials Science* , 5 (3A), 21-30

HYSTERESIS CURVE OF COMPOSITE MATERIAL

R. A. Kunale[1], R. H. Kadam[2], G. B. Todkar[3] and D. R. Mane[4]
[1]Kai. Rasika Mahavidyalaya, Deoni, Latur
[2]Shrikrishna Mahavidyalaya Gunjoti, Osmanabad
[3]Dayanand Science College, Latur
[4]Director of Higher Education, Pune

ABSTRACT

The ferrite (magnetic material) - ferroelectric (electric material) composites with general formula $(1-x)Ni_{0.5}Cu_{0.3}Mg_{0.2}Fe_2O_4+ (x) BaTiO_3$ in which x = 0, 0.20, 0.40, 0.60, 0.80,1 mol areprepared by conventional solid state reaction. The Hysteresis loop of above mentioned sample is obtained by using Vibrating Sample Magnetometer (VSM) at room temperature. The presence of ferroelectric phase($BaTiO_3$) affects the values of Saturaton magnetization (Ms), magneton numberand Remanent magnetization (Mr). From VSM study it is observed that the values of saturation magnetization and remanent magnetization decreases as the content of ferrite i.e. magnetic material decreases.

Keywords: Coercivity, Composite, Ferrite, Ferroelectric, Hysteresis loop.

1. INTRODUCTION

The material containing ferrite and ferroelectric composition this type of material is called magnetoelectric(ME) composites. ME composite possess maagnetoelectric effect in which the two effect i.e. electric and magnetic field coupled together. This effect would make the conversion between electric energy and magnetic energy possible, which provides opportunities for potential applications as ME memories, waveguides, transducer, actuators and sensors [1-5]. This effect in composites is due to strain induced in the ferrite phase, thereby resulting in polarization of the ferroelectric phase due to piezoelectric effect [6]. Thus the ME effect is result of inherent properties such as magnetostriction and piezoelectric effect of the constituent phases present in the composite. In spite of the low value observed in dE/dH, these composites are of scientific and technological interest. The study of such composites provides a unique tool to characterize the material simultaneously in single phase and in composite form. This effect also gives auxiliary information for determining the magnetic point groups and space groups [7,8]. This means that they provide a complementary tool to neutron diffraction, which seldom allows us to determine the magnetic point group and space group unequivocally, other scientific interests are accurate determination of magnetic phase transitions, electric field induced magnetic phase transitions, etc.

As reported the some ferrite is highly resistive and magnetostrictive [9] and $BaTiO_3$ has high dielectric permittivity. If the two compounds can be successfully incorporated into a composite, it is expected that the composites might have interesting properties. Hence we have chosen $Ni_{0.5}Cu_{0.3}Mg_{0.2}Fe_2O_4$ as a ferrite phase and $BaTiO_3$ as a ferroelectric phase to form the composites. There are different methods use to prepare composite material like molten-salt synthesis [10],situ grown [11] and Hydrothermal synthesis [12].Here the composite of ferrite $Ni_{0.5}Cu_{0.3}Mg_{0.2}Fe_2O_4$ + ferroelectric $BaTiO_3$ prepared by solid state reaction. The structuraland magnetic properties of composite material having general formula (1-x) $Ni_{0.5}Cu_{0.3}Mg_{0.2}Fe_2O_4$ + (x) $BaTiO_3$, where x=0.0, 0.2, 0.4, 0.6, 0.8 and 1studied.

2. EXPERIMENTAL

The components of present composites are $BaTiO_3$ as ferroelectric phaseand $Ni_{0.5}Cu_{0.3}Mg_{0.2}Fe_2O_4$ as a ferrite phase with general formula $(1-x)Ni_{0.5}Cu_{0.3}Mg_{0.2}Fe_2O_4+ (x) BaTiO_3$ in which x = 0, 0.20, 0.40, 0.60, 0.80,1 mol were prepared by conventional solid state reaction. The ferrite phase was prepared by NiO, CuO, MgO, and Fe_2O_3 in required molar proportions. These oxides were mixed and grind in agate mortar for couple of hours. The ferroelectric phase was prepared by using BaO and TiO_2 as starting materials. These oxides are also mixed and grind in agate mortar. The ME composites were prepared by mixing 0.8,0.6,0.4 and 0.2 mol of ferrite phase with 0.2,0.4,0.6,and 0.8 mol of ferroelectric phase respectively. The required molar proportions were mixed and grind for 3 hour. The grind powder mixture was pressed into pellets using hydraulic press. The pelletized sample was final sintered in programmable furnace and slow cooled to room temperature to yield the final product. The crystal structures of prepared sample and their constituent phases were determined by XRD technique using Philips X-ray diffraction using Cu-K$_\alpha$ radiation.The Hysteresis curve is obtained by VSM at room temperature.

3. RESULT AND DISCUSSION
3.1 X-ray Diffraction

The X-ray diffraction patterns are shown in Fig1. and Fig. 2 for a sample with x=0.40 and x=0.80 respectively. Fig.1 and Fig.2displays the formation of spinel cubic–perovskite mixed structure. They exhibit strong and broadened peaks around 2θ angles of 22.14°, 32.55°, 38.85°, 45.14°, and 56.14° together with weak and broadened peaks around 2θ angles of 50.72°, 65.67°, 69.79°and 74.44°indicating the perovskite ferroelectric with tetragonal structure. The peaks around the 2θ angles of 30.41°, 35.78°, 43.45°, 57.42° and 63.01°appear, indicating that the spinel Ni-Cu-Mg ferrite with cubic structure have been formed in the composite. It is also observed that the peak intensity of higher intensity peak of ferrite (311) plane decreases as the ferrite composition decreases and the peak intensity of higher intensity peak of ferroelectric (101) plane increases with increase in ferroelectric composition in the composites.
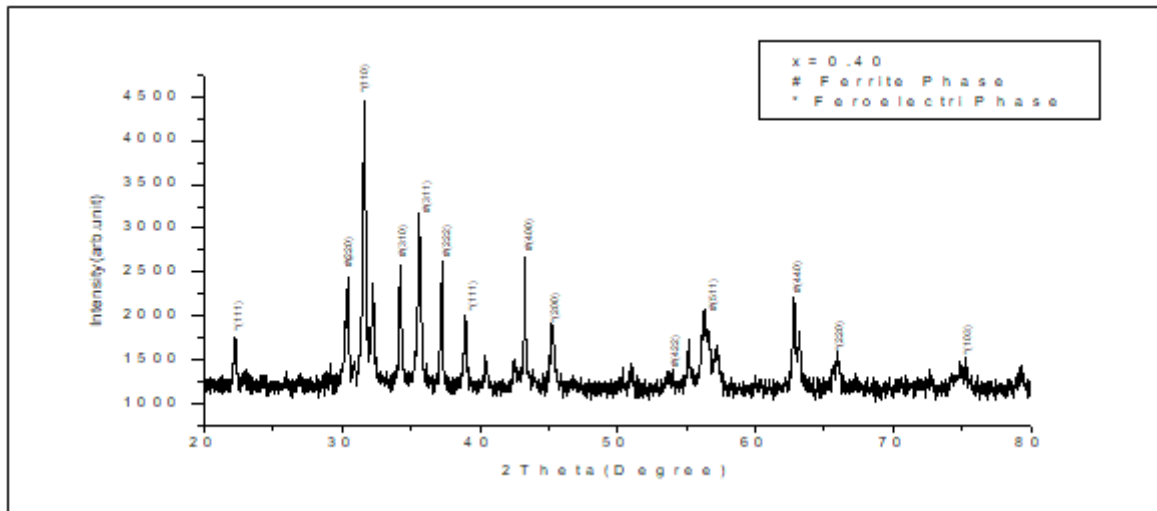

Fig-1: XRD pattern of $(1-x)$ $Ni_{0.5}Cu_{0.3}Mg_{0.2}Fe_2O_4+(x)$ $BaTiO_3$ for x=0.4.
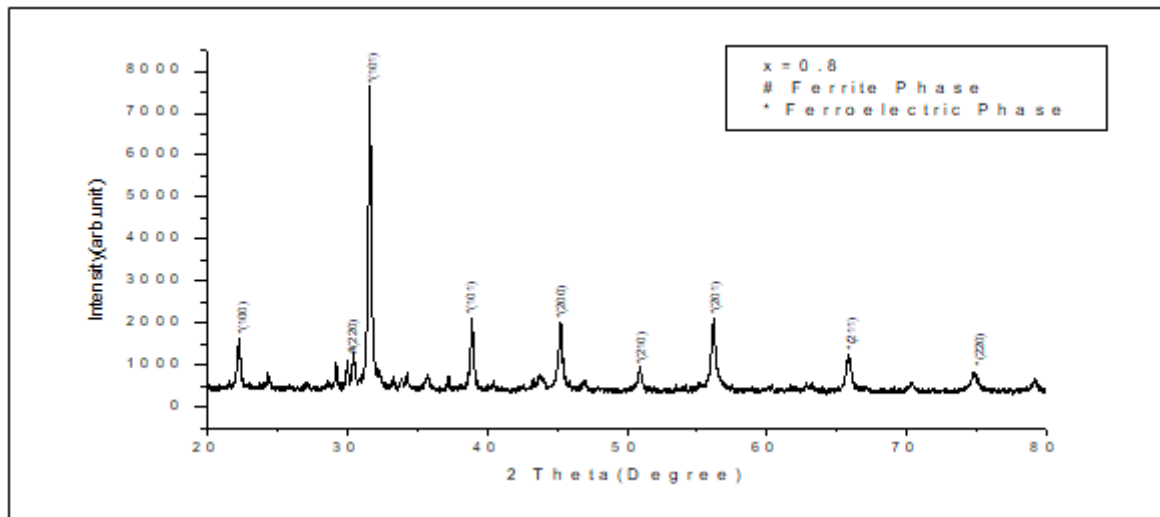
Fig-2: XRD Patterns of $(1-x)$ $Ni_{0.5}Cu_{0.3}Zn_{0.2}Fe_2O_4+(x)$ $BaTiO_3$ for x=0.8

3.2 Hysteresis Curve

From hysteresis loop magnetic parameters are studied as a function of both magnetic field and ferroelectric content. Magnetic hysteresis loop measurements were carried out using a vibrating sample magnetometer (VSM). The saturation magnetization (Ms) was obtained from magnetic hysteresis loops. The saturation magnetization (M_S) is a measure of the maximum amount of field that can be generated by a material. It will depend on the strength of the dipole moments on the atoms that make up the material and how densely they are packed together.

The hysteresis curve of the present composite $(1-x)$ $Ni_{0.5}Cu_{0.3}Mg_{0.2}Fe_2O_4 + (x)$ $BaTiO_3$,where x=0.0, 0.4, 0.6, 0.8 and 1.0, sample are shown in Fig.3. The values of saturation magnetization (M_s), remanent magnetization (M_r) and coercive field (H_c) are obtained from hysteresis curve.From Fig.1 it is clear that all composite possess magnetic hysteresis loop, it shows that the composites are magnetically ordered. It can be understood from

hysteresis loop that the composite hysteresis loops shift towards the field axis as ferrite content decreases. The magnetic moment per atom in Bohr magnetron for each composition is calculated using the experimental value of saturation magnetization. The formula for magnetic moment is given by

$$n_\beta = \frac{M_S \times M}{N \times \beta} \tag{1}$$

Ms is Saturation magnetization, M is molecular weight and N is Avogadro's number (6.024 x 10^{23} gm/mol),β is the conversion factor to express the magnetic moment per atom in Bohr magnetron (9.273X10^{-21}erg/gauss)
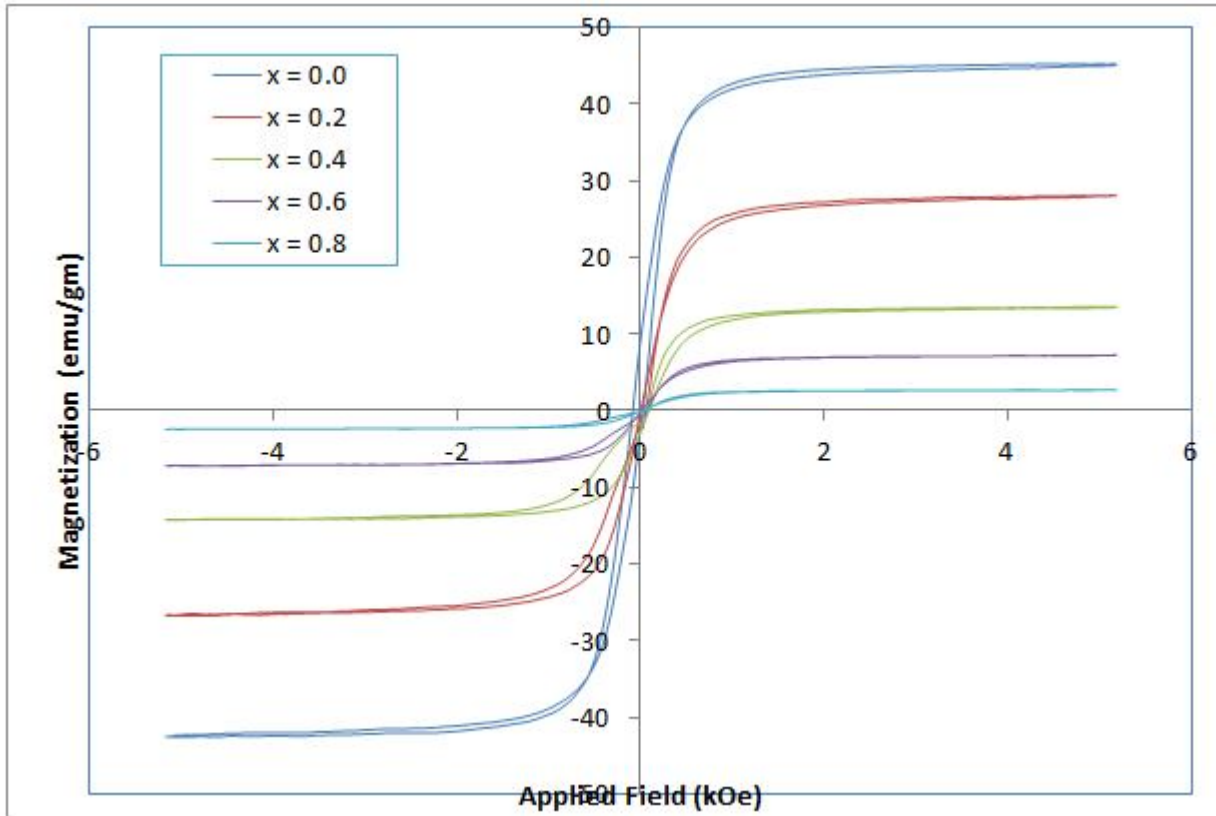

Fig-1: Variation of magnetization (M) with applied field (H)(1-x)Ni$_{0.5}$Cu$_{0.3}$Mg$_{0.2}$Fe$_2$O$_4$+(x)BaTiO$_3$ for (x = 0.0-1.0)
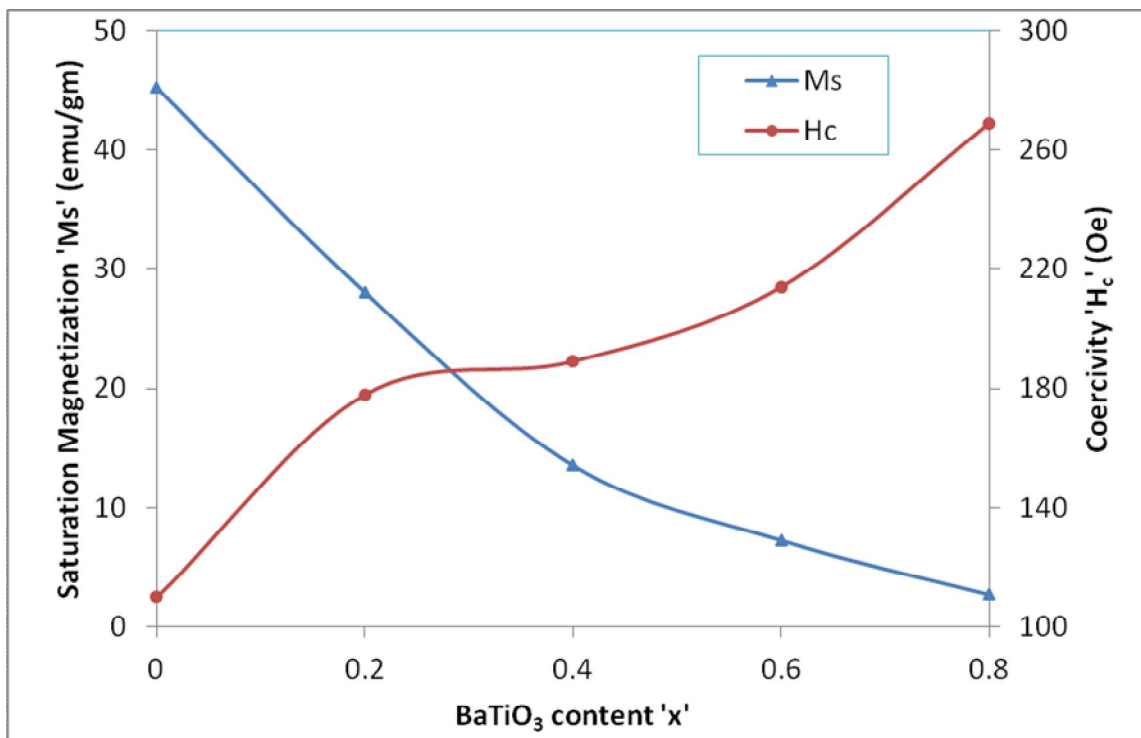

Fig-1: Variation of Msand Hc with BaTiO$_3$ content 'x' for (1-x)Ni$_{0.5}$Cu$_{0.3}$Mg$_{0.2}$Fe$_2$O$_4$+

$(x)BaTiO_3$ for $(x = 0.0-1.0)$

Table 1 shows the values of saturation magnetization, remnant magnetization, rem- nance ratio and magneton number. From Table 1 it is observed that the highest value of saturation magnetization is 45.2 emu/gm is obtained for sample with x=0.00 sample. The values of saturation magnetization and remanent magnetization decreases as the content of magnetic material i.e. ferrite decreases. It is also observed that the value of remanence ratio lies in the range of 0.31-0.74. Remnance ratio increases as ferrite content decreases. The decrease in value of saturaton magnetization and remanent magnetization (M_r) is due to increasing nonmagnetic ferroelectric $BaTiO_3$ content of the composite sample. It is also observed that the magnetron number decreases as ferrite content decreases.

Table-1: Saturation magnetization (Ms), remanent magnetization (Mr),remanence ratio (R) and magneton number for $(1-x)Ni_{0.5}Cu_{0.3}Mg_{0.2}Fe_2O_4+(x) BaTiO_3$ for $(x = 0.0-1.0)$.

Comp. 'x'	Saturation Magnetization Ms (emu/g)	Remanent Magnetization Mr (emu/g)	Remnance Ratio R=(Mr/ Ms)	Magneton Number η_B
0	45.2	14.33	0.31	1.85
0.2	28.07	9.51	0.33	1.16
0.4	13.56	4.89	0.36	0.56
0.6	7.27	3.48	0.47	0.30
0.8	2.73	2.03	0.74	0.11

4. CONCLUSION

The ME composites have been prepared successfully by conventional solid state reaction. The X-ray diffraction peaks are characteristics of both ferrite and ferroelectric phases. The intensity as well as number of ferroelectric peaks increases with increase in ferroelectric content in composites. It may be due to increase of molar percentage of ferroelectric.The magnetic properties of composites are investigated by using Vibrating Sample Magnetometer (VSM) at room temperature. The presence of hysteresis loop for all the sample of composite material under investigation indicates that the composites are magnetically ordered. The values of remanence ratio increases as ferrite content decreases, this is due to decrease in magnetic content. The saturation magnetization, remanent magnetization and magneton number decreases as the ferrite content decreases. Dielectric constant, dielectric loss and dielectric loss tangent were decreases with increase in frequency.

REFRENCES

1. Islam R. A., Priya S.(2006) Synthesis of high magnetoelectric coefficients composites using annealing and aging route. Int J Appl Ceram Technol, 3, 353–63.

2. Gupta A., Huang A., Shannigrahi S., Chatterjee R.(2011) Improved magnetoelectric coupling in Mn and Zn doped CoFe2O4–PbZr0.52Ti0.48O3 composites. ApplPhysLett, 98,112901–3.

3. Jaffe H. (1958). Piezoelectric Ceramics, J. Am. Ceram. Soc., 41(11) 494–98.

4. Nan C.W., Cai K.F., Yuan R.Z. (1996). A relation between multiple-scattering theory and micromechanical models of effective thermoelastic properties", Ceramics international, 22(6), 457-461.

5. Min X.M. Cai K.F., Nan C.W., Yuan R. Z.,(1996) structure, properties and quantum-chemistry studies on nonstoichiometric compounds of (NBYTI1-Y)C-X", Ceramics international, 22(3),193-196

6. Sukhov A., Horley P.P.,Jia, C.L., Chotorlishvili L., Berakdar J.(2014) Finite-size effects on the magnetoelectric coupling in a ferroelectric /ferromagnetic structure revealed by ferromagnetic resonance, EPJ Web of Conferences ,75, 09001-4.

7. Rivera J. P., (2011). On definitions, units, measurements, tensor forms of the linear magnetoelectric effect and on a new dynamic method applied to Cr-Clboracite, Ferroelectrics, Vol 161,165-180

8. Schmid H., (1994). Magnetic ferroelectric materials,Bulletin of Materials Science, Volume 17 (7), 1411–1414

9. Patankar K.K., Dombre P. D., Mathe V.L., Patil S.A., Patil R. N. (2001). Dielectric behavior and magnetoelectric effect in CuFe2O4–Ba0.8Pb0.2TiO3 composites, Mater. Sci. and Engg. B, 87 (2001) 53.

10. Nie J, Xu G, Yang Y, Cheng C.(2009). Strong magnetoelectric effect in $CoFe_2O_4$–$BaTiO_3$ composites prepared by molten-salt synthesis method. Mater Chem Phys.115400–3.

11. S. Mazumder, Battacharya G,S., (2003). Magnetoelectric behaviour in in situ grown piezoelectric and piezomagnetic composite phase system, Vol 38(2),303-310.

12. W. J. Dawson W. J.(1988)Hydrothermal Synthesis of Advanced Ceramic Powders," Am. Ceram. Soc.Bull., 67(10) 1673–38 (1988).

STRUCTURAL AND MAGNETIC PROPERTIES OF $Ba_{1.477}Ti_{2.744}Fe_{6.963}Li_{1.477}O_{19}$ and $Ba_{1.055}Ti_{3.166}Fe_{7.385}Li_{1.055}O_{19}$

V. H. Joshi[1], A. R. Ingle[2], N. N. Sardesai[3] and S. Radha[4]
Associate Professor[1,3] and Assistant Professor[2], Bhavans's Hazarimal Somani College, Mumbai
Asistant Professor[4], Department of Physics, University of Mumbai, Mumbai

ABSTRACT
AR grade powders of $Fe_2 O_3$, $BaCO_3$, Li_2CO_3 and TiO_2 were used to prepare samples of $Ba_{1.477}Ti_{2.744}Fe_{6.963}Li_{1.477}O_{19}$ and $Ba_{1.055}Ti_{3.166}Fe_{7.385}Li_{1.055}O_{19}$ by classical ceramic route. For comparison a pure sample of $BaFe_{12}O_{19}$ was also prepared. The structural and Magnetic properties have been studied by XRD, SEM, FTIR, Hysteresis loop and susceptibility curves. These samples of hexaferrites exhibit hexagonal magnetoplumbic structure. The room temperature remenance value M_R, coercive force Hc, squareness M_R/M_S and curie temperature T_c have been compared.

Keywords: x-ray diffraction, Magnetic susceptibility, Hysteresis, Hexaferrite.

PACS: 75.50.lk, 61.05.cp, 75.50.y, 75.30.Cr, 75.60.d

INTRODUCTION
Barium hexaferrite is a well known permanent magnet with great technical importance. Significant variations in the magnetic properties is reported in doped $BaFe_{12}O_{19}$.[1] Lithium Ferrite have attractive electric and magnetic properties for microwave and memory core applications.[2] Ba-Fe-Ti oxide system reveal existence of many compounds having wide variety of electronic applications. This has prompted us to study the influence of titanium and lithium substitution on the properties of barium hexaferrite.

EXPERIMENTAL TECHNIQUES
$BaFe_{12}O_{19}$(BFO) and its titanium and lithium substituted varieties namely, $Ba_{1.477}Ti_{2.744}Fe_{6.963}Li_{1.477}O_{19}$ (BTFLO1) and $Ba_{1.055}Ti_{3.166}Fe_{7.385}Li_{1.055}O_{19}$ (BTFLO2)were synthesized by maintaining the charge neutrality. The starting materials $Fe_2 O_3$, $BaCO_3$, Li_2CO_3 and TiO_2 (all 99.99% purity- AR grade) were dried in muffle furnace and mixed in stoichiometric proportion and then grounded and calcined in steps of 800^0 C and 900^0 C for 9 hours each for homogeneity. These mixtures were pressed into pellets and were finally sintered at 1150^0 C for 12 hours to ensure a complete reaction. The crystallographic structure was determined at room temperature using the X-ray diffraction pattern of powders using a highly sophisticated microprocessor based JEOL-JDX8030 diffractometer using a Cu target. The IR spectra of the compounds are recorded on the "Nicolet Instrument Corporation, USA" MAGNA 550 spectro Photometer at room temperature in the range from 50 cm^{-1} to 4000 cm^{-1}. The magnetic properties are obtained using hysteresis loop tracer.

RESULTs AND DISCUSSION
X-ray powder diffraction technique was used to confirm the structure and determine the lattice parameters of the prepared samples. FIGURE 1 shows the typical XRD pattern of BTFLO1 sample. All the x-ray pattern indicate a single phased hexagonal magnetoplumbitic structure as per the JCPDS data. The space group is presumed to be $P6_3$/mmc.[3] The physical properties show marked variation on doping.

Figure-1: XRD of $Ba_{1.477}Ti_{2.744}Fe_{6.963}Li_{1.477}O_{19}$
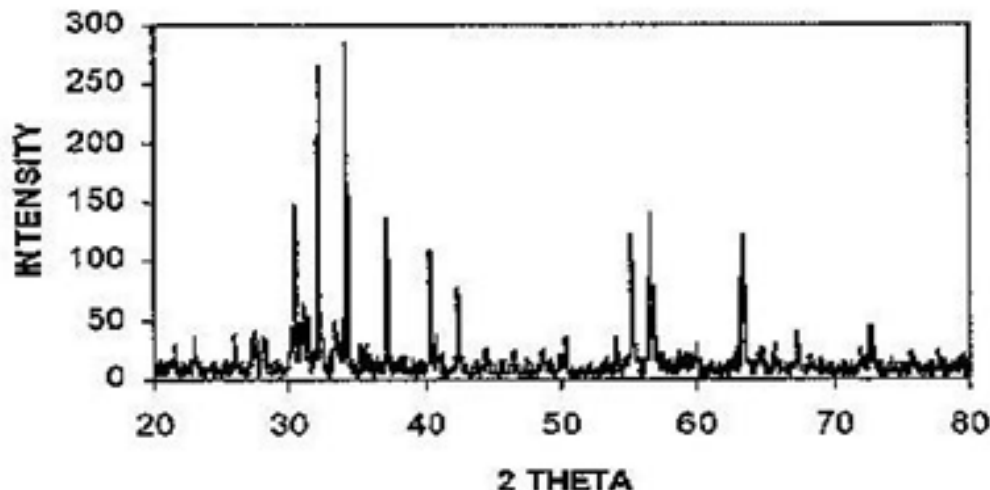
The 'a' and 'c' values calculated for all the samples are pertaining to the P6$_3$/mmc hexagonal unit cell structure. Lattice constant 'a' and 'c' varies for different samples and is maximum for BTFLO2. Lattice constant 'c' is increasing and density is decreasing with increasing the content of Titanium in samples. Particle size is increasing with increasing the content of lithium. The c/a ratio is minimum for BFO. The average particle size and the average grain size is more for the substituted samples.

Two prominent bands 590 cm^{-1} and 435 cm^{-1} appear in all the samples.[4] Random distribution may be the reason of broadening in the substituted samples. The SEMs are dense and homogeneous. Substitution results in an increase in grain size.

Figure-2: Magnetization versus field BTFLO1 at room temperature
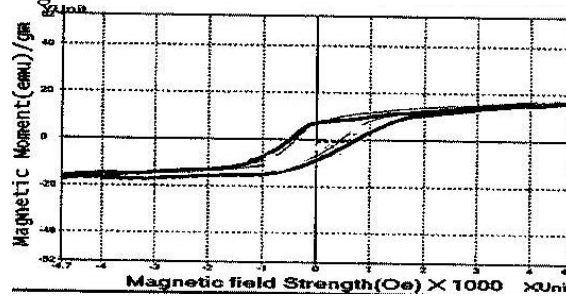
The results of room temperature saturation magnetization, remanence, coercivity, remanence ratio, anisotropy constant and curie temperature T_c are given in TABLE 1 with addition of Ti and Li and reduction of Fe in the M-type phase, the magnetic coupling becomes weak resulting in decrease in Curie point for the substituted samples. Magnetization verses field curve at room temperature for BTFLO1 sample is shown in FIGURE-2. With substitution there is a decrease in all the magnetic parameters. The substituted samples show soft magnetic features. The magnetic properties are shown in TABLE 1.

Table-1: Summary of Magnetic properties of hexaferrites

Properties	BFO	BTFLO1	BTFLO2
Coercive Force H_c (Oe)	1420	600	690
Remanence M_R (emu/g)	30	8	12
Saturation M_S (emu/g)	42	18	22
Squarness M_R/ M_S	0.7142	0.444	0.545
Anistropy constant K	21820	5400	7590
Curie temp (K)	750	490	580

CONCLUSION
Pure and lithium titanium doped samples of barium hexaferrite show the single phase hexagonal magnetoplumbic structure with space group P6$_3$/mmc. The decrease in values of M_R, M_R/M_S and T_c can be interpreted by assuming that the Li^{1+} ions replace Fe^{3+} ions of the octahedral 12k sites and hexahedral 2b sites, while Ti^{4+} ions replace the spin up fe^{3+} ions of the octahedral 4fv1 and 2a sites. Interesting variations in magnetic properties are observed in the substituted samples.

REFERENCES
1. Quanyuan, R. Lang, (2000). *Journal. of functional. Materials.***31(4)** 363.

2. S.K. Kulshreshta and G. Ritter, (1985) *Journal of . Material science. .***20** 3926.

3. Z. Somogyv et al, (2006) *Journal of .Magnetic. Materials.***302(2)** e775.

4. Huang, H.Zhaung, W. Li, (2003) Material. Research. Bulletin.**38(1)** 149.

FOCUSING SUPERIORITY OF S-R METHOD GROWN CRYSTAL OVER CONVENTIONALLY GROWN THIOUREA ZINC ACETATE (TZA) METAL COMPLEX CRYSTAL

Rupali B. Kulkarni[1,3], Siddique Aneesa Fatima[2], S. S. Hussaini[2] and Mahendra D. Shirsat[3]
[1]Department of Physics, Swa. Sawarkar Mahavidyalaya, Beed
[2]Crystal Growth Laboratory, Department of Physics, Milliya Arts, Science & Management Science College, Beed
[3]RUSA Centre for Advanced Sensor Technology, Department of Physics, Dr. Babasaheb Ambedkar Marathwada University, Aurangabad

ABSTRACT
Current scenario demands good quality crystals for the nonlinear optical (NLO) device applications. Hence present communication concentrates on the growth of Thiourea zinc acetate metal complex crystal (TZA) by novel Sankaran-Ramasamy(S-R) method as well as a conventional slow evaporation solution growth method. Present investigation deals with the study of comparative photoconductivity, thermal and electrical property of conventionally grown and S-R method grown Thiourea zinc acetate metal complex crystal (TZA). The resulting performance indicated superiority of S-R method over the conventionally grown TZA crystal for application for laser assisted NLO applications.

Keywords: Crystal growth, Photoconductivity, S-R method

1. INTRODUCTION
In the emerging photonic and optoelectronic technologies nonlinear optics is playing a major role. Novel nonlinear optical (NLO) frequency conversion materials have a significant impact on laser technology, optical communication and optical data storage **[1].** NLO crystals exhibiting high conversion efficiency performance has ever-increasing exigency become a challenging task for the research fraternity due to their extended umbrella of applications like photonics, laser fusion systems, laser imaging and sensing devices, telecommunication systems, SHG devices and many other laser-based industrial applications **[2].**

Organic crystals possess large susceptibilities but their inadequate transparency, poor optical quality, and lack of robustness, low LDT, and inability to grow to large size, volatility, low thermal stability, poor mechanical strength etc. impedes their use. **[2],** whereas inorganic crystals shows thermal and mechanical excelllency. The increasing demand of materials with large NLO property along with resistance to physical and chemical attack has led to the synthesis of semi-organic crystals **[3-4].**

Above mentioned qualities are actively expressed by Thiourea metal complex (TMC) family crystals. TMC crystals owe the contribution of the organic features of thiourea and the inorganic features of the metal ligand viz. Zn, Cd **[5].** Thiourea based organo metallic optical crystals like bis thiourea cadmium chloride, bis thiourea zinc acetate, bis thiourea bismuth chloride are some of the recent semi organic complexes **[6-19].** The thiourea zinc acetate (TZA) crystal with its growth, nucleation parameters and various fundamental properties was studied by many researchers. As per the literature survey, the TZA TMC crystal has eye catching effect due to its attractive NLO, electro-optic, physico-chemical and thermo-mechanical properties **[5].**In present investigation TZA crystal is grown by both the methods-conventional slow evaporation solution growth method and S-R Method and corresponding dielectric, photoconductivity and thermal traits are compared. Obtained results confirmed that the crystal grown by novel S-R method is superior to conventionally grown crystal.

2. EXPERIMENTAL PROCEDURE
Bis thiourea zinc acetate (TZA) was synthesized by mixing aqueous solution of zinc acetate and thiourea in the ratio of 1:2.The product was purified by repeated re-crystallization before it is used for crystal growth. The SR method growth setup consists of a heating coil, thermometer, inner container, temperature controller, growth vessel and water bath. The photograph of the grown crystals is shown in **Fig. 1.**Conventional slow evaporation method is also used to grow the TZA crystal at 34 °C.

Fig – 1: Conventionally & S-R method grown TZA crystal

3. RESULTS AND DISCUSSIONS
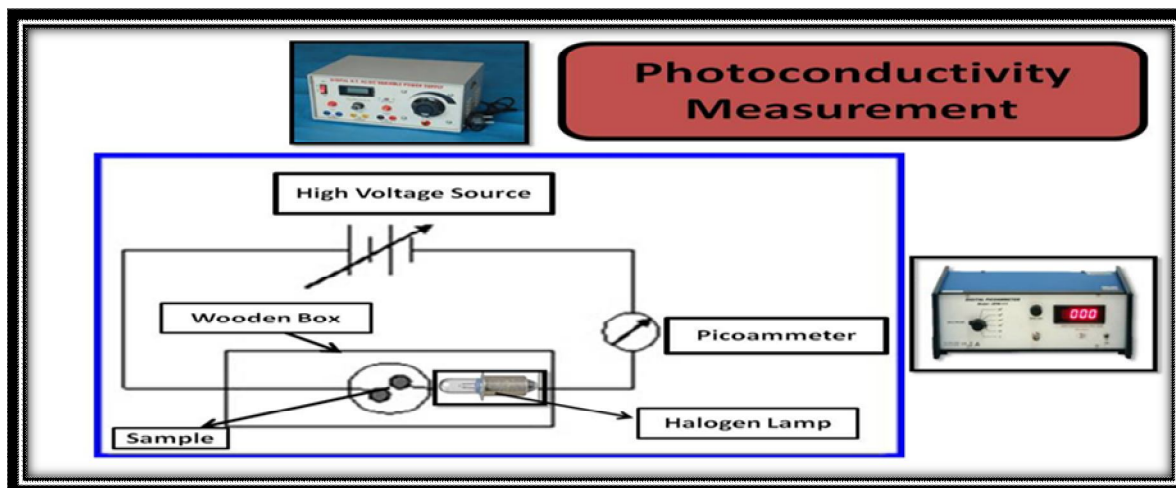### 3.1 Photoconductivity Measurement

Fig. – 2: Experimental set-up for photoconductivity measurement

Photoconductivity measurement of the SR method and conventionally grown TZA crystals is carried out using DPM111-C2-SES make computer interface picoammeter in the presence of DC electric field. By increasing the applied field from 20 to 140 V, the corresponding dark current without exposure to radiation was recorded. Then the photocurrent was recorded by exposing the crystal to a100 watt halogen lamp. **Fig. 3** shows the field dependent conductivity of both TZA crystals. From graph, for both the crystals, it is observed that at all instants of applied field the photo current is always less than the dark current, which reveals that both TZA crystals exhibits negative photoconductivity.

The negative photoconductivity of these crystals may be due to a decrease in either the number of free charge carriers or their lifetime when subjected to radiation. The negative Photoconductivity of the grown crystals can be explained according to the Stockman model as follows: the forbidden gap in the material contains two energy levels, one energy level is situated between the Fermi level and the conduction band, while the other energy level is located close to the valence band. The second state has a high capture cross section for electrons and holes. When it captures electrons from the valence band, the number of charge carriers in the conduction band decreases, and the current decreases in the presence of radiation [20-27].

3.2 Thermal study

The thermal stability of the SR method and conventionally grown TZA crystals have been determined by employing thermogravimetric analysis (TGA) in a temperature range of 100-400°C. The TGA thermogram shown in **Fig.4** was recorded by increasing the temperature of sample at a rate of 20°C per minute keeping the sample in homogeneous nitrogen atmosphere. The TGA curves reveals gradual and single step decomposition in

the range of 166-325°C for conventionally grown TZA crystal and 169-325°C for SR method grown TZA crystal **[5, 28]**.

Fig. – 3: Field dependent conductivity of BTCA crystal

Fig. – 4: TGA Thermogram

3.3 Electrical study

Fig. – 5: Variation of Dielectric Constant with Temperature

Fig. – 6:Variation of Dielectric Loss with Temperature

LCR cube meter HIOKI 3532-50 was used for the investigation of electrical properties of SR method and conventionally grown TZA crystals in the temperature range 30-100°C. Grown crystals were polished and coated with silver coat for accuracy. External electrical field and temperature have high impact on dielectric constant; hence the dielectric constant of crystal has been noted in steps of 20°C. The plot of variation in dielectric constant and dielectric loss with temperature of grown crystals is shown in **Fig.5 and Fig. 6.**

Active ionic, electronic, dipolar and space charge polarization governs the electrical behavior **[29-30].** Scientist Lower dielectric constant leads to higher SHG coefficient **[31]** which in turn has less power consumption. This property of grown crystals makes them highly suitable for EOMs(Electro-optic modulators),engineering microelectronics, THz wave generators, optoelectronics and photonic devices **[32–34].** The dissipation of electromagnetic energy in a crystal and energy contributed by variety of defects is represented by dielectric loss **[35, 36].** The dielectric loss of SR method grown crystal is significantly lower as compared to conventionally grown TZA crystal as shown in **Fig.6.** This evidences states the fact that the SR method grown crystal confirms the norms of improved quality crystal and also possesses minimum electrically active defects and vitalizes its suitability as a promising material for distinct technological, NLO and optoelectronic applications **[37, 39].**

4. CONCLUSIONS

Thiourea Zinc Acetate (TZA) crystals have been grown by conventional slow solution evaporation technique and SR method. The field dependent conductivity of both TZA crystals was measured. For both the crystals, it is observed that at all instants of applied field the photo current is always less than the dark current, which reveals that both TZA crystals exhibits negative photoconductivity. The thermal stability of the SR method and conventionally grown TZA crystals have been determined by employing thermogravimetric analysis (TGA) in a temperature range of 100-400°C. The TGA curves revealed the gradual and single step decomposition in the range of 166-325°C for conventionally grow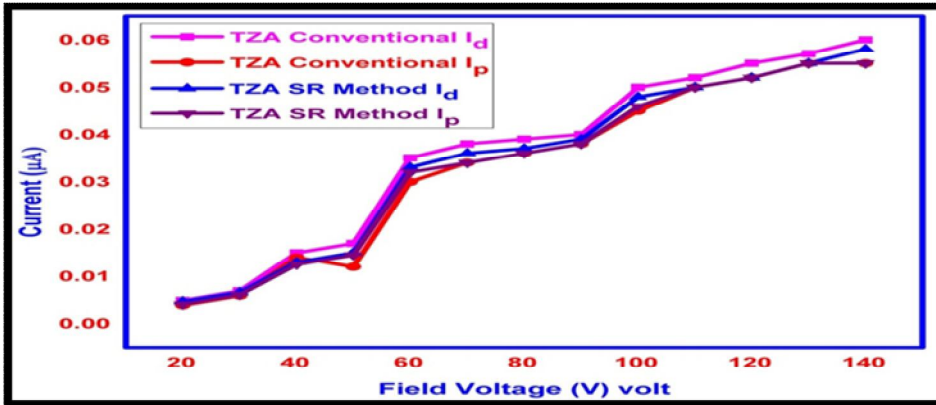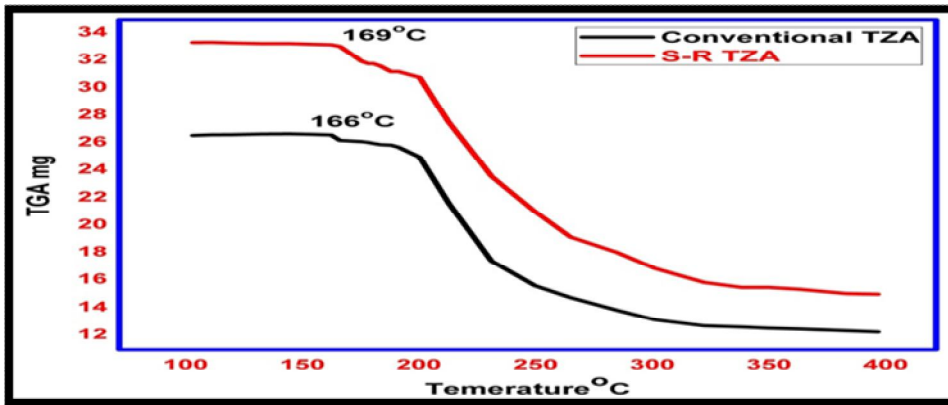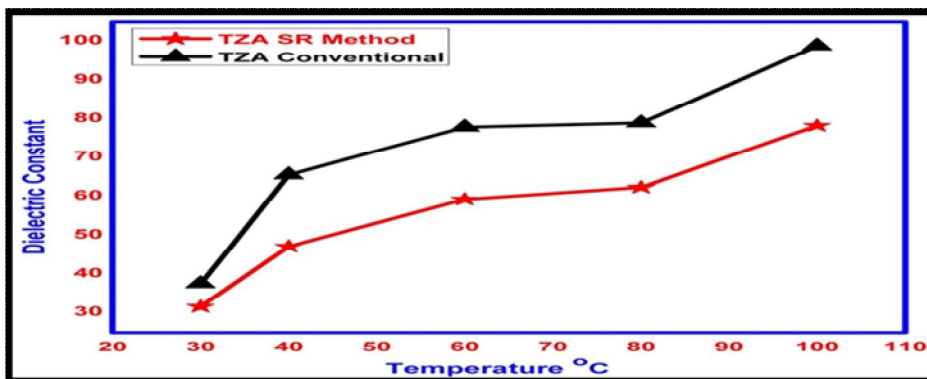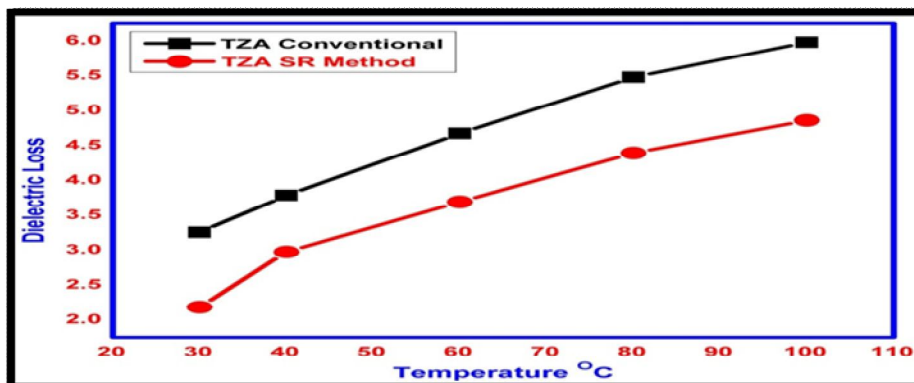n TZA crystal and 169-325°C for SR method grown TZA crystal. The investigation of electrical properties of SR method and conventionally grown TZA crystals was performed in the temperature range 30-100°C.In studied temperature range, the the SR method grown crystal attributed lower dielectric constant and dielectric loss as compared to conventionally grown crystal.

REFERENCES

1. M. Anis, R. N. Shaikh, M. D. Shirsat,S. S. Hussaini, Opt. Laser Technol.60 (2014)124–129.

2. M. Anis, G. G. Muley, G. Rabbani, M. D. Shirsat and S. S. Hussaini, Mater.Technol. Adv. Perform. Mater. 30(2015)129-133.

3. H.O. Mercy, M.J. Rosker, L.F. Warren, P.H. Cunningham, CA. Thomas, L.A. Deloach, S.P. Velsko, C.A. Ebbers, J.H. Liao, M.G. Kanatzidis, Opt. Lett. 20 (1995)252.

4. R. Mohankumar, D. RajanBabu, G. Ravi, R. Jayavel, J. Cryst. Growth 250 (2003)113.

5. Mohd Anis and G G Muley ,Phys. Scr. 91 (2016) 085801

6. Sabari Girisun T C, Dhanuskodi S, Mangalaraj D, Phillip J, Curr. Appl. Phys. 11(2011) 838

7. Anis M, Hussaini S S, Hakeem A, Shirsat M D and Muley G G, Optik 127(2016) 2137

8. Thomas Joseph Prakash J, Ruby Nirmala L 2010 Int. J.Comp. Appl. 67(2010)

9. Pabitha G and Dhanasekaran R, Opt. Laser Technol. 50(2013) 150

10. Jayalakshmi D, Kumar J, Cryst. Res. Technol. 41(2006) 37

11. Kannan V, Rajesh N P, Bairava Ganesh R, Ramasamy P. J. Cryst. Growth 269(2004) 565

12. Ruby Nirmala L, Thomas Joseph Prakash J,Spectrochem. Acta A 97(2011) 673

13. Lydia Caroline M and Vasudevan, Curr. Appl. Phys. (2009) 1054–1061

14. Felicita Vimala J, Thomas Joseph and Prakash J ,Spectrochem. Acta A 107 (2013)371

15. Shkir M, Ganesh V, AlFaify S, Algarni H, Bhagavannarayana G, Maurya K K, Abutalib M M ,Yahia I S , Mater. Res. Innov.(2016) (http://dx.doi.org/10.1080/14328917.2016.1192715)

16. Shkir M, Riscob B, Ajmal Khan M, AlFaify S, Ernesto D, Bhagavannarayana G Spectrochem. Acta A 124(2014) 571

17. D. Jayalakshmia,R. Sankarb,R. Jayavelb, Jou. of Crys. Growth 276 (2005) 243–246

18. A.Kanagavalli1, J. Thomas Joseph Prakash1, T. Seethalakshmi, Seethalakshmi T., International Journal of Research in Pharmaceutical and Nano Sciences. 5(2016) 326 - 336.

19. Divya Muthayya1 and M. Mary Freeda, International journal for research in emerging science and technology, 2(2015)

20. M. Packiya raja, S.M. Ravi Kumarb,, R. Srineevasanb, R. Ravisankar, Journal of Taibah University for Science (2015). Doi.org/10.1016/j.jtusci.2015.08.006

21. M. Kumar, S. Tamilselvan, M. Vimalana, P. Saravanana, S. Arunab, R. Kanagaduraic, Arch. Appl. Sci. Res.,5(2013) 220-227

22. Sagadevan Suresh, Journal of Crystallization Process and Technology,3(2013)87-91. Doi.org/10.4236/jcpt.2013.3301

23. S.M.Ravi Kumar, S. Selvakumar,P. Sagayaraj,A.Anbarasi, Materials Science and Engineering 73 (2015) ,doi:10.1088/1757-899X/73/1/012049

24. I.P. Bincy, R. Gopalakrishnan, Optical Materials 37 (2014) 267-276

25. K Rajesh, A Arun, A Mani, P Praveen Kumar, Mater. Res. Express, 3(2016)106203, Doi:10.1088/2053-1591/3/10/106203

26. A Serpi, phys. stat. sol. (a) 133, K73 (1992)

27. K. Sugandhi, M. Selvambikai, E. Shobhana,127(2016)1378-1383.

28. B. Suresh Kumar, M. R. Sudarsana Kumar, K. Rajendra Babu, Cryst. Res. Technol. 43(2008)745-750.

29. R.C. Miller, Appl. Phys. Lett. 5(1964)17-19.

30. S. M.Azhar, M.Anis, S.Hussaini, M.D. Shirsat,G.Rabbani,Optik 127(2016)4932-4936.

31. M.Anis, S.S. Hussaini, M.D. Shirsat, R.N. Shaikh, G.G. Muley, Mater. Res. Exp. 3 (2016)106204-106210.

32. Min-hua Jiang, Qi Fang, Adv. Mater. 11(1999)1147-1151.

33. N. Bhuvaneswari, K. Baskar, R. Dhanasekaran, Optik 126(2015)3731-3736.

34. Rais Shaikh, M. Anis, A.Gambhire, M.D. Shirsat, S.S. Hussaini, Mater. Res.Exp.1 (2014)15016-15023.

35. M. Anis, S.S. Hussaini, M.D. Shirsat, G.G. Muley, Mater.Res.Inn.20 (2016)312-316.

36. D. Zion, S. Devarajan, T. Arunachalam, J. Cryst. Processes Tech. 3(2013)5-11.

37. M.Anis, D.Hakeem, G.Muley, Results Phys. 6(2016)645-650.

38. M. Anis, G. Muley, V. Pahurkar, M.Baig, S. Dagdale,Mat. Res. Inn.22(2018)99-106.

39. M. Anis,S. Hussaini, M. Shkir, S. Alfaify,M.Baig, G.Muley, Optik 157(2018)592-596.

SYNTHESIS & CHARACTERIZATION OF CADMIUM SELENIDE NANOCRYSTALLINE THIN

Swapna Samanta[1], Mahendra S. Shinde[2] and R. S. Patil[3]
[1]Department of Physics, H. P. T. Arts & R.Y. K. Science College, Nasik
[2]Department of Physics, M. J. M. Arts, Commerce & Science College Karanjali (Peth), Dist-Nashik
[3]Department of Physics, P. S. G. V. P. Mandal's Arts, Commerce & Science College, Shahada. Nandurbar

ABSTRACT

The successive ionic layer adsorption and reaction (SILAR) method has been used to deposit the CdSe thin film on glass substrate at room temperature. The SILAR method also known as modified chemical bath deposition method (M-CBD) is based on immersion of the substrate into separately placed ionic and cationic precursors alternatively and the formation of thin film takes place on the glass substrate. The parameters such as concentration of the precursors, nature of complexing agent, temperature, pH of the precursor solutions and adsorption, reaction and rinsing time duration was optimized. A further study has been made for structural, surface morphological, electrical and optical properties of the film using the X-ray diffraction (XRD), EDAX, scanning electron microscope (SEM) and optical absorption method.

Keywords: Nanocrystalline, thin films, SILAR, X-Ray diffraction.

1. INTRODUCTION
Presently, nanocrystalline materials have opened a new chapter in the field of various applications, since material properties could be changed by changing the crystallite size and/ or the thickness of the film. The II-VI group semiconductor compounds (CdS, CdSe, ZnSe & CdTe) finds immense potential in the applications such as optoelectronic devices, photoelectrochemical solar cells (PEC), and gamma ray detectors [1-3]. These semiconducting nanocrystalline materials belongs to the state of matter between molecules and solids. Among the semiconductors of II-VI group, the CdSe is a promising photovoltaic material because of its high sensitivity, high absorption coefficient and a suitable band gap (1.7 eV) which lies in the solar spectrum [4-5]. CdSe is an important class of semiconductor which finds successful applications for the development of various modern technologies of solid state devices such as high efficiency thin film transistors and light emitting diodes, photodetectors, light amplifiers, solar cells, gas sensors, lasers, large screen liquid crystal display and photoluminescence response [6].

CdSe thin films have been prepared by several physical and chemical techniques such as spray pyrolysis [7], molecular beam epitaxy [8], electrodeposition [9-10], laser ablation [11], chemical bath deposition [12] and successive ionic layer adsorption and reaction (SILAR) [13]. Of these methods, the CBD and SILAR techniques can be used to deposit uniform thin films over large area having complex geometries. In CBD method, when solutions are mixed together, precipitation of the solution takes place and the reaction continues till the ionic product exceeds or becomes equal to the solubility product. As the reaction is not controllable , bulk precipitate is formed in the solution [14]. To overcome this difficulty, we have used the SILAR method which is also known as the modified CBD (M-CBD) for depositing the CdSe film. The SILAR method is based on immersion of the substrate into separately placed cationic and anionic precursors and rising between every immersion with ion exchanged water to avoid homogeneous precipitation in the solution. This method does not require any sophisticated instruments and conductive substrates. It is inexpensive, simple and convenient for large area deposition [15]. It is suitably used for growing thin multilayer structure due to low temperature as diffusion of ion is slow. The growth of the film can be controlled by optimizing the parameters such as concentration of cationic and anionic precursors, their pH values, immersion time, rinsing time, temperature of solution, complexing agents and pretreatment of substrates.

In this paper, we report the synthesis and characterization of nanocrystalline CdSe thin film deposited on glass substrate at room temperature using the SILAR technique. The deposition conditions were optimized to get good quality and well adherent film on the glass substrate. The films were characterized for structural, surface morphological, optical, UV-VIS. spectroscopy and electrical resistivity.

2. EXPERIMENTAL DETAILS
2.1. Substrate cleaning
Glass slides of dimension 76 mm X 26 mm X 2 mm were used as substrate for deposition of thin film. Initially the glass slides were cleaned thoroughly with distilled water and were then ultrasonically cleaned for 10 min. Then it was degreased using chromic acid and then rinsed with deionized water.

2.2. CdSe film formation on the substrate

Loba analytical reagent grade Cadmium sulphate ($3CdSO_4$, $8H_2O$) and sodium selenosulphite (Na_2SeSO_3) were used in the deposition of nanocrystalline CdSe thin film by successive ionic layer adsorption and reaction technique (SILAR). The cationic precursor for the CdSe thin film was 0.35 mol l^{-1} of cadmium sulphate. The source for Selenium ions was 0.12 mol l^{-1} sodium selenosulphite. $CdSO_4$ was complexed with tartaric acid at pH ~ 3. Sodium selenosulphite was prepared as follows [16]

Elemental selenium in the powder form was added to an aqueous solution of sodium sulphite (Na_2SO_3). The solution was heated to 90^OC with continuous stirring for 5 hrs. It was cooled and then filtered to get a clear solution of sodium selenosulphite (Na_2SeSO_3). The pH of the solution was 11. The adsorption and reaction time in growth of CdSe thin film was 40sec and rinsing time was 30sec. Thus a single SILAR deposition cycle consisted of 40 sec of adsorption of Cd^{2+} ions then 30 sec of rinsing with double distilled water, 40 sec adsorption and reaction of Se^{2-} ions with pre-adsorbed cadmium ions on the glass substrate and then again rinsing with double distilled water for 30 sec. Repeating such cycles, a thin film of CdSe with desired thickness was deposited on the glass substrate. Film thickness of 181nm was obtained after 60 such SILAR cycles. The temperature of the solution was 30^OC.

3. CHARACTERIZATION OF CDSE THIN FILM

The CdSe film thickness was determined by gravimetric weight difference method. For this, a sensitive microbalance was utilized and film density was assumed as the bulk density of CdSe (5.674 g cm^{-3}).

The X-ray diffraction studies were carried out in the range of the scanning angle $0–100^0$ with CuKα radiation (λ = 1.5406 Å) using PW-1710 diffractometer. Optical absorption was studied in the wavelength range 350–850 nm with spectrophotometer, Hitachi-220. The electrical resistivity of the film was measured using a d.c. two probe method in the temperature range 323–473 K. A brass block was used as a sample holder. A chromel–alumel thermocouple was used to measure the temperature difference. The area of the film was defined (0.25 cm^2) and silver paste was applied to ensure good ohmic contacts to the film. The microstructure and surface morphology was analyzed by taking Scanning Electron micrograph using SEM (model S-2400 Hitachi) equipped with an EDAX-DX-4 analyzer to measure qualitatively the sample stoichiometry.

Optical characterization was done by recording absorption spectra of the sample using a double beam spectrophotometer (Hitachi-220).
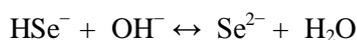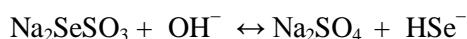
4. RESULTS AND DISCUSSION

4.1. Reaction Mechanism

The formation mechanism of the CdSe thin film is as follows

$$Se + Na_2SO_3 \rightarrow Na_2SeSO_3$$
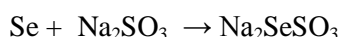
Sodium selenosulphite (Na_2SeSO_3) in alkaline solution gives Se^{2-} ions as

$$Na_2SeSO_3 + OH^- \leftrightarrow Na_2SO_4 + HSe^-$$

$$HSe^- + OH^- \leftrightarrow Se^{2-} + H_2O$$

The cadmium sulphate solution which is cationic precursor solution releases Cd^{2+} ions from complexed [Cd (tartaric acid)]$^{2+}$ as

$$[Cd \text{ (tartaric acid)}]^{2+} \rightarrow Cd^{2+} + \text{tartaric acid}$$
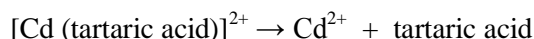
When the glass substrate is immersed in $CdSO_4$ complexed with tartaric acid solution, Cd^{2+} ions are adsorbed on the surface of the glass substrate. Rinsing the substrate and then again immersion in Na_2SeSO_3 solution, Se^{2-} ions now get adsorbed on the glass substrate. The reaction that takes place is as follows:

$$Cd^{2+} + Se^{2-} \rightarrow CdSe$$
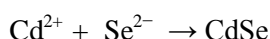
4.2. Structural Studies

The crystal structure of the SILAR deposited CdSe thin film on glass substrate by examining the X-ray diffractogram of the film. The XRD peak reveals that CdSe has nanocrystalline with hexagonal crystal structure [17]. The observed values are compared with JCPDS data (020330) and are found to be in good agreement with standard values. The lattice parameters were found to be a = 4.30 ^0A and c = 7.02 ^0A.
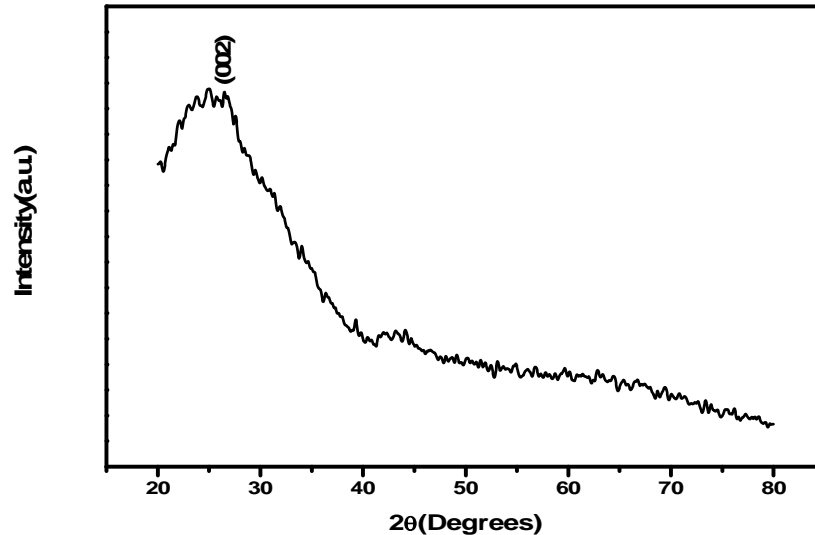
Fig.1 X-ray diffraction pattern of CdSethin film (303K)

The average crystallite size of the material was calculated from the XRD data by using the Scherrer's relation

$$D = \frac{0.94\lambda}{\beta cos\theta}$$

Where λ = 1.5406 A° for CuKα, β is the full width at half maximum (FWHM) of the peak and θ is the diffraction/Bragg's angle. The average crystallite size of the as deposited CdSe thin film was found to be 22.36 nm at optimized preparative parameter.

4.3. Surface Morphological Studies
The SEM micrographs of the CdSe thin film prepared from SILAR technique on a glass substrate at 303 K is shown in fig.2. The micrographs reveals that the film is well adherent, homogeneous and well covered to the substrate surface without any cracks and pinholes.
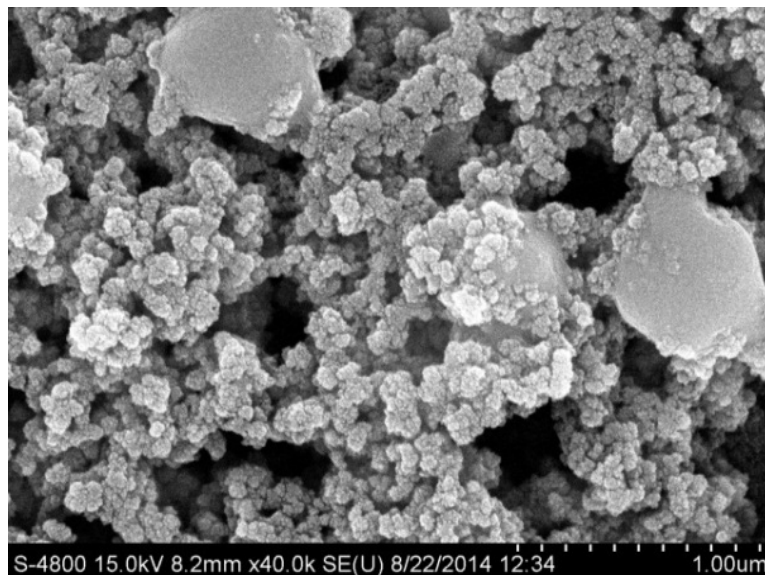
Fig. – 2: The SEM micrographs of CdSe film grown on glass substrate at 303 K.

The quantitative analysis of the films grown at room temperature was carried out by using the Energy Dispersive X-ray analysis (EDAX). The EDAX was recorded in the energy region 0-14 KeV. The EDAX micrograph gives quantitative analysis of Cd and Se in the as-deposited CdSe thin film. The average ratio of the atomic percentage of CdSe was 56:44 showing that the samples are consisting of 1:1 ratio of cadmium and selenide.

4.4 Optical absorption studies
To find out the optical band gap and involved transitions in CdSe thin film deposited by SILAR technique, optical absorption study was carried out.

Fig. – 3: Plot of $(\alpha h\nu)^2$ versus $h\nu$ for CdSe thin film
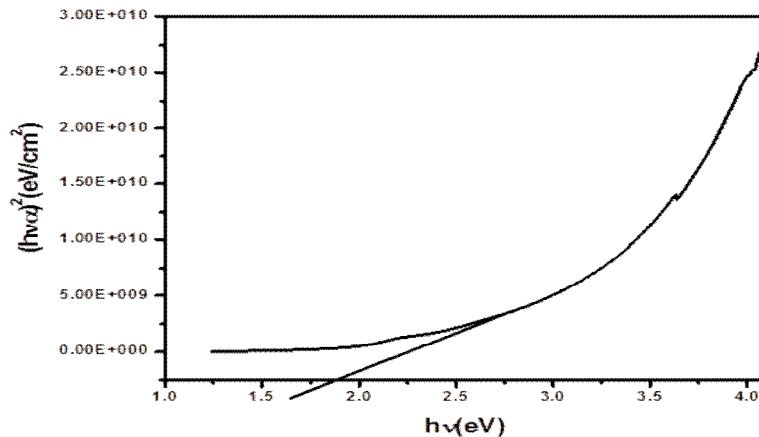
The optical properties of the CdSe films were measured by using UV-VIS. spectrophotometer at room temperature in the wavelength range of 300-1000nm. Fig.3. shows the plot of $(\alpha h\nu)^2$ versus $h\nu$. The nature of the transition was determined by using the relation [20]

$$\alpha = \frac{A(h\nu - E_g)^n}{h\nu}$$

where A is a constant, α the absorption coefficient and n is equal to ½ for direct band gap semiconductors. The variation of $(\alpha h\nu)^2$ versus $h\nu$ is linear showing direct transition. Extrapolating the straight position of the plot to the energy axis, the band gap energy of 1.88 eV is obtained. This value agrees well with the standard value reported earlier for CdSe thin film [18-19].

4.5. Thickness measurement studies
Film thickness is one of the important parameters in the study of film properties. The thickness of SILAR deposited CdSe thin film was measured using the weight difference method. The thickness of the CdSe thin film was dependent on the number of deposition cycles. The time of adsorption was 40 sec and the rinsing time 30 sec for deposition of the film. It was observed that each pair of adsorption-reaction period, the thickness of the film increased with increasing number of immersion cycles. After certain limit the thickness of the film was saturated for 60 cycles at 181 nm. For further cycles, no chemical species (Cd^{2+} ions) are available for further growth of CdSe thin film. Therefore the desired thickness can be achieved which is well adherent and uniform on the glass substrate. This is the novelty of the SILAR technique which is easily used directly for device applications.

4.6. Electrical resistivity
The electrical resistivity of the as-deposited CdSe film deposited on glass substrate was measured using a 2-probe method in air within the temperature region 323K-473K. Fig.4 shows the variation of logarithm of resistivity (log ρ) with reciprocal of temperature (1000/T). It is observed that resistivity decreases with increase in temperature, indicating semiconducting nature of CdSe film. The resistivity of the as-deposited CdSe film was found to be of the order of 10^3 Ω-cm which is comparable to chemical deposited film.
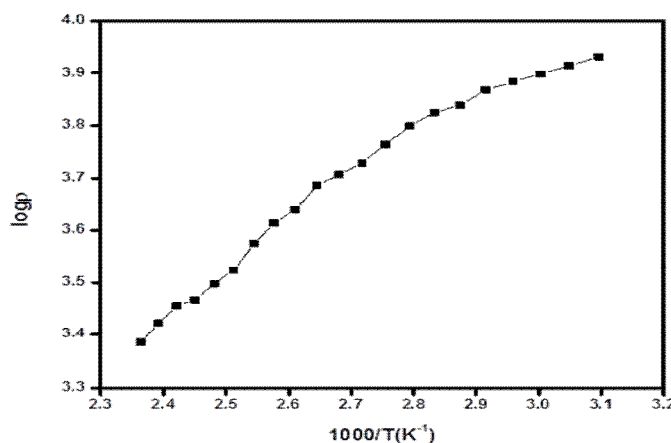

Fig. – 4: Plot of log ρ vs. (1000/T) for CdSe thin film

5. CONCLUSIONS

In summary, the optical, structural and electrical properties of the CdSe thin films are grown by the SILAR method have been investigated. The X-ray diffraction pattern of the sample shows the hexagonal structure. SEM micrographs shows that small spherical nanosized grains exists which indicates the nanocrystalline nature of CdSe. The optical band gap is found to be 1.88 eV. Electrical resistivity of CdSe film is of the order of 10^3 Ω-cm.

ACKNOWLEDGEMENTS

REFERENCES

1. K.R. Murali, V. Swaminathan, D.C. Trivedi, Solar Energy Mater. & Solar Cells, **113,** 81 (2004).

2. D.Hahn, K.K. Mishra, K.K. Rajeshwar, J. Electrochem. Soc. **100**, 138 (1991).

3. K.K. Mishra, K.K. Rajeshwar, J. Electro. Anal.Chem. **273**, 169 (1989).

4. R.B. Kale, C.D. Lokhande, Semicond. Sci. Technol. **1**, 20 (2005).

5. S.J. Lade, M.D. Uplane, C.D. Lokhande, Mater. Chem. Phys. **36**, 62 (2001).

6. P.P. Hankare et.al. J. Phys.Chem. Solid, **67**, 2506 (2006).

7. A.A. Yadav, M.A. Barote and E.U.Masumdar, Solar Energy **8**, 763 (2010).

8. N.Samarth, H.Luo, J.K. Furdyna, S.B. Qadri, Y.R. Lee, A.K. Ramdas, N. Otsuka, Appl. Phys. Lett, **268**0, 54, (1989).

9. K.R. Murali, V. Subramanian, N.Rangarajan, A.S. Laksmanan, S.K. Rangarajan, J.Electroanal. Chem. **95**, 368 (1995).

10. K.R. Murali, V. Subramanian, N.Rangarajan, A.S. Laksmanan, S.K. Rangarajan, J. Electroanal. Chem.**261**, 303 (1991).

11. G.Perna, V.Capozzi, M.Ambrico, J. Appl. Phys. **3337**, 83 (1998).

12. YunusAkhathun, M. Ali Yildirim, AytuneAtes and MuhammetYildirim, Optics Communication, **284**, 2307 (2008).

13. H.M. Pathan, B.R. Sankapal, J.D.Desai and C.D.Lokhande, Mat. Chem& Phys. **78**, 11 (2002).

14. Patil R.S., Lokhande C.D., Pathan H.M. Mater. Sc. &Eng.B.**129**, 59-63 (2006).

15. Nicolaue Y.F., Appl. Surf. Sci. **22-23**, 1061- 1074 (1985).

16. M.E.Rincon, M. Sanchez, A.Olea, I. Ayala, P.K. Nair, Solar Energy Mater. & Solar Cells, **399**, 52 (1998).

17. S.S. Kale, C.D. Lokhande, Mater. Chem. Phys. **62**,103 (2000).

18. S.S. Dhumure, C.D. Lokhande, Trans SAEST **27**, 142 (1992).

19. F.Cerdcira, I. Torriani, P.Motisukc, V.Lemos, F. Dekker, Appl. Phys. A **46**, 107 (1988).

20. J.N. Pankove, Optical Processes in Semiconductors, Dovers, New York (1971).

PHOTO LUMINE SCENCE AND FTIR STUDY OF CDS NPS CO-DOPED WITH Li⁺AND Cs⁺

S. S. Talwatkar[1], A. L. Sunatkari[2], Y. S. Tamgadge[3] and G. G. Muley[4]

Assistant Professor[1], Department of Physics, N. G. Aacharya and D. K. Maratha College of A. S. C., Mumbai
Associate Professor[2], Department of Physics, Siddhartha College of Arts, Science and Commerce, Mumbai
Assistant Professor[3], Department of Physics, Mahatma Phule Arts, Commerce & S. R. C. Science College, Warud
Assistant Professor[4], Department of Physics, Sant Gadge Baba Amravati University, Amravati

ABSTRACT

We report here the synthesis of CdS nanoparticle co-doped with Li⁺ and Cs⁺ using L- Arginine as a capping agent. The nanoparticle is prepared by adopting the chemical route method using sodium sulphide as a reducing agent. PL spectra show a shift in the emission peak towards longer wavelength side with increase in the doping concentration. The intensity of peak increases with increase in the doping concentration. FTIR spectra confirm the surface passivation of the CdS nanoparticle by L- Arginine.

Keywords: CdS, doped semiconductors, PL, FTIR, quantum confinement

1. INTRODUCTION

Doping effectively alters the electrical and optical properties of semiconductors. CdS nanoparticle with various metal dopants of different concentrations and size controlling capping agents are studied for their tunable band gap, size dependent optical properties and chemical stability to find out the potential candidate for opto-electronic device applications. The study of optical properties of doped semiconductor NPs with dimensions close to the Bohr radius of the electron- hole pair are of recent interest, due to their possible application in future high-capacity communication networks, optoelectronics and photonic devices [1-9].

Various methods are reported to synthesis semiconductor nanoparticles such as chemical method, micro emulsion, vacuum evaporation, sol gel technique, spray pyrolysis, molecular beam epitaxy etc. The most popular method of synthesis of CdS nanoparticle is chemical reduction method where CdS is reduced by sodium sulphide.

We synthesized Li⁺ and Cs⁺ co-doped CdS nanoparticles by chemical reduction method using L-Arginine as capping agent and Na_2S as reducing agent. We have studied the possible effects of co-doping on physical, chemical and optical properties of CdS nanoparticles and the result is recorded, analyzed, and reported. The synthesized nanoparticles are characterized by Fourier transform infrared (FT-IR) spectroscopy and photoluminescence (PL).

2. MATERIALS AND METHODS

Cadmium chloride ($CdCl_2$), sodium sulphide (Na_2S), lithium chloride, cesium chloride ($CsCl$,) and L-Arginine, all of analytical grade purity, were purchased from Sigma-Aldrich (Germany) and used without further purification for the synthesis. Double distilled water was used in the synthesis process.

2.1 Synthesis of L-Arginine Stabilized (Li⁺-Cs⁺) Doped CdS NPs

The CdS NPs were synthesized by using chemical reduction method. Firstly, 0.5 M stock solutions of cadmium chloride, L-Arginine, and sodium sulphide were prepared. 0.5 M solution of $CdCl_2$ was added to 200 ml double distilled water kept in three separate round bottom flasks each, kept on a magnetic stirrer. 1wt%, 2wt%, and 5wt% solutions of LiCl and CsCl were added drop by drop into three round bottom flask. 0.5 M solution of L-Arginine as capping agent was added to the solution. Finally of 0.5 M Na_2S solution was added to the solution under continuous stirring. Color of Solution turned to yellow, confirming the formation of CdS NPs. Stirring was continued for 2 hours for homogeneous mixing. It was centrifuged for 25 minutes at 4500 rpm. The resultant precipitate was dried at 40^oC for 16 hours to remove the solvents. The dried mass was powdered for further characterization.

The following chemical reaction takes place during synthesis of NPs:

$$(CdCl_2)n + (L\text{-}arginine)m + (Na_2S)n \longrightarrow (CdS)n + (L\text{-}arginine)m + 2n(NaCl)$$
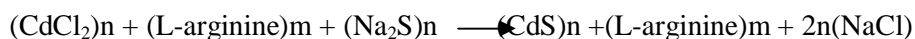
2.2 Characterization

The prepared powder is characterised by PL spectra is recorded by using F-7000, FL spectrophotometer in the range of 200-600 nm. FT-IR spectra is obtained with machine 3000 hyperion microscope with vertex 80 FT-IR system (Bruker, Germany) in the range of 450 - 7500 cm^{-1}.

3. RESULTS AND DISCUSSION
3.1 Photoluminescence Study
The PL spectra for CdS dpoed with Li and Cs is as shown in Figure 1 at an excitation wavelength of 370 nm along withthe optical absorption spectra. The PL spectra for CdS doped with Li and Cs exhibit the near band edge emission due to CdS nanoparticles at547, 540 and 532 nm for 1wt%, 2wt% and 5wt% respectively.The bands are blue shifted as the doping concentration is increased. In addition, for 1wt % co-doping a weak peak is observed at 510 nm, similarly for 2 wt% co-doping concentration a weak peak is observed at 500 nm for 5wt % co-doping weak peak is also observed at 500 nm. These multiple peaks may be due to the existence of Li^+ and Cs^+ ions present in the CdS host which acts as multiple luminescent centres[9-12]. An increase in the PL intensity is observed with increase in the doping content. Similar result is reported by Nazerdeylami, *et al.* [8].It is noticed from PL spectra that the intensity of emission peak increases as the doping concentration increased from 1to 5 wt%., have reported similar intensity-trend. Green emmision is observed. It is associated with the emmision due to electronic transition from conduction band to acceptor level due to interstitial sulphur. This confirms that the luminescence property of CdS nanoparticle enhances when Li and Cs ions were introduced in the CdS matrix. [13]
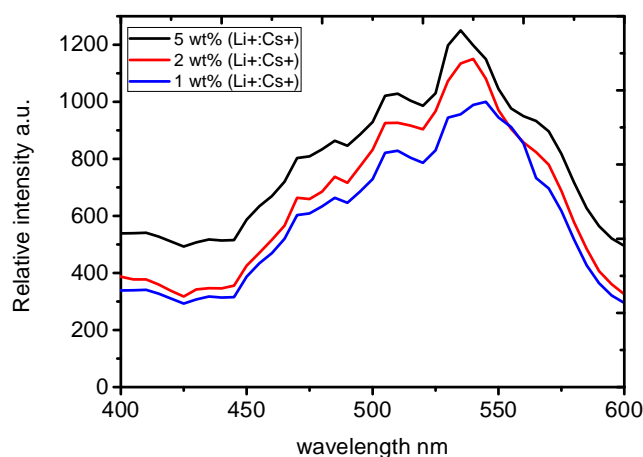

Figure-1: Photoluminescence spectra of L-arginine capped CdS nanoparticles co doped with 1, 2 and 5wt% doping concentration of Li^+ and Cs^+
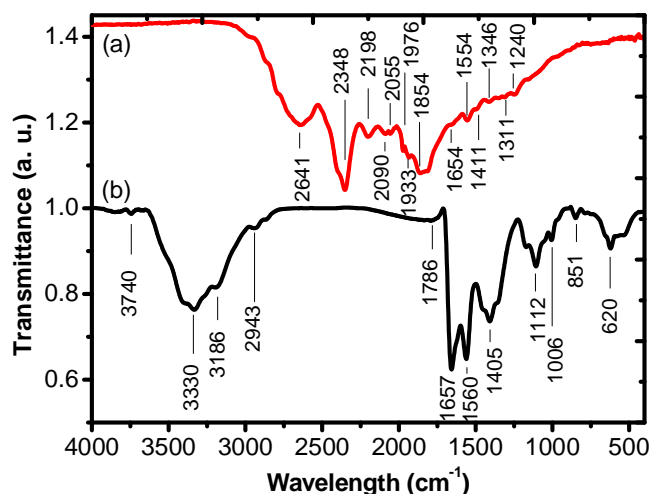
3.2 FTIR spectroscopy

Figure-2: FTIR spectra of (a) L-arginine capped CdS nanoparticles co doped with Li^+ and $Cs^+$and (b) Pure L-arginine.

The FT-IR spectra of the samples are depicted in Figure 2.Strong absorption peaks at 1050cm^{-1} and 1006 cm^{-1} in CdS-OHare attributed to the of hydroxyl groups ontothe surface of CdS nanoparticles. The characteristic vibration peaks of the L-Arginine 3330cm^{-1} is broaded and shifted confirms the passivation of CdS with L-Arginine. The C=O stretch vibration absorption of Li and Cs appears at 1554 cm^{-1}. Some absorption peaks at 1311 cm^{-1}and 1240 cm^{-1},among which the first peak may be assigned to the C=Ostretch absorption of a newly formed linkage between L- Arginine and CdS [9-10].The other important peaks in the FT-IR spectrum of L-Arginine capped Cds nanoparticles, is as given in the Table 1below[14-17].

Table-1: Important peaks in the FT-IR spectrum of L-Arinine capped Cds nanoparticles

Peaks (cm^{-1})	Assignment
3330	N-H strecthing
2943	Assymetric streching of CH$_3$ group
1657	NH2 group bending
1560	C-O stretching
1405	Assymetric bending of CH$_3$group
1410	Symetric bending of CH$_3$group
1112	CCC bond stretching
1006	C-H stretching
851	CC bond streching
620	C-N-H streching

4. CONCLUSION

CdS nanoparticle co-doped with Li$^+$ and Cs$^+$ capped by L-Arginine is prepared by chemical reduction method. From the photoluminescence study, it is found that the NPs show emission peaks at around 535, 540 and 545 nm. A blue shift is observed and the intensity of peak increases with increase in the doping concentration. It can be concluded that the doping ions acts as luminescent centers within the host matrix which enhances the relative intensity of luminescence of the material. The FT-IR spectra of cappedCdS NPs reveal the capping L-arginine ligands to the CdS nanoparticles. The method of surface passivation prevents aggregation of the prepared nanoparticles and their bulk crystal growth.

REFERENCES

1. SarkarR., TiwaryC S, Kumbhakar P., Basu S., Mitra A K., (2008)" Yellow – orange light emission from Mn2+doped ZnS nanoparticles",Physica E 40, 3115–3120

2. MahapatraN, Panja S., Mandal A., Halder M., (2014) "A single source-precursor route for the one-pot synthesis of highly luminescent CdS quantum dots as ultra-sensitive and selective photoluminescence sensor for Co2+ and Ni2+ ions",J. Mater Chem. C 2. 7373–7384.

3. Talwatkar S. S., Sunatkari A. L., Tamgadge Y. S., Muley G. G., "Nonlinear refraction of Nd3+-Li+ co-doped CdS-PVP nanostructure", AIP Conference Proceedings 1953 (1), 060004

4. Xuan T., Wang S., Wang X.J., Liu J.Q., Chen J.Y., Li H.L., Pan L.K., Sun Z., (2013) "Microwave synthesis of high luminescent aqueous CdSe/CdS/ZnS quantum dots for crystalline silicon solar cells with enhanced photovoltaic performance",Chem. Commum. 49, 9045–9047

5. Sun D, ZhongH., Yao X. , Chang Y, Zhao Y,. Jiang Y. , (2014)"Synthesis and Properties of Water-Soluble Blue-Emitting Mn-Alloyed CdTe Quantum Dots",Mater. Lett. 125 , 132–145

6. Sunatkari A. L., Talwatkar S. S., Tamgadge Y. S, & Muley G.G (2016) "Synthesis, characterization and properties of L-arginine-passivated silver nanocolloids ", AIP Conference Proceedings, 1728, 020663

7. Tauc J. (Ed.), (1974) "Optical properties of amorphous semiconductors." Amorphous and liquid semiconductors, Springer US,159-220.

8. Nazerdeylami S, Saievar-Iranizad E., Dehghani Z., Molaei M., (2011) "Synthesis and investigation of nonlinear optical properties of semiconductor ZnS nanoparticles",Physica B406 108-111.

9. Sunatkari A. L., Talwatkar S. S., Tamgadge Y. S, Muley G.G. "Synthesis, characterization and properties of L-arginine-passivated silver Nanocolloids", AIP Conference Proceeding,, 1728 (1), 020663

10. Herron N, Wang Y., Eckert H., (1990) J. Am. Chem. Soc. 112, 13226.

11. Murakoshi K., Hosokawa H., Saitoh M., Yugiwada, Sakata T., Mori H., Satoh M., Yanagida S., (1998) "Preparation of size-controlled hexagonal CdS nanocrystallites and the characteristics of their surface structures", J. Chem. Soc. Faraday Trans. 94, 579-582.

12. Tamgadge Y. S., Talwatkar S. S., Sunatkari A. L., Pahurkar V. G., & Muley G. G. (2015). "Thermo☐Optical Properties of Amino Acid Modified ZnO☐PVA Colloidal Suspension Under CW Laser Illumination", Macromolecular Symposia, 362 (1), 73-81.

13. Wu D. ,Ge X., Zhang Z.,Wang M., , (2004) "Novel One-Step Route for Synthesizing CdS/Polystyrene Nanocomposite Hollow Spheres", Langmuir20(13), 5192–5.xrd

14. Rao S., Kumar B.R., Rajgopal Reddy V., Suba Rao T., (2011), "Preparation and characterization of CdS nanoparticles by chemical co-precipitation technique", Chalcogenide Letters,Vol. 8, No. 3, March 2011, p. 177 – 185

15. Talwatkar S. S., Sunatkari A. L., Tamgadge Y. S., Muley G. G. (2018), "Nonlinear optical properties of Nd3+-Li+ co-doped ZnS-PVP thin films", AIP Conference Proceedings 1942 (1), 080060

16. Kumar S., Rai S.B., (2010) " Spectroscopic studies of L-arginine molecule" Indian Journal of Pure and Applied Physics, Vol 48, 251-255.

17. Tamgadge Y. S., Talwatkar S. S., Sunatkari A. L., Pahurkar V. G., & Muley G. G. (2015) "Studies on nonlocal optical nonlinearity of Sr–CuO–polyvinyl alcohol nanocomposite thin films", Thin Solid Films, 595, 48-55.

CO-DOPANT (LI+-CS+) DEPENDANT STRUCTURAL AND OPTICAL STUDY OF CDS NPS

S. S. Talwatkar[1], A. L. Sunatkari[2], Y. S. Tamgadge[3] and G. G. Muley[4]
Assistant Professor[1], Department of Physics, N. G. Aacharya and D. K. Maratha College of A. S. C., Mumbai
Associate Professor[2], Department of Physics, Siddhartha College of Arts, Science and Commerce, Mumbai
Assistant Professor[3], Department of Physics, Mahatma Phule Arts, Commerce & S. R. C. Science College, Warud
Assistant Professor[4], Department of Physics, Sant Gadge Baba Amravati University, Amravati

ABSTRACT
In this chapter the synthesis of CdS nanoparticles co-doped with Li^+ and Cs^+ using L-Arginine as a capping agent has been reported. The CdS NPs were prepared by adopting the chemical route method. As-prepared NPs were characterized to study their structural and optical properties. The UV visible absorption spectroscopy showed a strong blue shift in the absorption wavelength due to quantum confinement effect. The XRD patterns of Li^+-Cs^+ doped CdS NPs reveals hexagonal crystal structure. The XRD analysis confirmed that the size of the CdS NPs reduces as the co-doping concentration increased from 1 to 5 wt%. The average particle size for the sample doped with 5 wt% concentration is found nearly 5 nm.

Keywords: CdS nanoparticles, co-doping, quantum confinement, UV visible, XRD

1. INTRODUCTION
Semiconducting nanoparticles often exhibit novel physical properties as their size approaches nanometer scale. For example, the unique electronic and optical properties of nanocrystalline quantum dots may lead to future applications in electro optic devices and biomedical imaging. For many advanced and diverse applications, ranging from chemical sensing to magnetic recording, current research is increasingly focused on exploiting the high surface-to-volume ratio of nanoparticles which serve as a framework for the assembly of complex nanomaterials. [1-7]. CdS NPs possess a very fine-tuned electrical and optical properties, e.g. high carrier generation efficiency and mobility, broad absorption spectra, discrete energy bands and narrow emission profiles as well [8-12], that differ from the bulk counterparts of the same materials due to the spatial confinement imposed on electrons and excitations as a result of the particle's limited size [13-18], and thus have been considered as one of the most promising inorganicsemiconducting materials. Among the most popular methods adopted to synthesize CdS nanoparticle is chemical reduction method. Li^+ and Cs^+ co-doped CdS NPs by chemical route method using L-Arginine as capping agent. The synthesized NPs are characterized by UV-vis spectroscopy and Powder X-ray diffraction (XRD).

2. MATERIALS AND METHODS
Cadmium chloride ($CdCl_2$), sodium sulphide (Na_2S), lithium chloride, cesium chloride ($CsCl$,) and L-Arginine, all of analytical grade purity, were purchased from Sigma-Aldrich (Germany) and used without further purification for the synthesis. Double distilled water was used in the synthesis process.

2.1 Synthesis of L-Arginine Stabilized (Li^+ - Cs^+) Doped CdS NPs
The CdS NPs were synthesized by using chemical reduction method. Firstly, 0.5 M stock solutions of cadmium chloride, L-Arginine, and sodium sulphide were prepared. 0.5 M solution of $CdCl_2$ was added to 200 ml double distilled water kept in three separate round bottom flasks each, kept on a magnetic stirrer. 1wt%, 2wt%, and 5wt% solutions of LiCl and CsCl were added drop by drop into three round bottom flask. 0.5 M solution of L-Arginine as capping agent was added to the solution. Finally of 0.5 M Na_2S solution was added to the solution under continuous stirring. Color of Solution turned to yellow, confirming the formation of CdS NPs. Stirring was continued for 2 hours for homogeneous mixing. It was centrifuged for 25 minutes at 4500 rpm. The resultant precipitate was dried at 40^oC for 16 hours to remove the solvents. The dried mass was powdered for further characterization.

2.2 Characterization
The prepared powder is characterised by UV-vis spectometer (Black-C-SR, Stellarnet Inc. USA). Absorption spectra were recorded covering wavelength range from 190 -1000 nm. Powder XRD patterns is obtained by Rigakurotating anode (H-3R) diffractometer with irradiation from Kα line of copper (λ=1.5418 Å) and angle 2θ ranging from 20° to 80°.

3. RESULTS AND DISCUSSION
3.1 UV-visible spectroscopy
Figure1 illustrates the UV-vis absorption bands of CdS NPs with 1, 2 and 5 wt % of Li^+ -Cs^+ dopant concentration. The absorption peaks are blue-shifted from 430 nm to 370 nm when the dopant concentration is

increased from 1, 2 and 5 wt % as compared to those of bulk CdS (517 nm, Eg = 2.42 eV) due to the quantum confinement effect that occurs when the nanoparticle size is comparable with the Bohr radius of exciton of CdS (3.0 nm).
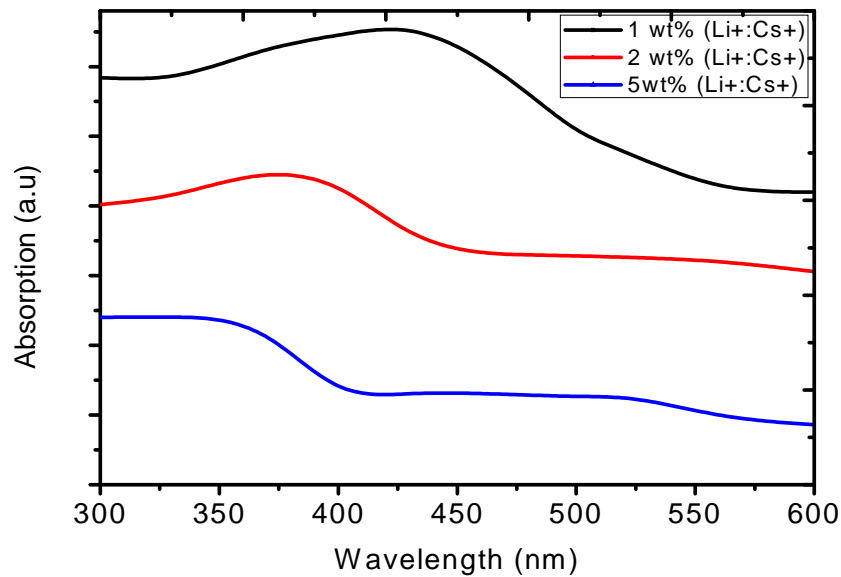

Figure-1: UV-vis absorption spectra of L-Arginine capped CdS NPs doped with 1, 2 and 5 wt % Li$^+$ - Cs$^+$ concentration

With the help of Tauc's relation [18], direct band gap of CdS can be estimated by extrapolating the curves on the x-axis (energy axis) the band gap of NPs with different concentration of doping can be determined. Figure 2 shows direct band gap of the CdS NPs. The UV thresholds of CdS NPs are found at 430, 400 and 370 nm, corresponding to the band gaps of 2.52, 2.62 and 2.72eV respectively. The band gap obtained by the graph is used to determine the particle size by Bruce's equation [19].

$$E_{np} = E_{bulk} + \frac{\pi^2 \mathrm{h}^2}{2R^2}\left(\frac{1}{m_e^*} + \frac{1}{m_h^*}\right) + \frac{-1.8e^2}{4\pi\varepsilon_0\varepsilon_r R}$$
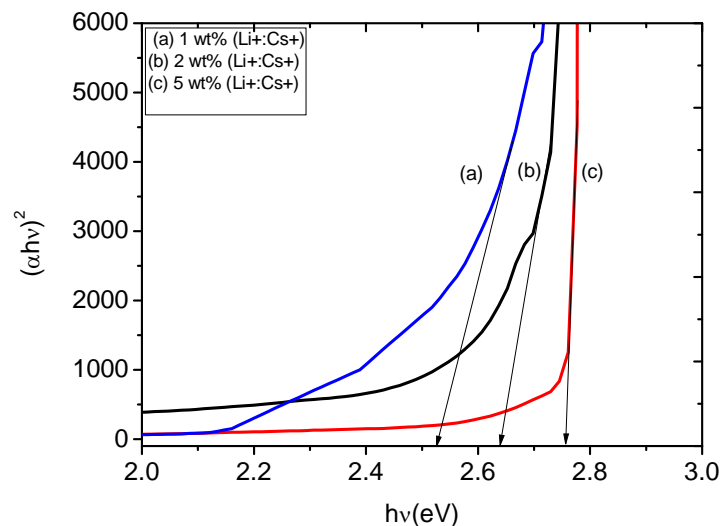

Figure-2: Graph of hυ vs. (αhυ)^2 for(a) 1, (b) 2 and (c) 5 wt% of (Li$^+$-Cs$^+$) co-doping.

3.2 Structural, Morphological and Elemental Analysis

As shown in *Figure 3*, the XRD patterns of Li$^+$-Cs$^+$ doped CdS NPs gives diffraction peaks located at 2θ values of 23.50, 26.85, 30.34, 36.30, 43.79, 48.20 and 49.99°. The corresponding planes for these peaks are (1 0 0), (0 0 2), (1 0 1), (1 0 2), (1 1 0), (1 0 3) and (2 0 0) respectively.The NPs formed have hexagonal crystal structure and the lattice parameters are a = b = 4.136 A. U. and c = 6.713 A. U. matches closely with the JCPDS NO. 77-2306.From the full width half maxima of the peaks above, we have calculated the average particle size of CdS nps calculated by the Debye-Scherrer formula [20].
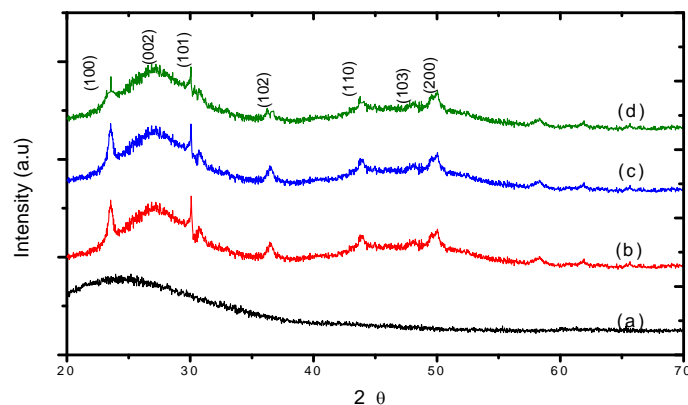
Figure-3: X ray diffraction spectra of (a) Pure CdS and L-Arginine capped CdS nanoparticles in (b)1, (c) 2 and (c) 5 wt % doping concentration of Li^+ and Cs^+.

The XRD analysis confirmed that the size of the CdS NPs reduces as the co-doping concentration increased from 1 to 5 wt%. The average particle size for the sample doped with 5 wt% concentration is found nearly 5 nm. The comparison of particle size estimated from XRD analysis andthat calculated with Brus equation is provided in the Table 1.

Table-1: Band gap and size of as-prepared (Li^+-Cs^+):CdS NPs

Cs^+ and Li^+ concentration (wt%)	Particle Size (nm)		Band gap in eV
	XRD	**EMA**	
1	7.74	6.82	2.52
2	6.08	4.30	2.62
5	5.67	3.35	2.75

4. CONCLUSION

CdS nanoparticle co-doped with Li^+ and Cs^+ capped by L-Arginine has been prepared by chemical reduction method. UV-vis spectroscopy confirms the blue shift in the absorption band of CdS NPs as the co-doping concentration increases. XRD studies show that the NPs have hexagonal primitive structure and particles have sizes that decrease from 7 to 4 nm with increase in concentration of co-dopant due to quantum confinement effect.

5. REFERENCES

1. Guyot-Sionnest P. (2007) Quantum Dots: An Emerging Class Of Soluble Optical Nanomaterials, Material Matters, Vol 2 No 1, 10.

2. Cornel R. M., &Schwertmann U., (1996),The Iron Oxides: Structure, Properties, Occurrence, Uses, VCH, Germany.

3. Tamgadge Y. S., Talwatkar S. S., Sunatkari A. L., Pahurkar V. G., &Muley G. G. (2015)"Studies on nonlocal optical nonlinearity of Sr–CuO–polyvinyl alcohol nanocomposite thin films",*Thin Solid Films*, 595, 48-55.

4. Ross C., (2001) Annual Review of Materials Research, 31,203.

5. Talwatkar S. S., Sunatkari A. L., Tamgadge Y. S., Muley G. G. (2018), "Nonlinear optical properties of Nd^{3+}-Li^+ co-doped ZnS-PVP thin films", *AIP Conference Proceedings* 1942 (1), 080060

6. Mornet S., Vasseur S., Grasset F., &Duguet E., (2004). "Magnetic nanoparticle design for medical diagnosis and therapy",*Journal of Materials Chemistry*, 14, 2161

7. Tamgadge Y. S., Talwatkar S. S., Sunatkari A. L., Pahurkar V. G., & Muley G. G. (2015). "Thermo☐Optical Properties of Amino Acid Modified ZnO☐PVA Colloidal Suspension Under CW Laser Illumination",*Macromolecular Symposia,* 362 (1), 73-81.

8. BoulesbaaA. ,IssacA., Stockwell D. , Huang Z., Huang J.,&Guo J, et al. (2007) " Ultrafast charge separation of CdS quantum dot",*J Am Chem. Soc,*.129(49),15132-15133

9. Lakowicz J., Gryczynski J.,Piszczek G. ,&Murphy C.J.(2002) "Luminescence Spectral Properties of CdS Nanoparticles",*J PhysChem B,* 106 (21), 5365-5370

10. Cui T. , Zhang J., Wang J , Cui F. , Chen W., &Xu F., (2005) "CdS□Nanoparticle/Polymer Composite Shells Grown on Silica Nanospheres by Atom□Transfer Radical Polymerization",*Adv.Funct. Mater.* 15(3), 481-486

11. Sunatkari A. L., Talwatkar S. S., Tamgadge Y. S, & Muley G.G (2016) "Synthesis, characterization and properties of L-arginine-passivated silver nanocolloids",*AIP Conference Proceedings,*1728, 020663

12. Burda C. , Chen X., Narayanan R. , &El-SayedM.A. (2005) "Chemistry and Properties of Nanocrystals of Different Shapes",*Chem Rev*105(4), 1025-1102

13. LeroueilP.R., Hong S., Mecke A. , Baker J.R. , Orr B.G., &BanaszakHoll M., (2007) "Nanoparticle interaction with biological membranes",*Acc. Chem. Res*. 40(5), 335-342

14. KuchibhatlaS., KarakotiA.S, BeraD.,& SealS. (2007) "One dimensional nanostructured materials",*Prog. Mater. Sci.* 52(5), 699-913

15. TasisD.,TagmatarchisN., BiancoN., &Prato M . (2006) "Chemistry of Carbon nanotubes",*Chem Rev.* 106 (3), 1105-1136

16. Talwatkar S. S., Sunatkari A. L., Tamgadge Y. S., Muley G. G., "Nonlinear refraction of Nd3+-Li+ co-doped CdS-PVP nanostructure", *AIP Conference Proceedings* 1953 (1), 060004

17. Tauc J. (Ed.), (1974), "Optical properties of amorphous semiconductors." Amorphous and liquid semiconductors, Springer US, 159 -220

18. Brus L.,(1986) "Electronic wave functions in semiconductor clusters: experiment and theory", *J Phys. Chem* 90, 2555 -2560

19. Klug H.P., Alexander L.E. (1959) X-ray diffraction procedures. New York: John Wiley and Sons Xrd,162.

20. Sunatkari A. L., Talwatkar S. S., Tamgadge Y. S, & Muley G.G (2015) "Influence of Surface Passivation by L-Arginine on Linear and Nonlinear Optical Properties of Ag-PVP Nanocomposite", *American Journal of Materials Science*, 5 (3A), 21-30

SYNTHESIS, CHARACTERIZATION AND DIELECTRICS PROPERTIES OF BaTiO₃ AT MICROWAVE FREQUENCY

B. K. Bongane and P. G. Gawali
Department of Physics, B. S. College, Basmathnagar, Dist: Hingoli

ABSTRACT
The dielectric properties of BaTiO₃ have been carried out at the X-band microwave frequency. The composite material was prepared by using solid state reaction method. The dielectric constant (ε'), dielectric loss (ε''), quality factor $Q = 1/\tan\delta$, relaxation time (τ) and conductivity (σ) of BT having particle sizes 500, 250, 176.5 and 125 microns have been studied at different temperatures i.e. $-10^0, +10^0, +30^0$ and $+50^0c$. The experimental dielectric values have been verified by using correlation formulae's of Landau-Lifshitz-Looyenga and Bottcher. It founds the good agreement with experimental values.

Keywords: Relative Permittivity, Ferroelectric, Relaxation Time, Dielectric Constant, Quality Factor

INTRODUCTION
BaTiO₃ was discovered during World War II in 1941 and 1944 in the United States, Russia, and Japan. At least in the U.S.A., the research was accelerated because of the war. Most ferroelectric materials undergo a structural phase transition from a high-temperature nonferroelectric (or paraelectric) phase into a low-temperature ferroelectric phase. Some ferroelectrics, like barium titanate, BaTiO₃, undergo several phase transitions into successive ferroelectric phases [1]. The transition into a ferroelectric phase usually leads to strong anomalies in the dielectric, elastic, thermal.

BaTiO₃ is a well-known ferroelectric and piezoelectric material having excellent dielectric properties. Its main application is as a dielectric in MLCC (Multi Layered Ceramic Capacitor) due to its high dielectric constant and low losses [2]. The dielectric properties are controlled by purity and microstructure which in turn is dependent on the method of preparation [3-6].

EXPERIMENTAL PROCEDURES
For preparation of BT ferroelectric ceramic material required following starting materials: (i) Barium carbonate (BaCO₃) – (sdfine –Chem) AR grade. (ii) Titanium dioxide (TiO₂) – (Loba-Chem).
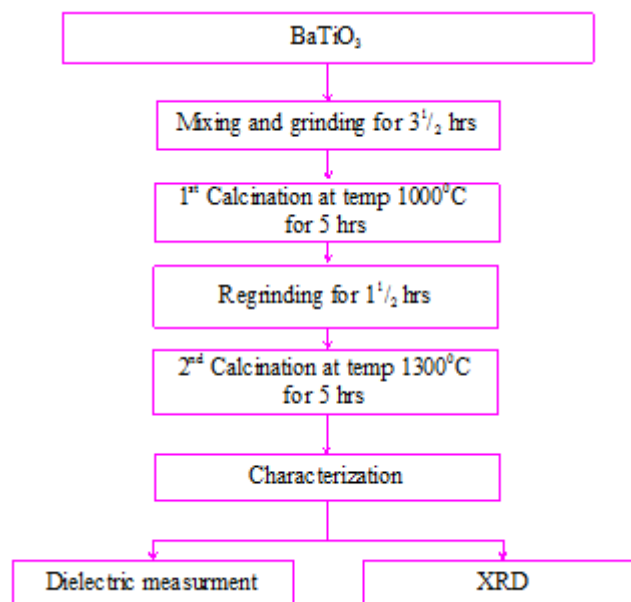

Fig. 1: Flow Chart for Preparation of BT

RESULTS AND DISCUSSION
Behavior of ε' and ε'' with δ_r & T: The graphical representation shows as the δ_r increases then ε' and ε'' are also increases systematically. It is due the density of BT material is to be increased material becomes more compact, as no voids are present. These values of ε' and ε'' are verified by using formulae of Bottcher's and L-L-L for solid bulk. The lowest particle size of 50 micron is considered as a solid bulk. It is found at $\delta_r = 1$, i.e. least particle size the values of ε' and ε'' are nearly same. Behavior of τ_r & σ_p with δ_r & temperature: As δ_r i.e.

packing density of BT material increases the values of τ_r & σ_p are also increases. The values are maximum at least particle size. The values of τ_r & σ_p decreases by increasing the temperature. From X-Ray diffraction study of BT: All the highest intensity peaks of BT sample are listed out and compared with the standard JCPDF (No. 01-075-0460). It is found the values of Bragg's angle (2θ), Interplanar spacing (d), intensity (I) and miller indices (hkl) are nearly matched with the values of BT sample.
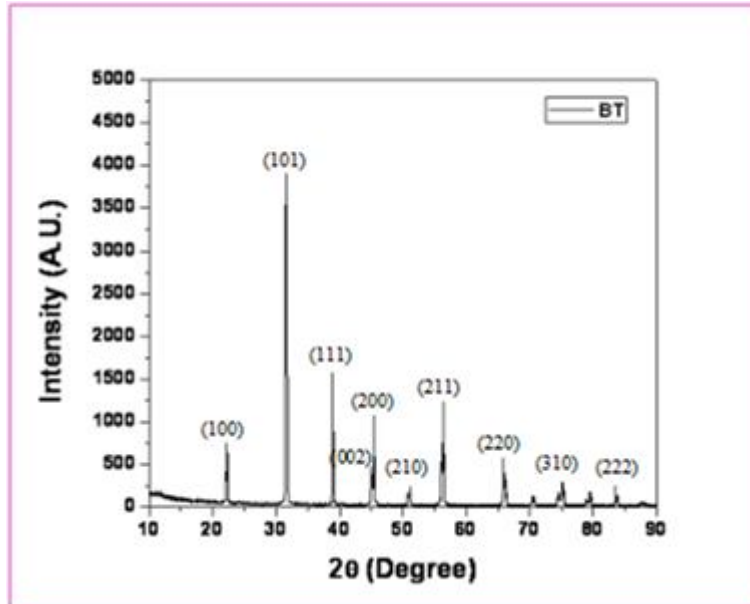

Fig. 2: XRD pattern of BaTiO$_3$

X-RAY DIFFRACTION

X-ray diffraction patterns of BaTiO$_3$ were recorded using X-ray diffractometer with Cu.ka (λ= 1.5418 A^0) radiation. (Make: Bruker AXS, Analytical instrument Pvt. Ltd. Germany, Model No. D2PHASER).

The Sharpness of BT diffraction peaks suggests better homogeneity and crystallization of the samples. The x-ray analysis indicates that the BaTiO$_3$ has single phase with tetragonal structure. All the reflection peaks were indexed using observed interplaner spacing d and lattice parameters with the JCPDS data of BT (Card no. 01-075-0460) were determined using a least squares refinement method. A good agreement between calculated and observed of values of all diffraction lines of BT suggests that (there is no change in the basic crystal structure) prepared sample is pervoskite ferroelectric material and it useful for electro optic waveguide.

The strongest reflection peak is observed at 2θ = 31.5208^0 (101) plane which is perfectly matched with the value form JCPDF as 2θ = 31.5208^0 (101). It is observed the 'd' spacing is at λ= 1.54184. The lattice parameters are as a= 3.994, b = 3.994, c = 4.034. The cell to axial ratio i.e. c/a = 1.010, a/b = 1.00 and c/b = 1.010. The crystal symmetry of BT is found to be centrosymmetric and cell volume is 64.35.
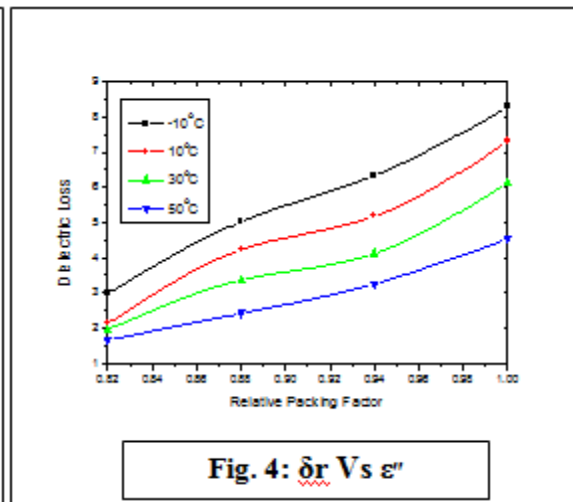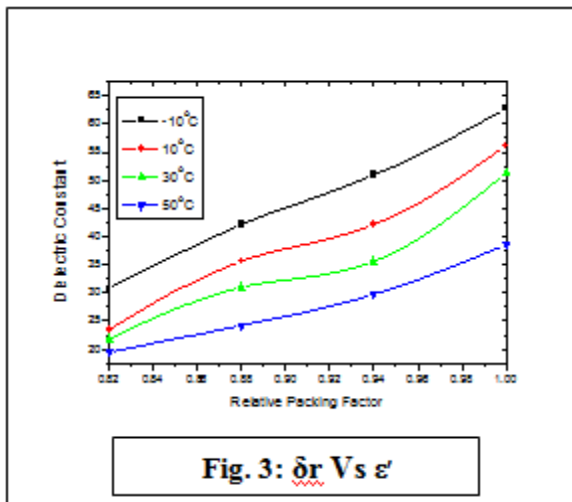
Table 1: Values of ϵ_p', ϵ_p'', Q x f, τ_p and σ_p of BaTiO$_3$ at different temperatures and particle sizes

Temperature (^{o}c)	Relative packing factor (δr)	ϵ_p'	ϵ_p''	tanδ	$Q = \dfrac{1}{tan\delta}$	Q x F GHz (9.85)	τ_p (P.S.)	σ_p
-10	0.82	30.80	3.00	0.097	10.31	101.55	1.57	1.64
	0.88	42.12	5.02	0.119	8.40	82.74	1.92	2.75
	0.94	50.98	6.34	0.124	8.06	79.39	2.00	3.48
	1.00	62.72	8.28	0.132	7.57	74.56	2.13	4.53
10	0.82	23.46	2.14	0.091	10.98	108.15	1.47	1.17
	0.88	35.62	4.22	0.118	8.47	83.42	1.91	2.31
	0.94	42.14	5.18	0.122	8.196	80.73	1.97	2.83
	1.00	56.18	7.31	0.130	7.69	75.74	2.10	4.00
30	0.82	21.79	1.96	0.089	11.23	110.61	1.44	1.07

	0.88	31.00	3.36	0.108	9.25	91.11	1.74	1.84
	0.94	35.62	4.12	0.115	8.69	85.59	1.86	2.25
	1.00	51.26	6.14	0.119	8.40	82.74	1.92	3.36
50	0.82	19.44	1.66	0.085	11.76	115.83	1.37	0.90
	0.88	24.22	2.42	0.099	10.10	99.48	1.60	1.32
	0.94	29.76	3.26	0.109	9.17	90.32	1.76	1.78
	1.00	38.54	4.54	0.117	8.54	84.11	1.89	2.48

Table 2: Measured and calculated Values of ϵ_s' and ϵ_s'', for solid bulk from BaTiO$_3$ at different temperatures and packing fractions

Temperature (°c)	Relative packing factor (δr)	Measured value ϵ_p'	Calculated from Bottcher's ϵ_s'	Calculated from L-L-L ϵ_s'	Measured value ϵ_p''	Calculated from Bottcher's ϵ_s'	Calculated from L-L-L ϵ_s'
- 10	0.82	30.80	41.58	41.58	3.00	4.45	4.10
	0.88	42.12	51.01	51.01	5.02	6.47	6.12
	0.94	50.98	55.87	55.87	6.34	7.16	6.96
	1.00	62.72	62.72	62.72	8.28	8.28	8.28
+ 10	0.82	23.46	31.53	31.5	2.14	3.17	2.92
	0.88	35.62	43.09	43.09	4.22	5.43	5.14
	0.94	42.14	46.15	46.16	5.18	5.85	5.69
	1.00	56.18	56.18	56.18	7.31	7.31	7.31
+ 30	0.82	21.79	29.24	29.24	1.96	2.90	2.68
	0.88	31.00	37.45	37.45	3.36	4.32	4.09
	0.94	35.62	38.99	38.99	4.12	4.65	4.52
	1.00	51.26	51.26	51.26	6.14	6.14	6.14
+ 50	0.82	19.44	26.02	26.02	1.66	2.45	2.27
	0.88	24.22	29.19	29.19	2.42	3.11	2.95
	0.94	29.76	32.55	32.55	3.26	3.68	3.58
	1.00	38.54	38.54	38.54	4.54	4.54	4.54

Fig. 3: δr Vs ε'

Fig. 4: δr Vs ε''

Fig. 5: δr Vs Q=1/tanδ

Fig. 6: δr Vs Q x F

Fig. 7: δr Vs τ_p

Fig. 8: δr Vs σ_p
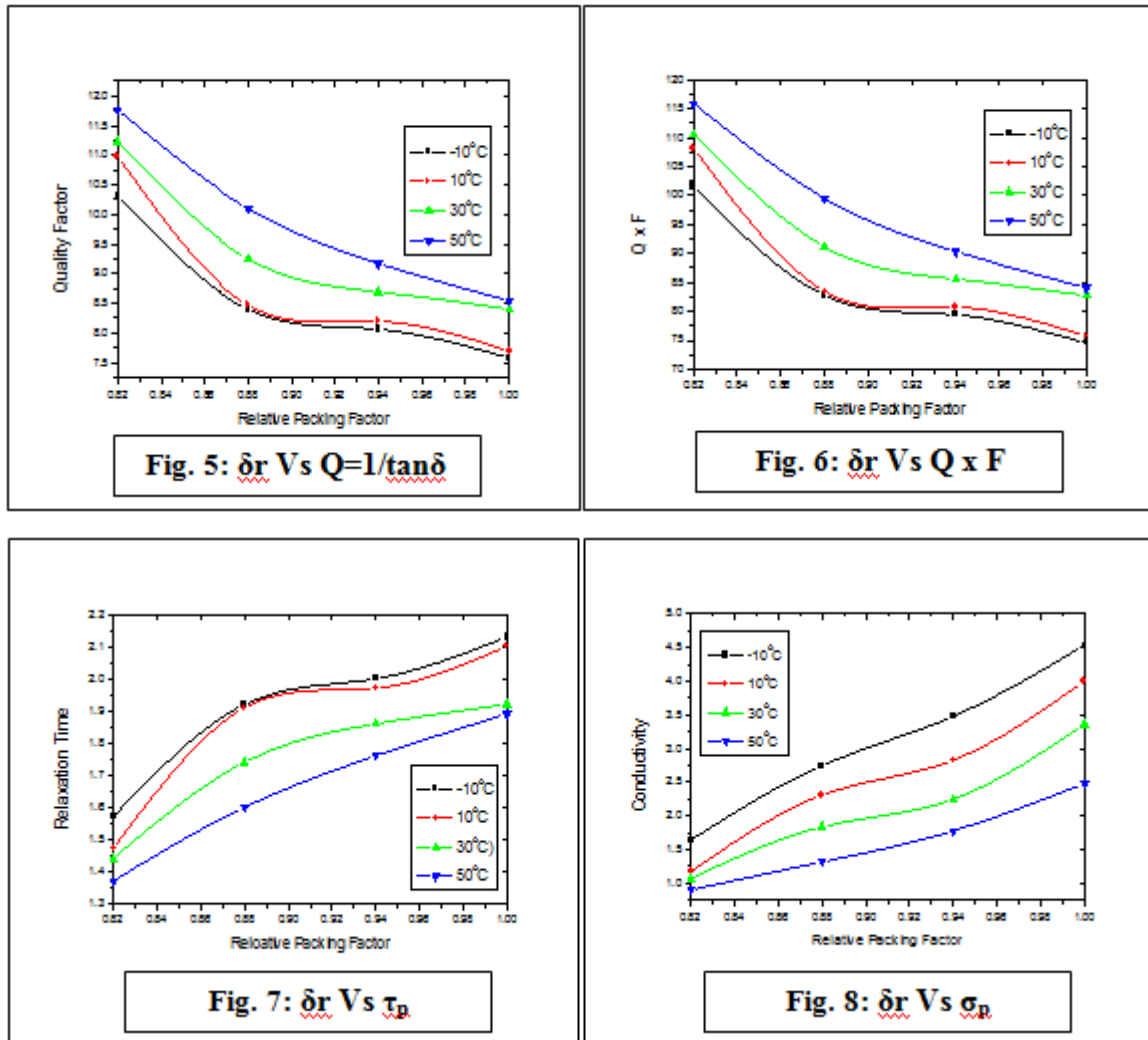
RESULTS AND DISCUSSION

The values of ε'_p and ε''_p , tan, Q, Q x F, τ , σ for various temperature and packing factor.

1. It is found systematic increase temperature. This is expected because at higher values of δr the interparticle hindrance offered to the dipolar motion for a compact medium is much higher than less bounded particles.

2. The calculations of quality factor (Q x F) where f is resonant microwave frequency are found decrease in Q x F values for decreasing particle size and by increasing temperature the Q x F values increases.

3. The values of relaxation time (τ_p) and conductivity (σ_p) are increases systematically by increasing δr and decreases by increasing of temp. It is due to, when polar molecules are very large, then under the influence of high frequency the rotary motion of polar molecules of a system is not sufficiently rapid to attain equilibrium with field.

4. The increase in τ_p by increasing δr is due to increasing hindrance to the process of polarization. The increase in σ_p suggests that at higher compaction, no microcracks develop in sample due to high mechanical pressure.

5. As temp increases, τ_p decreases may be due to increase in the effective length of dipole. Again increase in temp, causes an increase in energy loss due to the large number of collisions and thereby decreasing τ_p.

CONCLUSION

1. The highest value of ε'=62.72 is observed at temperature = -10°C and at δ_r =1. The lowest value of ε'=19.44, found dielectric constant varies from 19.44 to 62.72 at temperature range (50°C, 30°C, 10°C, -10°C).

2. There is fair agreement between the values obtained experimentally and theoretically. Hence, the formulae of Bottcher's and L-L-L work well between powder and solid bulk.

3. The crystal structure of BT material is orthorhombic.

4. From PDF card, the crystal data as a lattice parameters are a=3.994, b=3.994, c=4.034 and crystal data axial ratio are c/a=1.010, a/b=1.00, c/b=1.010.

5. The crystal symmetry of BT is centrosymmetric.

REFERENCES

1. S. Upadhyay, et.al., "Synthesis, Structure and electrical behavior of nickel-doped barium stannate", J. Alloys Compd., vol. 432, no. 1-2, pp. 258-264, (April 2007).

2. Yoon, S. M. and Ishiwara, H., Memory Operations of 1T2C-TypeFerroelectirc Memory Cell with Excellent Data Retention Characteristics. IEEE Trans. Electron. Dev. 48, 2002-2008, (2001).

3. Y. L. Wang, A. K. Tagantsev, D. Damjanovic, and N. Setter, "Giant domain wall contribution to the dielectric susceptibility in $BaTiO_3$ single crystals", *App. J. Phys. Leu.,* vol. 91, no. 6, p.062905, (Aug. 2007).

4. Y. L. Wang, Z. B. He, D. Damjanovic, A. K. Tagantsev, G. C. Deng, and N. Setter, "Unusual dielectric behavior and domain structure in rhombohedral phase of $BaTiO_3$ single crystals," *J. Appl Phys.,* vol. 110, no. 1, p. 014101, (Jul. 2011).

5. M. B. Smith, K. Page, T. Siegrist, P. L. Redmond, E. C. Walter, R. Seshadri, L. E. Brus, and M. L. Steigerwald, "Crystal Structure and the Paraelearic-to-Ferroelectric Phase Transition of Nanoscale BaTiO3," *J. Am. Chem. Soc.,* Vol. 130, no. 22, pp. 6955-6963, (June 2008)

6. S. Lin, T. Lu, C. Jin, and X. Wang, "Size effect on the dielectric properties of $BaTiO_3$ nanoceramks in a modified Ginsburg-Landau Devonshire diermodynamic theory", *Phys. Rev. B,* vol. 74, no. 13, p. 134115, (Oct. 2006).

SOL-GEL AUTO COMBUSTION SYNTHESIS, STRUCTURAL AND INFRARED PROPERTIES OF NICKEL FERRITE NANOPARTICLES

Avinash Patil[1], Ankush Bhosale[1], Vishnu Raut[2], Mahesh M. Hivrekar[2], P. S. Aghav[1], V. D. Murumkar[1]
[1]Department of Physics, Vivekanand College, Aurangabad
[2]Department of Physics, Dr. Babasaheb Ambedkar Marathwada University, Aurangabad

ABSTRACT

Nickel ferrite ($NiFe_2O_4$) in nanocrystalline form with maximum yield and phase purity was obtained through citric acid assisted sol-gel auto combustion synthesis. The prepared nanoparticles were sintered at 600 °C for 4 h to make pure phase formation. Further, the sintered nanoparticles were characterized by X-ray diffraction (XRD) and spectrophotometer for structural and infrared characterizations respectively. The room temperature XRD pattern confirmed the formation of single phase with cubic spinel structure of the sintered nickel ferrite nanoparticles. The particle size estimated through Scherrer's formula was found to be 28 nm, which confirms the nanocrystalline nature of the prepared nickel ferrite nanoparticles. The IR spectra recorded in the range 400 cm^{-1} to 1000 cm^{-1} has confirmed the formation of spinel structure with two characteristic bands near 400 cm^{-1} and 600 cm^{-1}.

Keywords: Sol-gel auto combustion, Nickel ferrite, XRD, IR

1. INTRODUCTION
In the recent years, nanosized spinel ferrites have gained much importance from basic and applied research point of view. The applications of nanocrystalline spinel ferrites have opened new prospects in various field viz. electronics, information technology, storage media, biomedical, transport, ferrofluids, etc [1-3]. The spinel ferrites at nanoscale exhibit the novel properties like superparamagnetism, quantum confinement, single domain structure, high permeability, and chemical stability. The magnetic and electrical properties of spinel ferrites primly depend on many parameters like synthesis methods, synthesis parameters, cation distribution, nature and type of dopant and exposure to various radiations [4, 5].

Recently, technologically important nickel spinel ferrite has attracted considerable research interest because of the necessity of the miniaturization of the electronic devices in which it is being employed. It has high electrical resistivity, low dielectric loss, good chemical stability etc. which finds application in microwave devices, recording heads, antenna rods etc [6, 7]. Nanostructured nickel ferrite exhibits small hysteresis and hence, is considered as a good core material for power transformers and telecommunication applications. Nanoparticles of nickel ferrite are also used in gas and humidity sensing, and catalytic applications.

In last decade, spinel ferrite nanoparticles have been synthesized by several methods, such as, co-precipitation, hydrothermal, solvothermal, sonochemical, reverse micelles, sol–gel auto-combustion, etc [8-9]. Among the synthesis methods, the combustion synthesis has enthralled a significant interest in fabricating the homogeneous, un-agglomerated, multi component metal oxides, because of its inexpensive precursors, short preparation time, modest heating and relatively simple manipulations. The combustion method is based on the mixing of metal nitrates which is oxidizing agent and fuel acts as a reducing agent.

The fuel in combustion method plays a vital role in determining morphology, grain size and crystal structure and consequently its physical properties. Nowadays, green synthesis route emerged as a simple and viable alternative to the chemical synthesis methods and physical methods. Herein we report, the sol–gel auto combustion synthesis of $NiFe_2O_4$ nanoparticles and their structural and infrared properties.

2. EXPERIMENTAL
Nickel ferrite ($NiFe_2O_4$) nanoparticles were prepared by sol-gel auto combustion method using citric acid as a fuel. AR grade chemicals such as nickel nitrate ($Ni(NO_3)_2 \cdot 6H_2O$), ferric nitrate ($Fe(NO_3)_3 \cdot 9H_2O$) and citric acid ($C_6H_8O_7$) were used for the sol-gel synthesis. The prepared nanoparticles were sintered at the temperature 600°C for 4 h. The powder X-ray diffraction pattern of sintered nanoparticles was carried out using Bruker D8 Advance X-ray diffractometer with Cu-Kα radiation ($\lambda = 0.15406$ nm) to confirm the phase and structure of the prepared nanoparticles. The IR spectra were recorded with the help of spectrophotometer in the range of 400 cm^{-1} to 1000 cm^{-1}.

3. RESULTS AND DISCUSSIONS
3.1 X-ray diffraction studies
X-ray diffraction pattern of nickel ferrite nanoparticles is shown in fig. 1. The X-ray diffraction pattern reveals all the allowed cubic spinel structured planes. All the peaks in the XRD pattern matches well with the JCPDS Card no. #10-325. The analysis of XRD pattern also revealed the formation of single phase compound with nanocrystalline nature. Using XRD data various structural parameters were investigated.

The average crystallite size (t) was obtained from the Scherrer's equation,

$$t = \frac{0.9\lambda}{\beta \cos\theta} \quad nm \qquad \dots 1$$

Using the values of Bragg's angle 2θ and interplanar spacing d, the values of lattice constant for all the composition are calculated using the following relation.

$$a = d\sqrt{h^2 + k^2 + l^2} \; \mathring{A} \qquad \dots 2$$

The X-ray density of nickel ferrite nanoparticles was calculated using the standard relation given by equation,

$$d_X = \frac{Z \times M}{V \times N_A} \quad gm/cm^3 \qquad \dots 3$$

The bulk density of the present sample was determined using Archimedes principle. Toluene was used as a liquid medium to measure the bulk density. The value of bulk density is given in table 1.

The percentage porosity of the present sample was calculated from the following relation;

$$P = 1 - \frac{d_B}{d_X} \; \% \qquad \dots 4$$

The obtained values of crystallite size (t), lattice constant (a), X-ray density (d_X), bulk density (d_B) and porosity (P%) are listed in table 1.
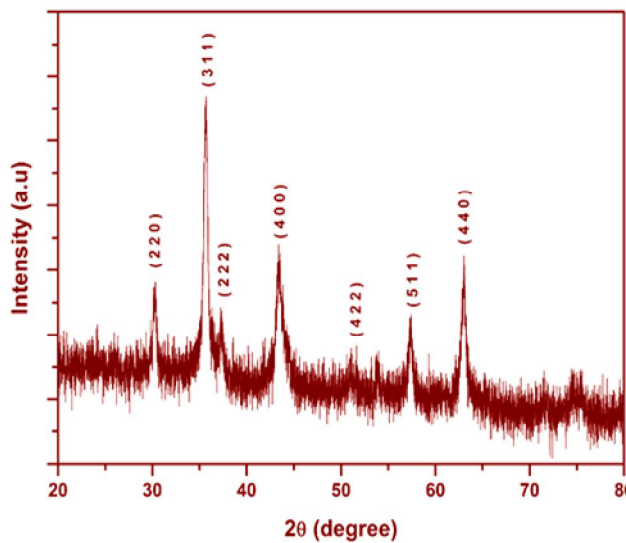

Fig. – 1: X-ray diffraction pattern of $NiFe_2O_4$ nanoparticles

Table 1 Crystallite size (t), Lattice parameter (a), X-ray density (d_x), bulk density (d_B) and porosity (P %) $NiFe_2O_4$ nanoparticles

Composition	t (nm)	a (Å)	d_x (gm/cm³)	d_B (gm/cm³)	P (%)
NiFe₂O₄	28	8.314	5.41	3.78	30.12

3.2 Infrared studies
The IR spectrum of the sample was recorded in the range from 1000 cm⁻¹ to 400 cm⁻¹ which is shown in Fig. 2. Generally, it is assigned to the vibrations of ions in the crystal lattice of the solids. In particular, there are two main broad metal-oxygen bonds which confirm the formation of all spinel oxides. The presence of the peak which is noticed at 608 cm⁻¹ (corresponding to the stretching vibrations of metal at the tetrahedral site (M_{tetra}–O)) and the peak which is noticed at 415 cm⁻¹ (corresponding to the stretching vibration of the metal at the octahedral site (M_{octa}–O)) proves that the formed product is spinel ferrite.
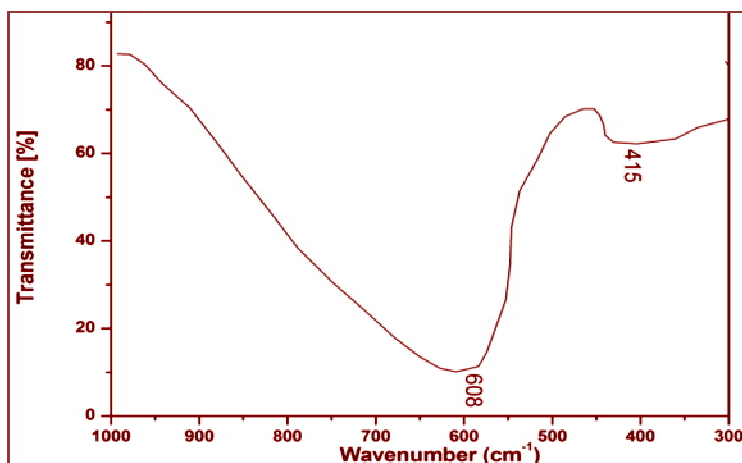
Fig. – 2: IR spectrum of NiFe$_2$O$_4$ nanoparticles

4. CONCLUSION

Nickel ferrite nanoparticles were successfully obtained using sol-gel auto combustion synthesis method. The XRD pattern analysis confirmed the pure phase cubic formation and nanocrystalline nature of the prepared nanoparticles. The particle size estimated through Scherrer's formula was found to be 28 nm, which confirms the nanocrystalline nature of the prepared nickel ferrite nanoparticles. The IR spectra recorded in the range 400 cm^{-1} to 1000 cm^{-1} has confirmed the formation of spinel structure with two characteristic bands near 400 cm^{-1} and 600 cm^{-1}.

5. REFERENCE

[1]   M. Pardavi-Horvath, Microwave applications of soft ferrites, Journal of Magnetism and Magnetic Materials, 215 (2000) 171-183.

[2]   J. Smit, H.P.J. Wijn, Ferrites: physical properties of ferrimagnetic oxides in relation to their technical applications, (1959).

[3]   R. Valenzuela, Novel applications of ferrites, Physics Research International, 2012 (2012).

[4]   R.F. Soohoo, Theory and application of ferrites, (1960).

[5]   J. Smit, H. Wijn, Physical properties of ferrites, Advances in Electronics and Electron Physics, 6 (1954) 69-136.

[6]   E. Gorter, Some properties of ferrites in connection with their chemistry, Proceedings of the IRE, 43 (1955) 1945-1973.

[7]   F. Bertaut, R. Pauthenet, Crystalline structure and magnetic properties of ferrites having the general formula 5Fe2O3. 3M2O3, Proceedings of the IEE-Part B: Radio and Electronic Engineering, 104 (1957) 261-264.

[5]   D.R. Jimenez, M. Gilliam, Ultrastructure of the ventriculus of the honey bee, Apis mellifera (L.): cytochemical localization of acid phosphatase, alkaline phosphatase, and nonspecific esterase, Cell and Tissue Research, 261 (1990) 431-443.

[6]   E.R. Balasooriya, C.D. Jayasinghe, U.A. Jayawardena, R.W.D. Ruwanthika, R. Mendis de Silva, P.V. Udagama, Honey mediated green synthesis of nanoparticles: new era of safe nanotechnology, Journal of Nanomaterials, 2017 (2017)

[7]   M. George, A.M. John, S.S. Nair, P. Joy, M. Anantharaman, Finite size effects on the structural and magnetic properties of sol–gel synthesized NiFe2O4 powders, Journal of Magnetism and Magnetic Materials, 302 (2006) 190-195.

[8]   Pardavi-Horvath, Martha. "Microwave applications of soft ferrites." Journal of Magnetism and Magnetic Materials 215 (2000): 171-183.

[9]   Sugimoto, Mitsuo. "The past, present, and future of ferrites." Journal of the American Ceramic Society 82.2 (1999): 269-280.

[10]   K. Nejati, R. Zabihi, Preparation and magnetic properties of nano size nickel ferrite particles using hydrothermal method, Chemistry Central Journal, 6 (2012) 23.

INFLUENCE OF PARTICLE SIZE ON STRUCTURE AND MAGNETIC PROPERTIES OF CADMIUM FERRITE (CDFE$_2$O$_4$) NANOPARTICLES

Atul P. Keche[1], Ashok V. Humbe[2], S. S. Deshmukh[3], Manisha R. Patil[3], M. N. Sarnaik[1], S. J. Shukla[2], K. M. Jadhav[2]

[1]Department of Physics, Muktanand College, Gangapur, Aurangabad
[2]Department of Physics, Dr. B. A. M. University, Aurangabad
[3]Department of Physics, Deogiri College, Aurangabad

ABSTRACT

In the present work, influence of varying particle size of cadmium ferrite nanoparticles synthesized via ceramic and sol-gel auto combustion method on the structure and magnetic properties is reported. Cadmium ferrite in bulk and nanosize form was prepared by ceramic technique using AR grade oxides of respective ions (CdO and Fe$_2$O$_3$) and sol-gel auto combustion method using AR grade nitrates of respective ions (Cd (NO$_3$)$_2$ • 6H$_2$O and Fe (NO$_3$)$_3$ • 9H$_2$O). The X-ray diffraction technique was used to study the structure while pulse hysteresis loop technique was used to study the magnetic properties. The analysis of XRD patterns reveals the formation of single phase cubic spinel structure. The XRD data was used to obtain the particle size. The particle size of the ceramically and sol-gel synthesized CdFe$_2$O$_4$ calculated using Scherrer's formula was found to be – nm and – nm respectively. The lattice constant of both the samples is in reported range. The M-H hysteresis curve shows remarkable changes in saturation magnetization and coercivity. Thus, the particle size shows strong influence on the structure and the magnetic properties of cadmium ferrite.

Keywords: CdFe$_2$O$_4$, ceramic method, sol-gel auto combustion synthesis, magnetic properties.

1. INTRODUCTION

Ferrites composed of iron oxide and metal oxide are the ferrimagnetic materials exhibits remarkable electrical and magnetic properties which are useful in many technological applications. Ferrites in bulk form are used in transformers cores, antenna rods, memory storages etc. The nanosize ferrites are of current interest to the scientist and technologist due to their smaller size and large surface area. The nanosize ferrites have applications in the field of sensors, catalysts, water purification, drug delivery, hyperthermia etc [1-3].

The important electrical and magnetic properties are mostly depends on the particle size that obtained through synthesis method. On the basis of crystal structure, ferrites are divided into three classes namely spinel ferrite, rare earth garnet and hexagonal ferrites. Spinel ferrites are soft in nature and are studied by many researchers due to their overwhelming properties. The spinel ferrite is represented by the formula MFe$_2$O$_4$ where, M stands for divalent metal ion like Zn, Cd, Co, Ni etc [4-5]. The structure of spinel ferrite is cubic with space group Fd3mO^h$_7$. The structures of spinel ferrite possess two intestinal sites namely tetrahedral (A) and octahedral [B] sites in which cations of different valence can occupy. Usually, spinel ferrites are prepared in bulk form by ceramic method. The ceramic method involves high temperature sintering. Wet chemical methods like chemical coprecipitation, hydrothermal, sol-gel auto combustion etc are nowadays commonly used for the synthesis of nanosized spinel ferrite. The wet chemical method requires low temperature of the order of 60℃ to 100℃ [6-7].

It is reported in literature that, the structural, electrical, magnetic, dielectric and other properties of nanosize spinel ferrites are superior to that of the bulk spinel ferrite. However, to establish this fact, very few reports are available in literature [8-11]. In the present communication, attempt is made to understand the influence of particle size on the structural and magnetic properties of CdFe$_2$O$_4$.

2. EXPERIMENTAL

2.1 Synthesis of Bulk cadmium ferrite (Ceramic method)

In ceramic synthesis, cadmium oxide (CdO) and ferric oxide (Fe$_2$O$_3$) of AR grade were mixed together in stoichiometric proportion and ground using Agate pestle mortar for few hours to obtain homogeneous mixture. The mixed homogeneous powders were presintered at 900℃ for 12 h and again reground for 4 h. In the final sintering, the material is held at 1100℃ for 12 h and slowly cooled to room temperature to obtain pure cadmium ferrite.

2.2 Synthesis of nanosized cadmium ferrite (Sol-gel auto combustion method)

The cadmium ferrite in nanosized form was prepared by sol-gel auto combustion method using AR grade nitrates of respective ions (Cd (NO$_3$)$_2$ • 6H$_2$O and Fe (NO$_3$)$_3$ • 9H$_2$O). The citric acid was used as a fuel. The detailed method of synthesis is explained in our previous reports.

2.3 Characterization

Room temperature X-Ray diffraction patterns were recorded using Philips X-ray diffractometer (model 3710, at TIFR Mumbai). XRD patterns were recorded in the 2θ range of 20º to 80º using Cu-ka radiation. The magnetic properties were measured using pulse field hysteresis loop technique (Magneta).

3. RESULTS AND DISCUSSION

3.1 X-ray diffraction

Room temperature X-ray diffraction patterns of ceramically and sol-gel synthesized cadmium ferrite is depicted in fig. 1. It is evident from figure 1 that, the XRD pattern shows all the reflections which belongs to cubic spinel structure. A marked difference in reflections is observed. Ceramically prepared samples shows sharp and intense reflection, while sol-gel synthesized cadmium ferrite shows slightly broader reflections. The analysis of both the XRD patterns proves that, the samples possess cubic spinel structure. No extra peak other than cubic spinel structure is observed in the XRD pattern.

The most intense peak (311) of the XRD pattern was selected to estimate the particle size. Debye Scherrer formula given by equation (1) was used to estimate the particle size.

$$D = 0.9 \, \lambda / \, \beta \cos\theta \qquad \qquad \dots 1$$

The particle size of ceramically prepared cadmium ferrite is of the order of – nm. While the particle size of sol-gel prepared cadmium ferrite is of the order of – nm. Thus, it is observed from particle size of ceramically prepared sample is greater than that of sol-gel synthesized sample.

To establish the influence of particle size on structural properties, the lattice constant, unit cell volume and X-ray density structural parameters were obtained by standard relations. The values of all these structural parameters along with particle size are summarized in table 1. It is evident from table 1 that, the values of lattice constant, X-ray density and unit cell volume of sol-gel synthesized $CdFe_2O_4$ are greater than that of ceramically prepared samples. Thus, it is confirmed that, the particle size influences strongly the structural properties of cadmium ferrite.
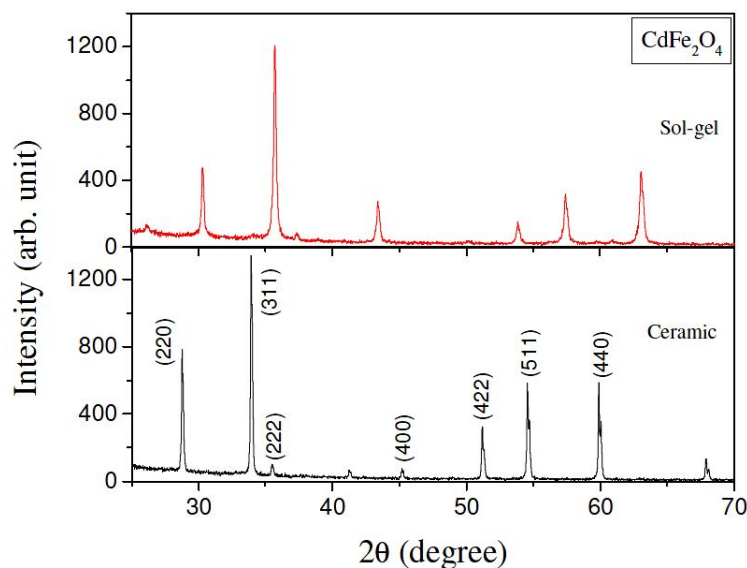

Fig. – 1: XRD pattern of ceramically and sol-gel synthesized $CdFe_2O_4$

Table – 1: Values of lattice constant (a), unit cell volume (V), X-ray density (d_x) and crystallite size (t) of ceramically and sol-gel synthesized $CdFe_2O_4$

Parameter	a (Å)	V (Å³)	d_x (gm/cm³)	t
Ceramic	5.329	151.33	5.744	3.2 μm
Sol-gel	5.342	152.44	5.445	31 nm

3.2 Magnetic properties

Figure 2 shows the M-H hysteresis curves for ceramically and sol-gel synthesized $CdFe_2O_4$ samples recorded at room temperature using pulsed field hysteresis loop technique. The M-H curve exhibits typical ferrimagnetic behavior characterizing the spinel structure of the prepared samples. Using M-H curve the values of saturation

magnetization, coercivity and remenance magnetization were measured and their values are given in table 2. It is evident from table 2 that, the magnetic properties represented by saturation magnetization show enhanced value for sol-gel synthesized cadmium ferrite while, coercivity shows decreased value for sol-gel synthesized cadmium ferrite. Thus, it can be noticed from table 2 that, the particle size has a strong influence on the magnetic properties of cadmium ferrite.
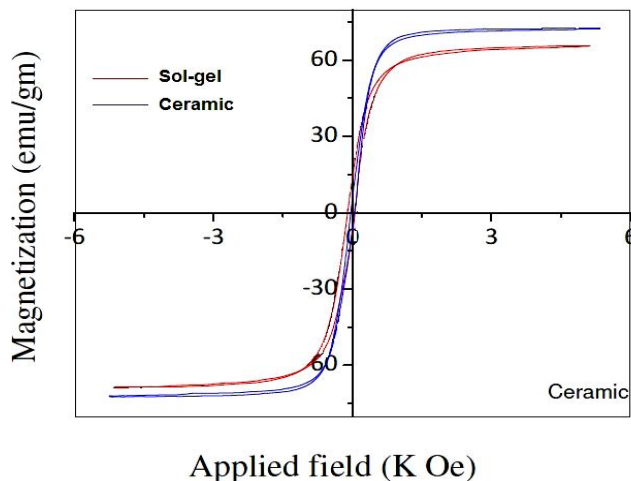

Fig. – 2: M-H curves of ceramically and sol-gel synthesized $CdFe_2O_4$

Table – 2: Values of saturation magnetization (M_S), remenance magnetization (M_r) and coercivity (H_C) of ceramically and sol-gel synthesized $CdFe_2O_4$

Parameter	M_S (emu/gm)	M_r (emu/gm)	H_C (Oe)
Ceramic	65.47	15.22	108.23
Sol-gel	57.94	12.89	121.70

4. CONCLUSION

Cadmium ferrite in bulk and nanosized form has been prepared successfully using ceramic and sol-gel auto combustion method respectively. The lattice constant, X-ray density and other structural parameters shows enhanced values for sol-gel synthesized cadmium ferrite sample. The saturation magnetization also shows enhanced value for sol-gel synthesized cadmium ferrite sample. The coercivity of the sol-gel synthesized sample show decreased for sol-gel synthesized cadmium ferrite. Thus, the structural and magnetic study of th ceramically and sol-gel auto combustion synthesized cadmium ferrite show strong influence of particle size.

REFERENCES

[1] K. Rama Krishna , Dachepalli Ravinder , K. Vijaya Kumar, Utpal S. Joshi , V. A. Rana , Abrham Lincon: World J. Conden. Matter Phys., 2 (2012) 57.

[2] J. L. Dormann and M. Nogues: J. Phys. Conden. Mater. 2 (5) (1990) 1223.

[3] N. Rezlescu, E. Rezlescu, C. Pasnicu and M. L. Craus: J. Phys. Conden. Matter. 6(29) (1994) 5707.

[4] A. E. Virden and K. O. Grady: J. Magn. Magn. Mater. 290-291(2) (2005) 868.

[5] E. De Fazio, P. G. Bercoff, S. E. Jacobo: J. Magn. Magn. Mater. 323 (22) (2011) 2813.

[6] V. Tsakaloudi, V. T. Zaspalis: J. Magn. Magn. Mater. 322 (2010) 517.

[7] Souilah Zahi, Mansor Hashim, A. R. Daud: J. Magn. Magn. Mater. 308 (2007) 177.

[8] Uzma Ghazanfar, S. A. Siddiqi, G. Abbas: Mater. Sci. & Engineering B 118 (2005) 132.

[9] C. Radhakrishanmurthy, S. D. Likhite and P. W. Sahastrabudhe: Ind. Acd. Sci. 87 (a) (1978) 245.

[10] Q. J. Han, D. H. Ji, G. D. Tang, Z. Z. Li, X. Hou, W. H. Qi, R. R. Bian and S. R. Liu: J. Phys. Status Solid. 209, (4) (2012) 766–772.

[11] P. A. Shaikh, R. C. Kambale, A. V. Rao, Y. D. Kolekar: J. Magn. Magn. Mater. 322 (2010) 718.

MANUSCRIPT SUBMISSION

GUIDELINES FOR CONTRIBUTORS

1. Manuscripts should be submitted preferably through email and the research article / paper should preferably not exceed 8 – 10 pages in all.

2. Book review must contain the name of the author and the book reviewed, the place of publication and publisher, date of publication, number of pages and price.

3. Manuscripts should be typed in 12 font-size, Times New Roman, single spaced with 1" margin on a standard A4 size paper. Manuscripts should be organized in the following order: title, name(s) of author(s) and his/her (their) complete affiliation(s) including zip code(s), Abstract (not exceeding 350 words), Introduction, Main body of paper, Conclusion and References.

4. The title of the paper should be in capital letters, bold, size 16" and centered at the top of the first page. The author(s) and affiliations(s) should be centered, bold, size 14" and single-spaced, beginning from the second line below the title.

<div align="center">

First Author Name1, Second Author Name2, Third Author Name3

1Author Designation, Department, Organization, City, email id

2Author Designation, Department, Organization, City, email id

3Author Designation, Department, Organization, City, email id

</div>

5. The abstract should summarize the context, content and conclusions of the paper in less than 350 words in 12 points italic Times New Roman. The abstract should have about five key words in alphabetical order separated by comma of 12 points italic Times New Roman.

6. Figures and tables should be centered, separately numbered, self explained. Please note that table titles must be above the table and sources of data should be mentioned below the table. The authors should ensure that tables and figures are referred to from the main text.

EXAMPLES OF REFERENCES

All references must be arranged first alphabetically and then it may be further sorted chronologically also.

- **Single author journal article:**

Fox, S. (1984). Empowerment as a catalyst for change: an example for the food industry. *Supply Chain Management*, *2*(3), 29–33.

Bateson, C. D.,(2006), 'Doing Business after the Fall: The Virtue of Moral Hypocrisy', Journal of Business Ethics, 66: 321 – 335

- **Multiple author journal article:**

Khan, M. R., Islam, A. F. M. M., & Das, D. (1886). A Factor Analytic Study on the Validity of a Union Commitment Scale. *Journal of Applied Psychology*, *12*(1), 129-136.

Liu, W.B, Wongcha A, & Peng, K.C. (2012), "Adopting Super-Efficiency And Tobit Model On Analyzing the Efficiency of Teacher's Colleges In Thailand", International Journal on New Trends In Education and Their Implications, Vol.3.3, 108 – 114.

- **Text Book:**
Simchi-Levi, D., Kaminsky, P., & Simchi-Levi, E. (2007). *Designing and Managing the Supply Chain: Concepts, Strategies and Case Studies* (3rd ed.). New York: McGraw-Hill.

S. Neelamegham," Marketing in India, Cases and Reading, Vikas Publishing House Pvt. Ltd, III Edition, 2000.

- **Edited book having one editor:**
Raine, A. (Ed.). (2006). *Crime and schizophrenia: Causes and cures.* New York: Nova Science.

- **Edited book having more than one editor:**
Greenspan, E. L., & Rosenberg, M. (Eds.). (2009). *Martin's annual criminal code:Student edition 2010.* Aurora, ON: Canada Law Book.

- **Chapter in edited book having one editor:**
Bessley, M., & Wilson, P. (1984). Public policy and small firms in Britain. In Levicki, C. (Ed.), *Small Business Theory and Policy* (pp. 111–126). London: Croom Helm.

- **Chapter in edited book having more than one editor:**
Young, M. E., & Wasserman, E. A. (2005). Theories of learning. In K. Lamberts, & R. L. Goldstone (Eds.), *Handbook of cognition* (pp. 161-182). Thousand Oaks, CA: Sage.

- **Electronic sources should include the URL of the website at which they may be found, as shown:**
Sillick, T. J., & Schutte, N. S. (2006). Emotional intelligence and self-esteem mediate between perceived early parental love and adult happiness. *E-Journal of Applied Psychology*, 2(2), 38-48. Retrieved from http://ojs.lib.swin.edu.au/index.php/ejap

- **Unpublished dissertation/ paper:**
Uddin, K. (2000). A Study of Corporate Governance in a Developing Country: A Case of Bangladesh (Unpublished Dissertation). Lingnan University, Hong Kong.

- **Article in newspaper:**
Yunus, M. (2005, March 23). Micro Credit and Poverty Alleviation in Bangladesh. *The Bangladesh Observer*, p. 9.

- **Article in magazine:**
Holloway, M. (2005, August 6). When extinct isn't. *Scientific American, 293*, 22-23.

- **Website of any institution:**
Central Bank of India (2005). *Income Recognition Norms Definition of NPA*. Retrieved August 10, 2005, from http://www.centralbankofindia.co.in/ home/index1.htm, viewed on

7. The submission implies that the work has not been published earlier elsewhere and is not under consideration to be published anywhere else if selected for publication in the journal of Indian Academicians and Researchers Association.

8. Decision of the Editorial Board regarding selection/rejection of the articles will be final.